PB84-224393

# Evaluation and Demonstration of Low-NOx Burner Systems for TEOR (Thermally Enhanced Oil Recovery) Steam Generators Design Phase Report

Energy and Environmental Research Corp.
Irvine, CA

Prepared for

Industrial Environmental Research Lab.
Research Triangle Park, NC

Jul 84

U.S. Department of Commerce
National Technical Information Service
NTIS

PB84-224393

EPA-600/7-84-076
July 1984

# EVALUATION AND DEMONSTRATION OF LOW-$NO_x$ BURNER SYSTEMS FOR TEOR STEAM GENERATORS

## Design Phase Report

by

G. C. England
M. P. Heap
Y. Kwan
R. Payne

Energy and Environmental Research Corporation
18 Mason
Irvine, CA 92714-4190

EPA Contract 68-02-3692

Project Officer:

W. S. Lanier
Industrial Environmental Research Laboratory
U.S. Environmental Protection Agency
Research Triangle Park, NC 27711

INDUSTRIAL ENVIRONMENTAL RESEARCH LABORATORY
OFFICE OF RESEARCH AND DEVELOPMENT
U.S. ENVIRONMENTAL PROTECTION AGENCY
RESEARCH TRIANGLE PARK, NC 27711

REPRODUCED BY
NATIONAL TECHNICAL
INFORMATION SERVICE
U.S. DEPARTMENT OF COMMERCE
SPRINGFIELD, VA. 22161

## TECHNICAL REPORT DATA

*(Please read Instructions on the reverse before completing)*

| | | |
|---|---|---|
| 1. REPORT NO.<br>EPA-600/7-84-076 | 2. | 3. RECIPIENT'S ACCESSION NO.<br>PB8 4 224393 |
| 4. TITLE AND SUBTITLE Evaluation and Demonstration of Low-NOx Burner Systems for TEOR Steam Generators--Design Phase Report | | 5. REPORT DATE<br>July 1984 |
| | | 6. PERFORMING ORGANIZATION CODE |
| 7. AUTHOR(S) G. C. England, M. P. Heap, Y. Kwan, and R. Payne | | 8. PERFORMING ORGANIZATION REPORT NO. |
| 9. PERFORMING ORGANIZATION NAME AND ADDRESS<br>Energy and Environmental Research Corporation<br>18 Mason<br>Irvine, California 92714-4190 | | 10. PROGRAM ELEMENT NO. |
| | | 11. CONTRACT/GRANT NO.<br>68-02-3692 |
| 12. SPONSORING AGENCY NAME AND ADDRESS<br>EPA, Office of Research and Development<br>Industrial Environmental Research Laboratory<br>Research Triangle Park, NC 27711 | | 13. TYPE OF REPORT AND PERIOD COVERED<br>Phase report; 10/81 - 2/83 |
| | | 14. SPONSORING AGENCY CODE<br>EPA/600/13 |

15. SUPPLEMENTARY NOTES IERL-RTP project officer W. S. Lanier is no longer with the Agency. For details, contact Michael C. Osborne, Mail Drop 65, 919/541-4113.

16. ABSTRACT

The report documents the detailed scale-up and design phase of a program to develop a low-NOx burner system that can be retrofitted to an existing thermally enhanced oil recovery (TEOR) steam generator. The emission design goal for the 16 MW commercial grade burner system is to maintain NOx emissions below 85 ppm (at 3 percent O2) while firing a heavy fuel oil containing above 0.6 percent bound nitrogen. The burner system selected to achieve this emission goal utilizes a staged combustion process in which the first stage is thermally isolated and provides long residence time under high temperature, optimally fuel-rich conditions. Results from earlier tests at three scales (21 kW, 0.6 MW, and 3 MW) are compared to identify design parameters for the 16 MW full-scale burner. This comparison shows that residence time and temperature in the first stage are the most important scaling parameters. Detailed thermodynamic/mechanical design features of the full-scale burner hardware are discussed. Initial evaluation of this burner in a test furnace and results from long-term tests in a field operating steam generator are documented in two other volumes.

17. KEY WORDS AND DOCUMENT ANALYSIS

| a. DESCRIPTORS | | b. IDENTIFIERS/OPEN ENDED TERMS | c. COSATI Field/Group |
|---|---|---|---|
| Pollution | Boilers | Pollution Control | 13B |
| Fuel Oil | | Stationary Sources | 21D |
| Combustion | | Low-NOx Burners | 21B |
| Nitrogen Oxides | | Retrofit | 07B |
| Burners | | | 13A |
| Tests | | | 14B |

| | | |
|---|---|---|
| 18. DISTRIBUTION STATEMENT<br>Release to Public | 19. SECURITY CLASS *(This Report)*<br>Unclassified | 21. NO. OF PAGES<br>364 |
| | 20. SECURITY CLASS *(This page)*<br>Unclassified | 22. PRICE |

## NOTICE

This document has been reviewed in accordance with U.S. Environmental Protection Agency policy and approved for publication. Mention of trade names or commercial products does not constitute endorsement or recommendation for use.

# ABSTRACT

A program to translate design criteria developed in bench-scale and pilot-scale combustors to a 16 MW commercial grade prototype burner which can be retrofitted to existing thermally-enhanced oil recovery (TEOR) steam generators is currently in progress.

Laboratory and pilot-scale data has been used to develop a low-$NO_x$ burner which is capable of operating with high-nitrogen liquid fuels such as crude oils and synthetic fuels. Emissions of $NO_x$ can be minimized by application of a staged combustion process in which the first stage is thermally isolated and provides long residence time under high temperature, optimally fuel-rich conditions. The design criteria for this process were developed in a previous study which was carried out in a 21 kW (70,000 Btu/hr) tunnel furnace and applied to two pilot-scale prototype burners at 0.6 MW ($2 \times 10^6$ Btu/hr) and 3 MW ($10 \times 10^6$ Btu/hr).

This report describes the results of the design development tests and compares results of all three scales of experiment. Firing a heavy fuel oil containing above 0.6 percent bound nitrogen, test results indicate that $NO_x$ emissions below 85 ppm (at 3 percent $O_2$) are possible while carbon monoxide and smoke are low. Translation of the design requirements to practical burner designs, and additional requirements for initial fuel/air contacting and second-stage air addition are presented and discussed. Data obtained over a scale range of 30:1 shows that residence time and temperature in the first stage are the most important scaling parameters for this low-$NO_x$ burner design and aerodynamic effects are second order parameters. Detailed design of the 16 MW prototype burner is also discussed, which was selected to meet the design criteria as well as requirements for commercial-grade oil field equipment. Key aspects of the hardware design are the use of commercial primary burner equipment, a refractory lined first stage chamber which is regeneratively-air cooled, and variable second-stage air injection to allow optimization of emissions and flame shape. Discussion of the detailed design includes retrofit requirements and specifications for primary throat/atomizer design, first-stage residence time and temperature, refractory lining design, and preliminary requirements for second-stage air injection. The burner will be briefly evaluated in a test furnace prior to retrofit and performance testing in a field-operating steam generator in Kern County, California.

# FOREWORD

Enhanced oil recovery processes are applied to oil field production in order to extract heavy, viscous crude oil and tar sands which connot otherwise be produced. A significant fraction of total U.S. oil reserves require application of enhanced oil recovery in order to be realized. Thermally enhanced oil recovery (TEOR) involves injection of wet steam which is produced by combusting crude oil in oil field steam generators typically ranging in size from 7 to 15 MW capacity. More than 90 percent of all oil field steam generators in the United States are located in California, one-third (approximately 1000 units) of which are located in Kern County. Approximately one-third of the produced crude oil is consumed by the steam generator, amounting to over 200,000 barrels of crude oil consumed per day at full capacity. The crude oils which are fired in these steam generators are typically high in nitrogen (~0.8 to 1.0 percent) and sulfur content. Uncontrolled emissions of $NO_x$ and $SO_x$ can therefore reach high levels and potentially worsen ambient air quality.

Local legislation regulating emissions of $NO_x$ from oil field steam generators threatens to limit oil production unless $NO_x$ control methods are applied. A ceiling on total $NO_x$ emissions from all steam generators in Kern County has been established which limits total emissions to 1979 levels; thus new generators cannot be brought on line without reducing emissions from existing ones. New generators are required to have "best available control technology" (BACT) which may include low-$NO_x$ burners, postflame $NH_3$ injection, or other postflame treatment methods. In addition, if ambient $NO_2$ level in Bakersfield exceeds a specified level, the total $NO_x$ ceiling is lowered to the equivalent of 0.14 lb $NO_x$/MM Btu (60 mg/MJ) or 105 ppm NO, corrected to 3 percent oxygen if all steamers were in operation. Enhanced oil recovery operations are projected to expand through 1995. The level of $NO_x$ control required to meet both growth and air quality goals has typically been difficult to achieve with available technology while maintaining acceptable carbon monoxide and particulate emissions and practical flame conditions within the steamer.

This program addresses the need for advanced $NO_x$ control technology for oil-field steam generators, and concerns the development of a full-scale burner system, for which the concept is based on fundamental studies. The burner will be retrofittable to existing steam generators and will produce acceptable emissions of CO and particulate while maintaining a flame form compatible with the steamer design. The emission goals for $NO_x$ are to achieve less than 85 ppm $NO_x$ at 3 percent excess oxygen.

The major elements of this program are:

1. Conceptual design development--to verify and refine design scaling criteria developed under previous EPA contracts in order to develop hardware designs.
2. Detailed burner design and construction--to produce a commercial-grade full-scale burner suitable for retrofit on an existing steam generator.
3. Burner optimization and evaluation--to minimize pollutant emissions in a field-operating TEOR steam generator firing high-nitrogen crude oil and evaluate performance over an extended period of time.

This report discusses the first two elements of the project through completion of the detailed engineering design of the full-scale (16 MW) commercial prototype burner.

A second report will be prepared immediately following the first test series conducted in one of EER's test tunnels, documenting initial burner performance. Results of the field testing and evaluation will be included in the final report.

TABLE OF CONTENTS

Section Page

Abstract . . . . . . . . . . . . . . . . . . . . . . . . . . iii

Foreword . . . . . . . . . . . . . . . . . . . . . . . . . . iv

Acknowledgment . . . . . . . . . . . . . . . . . . . . . . . xx

1.0 SUMMARY . . . . . . . . . . . . . . . . . . . . . . . 1-0

1.1 Test Equipment . . . . . . . . . . . . . . . . . . . 1-3
1.2 First-Stage Parameters . . . . . . . . . . . . . . . 1-6
1.3 Second-Stage Effects . . . . . . . . . . . . . . . . 1-12
1.4 Scaling and Full-Scale Burner Design . . . . . . . . 1-14

2.0 LOW-$NO_x$ COMBUSTOR CONCEPT DEFINITION . . . . . . . . . . 2-1

2.1 The Chemistry of $NO_x$ Formation and Control . . . . . . . 2-1
2.2 Bench-Scale Experiments . . . . . . . . . . . . . . 2-6
2.2.1 Fuel Preparation Zone . . . . . . . . . . . . . 2-8
2.2.2 Fuel-Rich First Stage . . . . . . . . . . . . . 2-8
2.2.3 Second Stage . . . . . . . . . . . . . . . . . 2-13
2.2.4 Fuel Effects . . . . . . . . . . . . . . . . . 2-15
2.3 Pilot-Scale Studies . . . . . . . . . . . . . . . . 2-22
2.3.1 First-Stage Parameters . . . . . . . . . . . . 2-25
2.3.2 Second-Stage Parameters . . . . . . . . . . . . 2-28
2.4 Summary . . . . . . . . . . . . . . . . . . . . . . 2-31

3.0 CONCEPTUAL DESIGN DEVELOPMENT . . . . . . . . . . . . . . 3-1

3.1 3 MW Pilot-Scale Experiments . . . . . . . . . . . . 3-1
3.1.1 Experimental Hardware . . . . . . . . . . . . . 3-2
3.1.2 Results: First-Stage Effects . . . . . . . . . . 3-11
3.1.3 Second-Stage Effects . . . . . . . . . . . . . . 3-26
3.1.4 Optimized Burner Performance . . . . . . . . . . 3-36
3.2 Isothermal Screening . . . . . . . . . . . . . . . . 3-39
3.2.1 Experimental Equipment . . . . . . . . . . . . . 3-39
3.2.2 Measurements . . . . . . . . . . . . . . . . . . 3-52
3.2.3 Flow Test Results . . . . . . . . . . . . . . . 3-55

Preceding page blank

TABLE OF CONTENTS (Continued)

Section Page

3.2.4 Full-Scale Atomizer Performance . . . . . . . . . . 3-78
3.2.5 Discussion . . . . . . . . . . . . . . . . . . . . 3-78

3.3 Preferred Conceptual Design . . . . . . . . . . . . . . 3-86

4.0 FIELD RETROFIT . . . . . . . . . . . . . . . . . . . . . 4-1

4.1 Review of Steam Generator Designs . . . . . . . . . . . 4-1
4.1.1 Steam Generator Design . . . . . . . . . . . . . . 4-1
4.1.2 Burner Designs . . . . . . . . . . . . . . . . . . 4-5
4.2 Steam Generator Selection . . . . . . . . . . . . . . . 4-9
4.2.1 Approach to Selection . . . . . . . . . . . . . . . 4-9
4.2.2 Description of Host Steam Generator . . . . . . . . 4-11
4.3 Retrofit Constraints . . . . . . . . . . . . . . . . . . 4-15
4.3.1 Physical Requirements . . . . . . . . . . . . . . . 4-18
4.3.2 Control System Constraints . . . . . . . . . . . . 4-20
4.3.3 Flame Shape . . . . . . . . . . . . . . . . . . . . 4-21

5.0 FULL-SCALE BURNER DESIGN . . . . . . . . . . . . . . . . 5-1

5.1 Design Definition . . . . . . . . . . . . . . . . . . . 5-3
5.1.1 First-Stage Dimensions . . . . . . . . . . . . . . 5-5
5.1.2 First-Stage Geometry . . . . . . . . . . . . . . . 5-10
5.1.3 First-Stage Air/Fuel Mixing . . . . . . . . . . . . 5-14
5.2 Refractory Materials . . . . . . . . . . . . . . . . . . 5-14
5.2.1 Refractory Properties . . . . . . . . . . . . . . . 5-16
5.2.2 Materials for Prototype Commercial Burner Concepts . . . . . . . . . . . . . . . . . . . . 5-30
5.3 First-Stage Concept A--Insulated Lining Design . . . . . 5-34
5.3.1 Design Considerations . . . . . . . . . . . . . . . 3-37
5.3.2 Preliminary Analysis . . . . . . . . . . . . . . . 5-40
5.3.3 Recommended Design Analysis . . . . . . . . . . . . 5-45
5.4 First-Stage Concept B--Regenerative Design . . . . . . . 5-53
5.4.1 Results of Thermal Analysis . . . . . . . . . . . . 5-53
5.4.2 Mechanical Design . . . . . . . . . . . . . . . . . 5-62

TABLE OF CONTENTS (Concluded)

Section Page

5.5 Second-Stage Air Injection . . . . . . . . . . . . . . . . . 5-66
5.6 Burner Controls . . . . . . . . . . . . . . . . . . . . . . 5-76
5.7 Final Selection . . . . . . . . . . . . . . . . . . . . . . 5-81

6.0 BURNER CONSTRUCTION AND TESTING . . . . . . . . . . . . . . . . 6-1

6.1 Preliminary Evaluation . . . . . . . . . . . . . . . . . . 6-1
6.2 Field Optimization Tests . . . . . . . . . . . . . . . . . 6-6
6.3 30-Day Performance Evaluation . . . . . . . . . . . . . . 6-9

7.0 REFERENCES . . . . . . . . . . . . . . . . . . . . . . . . . . 7-1

APPENDIX A--LOW $NO_x$ BURNER REFRACTORY LINING DESIGN STUDIES . . . . . . A-1

APPENDIX B--THE DEVELOPMENT OF DESIGN CRITERIA FOR LOW-$NO_x$ OIL BURNERS SUITABLE FOR APPLICATION TO TEOR STEAMERS . . . . . B-1

APPENDIX C--COMMERCIAL PRACTICE BURNER DESIGN DRAWINGS . . . . . . . . . C-1

APPENDIX D--MEMBERS OF THE AD HOC COMMITTEE . . . . . . . . . . . . . . D-1

# LIST OF FIGURES

Figure Page

1-1 Prototype burners and experimental test furnace . . . . . . . 1-4

1-2 Secondary air injection configurations investigated with 3 MW pilot-scale burner (ports shown in axial orientation) . 1-7

1-3 Influence of scale on combustor performance . . . . . . . . . 1-8

1-4 Influence of load on emissions from IP burner . . . . . . . . 1-10

1-5 Effect of (a) swirl and (b) atomizer type on $NO_x$ emissions . 1-11

1-6 Second-stage mixing effects . . . . . . . . . . . . . . . . 1-13

1-7 Second-stage $NO_x$ production and first-stage TFN decay for bench scale and pilot scale . . . . . . . . . . . . . . . . 1-16

1-8 Drop size from ultrasonic and Y-jet atomizers . . . . . . . . 1-18

1-9 Influence of fuel nitrogen on second-stage $NO_x$--bench-scale and pilot-scale data . . . . . . . . . . . . . . . . . . . 1-20

1-10 Conceptual burner designs for TEOR steam generators . . . . . 1-21

2-1 Equilibrium TFN concentrations calculated for methane fuel containing 1 percent by weight of nitrogen . . . . . . . . . 2-3

2-2 Calculation of (a) total fixed nitrogen decay and (b) decay of individual fixed nitrogen species . . . . . . . . . . . . 2-5

2-3 Bench-scale tunnel furnace . . . . . . . . . . . . . . . . . 2-7

2-4 Influence of heat extraction rate in the fuel preparation zone . . . . . . . . . . . . . . . . . . . . . . . . . . . 2-9

2-5 Detailed in-flame measurements with Kern County crude oil (R14) (21 kW) . . . . . . . . . . . . . . . . . . . . . . . 2-10

2-6 The influence of fuel-rich hold-up zone temperature profile on exhaust $NO_x$ . . . . . . . . . . . . . . . . . . . . . . 2-11

2-7 CO oxidation and decay of XN species for two temperature profiles . . . . . . . . . . . . . . . . . . . . . . . . . 2-12

2-8 Influence of first-stage exit composition on second-stage $NO_x$ formation (tunnel furnace-->454°C shale fraction) . . . . 2-14

LIST OF FIGURES (Continued)

| Figure | | Page |
|---|---|---|
| 2-9 | The effect of fuel type and stoichiometry on the production of TFN ($\Sigma XN$) for (A) petroleum oils, and (B) alternate fuels | 2-18 |
| 2-10 | Relationship between fuel nitrogen content and first-stage TFN | 2-19 |
| 2-11 | The conversion of fuel-bound nitrogen to XN species | 2-21 |
| 2-12 | Effect of fuel-bound nitrogen content on exhaust NO (3 Percent excess $O_2$, 21 kW) | 2-23 |
| 2-13 | Prototype burners and experimental test furnaces | 2-24 |
| 2-14 | Influence of first-stage stoichiometry on $NO_x$, CO, and smoke emissions (bench scale and pilot scale, California residual fuel oil) | 2-26 |
| 2-15 | Second-stage $NO_x$ production and first-stage TFN decay for bench scale and pilot scale | 2-27 |
| 2-16 | Pilot-scale second-stage $NO_x$ emissions for premixed and non-premixed first-stage reactants (0.6 MW; California residual oil; 350 msec first-stage residence time at $SR_1$ = 0.7) | 2-29 |
| 2-17 | Pilot-scale second-stage $NO_x$ emissions with and without interstage heat extraction (0.6 MW; 35 kW interstage heat removal in cooled case) | 2-30 |
| 2-18 | Influence of excess air on second-stage $NO_x$ IP burner | 2-32 |
| 2-19 | Influence of fuel nitrogen on second-stage $NO_x$ bench-scale and pilot-scale data | 2-33 |
| 3-1 | 3 MW pilot-scale test burner | 3-4 |
| 3-2 | Small Watertube Simulator (SWS) test furnace | 3-5 |
| 3-3 | 3 MW premixer assembly | 3-9 |
| 3-4 | Atomizers tested in 3 MW pilot-scale burner | 3-10 |
| 3-5 | Secondary air injection configurations investigated with 3 MW pilot-scale burner (ports shown in axial orientation) | 3-13 |
| 3-6 | Baseline $NO_x$ emissions (2.9 MW) | 3-16 |

## LIST OF FIGURES (Continued)

Figure Page

3-7 Baseline smoke emissions (2.9 MW) . . . . . . . . . . . . . . . . . 3-18

3-8 Effect of load--baseline configuration . . . . . . . . . . . . 3-19

3-9 Effect of load on smoke emissions . . . . . . . . . . . . . . . . . 3-20

3-10 Effect of swirl--premixer (2.9 MW, Configuration I) . . . . . 3-21

3-11 Effect of first-stage throat geometry (2.9 MW; ultrasonic atomizer; primary air temp = $52^{\circ}$C) . . . . . . . . . . . . . . 3-22

3-12 Effect of first-stage air distribution . . . . . . . . . . . . 3-24

3-13 Effect of atomizer type on baseline $NO_x$ emissions (2.9 MW, Configuration I) . . . . . . . . . . . . . . . . . . . . . . 3-25

3-14 Effect of atomizing fluid and pressure on $NO_x$ emissions (2.9 MW; primary air temp = $52^{\circ}$C) . . . . . . . . . . . . . . . . . 3-27

3-15 Effect of annular air swirl and air distribution . . . . . . 3-28

3-16 Second-stage mixing--effect of first-stage exit velocity . . 3-29

3-17 Second-stage air port injectors . . . . . . . . . . . . . . . . 3-31

3-18 Effect of port geometry on $NO_x$ emissions . . . . . . . . . . 3-32

3-19 Optimized $NO_x$ emissions using ports and annular secondary air injectors . . . . . . . . . . . . . . . . . . . . . . . . . 3-35

3-20 Emissions from crude oil and residual oil (baseline conditions) . . . . . . . . . . . . . . . . . . . . . . . . . . . . . 3-37

3-21 Particulate measurement--baseline conditions (residual oil) . 3-38

3-22 Small spray characterization rig (SSR). . . . . . . . . . . . . 3-40

3-23a Annular swirler used in Confuguration II (SSR) . . . . . . . . 3-43

3-23b Primary zone fuel/air premixer (SSR) . . . . . . . . . . . . 3-43

3-24 Schematic of LSR facilities . . . . . . . . . . . . . . . . . . 3-45

3-25 18 MW-equivalent premixer used in LSR tests . . . . . . . . . . 3-50

3-26 Schematics of two twin-fluid nozzles characterized . . . . . 3-51

3-27 Installation of laser diffraction system . . . . . . . . . . . 3-54

## LIST OF FIGURES (Continued)

Figure Page

3-28 Effect of swirl levels on flow pattern generated by low exit velocity divergent burner quarl (SSR) 3-57

3-29 Effect of the premixer on flow pattern in a cylindrical burner quarl (SSR, Configuration III) 3-58

3-30 Effect of swirl level on flow pattern generated in a high exit velocity divergent burner quarl (SSR) 3-59

3-31 Effect of swirl level on flow pattern generated with the addition of atomizing air in a divergent burner quarl (SSR, Configurement I) 3-61

3-32 Flow pattern produced in a cylindrical burner quarl with the addition of atomizing air jet (SSR, Configuration III) 3-62

3-33 Effect of swirl level on flow pattern with the addition of atomizing air stream in a high exit velocity divergent burner quarl (SSR) 3-63

3-34 Influence of swirl level on volume distribution in a low exit velocity burner quarl (SSR) 3-64

3-35 Volume distribution for a cylindrical burner quarl (SSR, Configuration III) 3-65

3-36 Effect of swirl level on distribution in a high exit velocity divergent burner spray quarl (SSR) 3-66

3-37 Effect of burner geometry and swirl level air flow pattern (large spray rig) 3-70

3-38 Ultrasonic atomizer-spray distribution produced in a divergent burner quarl (S=0.39--LSR Configuration I) 3-72

3-39 Ultrasonic atomizer-spray distribution produced in divergent burner quarl (S=0.29--LSR Configuration II) 3-73

3-40 Ultrasonic atomizer-spray distribution produced in a cylindrical burner quarl (S=0.39--LSR Configuration III) 3-74

3-41 Y-jet spray distribution produced in a divergent burner quarl with S-0.39--LSR Configuration I 3-75

3-42 Y-jet spray distribution produced in a divergent burner quarl with S=0.29--LSR Configuration II) 3-76

3-43 Y-jet spray distribution produced in a cylindrical burner quarl with S=0.39 (Configuration III) 3-77

LIST OF FIGURES (Continued)

Figure Page

3-44 Effect of atomizing air pressure on ultrasonic nozzle spray distribution in Configuration III (large spray rig) . . 3-79

3-45 Effect of atomizing air pressure on Y-jet spray distribution in Configuration III (large spray rig) . . . . . . . . . 3-80

3-46 Influence of atomizing air pressure on Rosin-Rammler mean diameter from 15 MW Y-jet nozzle (Hyvis 04, 55 cSt, oil flow rate, 0.26 kg/s) . . . . . . . . . . . . . . . . . . . . 3-81

3-47 Influence of atomizing air pressure on Rosin-Rammler mean diameter from 15 MW Ultrasonic nozzle (Hyvis 04, 55 cSt, oil flow rate = 0.26 kg/s) . . . . . . . . . . . . . . . . . . 3-82

3-48 Influence of oil flow rate on Rosin-Rammler mean diameter for 12-hole Y-jet nozzle (Hyvis 04, 55 cSt, air pressure = 310 kPa) . . . . . . . . . . . . . . . . . . . . . . . 3-83

4-1 Typical 15 MW ($50 \times 10^6$ Btu/hr) steam generator for thermal enhanced oil recovery. The horizontal radiant section is typically about 12 meters long and 3 meters in diameter . . . 4-3

4-2 The conventional North American burner design and flame pattern . . . . . . . . . . . . . . . . . . . . . . . . . 4-7

4-3 The conventional Coen burner design and flame pattern . . . . 4-8

4-4 Host steam generator arrangement . . . . . . . . . . . . . . . 4-12

4-5 Kern front host steam generator site . . . . . . . . . . . . 4-16

5-1 Example of refractory lining failure due to inadequate design and thermal shock . . . . . . . . . . . . . . . . . . 5-2

5-2 Conceptual burner designs for TEOR steam generators . . . . . 5-4

5-3 Specific gravity of rich equilibrium combustion products . . 5-8

5-4 Variation of residence time with stoichiometry and temperature . . . . . . . . . . . . . . . . . . . . . . . . . . 5-9

5-5 Required first-stage volume versus stoichiometry . . . . . . 5-11

5-6 Internal dimensions of burner for different length-to-diameter ratios . . . . . . . . . . . . . . . . . . . . . . . 5-13

LIST OF FIGURES (Continued)

Figure Page

5-7 Temperature ranges for various refractory materials (from Fryling, 1966) . . . . . . . . . . . . . . . . . . . . . 5-18

5-8 Features of insulated first-stage lining design (Concept A) . 5-36

5-9 Approximate reversible thermal expansion of refractory brick (from Harbison Walker Refractories, 1979) . . . . . . . 5-39

5-10 Temperature distribution through several lining arrangements . . . . . . . . . . . . . . . . . . . . . . . . . . 5-42

5-11 Effect of external convection and lining thickness for thin refractory linings . . . . . . . . . . . . . . . . . . 5-43

5-12 Temperature profile through monolayer lining after heating from ambient temperature . . . . . . . . . . . . . . . . . . 5-44

5-13 Transient temperature profiles through lining after loss of flame . . . . . . . . . . . . . . . . . . . . . . . . . . . 5-46

5-14 Recommended design model . . . . . . . . . . . . . . . . . . 5-47

5-15 Steady state temperature distribution . . . . . . . . . . . . 5-49

5-16 Steady-state axial temperature distribution . . . . . . . . . 5-50

5-17 Steady-state radial stress distribution through multilayer liner (purely elastic) . . . . . . . . . . . . . . . . . 5-51

5-18 Hot face temperature during startup . . . . . . . . . . . . . 5-52

5-19 Regenerative first-stage design . . . . . . . . . . . . . . . 5-54

5-20 Heat transfer through regenerative air-cooled lining . . . . 5-55

5-21 Thermal design characteristics of regenerative lining with external insulation . . . . . . . . . . . . . . . . . . 5-58

5-22 Regenerative first-stage design . . . . . . . . . . . . . . . 5-63

5-23 Unconventional construction concepts to reduce thermal stress . . . . . . . . . . . . . . . . . . . . . . . . . . . 5-65

5-24 Radial expansion allowance for regenerative first-stage concept . . . . . . . . . . . . . . . . . . . . . . . . . . . 5-67

5-25 Variable second-state air addition section . . . . . . . . . 5-69

## LIST OF FIGURES (Concluded)

Figure Page

5-26 Secondary air penetration for $SR_1$ = 0.65 . . . . . . . . . . . 5-71

5-27 Secondary air penetration for $SR_1$ = 0.80 . . . . . . . . . . . 5-72

5-28 Secondary air penetration for 8 and 16 ports . . . . . . . . . 5-73

5-29 Comparison of secondary air penetration calculations for 3 MW pilot-scale burner and full-scale prototype . . . . . . 5-75

5-30 Typical safety control system for packaged firetube boilers . 5-77

5-31 Burner control schematic . . . . . . . . . . . . . . . . . . 5-80

6-1 Medium tunnel test facility . . . . . . . . . . . . . . . . . . 6-2

6-2 Sampling equipment for reduced nitrogen species . . . . . . . 6-5

# LIST OF TABLES

Table Page

1-1 First-Stage Hardware Configurations Tested in 3 MW Tests . . 1-5

2-1 Detailed Fuel Analyses . . . . . . . . . . . . . . . . . . . 2-16

3-1 Variables Investigated in 3 MW Studies . . . . . . . . . . . 3-3

3-2 SWS Furnace Characteristics . . . . . . . . . . . . . . . . 3-6

3-3 SWS Continuous Monitors . . . . . . . . . . . . . . . . . . 3-7

3-4 First-Stage Hardware Configurations Tested in 3 MW Tests . . 3-8

3-5 Summary of Second-Stage Air Variations . . . . . . . . . . . 3-12

3-6 Analysis of Heavy Fuels Tested in Pilot-Scale Testing . . . . 3-14

3-7 Baseline Test Conditions . . . . . . . . . . . . . . . . . . 3-15

3-8 Results of Second-Stage Air Port Variations (3.6 MW; No air preheat) . . . . . . . . . . . . . . . . . . . . . . . 3-33

3-9 Burner Configurations Tested in Subscale Spray Rig . . . . . 3-41

3-10 Capacity of LSR Fluid Transport Devices . . . . . . . . . . 3-46

3-11 Properties of Hyvis 04 Oil . . . . . . . . . . . . . . . . . 3-47

3-12 Burner Configurations Tested in LSR . . . . . . . . . . . . . 3-49

3-13 Test Conditions Investigated in Small-Scale Spray Rig (SSR) . 3-56

3-14 Test Conditions Investigated in Large-Scale Spray Rig (SSR) . 3-69

4-1 Typical Radiant Section Characteristics for 14.7 MW ($50 \times 10^6$ Btu/hr) Steam Generator . . . . . . . . . . . . . . 4-4

4-2 Host Steam Generator Characteristics . . . . . . . . . . . . 4-13

4-3 Host Steam Generator Site Characteristics . . . . . . . . . . 4-14

4-4 Host Steam Generator Fuel Characteristics . . . . . . . . . . 4-17

4-5 Primary Retrofit Requirements . . . . . . . . . . . . . . . . 4-19

5-1 First-Stage Conceptual Design Requirements . . . . . . . . . 5-6

5-2 Burner Design Point--18.3 MW ($62.5 \times 10^6$ Btu/hr) . . . . . . 5-6

LIST OF TABLES (Continued)

| Table | | Page |
|---|---|---|
| 5-3 | Overall Hardware Design Criteria for First Stage . . . . . . | 5-15 |
| 5-4 | General Physical and Chemical Characteristics of Refractory Brick (from Perry and Chelton, 1973) . . . . . . | 5-19 |
| 5-5 | Properties of High Temperature Refractories (Courtesy of Harbison Walker Refractories) . . . . . . . . . . . . . . . | 5-22 |
| 5-6 | Typical Material Specification for Lightweight High-Alumina Brick (Norton Company, 1982) . . . . . . . . . . . . | 5-23 |
| 5-7 | Typical Materials Specification for Lightweight High-Alumina Brick (Harbison-Walker Inc., 1982) . . . . . . . . . | 5-24 |
| 5-8 | Typical ASTM Tests for Refractory Materials . . . . . . . . . | 5-26 |
| 5-9 | Properties of Various High-Alumina Brick (from Larson, et al., 1974) . . . . . . . . . . . . . . . . . . . . . . . | 5-27 |
| 5-10 | Physical Properties of Pure Refractories (from Baumeister, et al., 1978) . . . . . . . . . . . . . . . . . . . . . . . | 5-28 |
| 5-11 | Normal Total Emissivities of Various Surfaces (Hottel and Sarofim, 1967) . . . . . . . . . . . . . . . . . . . . . . . | 5-29 |
| 5-12 | Known Properties of Materials Selected for Concept A, Multilayer Castable Refractory Lining . . . . . . . . . . . | 5-31 |
| 5-13 | Estimated Material Properties Used in Engineering Analysis of Concept A . . . . . . . . . . . . . . . . . . . . . . . . | 5-33 |
| 5-14 | Manufacturer's Data on Material Selected for Regenerative Liner (from A. P. Green Refractories Co.) . . . . . . . . . . | 5-35 |
| 5-15 | Heat Transfer Equations for Regenerative Shell Design . . . | 5-56 |
| 5-16 | Nomenclature for Figure 5-20 and Table 5-15 . . . . . . . . | 5-57 |
| 5-17 | Predicted Regenerative Liner Performance--Low Conductivity . | 5-60 |
| 5-18 | Predicted Regenerative Liner Performance--High-Conductivity Refractory . . . . . . . . . . . . . . . . . . . . . . . . | 5-61 |
| 5-19 | Control Requirements Beyond Existing Steamer Controls . . . | 5-79 |
| 5-20 | Comparison of Insulated and Regenerative First-Stage Concepts . . . . . . . . . . . . . . . . . . . . . . . . . | 5-82 |

## LIST OF TABLES (Concluded)

Table Page

6-1 Measurement Techniques for Evaluation and Optimization Testing . . . . . . . . . . . . . . . . . . . . . . . . . . 6-4

6-2 Initial Operational Evaluation Measurements . . . . . . . . . 6-7

6-3 System Output Measurements During 30-Day Test . . . . . . . . 6-11

# ACKNOWLEDGMENT

The authors wish to acknowledge the following people and organizations for their contributions in developing and reviewing the full-scale burner designs: Berwin King of Struthers Thermo-Flood Corporation; Ross Firestone of Illinois Institute of Technology Research Institute; Sherman Eaton of Coen Company; Jack Hagan of Peabody Engineering Company; A. P. Green Refractories Company; Harbison-Walker Refractories; and Richard Harkness of Davy-McKee Corporation. The authors wish to thank the members of the Ad Hoc committee, formed for this program, for their assistance and cooperation, in particular Sam Davis of Chevron U.S.A., Inc.

## 1.0 SUMMARY

Nitrogen oxide emissions from stationary combustors can be reduced by combustion modification techniques which involve staging the heat release process. However, optimization of these techniques to control $NO_x$ emissions from liquid-fuel-fired combustors has proven difficult because of the limited knowledge of the controlling phenomena and the problems associated with the scaling of combustion systems. This report describes the development and testing of a low-$NO_x$ liquid-fuel-fired combustor whose design was based upon fundamental information generated in bench-scale reactors. These criteria are currently being applied in the design and construction of a 60 x $10^6$ Btu/hr (17.5 MW) low-$NO_x$ burner for field demonstration on a steam generator for thermally enhanced oil recovery (TEOR).

Many studies have been carried out to determine the mechanism of NO formation in flames both from molecular nitrogen (thermal NO) and from nitrogen contained in the fuel (fuel NO). Field test data (Cato et al, 1976) and laboratory studies (Pershing et al, 1979; England et al, 1981) have established the importance of fuel NO to the total emission of nitrogen oxides from residual fuel oil flames. Thermal NO formation is strongly dependent upon temperature and its formation can be reduced by decreasing flame temperatures by techniques such as the addition of cooled combustion products to the combustion air (flue gas recirculation). However, since the majority of NO formed in residual fuel oil flames is fuel NO and its formation is not strongly dependent upon temperature, flue gas recirculation is not an effective $NO_x$ control technique (Heap et al, 1976). Fuel NO formation is very sensitive to reactant stoichiometry. Fuel-rich conditions promote the formation of molecular nitrogen form-fixed nitrogen species ($NO + NH_3 + TFN$) which are formed as the liquid fuel decomposes. Consequently, staged combustion which involves the formation of a fuel-rich zone either by delaying fuel/air mixing or by dividing the combustion air supply into two and injecting one portion downstream from the burner is the most effective $NO_x$ control technique for residual fuels (Beer et al, 1981).

In a previous study (England et al, 1981) the parameters controlling the effectiveness of staged combustion for a wide range of liquid fuels containing bound nitrogen were defined in a series of bench-scale studies which were carried out in a refractory tunnel furnace. Exhaust NO levels from a staged combustion system are dependent upon:

1. First-Stage Processing. TFN is minimized if the residence time of the fuel-rich reactants is maximized at high temperatures and at an optimum stoichiometry which is temperature dependent.
2. Mixedness. Since stoichiometry must be controlled it is important that the reactants are well mixed.
3. Second-Stage Processing. Exhaust NO levels are the sum of thermal NO formation and conversion (or retention) of TFN species to NO during heat release in the second stage and the second stage must be designed to minimize these effects.
4. Fuel Properties. The rate of evolution of nitrogen species from the liquid fuel droplets has an impact because it dictates the time available for $N_2$ formation in the first zone. This can be overcome by minimizing droplet size.

This information has been used to construct bench- and pilot-scale combustors having $NO_x$ emissions below 100 ppm (corrected to 0 percent oxygen) and acceptable emission levels for CO and smoke when firing fuels containing greater than 0.5 percent fuel-bound nitrogen.

The bench-scale tests indicated that TFN concentration is minimized most effectively by increasing the temperature of the fuel-rich zone. The combination of high first-stage temperature, optimum stoichiometry, and long first-stage residence time resulted in exhaust $NO_x$ levels below 100 ppm irrespective of the nitrogen content of the liquid fuel. To translate this information into a full-scale (i.e., 18 MW) burner design requires information on how the controlling parameters scale. The approach used was to obtain experimental data with $2 \times 10^6$ Btu/hr (0.6 MW) and $10 \times 10^6$ Btu/hr (3 MW) prototype combustors, and thereby confirm the appropriate criteria for the design and fabrication of the full-scale combustor. In addition, isothermal (cold flow) spray/flow field tests were conducted to assess mixing and atomization characteristics produced by full-scale hardware in the region near the burner throat.

## 1.1 Test Equipment

Two prototype low-$NO_x$ burners, shown in Figure 1-1, were constructed with nominal design firing rates of 2 x $10^6$ Btu/hr (0.6 MW) (small pilot-scale or SP) and 10 x $10^6$ Btu/hr (3 MW) (intermediate pilot-scale or IP). Each of the two test burners contains three major elements:

1. An air/fuel injection system
2. A fuel-rich hold-up zone
3. A secondary air injection section

The primary zone is constructed from high temperature refractories and insulation to minimize heat loss through the walls and permit near-adiabatic conditions in the primary zone. Fuel and primary air injected at the entry of a divergent which forms the initial section of the fuel-rich hold-up zone. The residence time in the fuel-rich zone calculated at a first-stage stoichiometric ratio of 0.7 is approximately 0.50 sec for the SP burner and 0.42 sec for the IP burner. The primary products are directed through a convergent section which serves to minimize radiative heat loss, ensure complete mixing of the primary products, and minimize backmixing of secondary air into the primary zone. Secondary air is injected parallel to the burner axis annularly around the primary exit.

A number of different commercial atomizers were used in the two combustors. Most of the data was, however, obtained with an ultrasonic, air-assist atomizer and an internal-mixing steam-assist atomizer. At the 0.6 MW scale, the ultrasonic atomizer produced droplets with a narrow size distribution about a mean diameter of 20 μm, and the internal-mixing atomizer produced droplets with a much broader size distribution about a mean diameter of 40 μm. At larger scales the ultrasonic atomizer has been found to produce droplets with a mean size greater than 120 μm.

Several air/fuel injection hardware changes were investigated during the 3.5 MW burner testing. Table 1-1 summarizes the first-stage hardware variations which were evaluated. Most of the configurations were variations on the fuel/air premixer concept with different exit geometries. The premixer design is scaled up on the basis of constant velocity and swirl numbers from the 0.9 MW design utilized in the small pilot-scale prototype.

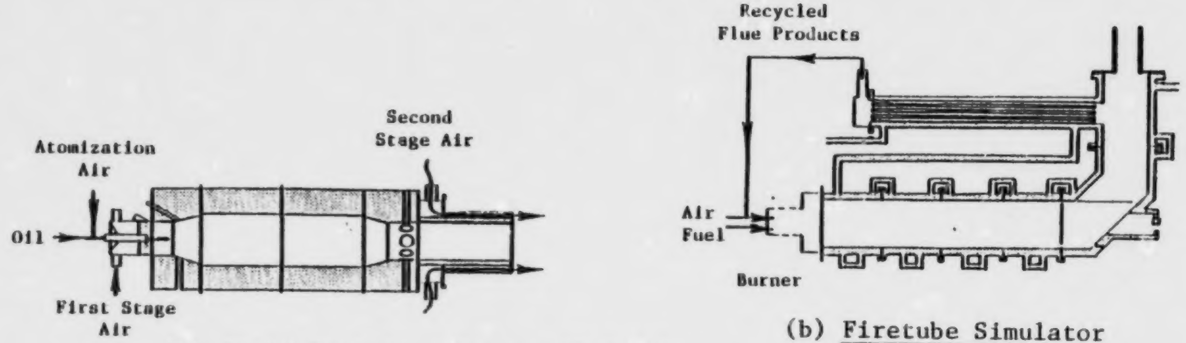
Atomization
Air
Oil
First Stage
Air
Second
Stage Air
Recycled
Flue Products
Air
Fuel
Burner

(a) Small Prototype Burner (0.6 MW)

(b) Firetube Simulator

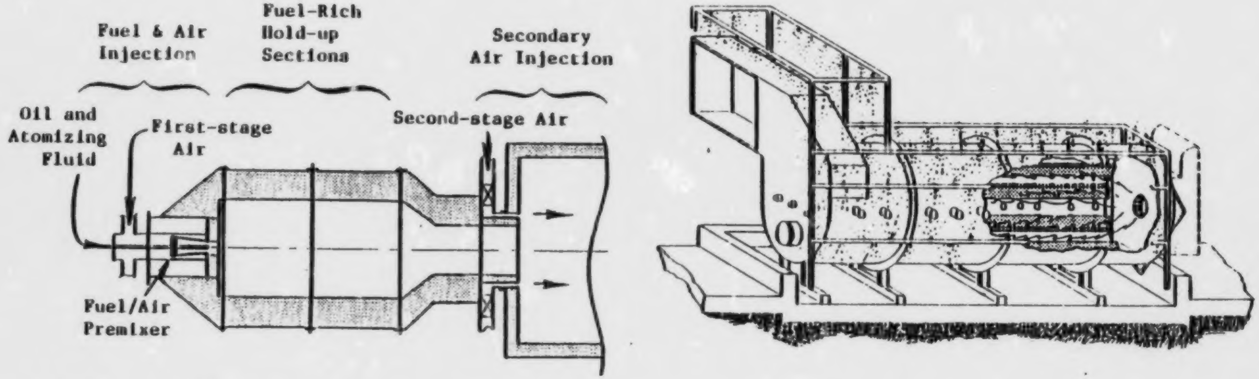
Fuel & Air
Injection
Fuel-Rich
Hold-up
Sections
Secondary
Air Injection
Oil and
Atomizing
Fluid
First-stage
Air
Second-stage Air
Fuel/Air
Premixer

(c) Intermediate Prototype Burner (3 MW)

(d) Small Watertube Simulator

Figure 1-1. Prototype burners and experimental test furnace.

TABLE 1-1. FIRST-STAGE HARDWARE CONFIGURATIONS TESTED IN 3 MW TESTS

| CONFIGURATION | FIRST-STAGE | SECOND-STAGE |
|---|---|---|
| 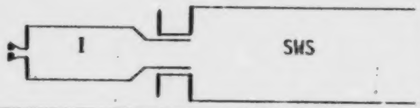 | – PREMIXER<br>– SWIRL (S=0.4)<br>– PARALLEL EXIT | – AXIAL AIR INJECTION<br>– ANNULUS INJECTOR<br>– 51 CM FIRST-STAGE EXIT DIAMETER |
| 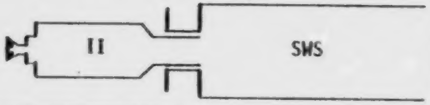 | – PREMIXER<br>– SWIRL (S=0.4)<br>– SET BACK PARALLEL EXIT | – AXIAL AIR INJECTION<br>– ANNULUS INJECTOR<br>– 51 CM FIRST-STAGE EXIT DIAMETER |
| 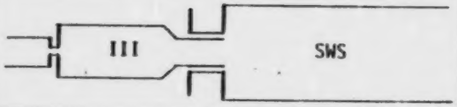 | – PREMIXER<br>– NO SWIRL<br>– PARALLEL EXIT | – AXIAL AIR INJECTION<br>– ANNULUS INJECTOR<br>– 51 CM FIRST-STAGE EXIT DIAMETER |
| 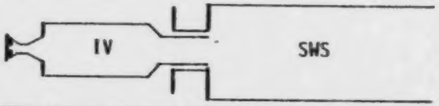 | – PREMIXER<br>– SWIRL (S=0.4)<br>– DIVERGENT EXIT (L/D=2.6) | – AXIAL AIR INJECTION<br>– ANNULUS INJECTOR<br>– 51 CM FIRST-STAGE EXIT DIAMETER |
| 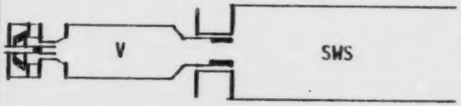 | – ℄ CHANNEL (LOW VELOCITY)<br>– SWIRL<br>– DIVERGENT EXIT (L/D=1.1) | – AXIAL AIR INJECTION<br>– ANNULUS INJECTOR<br>– 36 CM FIRST-STAGE EXIT DIAMETER |
| 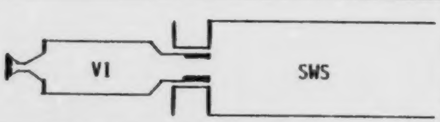 | – PREMIXER<br>– SWIRL (S=0.4)<br>– DIVERGENT EXIT (L/D=2.6) | – AXIAL AIR INJECTION<br>– ANNULUS INJECTOR<br>– 36 CM FIRST-STAGE EXIT DIAMETER |
| 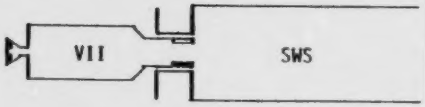 | – PREMIXER<br>– SWIRL (S=0.4<br>– PARALLEL EXIT | – AXIAL AIR INJECTION<br>– ANNULUS INJECTOR<br>– 36 CM FIRST-STAGE EXIT DIAMETER |

Second-stage mixing effects were extensively evaluated in the 3-MW studies, to determine limits of additional NO reduction possible through variations in the second-stage mixing and to develop practical information on the tradeoffs between $NO_x$/smoke emissions and flame shape. In addition to the first-stage exit sleeve shown in the previous table, several air injection port configurations were tested to vary second-stage mixing. The number of ports, diameter (yielding two velocity levels), and distance from the centerline were varied. Figure 1-2 illustrates the different hardware configurations used.

The combustor tests were conducted in two different combustors:

- Firetube Simulator (FS) (Previous Study). The combustion chamber is 3.2 m long with an internal diameter of 0.6 m. The chamber is composed of calorimetric sections cooled by heat transfer fluid and has a nominal wall temperature of 230°C. Only the SP burner was tested in this facility.
- Small Watertube Simulator (SWS) (This Study). The furnace is 5.2 m in length and 1.8 m inside diameter, is externally spray-cooled, and has a partial refractory lining. The total heat extraction is controlled by varying the percentage of internal surface which is covered by refractory. Both the SP and IP burners were tested in this facility.

## 1.2 First Stage Parameters

Figure 1-3 shows the influence of the first-stage stoichiometric ratio ($SR_1$) on exhaust emissions from the bench-scale studies carried out in the tunnel furnace and the prototype tests with different residual oils containing approximately 0.6 percent nitrogen. The curves are generally lower but similar in shape to those obtained in other staged combustion studies. As $SR_1$ decreased, $NO_x$ emissions decreased rapidly until a minimum was reached and then increased. Smoke and CO emissions from the SP burner were low for $SR_1 > 0.7$, but under more fuel-rich conditions emissions increased sharply. CO was less than 100 ppm and smoke number was generally less than 5 at the point where the minimum $NO_x$ level occurred. CO and smoke emissions from the IP burner were also low for $SR_1$ greater than the point where minimum $NO_x$

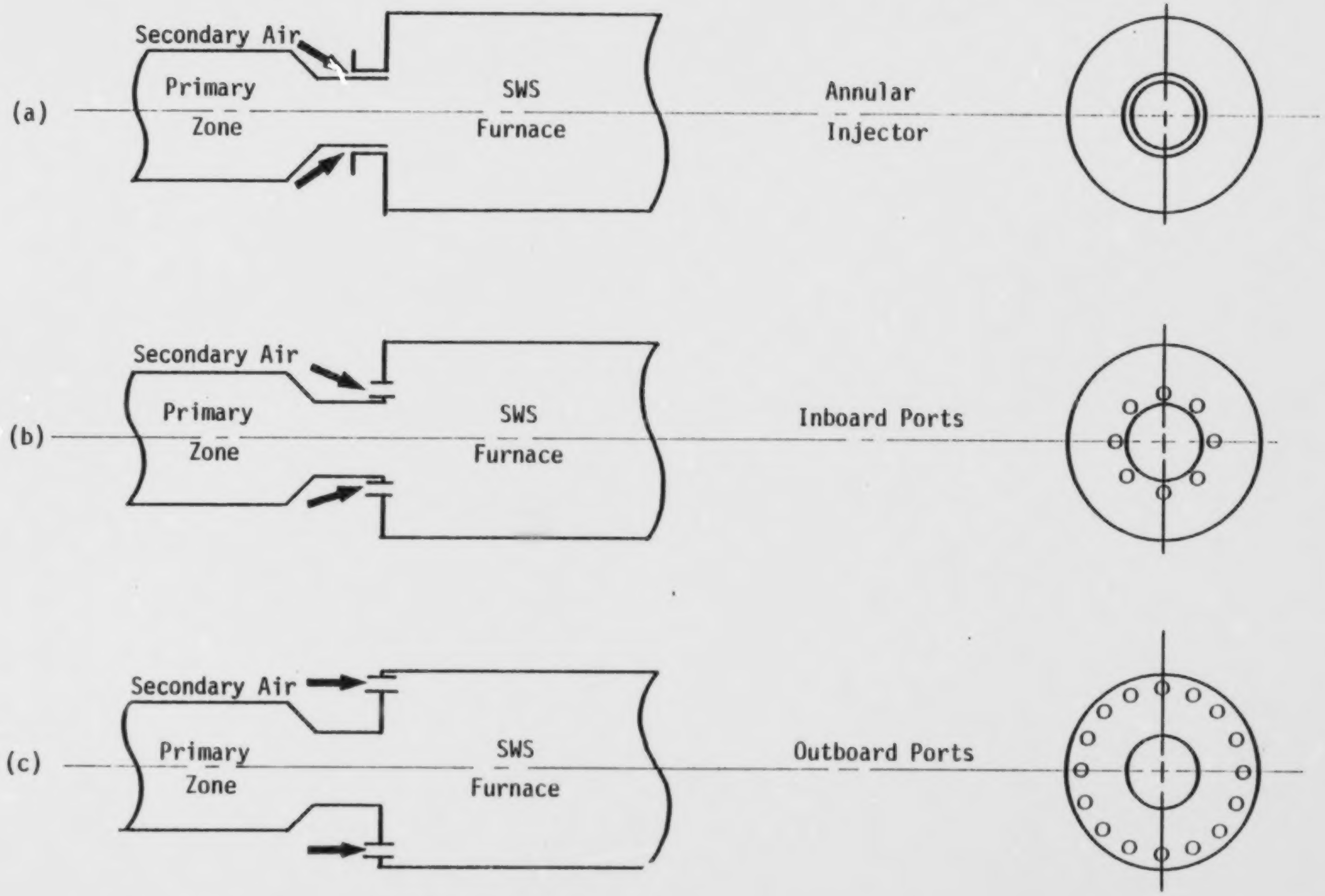
Secondary Air
Primary
Zone
(a)
SWS
Furnace
Annular
Injector
Secondary Air
Primary
Zone
(b)
SWS
Furnace
Inboard Ports
Secondary Air
Primary
Zone
(c)
SWS
Furnace
Outboard Ports

Figure 1-2. Secondary air injection configurations investigated with 3 MW pilot scale burner (ports shown in axial orientation).

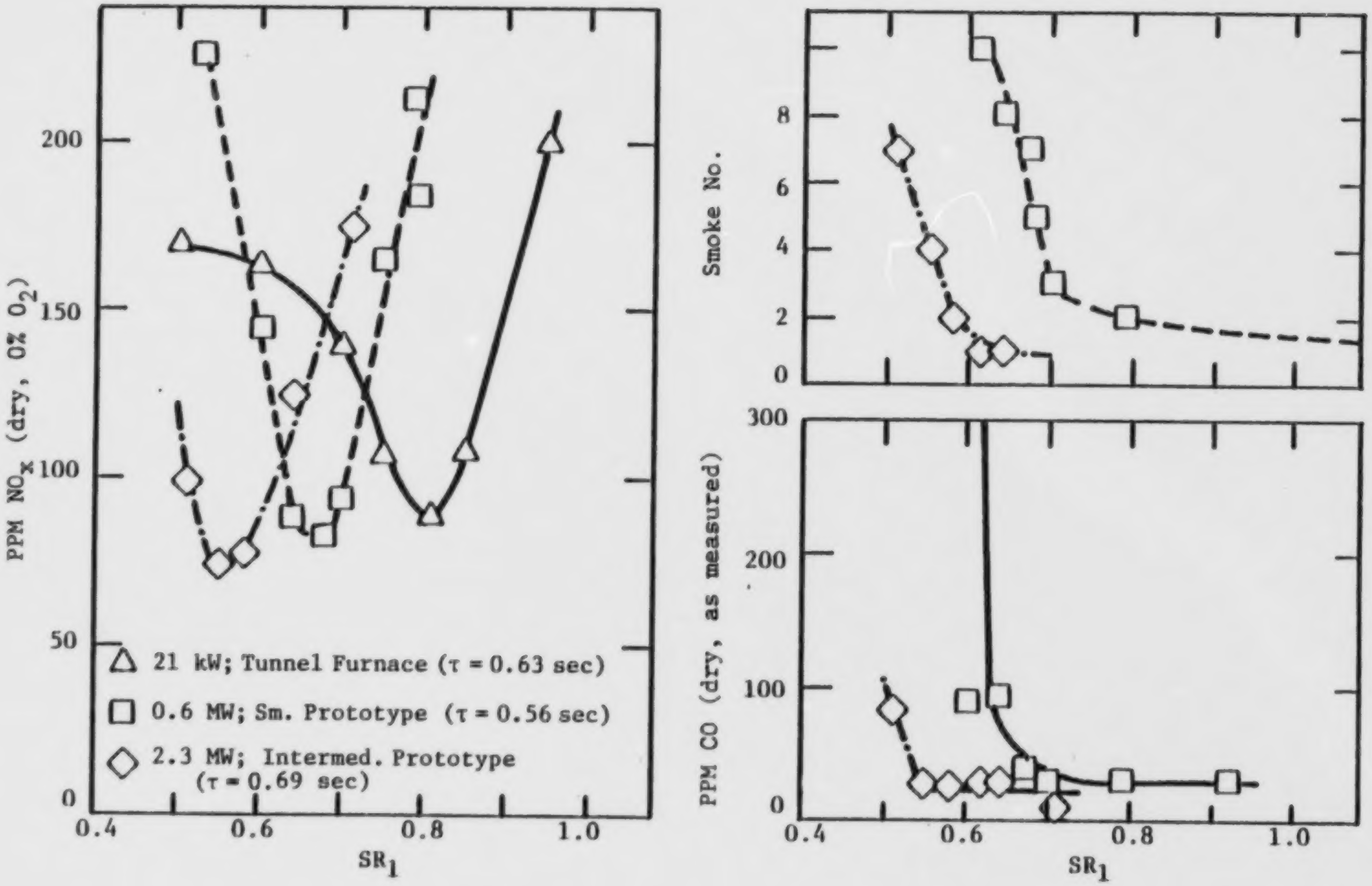

Figure 1-3. Influence of scale on combustor performance.

level occurred. CO and smoke emissions from the IP burner were also low for $SR_1$ greater than the point where minimum NO occurred; however, for many of the configurations tested, the sharp increase in emissions below this point was less severe. Differences in second-stage thermal environment between the 2 x $10^6$ Btu/hr (0.6 MW) firetube simulator and the 10 x $10^6$ Btu/hr (3 MW) small watertube simulator may contribute to the observed difference in burnout of CO and smoke. Comparison of the three sets of results indicates that concept scaleup shifted the optimum $SR_1$ from 0.8 to 0.7 in going from 70,000 Btu/hr (0.02 MW) to 2 x $10^6$ Btu/hr (0.6 MW), and to 0.56 in going to 8 x $10^6$ Btu/hr (2.5 MW). This shift can be attributed to reduced heat losses and therefore higher temperatures, and to changes in fuel/air mixing characteristics, associated with the increase in scale.

The influence of burner load with the IP burner is shown in Figure 1-4 with and without air preheat. Fuel flowrate was varied above and below the baseline load from 2.3 MW to 3.5 MW throughput. Minimum $NO_x$ emissions increased with load, ranging from 95 ppm to 77 ppm at 3.5 to 2.3 MW load, respectively, without first-stage air preheat. With first-stage air preheat, minimum $NO_x$ ranged from 88 to 63 ppm at the same loads, respectively. The optimum stoichiometry in the first stage was not shifted significantly. Optimum $SR_1$ varied from 0.54 to 0.56 with preheat and from 0.55 to 0.57 without preheat. Smoke emissions were insensitive to load.

The effect of atomizer and air distribution variations can be seen in Figure 1-5. $NO_x$ emissions increased substantially when the swirl vanes were removed from the premixer assembly (Configuration III). Optimum stoichiometry was also shifted to the fuel-lean side. The steep dependence of $NO_x$ on $SR_1$ was somewhat reduced at high primary air preheat for Configuration III; however, only limited data was obtained. Observation of the flame from the rear of the SWS indicated a rather bright, narrow jet flame was formed in the first stage chamber. Utilization of available volume for residence time is probably very poor in this configuration, accounting for the increased $NO_x$ emission.

The experimental narrow-angle Y-jet atomizer and ultrasonic atomizer produced similar $NO_x$ emissions under equivalent conditions, although slightly higher than baseline in both cases. Smoke numbers from the Y-jet and internal-mixing atomizer were 2 for all data shown in the figure.

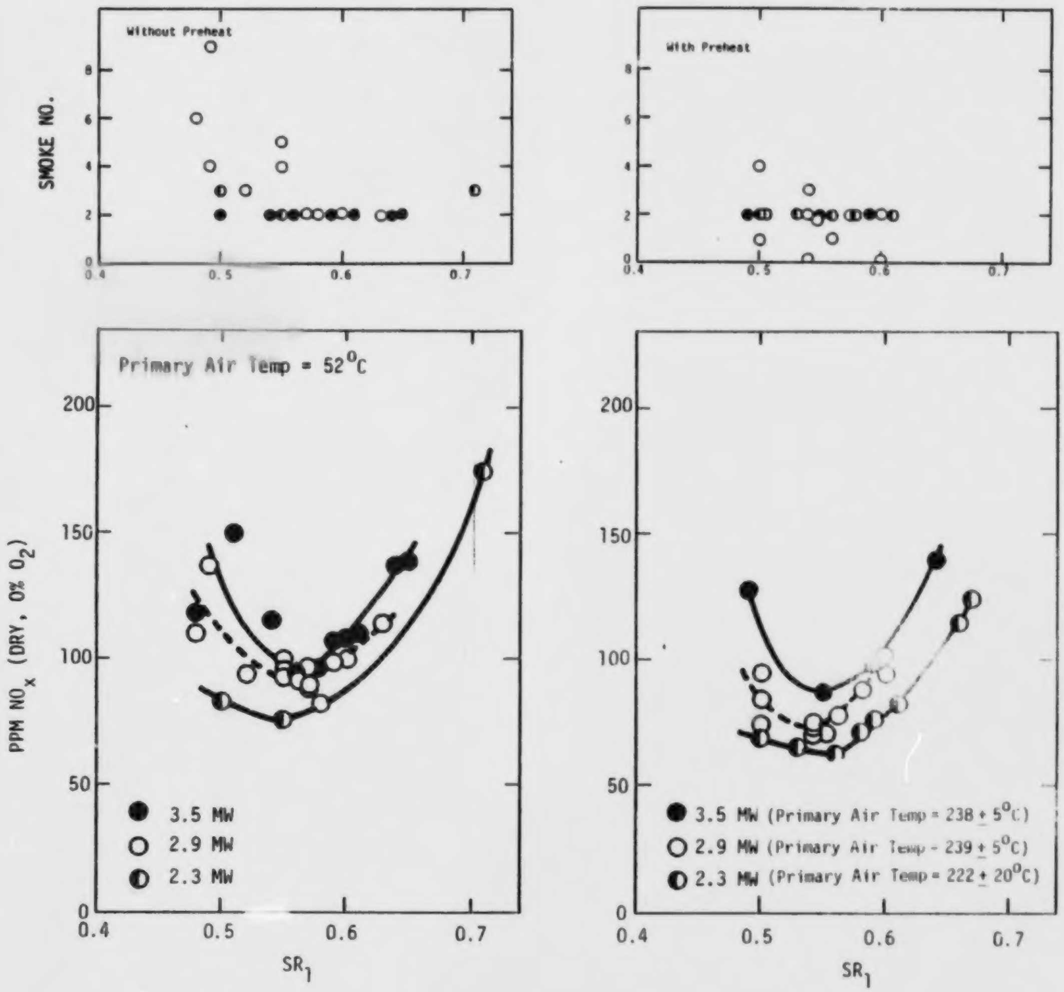

Figure 1-4. Influence of load on emissions from IP burner.

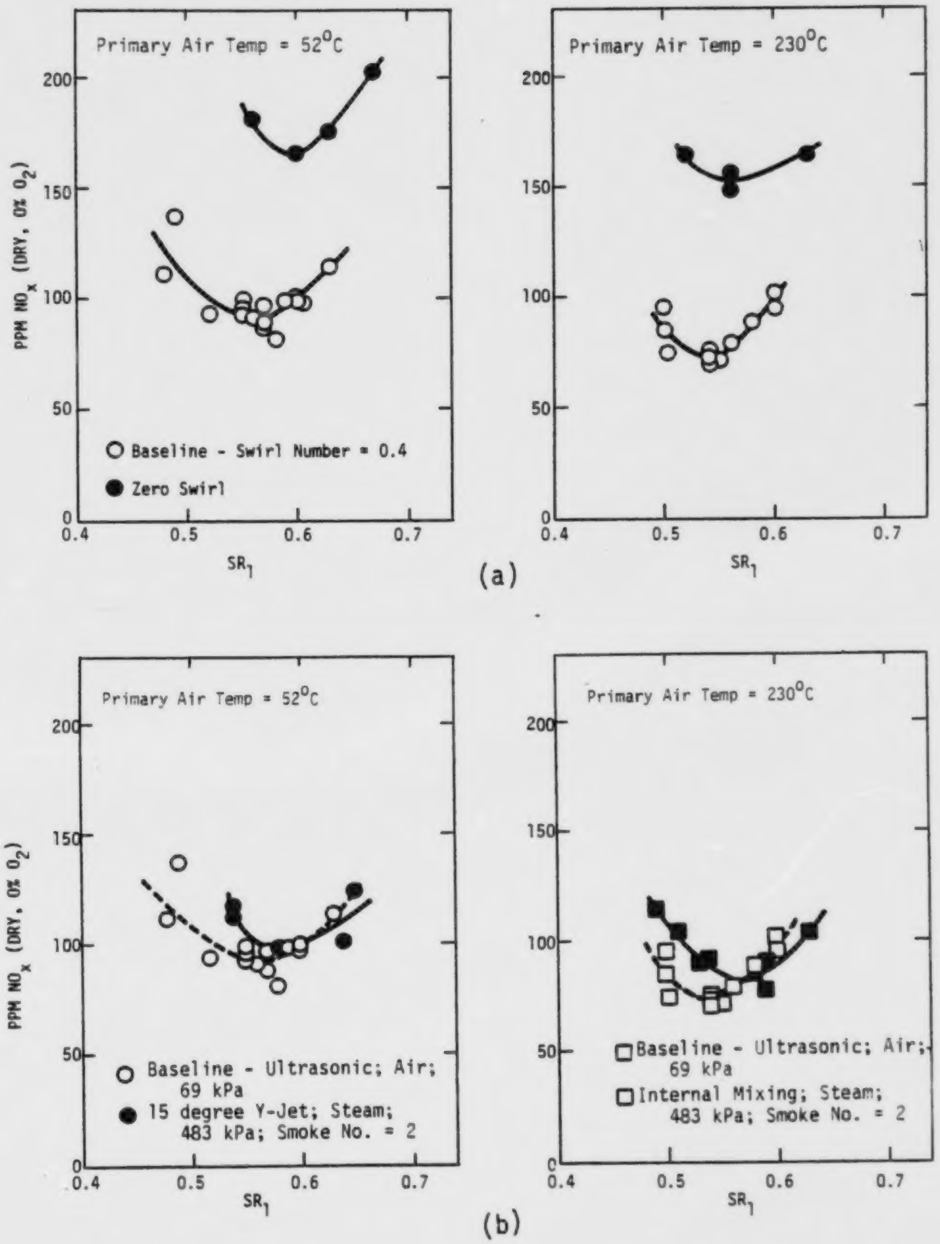

Figure 1-5. Effect of (a) swirl and (b) atomizer type on NO$_x$ emissions.

## 1.3 Second-Stage Effects

The method of secondary air injection can potentially impact exhaust $NO_x$ levels, and different modes of injection have been examined in both prototype burner systems. The standard annular (parallel) air injection system provided a relatively slow mixing rate and tended to result in long diffusion-type flames. In the small prototype burner, rapid mixing was obtained by injecting the second-stage air radially through a water-cooled boom inserted along the firetube axis from the rear. $NO_x$ emissions remained essentially constant when the ratio of air between the axial and radial injectors was varied: however, smoke emissions were substantially decreased as secondar- air was transferred from the parallel injector to the radial injector. Similar results were obtained in both prototype burners when swirl vanes were added to the annular second-stage air injection system, suggesting a relative insensitivity of $NO_x$ emissions to changes in mixing while providing some measure of control over flame shape. In larger practical scale burner systems, however, mechanical considerations may well preclude the use of narrow annular passages for secondary air injection. To overcome this limitation the potential use of discrete secondary air injection ports has been investigated in the intermediate prototype burner. Typical data are presented in Figure 1-6a, and show that with axial injection there is no difference in minimum $NO_x$ between the annulus and discrete ports; with radial injection to induce rapid mixing, an increase of some 25 ppm $NO_x$ was observed. This configuration produced short intense flames and, although the level of smoke emission was generally low, the range of operation over which low smoke could be maintained was extended. The reason for this apparent increased sensitivity to mixing at the larger scale is not immediately apparent from the data, but is believed to be due to increased formation of thermal $NO_x$ in local high-intensity combustion zones close to the air jets.

Figure 1-6b shows the results of doubling the velocity of first-stage combustion products entering the second stage. This was accomplished by adding a sleeve to the first-stage exit. The flame produced by this configuration was very short without a visible smoky trail. The increase in velocity by a factor of two decreased flame length by a factor of 3 to 4, and increased $NO_x$ emissions to 95 ppm from 72 ppm. Entrainment rate of unconfined jets increases approximately as the square of velocity, hence

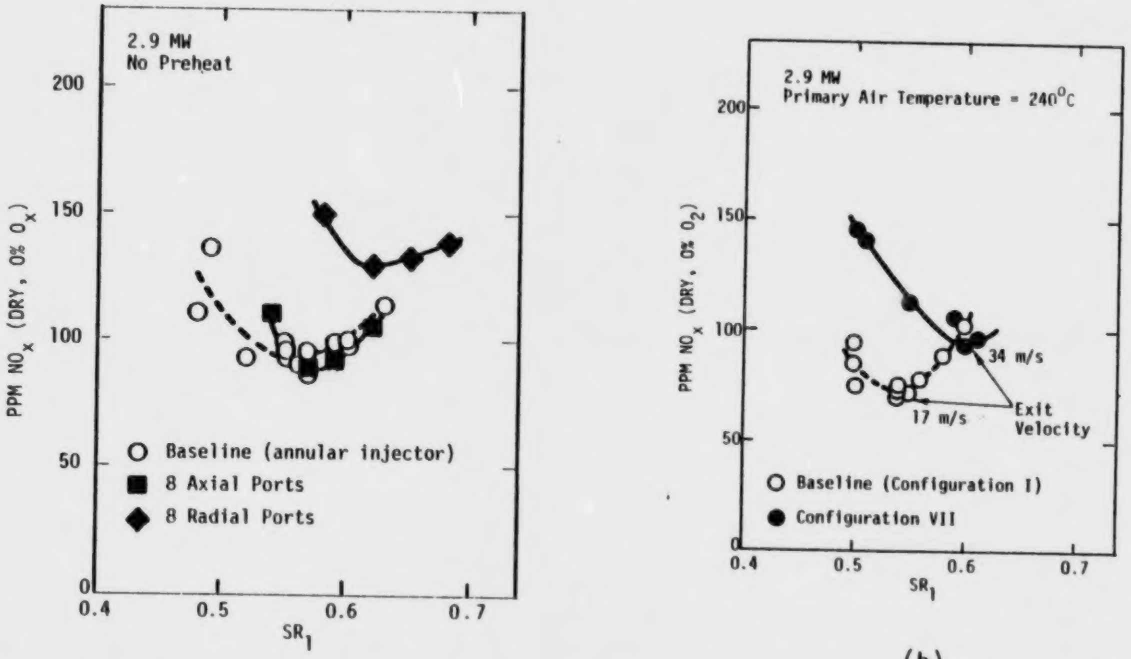

(a)

(b)

Figure 1-6. Second-stage mixing effects.

the flame length seems to be proportional to entrainment rate. Further optimization of exit velocity and swirl level may be possible to improve $NO_x$ and flame shape characteristics with the annular air injector.

All the TFN which exists in the first stage does not result in NO in the combustion products of the second stage. Thus, it is important to design the second-stage air injection system to minimize NO formation from TFN species. In addition, thermal NO formation must be minimized which requires that second-stage flame temperatures must be maintained below some critical threshold. Heat extraction between the fuel-rich zone and the secondary air injection system allows some control over temperature in the second stage. Tests in the SP burner showed that interstage cooling in the form of coils around the periphery of the second-stage throat (approximately 6 percent of the heat input was removed), decreased the minimum exhaust $NO_x$ by approximately 20 ppm. Exactly analogous results were achieved when 40 percent flue gas recycle was introduced with the second-stage air ($\Delta NO$ = 18 ppm). In both tests there was a minor impact on smoke emissions; thus, it appears that at the optimum operating conditions, second-stage thermal NO formation accounts for approximately 20 percent of the total exhaust NO emissions. Use of interstage cooling may become more important in subsequent scaleup if air preheat is added and/or rich-zone heat loss is reduced further. Tests in the IP burner at 3.8 MW in which excess air was varied from 0.3 percent to 4.5 percent produced a 16 ppm variation in $NO_x$, suggesting about the same order of magnitude for thermal NO formation as in the SP tests.

### 1.4 Scaling and Full-Scale Burner Design

The results of the experimental work carried out on the bench and prototype combustors has provided an understanding of the controlling mechanisms of $NO_x$ formation and control in staged liquid fuel combustion. The data suggests that application of these concepts can be achieved in a staged burner which consists of three major components with the following characteristics:

- Fuel Injection System
  - High quality atomization to produce a small mean droplet size.
  - Rapidly mixed fuel and air.

  - Minimal heat extraction and air preheat to maximize fuel vaporization rate.
- First-Stage Fuel-Rich Zone
  - Stoichiometric ratio approximately 0.7 or lower to minimize TFN concentration.
  - Residence time in excess of 400 msec to allow sufficient TFN decay.
  - Control of heat loss to produce a first-stage exit temperature in excess of 2600°F (1425°C).
- Second-Stage Air Injection
  - Partial quenching to minimize thermal NO formation in the second stage.
  - Refractory choke to prevent backmixing and reduce heat loss.
  - Intermediate second-stage mixing to reduce smoke formation without affecting minimum $NO_x$.

The residence time in the fuel-rich zone required to achieve the desired TFN concentration is an important practical design parameter. Figure 1-7 summarizes minimum exhaust $NO_x$ and TFN data for the tunnel furnace and the prototype burners firing in both the firetube simulator and the small watertube simulator as a function of the first-stage residence time. At both bench and small pilot scales, increasing the first-stage residence time significantly decreased exhaust $NO_x$ because of an associated decrease in TFN. (Increasing first-stage residence time allows HCN, $NH_3$, and NO to decay further toward equilibrium values.) Both the exhaust $NO_x$ and the TFN from the SP burner were lower than from the tunnel furnace because of the increased rich-zone temperature associated with the increase in scale.

Variations in first-stage residence time were achieved in the SP burner/firetube simulator tests by altering the firing rate, and in the SP burner/watertube simulator tests by changing the reactor length at a fixed firing rate. A strong correlation between the two sets of experiments suggests that the controlling processes are dominated by kinetic effects (time and

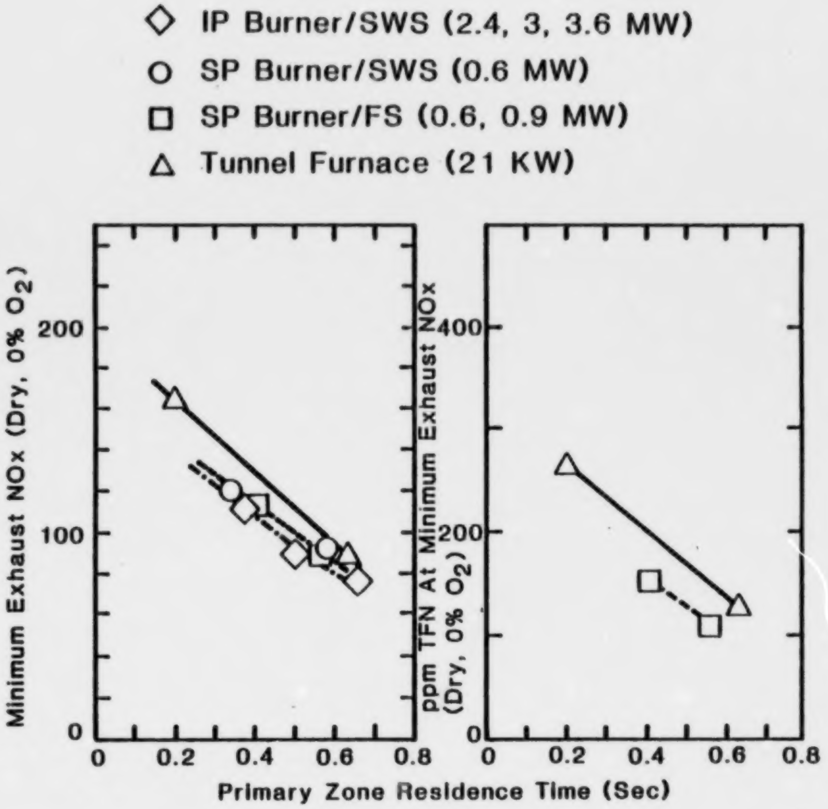

Figure 1-7. Second-stage $NO_x$ production and first-stage TFN decay for bench scale and pilot scale.

temperature) and not by aerodynamics and that the principal influence of firing rate is on residence time. Clearly, increasing firing rate also increases first-stage temperature, but this effect is small because even at 2 x $10^6$ Btu /hr (0.6 MW) the prototype heat losses were low. First-stage exit temperatures measured at $SR_1$ of 0.7 were 2950°F (1620°C) compared to adiabatic flame temperature of 3180°F (1750°C).

The key elements in these design characteristics are the requirements for a high-temperature, optimally fuel-rich, primary combustion zone with a long residence time. A number of the remaining parameters are scale-dependent and must be optimized at the burner scale under consideration. The mean droplet size produced by a given atomizer design, for example, does not remain constant with scale, but tends to increase as size increases. Drop-size distributions produced by full-scale (18 MW) atomizers under isothermal conditions showed that the mean drop size was similar for an ultrasonic atomizer and a Y-jet atomizer (Figure 1-8); however, radial distribution of fuel mass within the swirling flow field was very different. While small droplets are more favorable, combustion conditions are such that droplet size alone does not have a large impact on minimum $NO_x$. Rather, increased droplet size leads to greater sensitivity to those parameters which control fuel/air mixing and spray penetration. For practical applications, optimum results are obtained by selecting and matching spray angles and air register designs to provide for uniform distribution and rapid mixing.

Similarly, the overall burner performance has been shown to be more sensitive to the mode of secondary combustion air injection at larger burner scales. Rapid mixing is required to suppress smoke formation, but may impact minimum $NO_x$ performance. In practical applications a major additional concern is the shape of the second-stage flame and its interaction with its heat transfer surroundings, which can be strongly influenced by mixing. Final designs of secondary air injection will therefore represent a compromise between $NO_x$ emissions, flame shape and other pollutants such as particulates and CO.

The impact of fuel type on the ability of such burners to achieve low-$NO_x$ emissions is also of importance. The influence of fuel-nitrogen content on the performance of the small-scale low-$NO_x$ prototype burner was established by conducting tests with a distillate oil, residual oils, a coal

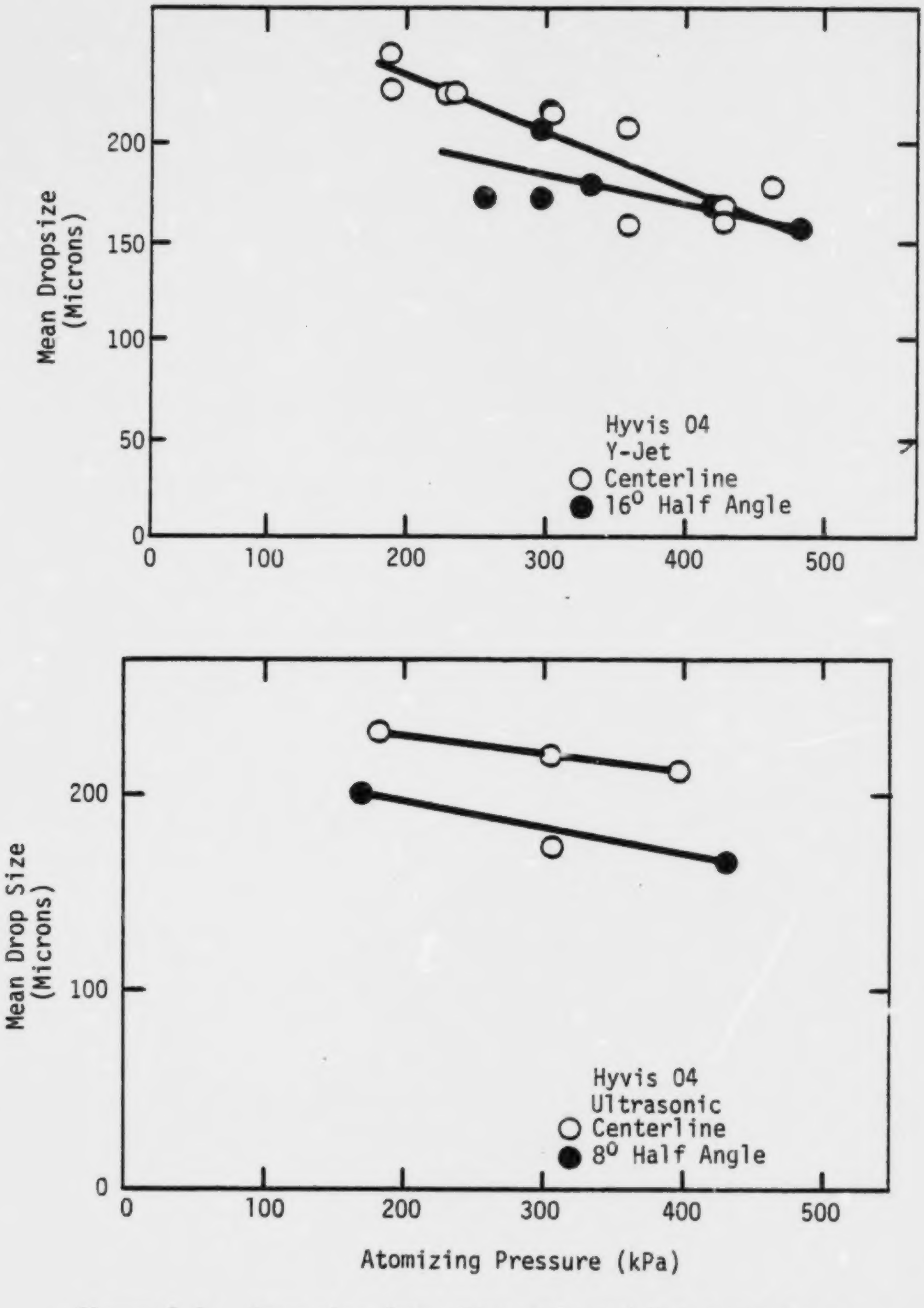

Figure 1-8. Drop size from ultrasonic and Y-jet atomizers.

liquid and propane $NH_3$. Data obtained in these tests are shown in Figure 1-9 which indicates that with the SP burner minimum NO emissions are only weakly dependent upon total fuel nitrogen content. Figure 1-9 also summarizes data obtained in the small-scale tunnel furnace, and in the larger $10 \times 10^6$ Btu/hr (3 MW) prototype. Concept scaleup reduced the dependence on fuel-nitrogen; this is probably because of the increased fuel-rich temperature. Thus this low $NO_x$ concept should be capable of producing $NO_x$ emissions less than 100 ppm at 0% $O_2$ (85 ppm at 3% $O_2$) even when firing the high-nitrogen crude oils typical, for example, of the Kern County oil fields.

The current program under EPA sponsorship has implemented these low-$NO_x$ criteria into the design of a full-scale, 18 MW commercial prototype burner. Two full-scale designs, illustrated in Figure 1-10 were developed as a result of the detailed engineering study: a regenerative system in which the refractory chamber is designed to provide primary air preheat by flowing air through a hollow cylindrical shell; and a design employing a multilayer refractory construction to minimize heat loss. Both concepts employ commercially available primary burner components and secondary air injection through two sets of discrete ports, oriented axially and radially. After detailed evaluation of the relative performance potential of the two designs, the regenerative concept was chosen for construction. The selection was made after considering structural integrity of the refractory lining, heat loss to surroundings, temperature profile within the first-stage, and other characteristics such as space-efficiency (compactness) and transient performance.

The regenerative first-stage chamber is 2.1 meters inside diameter and approximately 5.5 meters long. The shell is lined with 15 cm of 90 percent alumina refractory brick, and incorporates an annular passage for primary air. The annular gap is designed for air velocity of 19 meters/second for convective heat transfer. The entire shell is externally lined with ceramic fiber insulation to reduce external heat losses.

Burner construction is scheduled for completion in May of 1983 followed by the laboratory and field testing.

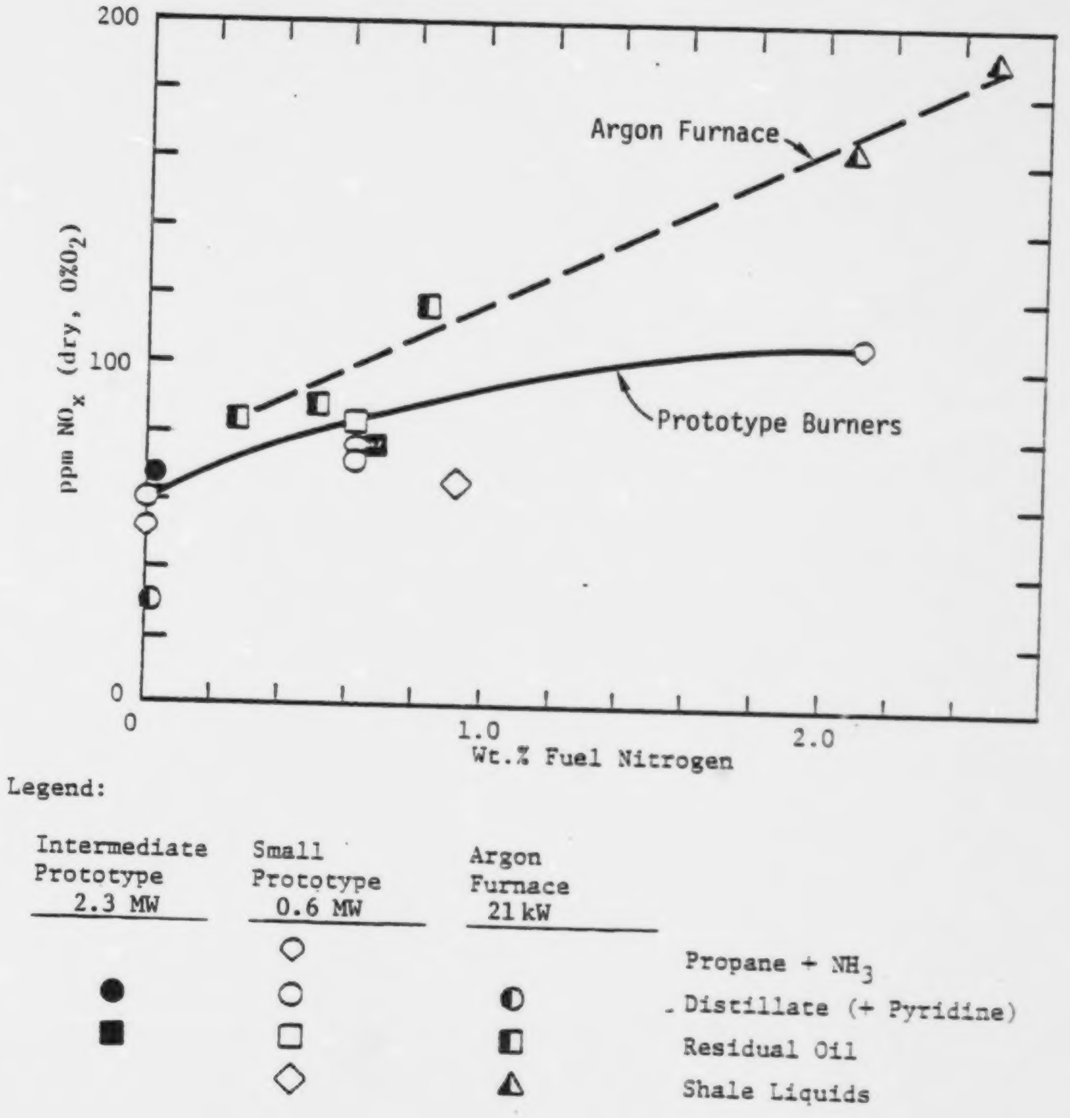

Figure 1-9. Influence of fuel nitrogen on second-stage NO$_x$ - bench-scale and pilot-scale data.

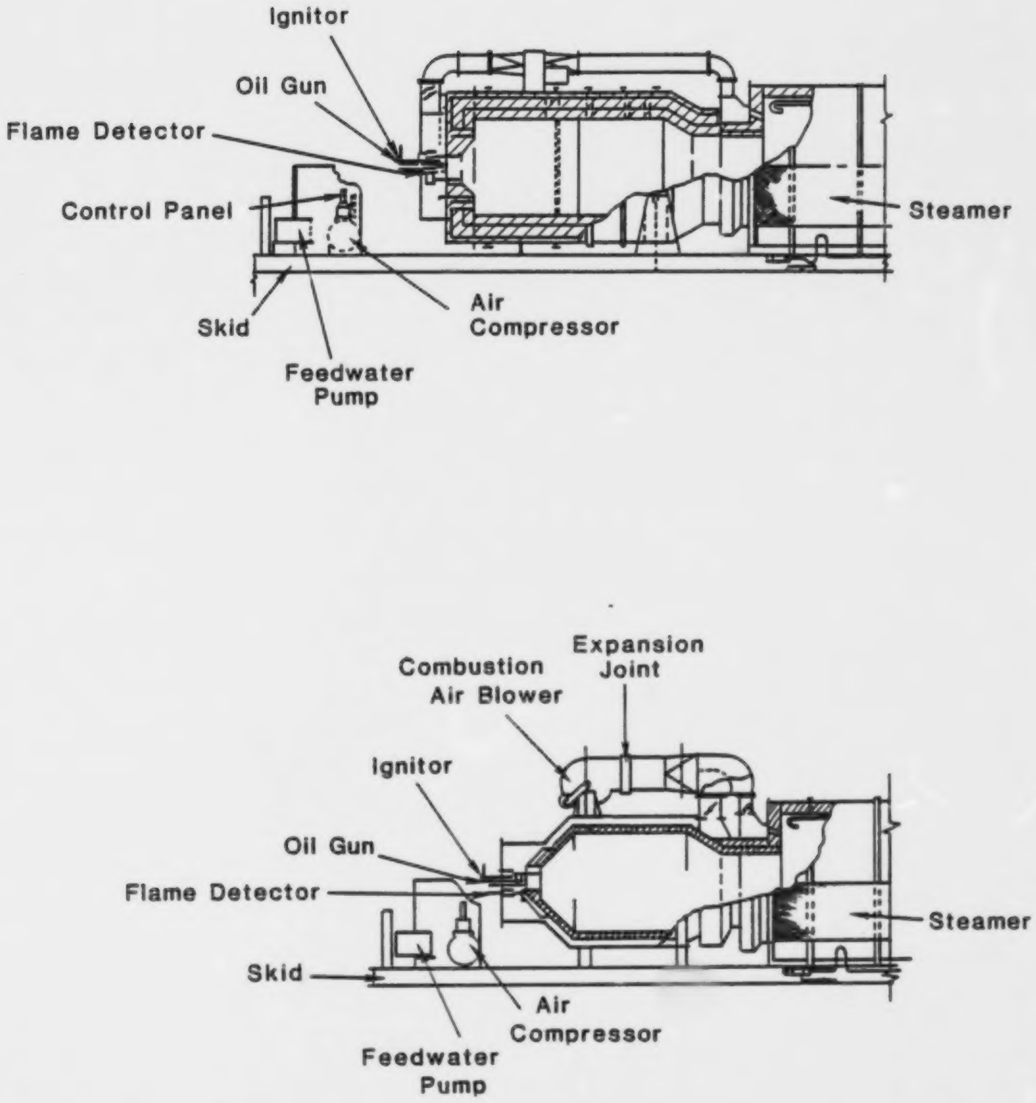
Ignitor
Oil Gun
Flame Detector
Control Panel
Steamer
Skid
Air Compressor
Feedwater Pump
Expansion Joint
Combustion Air Blower
Ignitor
Oil Gun
Flame Detector
Steamer
Skid
Air Compressor
Feedwater Pump

Figure 1-10. Conceptual burner designs for TEOR steam generators.

## 2.0 LOW $NO_x$ COMBUSTOR CONCEPT DEFINITION

This section of the report describes briefly the background and the early development leading to definition of a low-$NO_x$ combustor for retrofit to existing thermally enhanced oil recovery (TEOR) steam generators.

### 2.1 The Chemistry of $NO_x$ Formation and Control

Nitrogen oxides emissions from stationary combustors can be reduced by combustion modification techniques which involve staging the heat-release process to produce consecutive fuel-rich and fuel-lean zones. However, the application of these techniques to residual fuel/oil fired combustors has been only partly successful, because of a trade-off in pollutants. The decrease in $NO_x$ emissions is quite often accompanied by an increase in particulate emissions. The optimization of combustion modification techniques to control $NO_x$ emissions from liquid-fuel fired combustors has also proved difficult because of the limited knowledge of the phenomena $NO_x$ formation and destruction during the combustion of fossil fuel.

Two sources of nitrogen have been identified which produce nitric oxide, NO, during combustion, these are:

- Molecular nitrogen, $N_2$ which is supplied with the combustion air and its fixation results in the formation of thermal NO. There are two mechanisms which allow the N≡N to be broken, giving a path for NO formation. The first requires oxygen atoms whose concentration is a strong function of temperature (therefore the term thermal NO) by $N_2 + O \rightarrow NO + N$ (2.1)

It has also been shown that hydrocarbon radicals will react with molecular nitrogen, and equation 2.2 is an example.

$$N_2 + CH \rightarrow CN + NH \tag{2.2}$$

Nitrogen-containing radicals (N, CN, NH) can then be converted to NO by oxidative radicals.

- Nitrogen chemically bound with the fuel can be converted to NO (termed fuel NO) during the normal combustion process. It is generally accepted that the major nitrogen product of fuel pyrolysis is HCN which can be converted rapidly to NO.

Field-testing results have shown that staged-combustion techniques are far more effective for $NO_x$ control than flue-gas recirculation, thereby suggesting the importance of fuel-nitrogen oxidation (Cato et al., 1976). Pershing, Martin, and Berkau (1975) conducted pilot-scale studies with actual residual fuel oils and proved that fuel-nitrogen oxidation is significant in flames and suggested its importance in practical systems. Staged heat release (staged combustion) provides the most effective $NO_x$ control technique for nitrogen-containing fuels because fuel NO formation is mainly dependent upon local stoichiometry. It can be accomplished either by separating the combustion chamber into two zones and dividing the total combustion air into two streams, or by an appropriate burner design which promotes localized fuel-rich conditions. Under fuel-rich conditions, the conversion of fuel nitrogen to fuel NO is reduced significantly (Fenimore, 1979). Thus, there are two overall fuel nitrogen reaction paths leading to the production of $N_2$ or NO from fuel nitrogen fragments (N), namely:

Path A. Fuel-lean

$$XN + \text{Oxidant} \longrightarrow NO + \ldots . \tag{2.3}$$

Path B. Fuel-rich

$$XN + \ldots . \longrightarrow N_2 + \ldots . \tag{2.4}$$

The objective of staged combustion emission control techniques is the provision of conditions which maximize $N_2$ production via Path B.

Figure 2-1 shows the results of equilibrium calculations for methane combustion with 1 weight-percent nitrogen in the fuel. As the stoichiometric ratio is reduced below 1.0, the equilibrium NO decreases markedly and $NH_3$ and HCN begin to rise (see Figure 2-1a). The minimum total fixed nitrogen ($TFN = NO + HCN + NH_3$) is a strong function of temperature as shown in Figure 2-1b. Increasing the temperature reduces the stoichiometry at which the minimum occurs. In addition, below $SR_1 = 0.9$, equilibrium TFN concentrations are less than 10 ppm for all conditions for practical interest. Consequently, equilibrium calculations suggest that the concentration of nitrogen-containing species (TFN) which can be converted to NO in the second stage of a staged combustion system can be very low under optimum conditions. Thus, the optimization of path B (equation 2-4) will minimize NO formation during staged

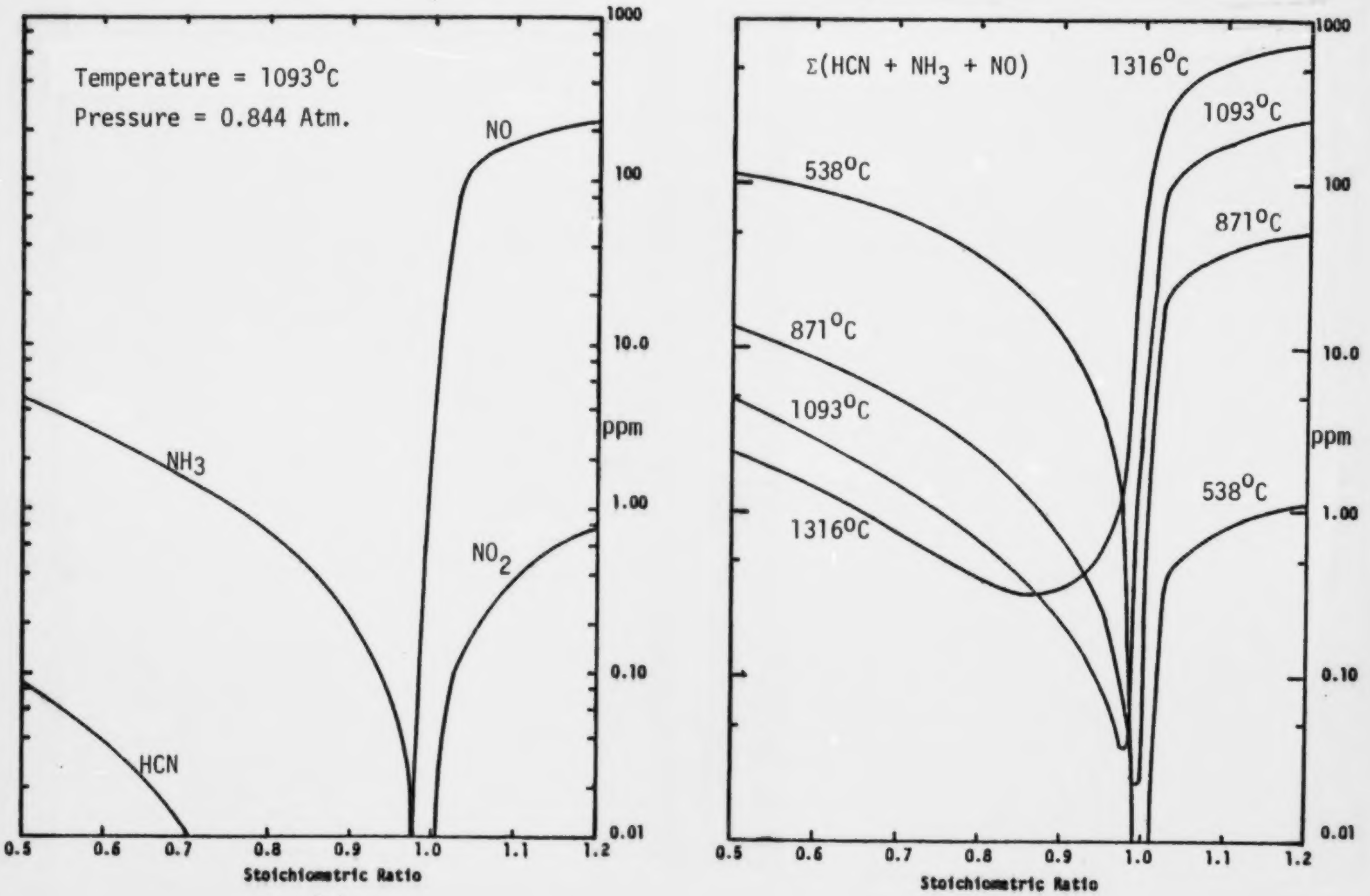

(a) (b)

Figure 2-1. Equilibrium TFN concentrations calculated for methane fuel containing 1 percent by weight of nitrogen.

combustion providing thermal NO is not formed in the second fuel-lean zone. The key reactions associated with $N_2$ production appear to be

$$HCN + OH \longrightarrow HNCO + H \tag{2.5}$$

$$HNCO \longrightarrow NH + CO \tag{2.6}$$

$$HNCO + OH \longrightarrow NCO + H_2O \qquad (2.7$$

$$NCO + H \longrightarrow NH + CO \tag{2.8}$$

NH can be transformed to N, NH, or $NH_3$. $N_2$ can be formed from reactions involving these radicals and NO, thus

$$N + NO \longrightarrow N_2 + O \tag{2.9}$$

$$NO + NH_2 \longrightarrow N_2 + H_2O \tag{2.10}$$

There is some question whether equation 2.10 is an elementary reaction but the pathway it represents appears to be significant at low temperatures.

The reactions listed above give no indication that NO, once formed can be destroyed other than by reactions such as 2.9 and 2.10. However, it appears that NO can react with hydrocarbon to produce CN which can be transformed to NH

$$NO + CH \longrightarrow CN + OH \tag{2.11}$$

$$NO + CH \longrightarrow HCN + H \tag{2.12}$$

Figure 2-2 shows the results of a calculation to illustrate how the TFN concentration decays in the rich zone and the parameters controlling this decay. The model used assumed a 2 msec well-stirred reaction-ignition zone followed by a variable-length plug-flow reactor. The fuel was $CH_4$ containing one weight-percent N as HCN. Preliminary runs showed that the initial fuel nitrogen speciation input to the first stage had little effect on the ultimate TFN level. Rich-zone temperature was assumed to decay linearly from 2925°F (1600°C) to the specified final temperature over 660 msec. Figure 2-2 summarizes results obtained with the kinetic model. Under fuel-rich conditions, the rate of TFN decay slows dramatically when the gas temperature drops below approximately 2600°F (1425°C). The dotted line on this figure shows the residence time at which the various temperature ramps have decayed to 2600 F. Further, even if the fuel-rich temperature is maintained at a high level

F2-2

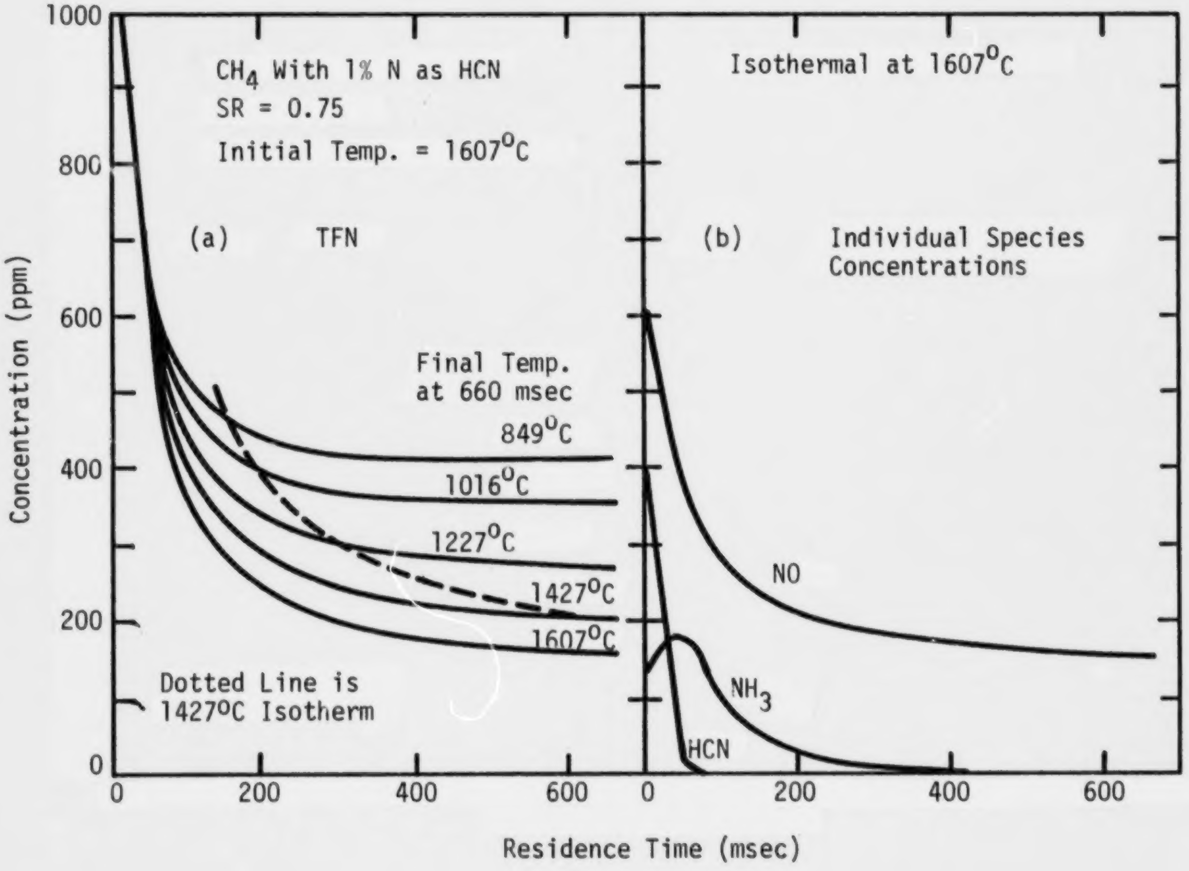

Figure 2-2. Calculation of (a) total fixed nitrogen decay and (b) decay of individual fixed nitrogen species.

(e.g., 1607°C case on Figure 2-2b), the rate of NO decay decreases precipitously when the $NH_3$ concentration falls to zero indicating that TFN speciation is important in the first-stage processing. These calculations support the concept that reactions of the form

$$NO + NH_i \longrightarrow N_2$$

are controlling the fuel-rich TFN reduction and that it is essential to have both high temperature (>1400°C), and a proper TFN species distribution to achieve very low exhaust $NO_x$. The calculations also indicate the need for a long residence time in the primary zone but that this requirement decreases with increasing first-stage temperatures for a fixed TFN level.

In summary, it appears that:

1. Limits imposed by thermodynamic equilibrium are far below the NO levels achieved in practical staged combustion systems.
2. Chemical paths exist which allow the destruction of NO and the formation of $N_2$ under fuel-rich conditions.
3. High temperatures and long times are required to maximize the formation of $N_2$ in the fuel-rich zone.

Based upon this, a low-$NO_x$ combustor for liquid fuels containing bound nitrogen can be divided conceptually into four zones:

- Fuel preparation zone to convert the fuel rapidly into gaseous fragments.
- Fuel-rich first-stage to maximize $N_2$ formation.
- Secondary air addition stage to minimize the conversion of the remaining TFN to $N_2$.
- Second stage to ensure complete heat release, minimize the formation of thermal NO and soot

## 2.2 Bench-Scale Experiments

England (1981) described in detail a series of experiments which were conducted in the 21 kW (70,000 Btu/hr) tunnel furnace shown in Figure 2-3 to identify the conditions which produced low-$NO_x$ emissions from the type of combustor defined at the end of the previous subsection. The original, small-scale

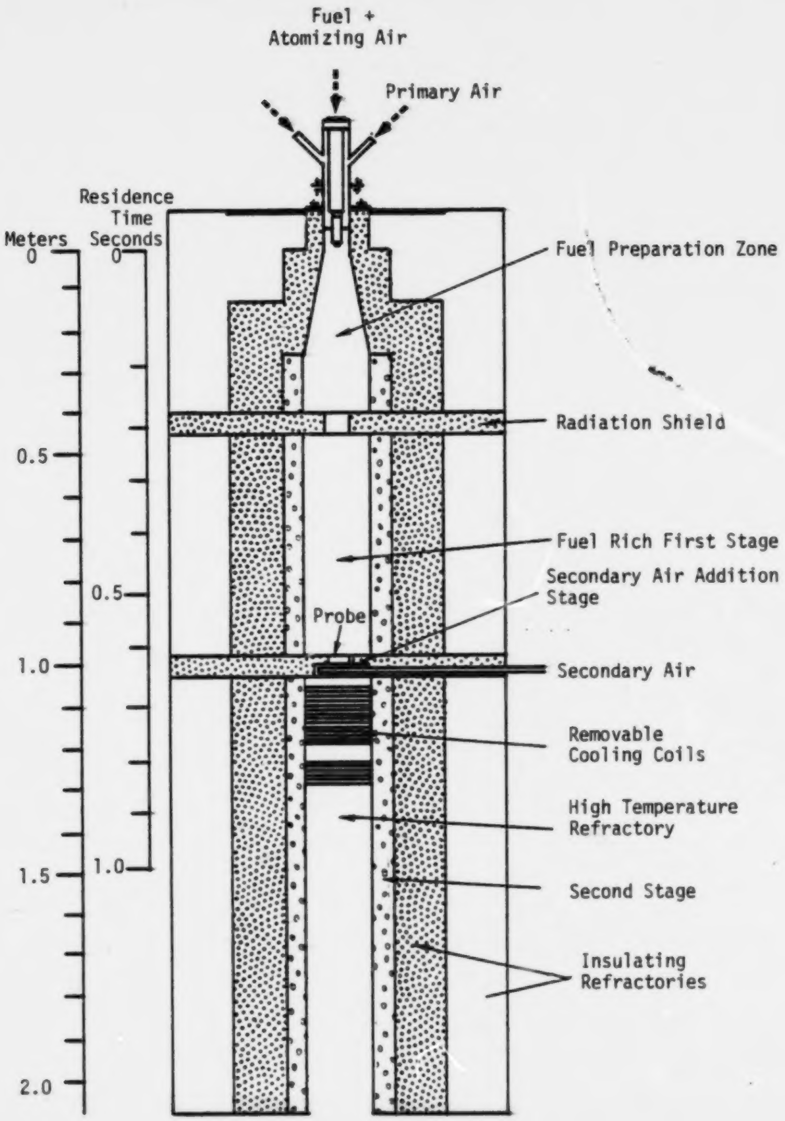
Fuel +
Atomizing Air
Primary Air
Residence Time Seconds
Meters
0
0
0.5
0.5
1.0
1.0
1.5
2.0
Fuel Preparation Zone
Radiation Shield
Fuel Rich First Stage
Secondary Air Addition Stage
Probe
Secondary Air
Removable Cooling Coils
High Temperature Refractory
Second Stage
Insulating Refractories

Figure 2-3. Bench-scale tunnel furnace.

tunnel furnace was modified to allow in-flame sampling of the TFN (NO, HCN, $NH_3$) species and cooling of the first-stage and/or second-stage combustion regions, as illustrated in Figure 2-3. A "radiation shield" or (choke) was installed near the top of the furnace to minimize the effects of downstream changes on the fuel preparation zone. A secondary air injection ring and cast refractory choke were installed at 1.04 m to insure isolation of the first stage. Variable cooling was achieved by insertion of multiple stainless steel water-cooling coils.

### 2.2.1 Fuel Preparation Zone

The "effective residence" in the fuel-rich stage is controlled by the conditions in the fuel preparation zone. Figure 2-4 shows the influence of heat extraction rate in the near-burner zone on exhaust $NO_x$ emissions. In these studies, water-cooling coils were placed in the first stage, and in half of the tests a refractory "radiation shield" was installed to block the radiant cooling of the vaporization zone. The data indicate that slowing the vaporization rate significantly increases the exhaust emissions. A similar effect was achieved by altering the mean drop size. Results indicated that reducing the mean droplet size generally resulted in lower minimum $NO_x$ emissions and reduced smoke production.

### 2.2.2 Fuel-Rich First Stage

In an effort to increase the understanding of the mechanisms controlling NO formation under staged combustion conditions, detailed in-flame measurements of TFN species (NO, HCN, $NH_3$) were made at the end of the fuel-rich first stage. Figure 2-5 shows typical results for a Kern County Crude Oil firing at 21 kW (70 x $10^3$ Btu/hr) in the tunnel furnace. In general, decreasing the first-stage stoichiometric ratio reduced the NO concentration leaving the first stage. However, below a stoichiometric ratio of approximately 0.8 significant amounts of $NH_3$ and HCN were measured. Thus, there exists a minimum in exhaust $NO_x$ ($((NO_x)_E)$) concentrations because of a competition between decreased first-stage NO and increased oxidizable nitrogen species such as HCN.

The results presented in Figures 2-6 and 2-7 were obtained in the tunnel furnace with a shale crude, and they demonstrate the impact of fuel-rich first-stage heat loss on the fate of fuel nitrogen. The hot conditions refer

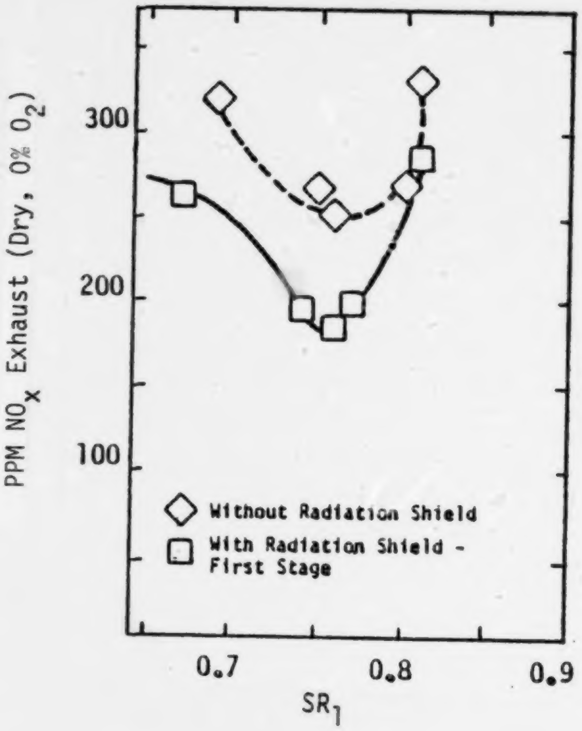

Figure 2-4. Influence of heat extraction rate in the fuel preparation zone.

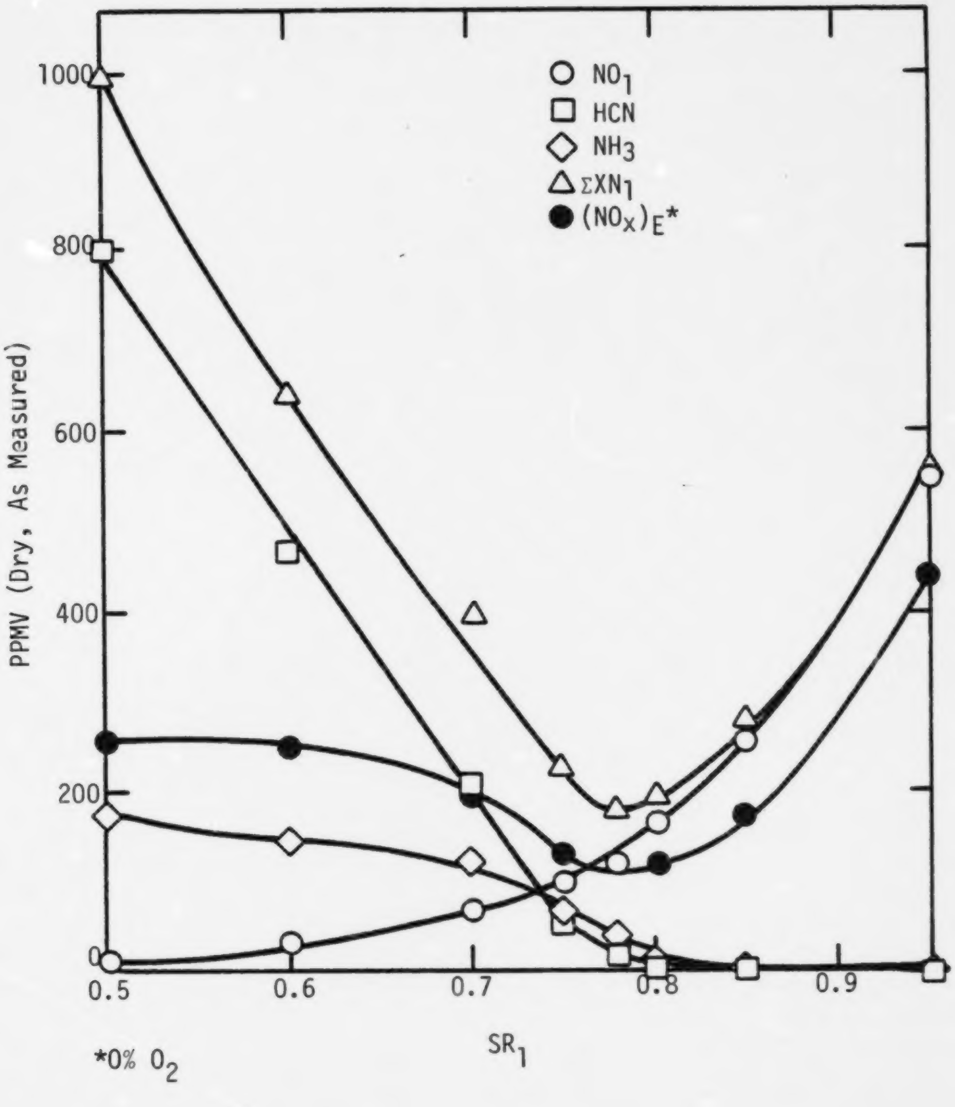

Figure 2-5. Detailed in-flame measurements with Kern County crude oil (R14) (21 kW).

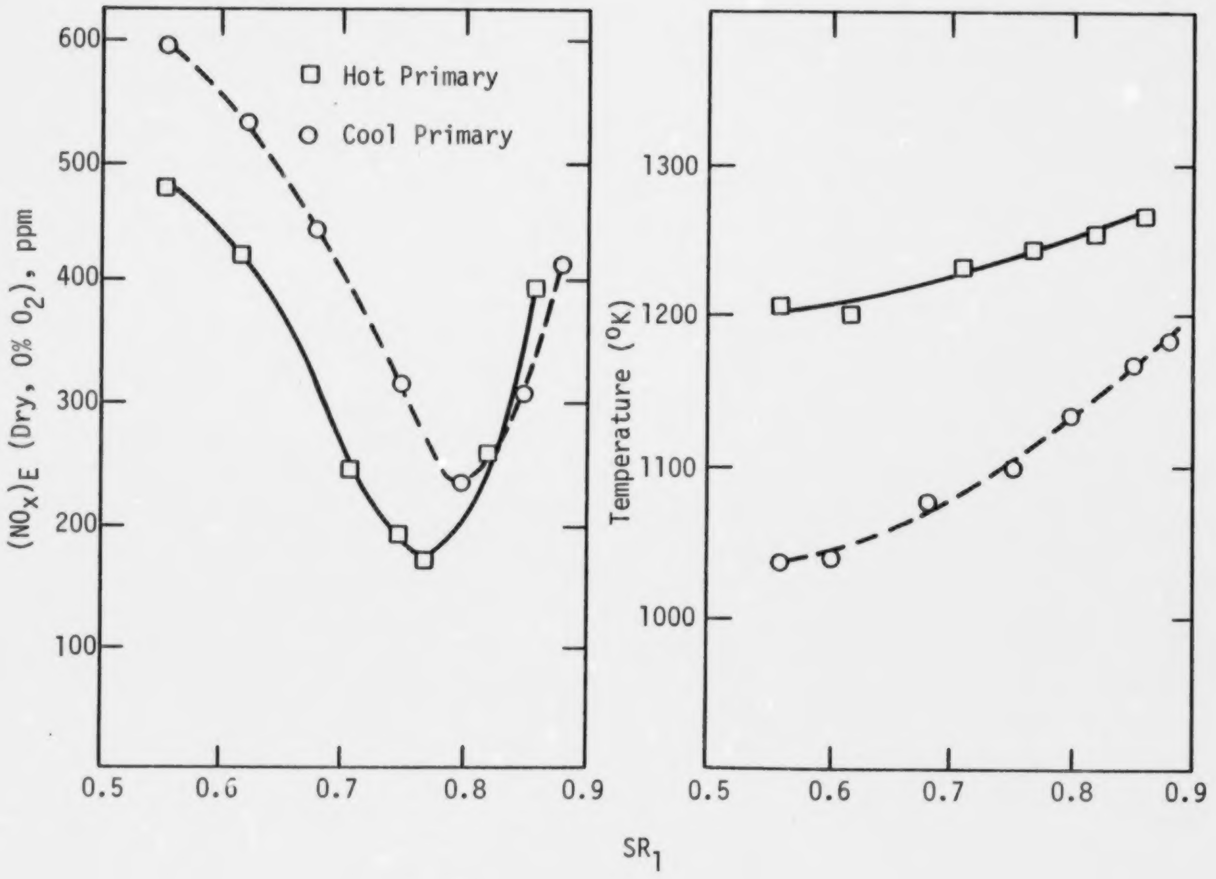

Figure 2-6. The influence of fuel-rich hold-up zone temperature profile on exhaust $NO_x$.

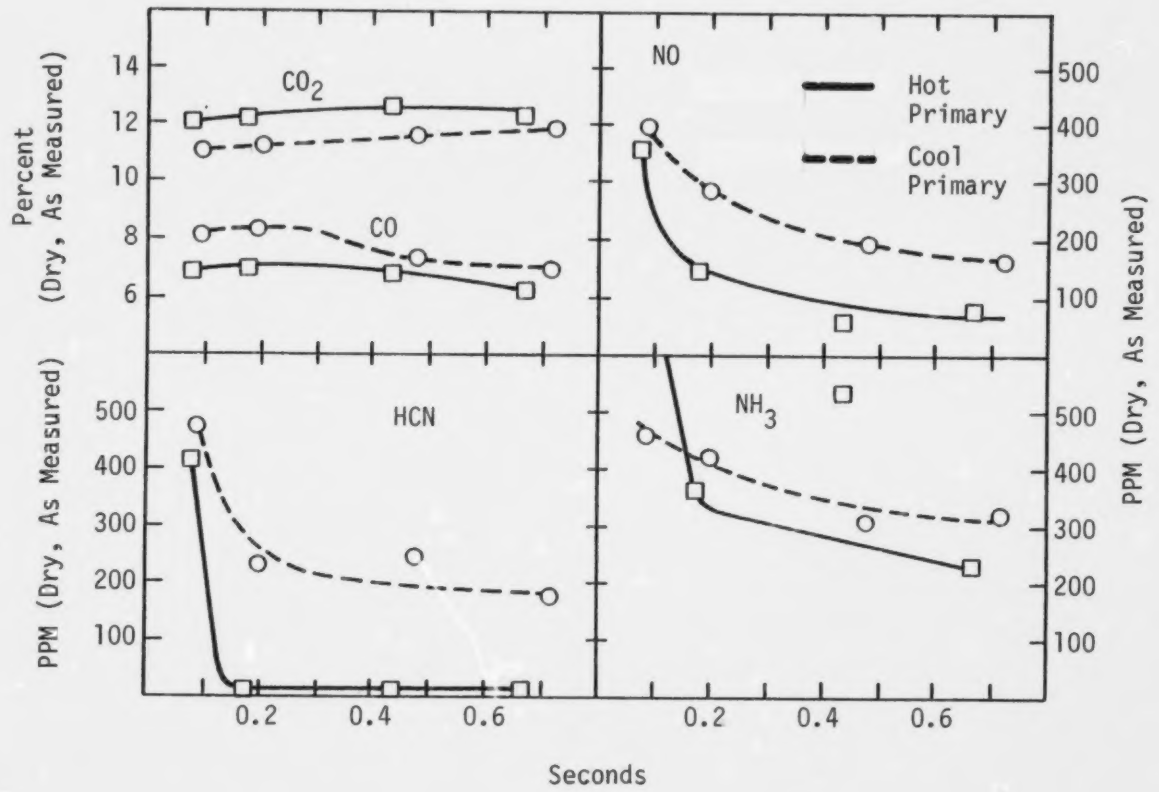

Figure 2-7. CO oxidation and decay of XN species for two temperature profiles.

to the furnace without primary zone cooling and with the radiation choke (as shown in Figure 2-3). To cool the furnace, cooling coils were added prior to the second stage choke and the radiation choke was removed. Figure 2-6 shows exhaust $NO_x$ and primary zone gas temperature as a function of stoichiometric ratio for the two conditions. Minimum $NO_x$ emissions were reduced for the hot case, and the optimum stoichiometry was shifted toward more fuel-rich conditions. This effect is in agreement with the discussion in the previous section. The experimentally measured axial profiles presented in Figure 2-7 provide an explanation for this shift in the minimum emission levels. Heat extraction in the first stage impacts the rate of decay of TFN. Under cold conditions, both NO and HCN essentially freeze, whereas without heat extraction the initial rate of decay for all three species is much faster, leading to low TFN concentrations at the exit of the fuel-rich first stage. It should be noted that heat extraction also affects the rate of CO oxidation.

### 2.2.3 Second Stage

Four factors affect the level of exhaust $NO_x$ emissions measured for a specified set of primary and interstage conditions:

- The amount of TFN species entering the second-stage flame.
- The relative conversion efficiencies of the TFN species.
- The influence of other partial combustion products in the TFN conversion chemistry.
- The thermal and concentration history of the second-stage flame.

As noted previously, measurements within the fuel-rich first stage show that at the optimum stoichiometry NO, HCN, and $NH_3$ coexist. TFN exists mainly as HCN and $NH_3$ for more fuel-rich conditions, and for conditions less fuel-rich than the optimum, NO is the primary fixed nitrogen species. Figure 2-8a shows the percentage conversion of the first stage TFN for a + 454°C shale fraction burning at 21 kW in the tunnel furnace. As the first-stage stoichiometry was progressively reduced from $SR_1 = 1.05$, the TFN decreased (due to decreased first-stage NO formation) and the percent conversion also decreased (due to increased second-stage combustion). These two effects resulted in a rapid decrease in exhaust $NO_x$. Below $SR_1 = 0.8$,

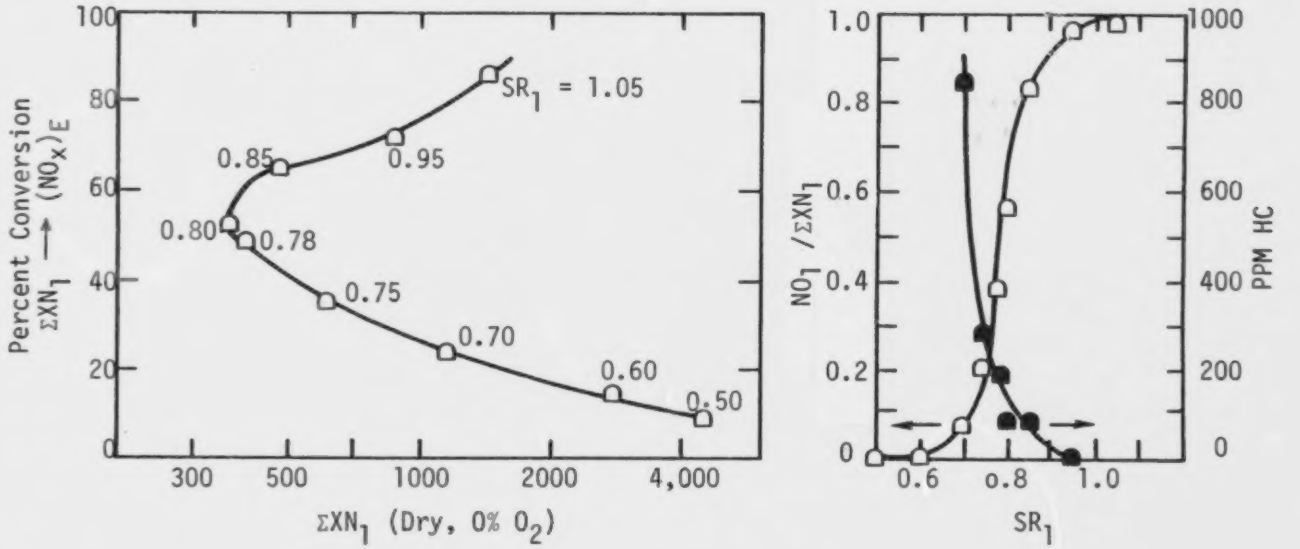

(a) (b)

Figure 2-8. Influence of first-stage exit composition on second-stage $NO_x$ formation (tunnel furnace--+454°C shale fraction).

the TFN began to rise dramatically because of HCN and $NH_3$ formation, but the percent conversion continued to decrease. Thus, in general, there can exist two first stage stoichiometries with identical TFN levels (e.g., 1000 ppm) but with vastly different conversion efficiencies (77 percent versus 26 percent) and, hence, different exhaust emissions.

Figure 2-8b indicates that there are two major differences between the upper and lower percent conversion curves shown in Figure 2-8a. First, below approximately $SR_1 = 0.8$, the major TFN species shifted from NO to HCN. Second, at first-stage stoichiometries less than 0.8, significant amounts of unburned hydrocarbons were carried into the second-stage flame. Folsom (1979) showed that in a simple diffusion flame the conversion of HCN and $NH_3$ to NO and the retention of NO are affected by the hydrocarbon content of the fuel. $NH_3$ conversion is low when hydrocarbons are absent, and hydrocarbons are necessary for the reduction of NO or HCN to $N_2$. Thus, staged combustion requires the minimization of TFN, as well as the production of an optimum TFN/fuel mixture for burnout.

### 2.2.4 Fuel Effects

A total of twenty-six distillate and residual petroleum and alternate (coal- and shale-derived) fuels were burned in the tunnel furnace to assess the sensitivity of the conclusions to fuel properties (Table 2-1) presents a complete analysis of all the fuels tested. Figure 2-9 shows the total fixed nitrogen (TFN) measured at the exit of the fuel-rich first zone as a function of stoichiometric ratio for the Alaskan diesel oil, three petroleum-derived liquid fuels, three alternate liquid fuels, and methane doped with 0.79 weight-percent nitrogen as ammonia. All fuels investigated showed similar trends. TFN reached a minimum concentration at approximately $SR_1 = 0.8$, and then increased significantly as the primary zone became more fuel-rich. The TFN for both the ammonia-doped methane and the fuel oil of similar nitrogen content (R14) showed similar characteristics under fuel-lean conditions. However, below $SR_1 = 0.7$ the heavy oil produces significantly less TFN than the gaseous fuel.

Figure 2-10 shows the TFN concentration at the stoichiometry corresponding to the minimum exhaust NO as a function of total fuel nitrogen content for the seven liquid fuels and the $CH_4/NH_3$. (In general, the minimum exhaust

# TABLE 2-1. DETAILED FUEL ANALYSES

|  | D1 | D2 | D3 | R1 | R2 | R3 | R4 | R5 | R6 | R7 | R8 | R9 | R10 |
|---|---|---|---|---|---|---|---|---|---|---|---|---|---|
|  | Alaskan Diesel | W. Texas Diesel | California No. 2 Oil | East Coast | Middle East | Low Sulfur No. 6 Oil | Indo/Malaysian | Venezuelan Desulfurized | Pennsylvania (Amarada Hess) | Gulf Coast | Venezuelan | Alaskan | California |
| Symbol | ◆ | ▲ | ◑ | ⬡ | ◺ | ✙ | △ | ⌂ | ◺ | ◇ | ⌂ | □ | ▽ |
| Ultimate Analysis: |  |  |  |  |  |  |  |  |  |  |  |  |  |
| Carbon, % | 86.99 | 88.09 | 86.8 | 86.54 | 86.78 | 86.57 | 86.53 | 85.92 | 84.82 | 84.62 | 85.24 | 86.04 | 85.75 |
| Hydrogen, % | 12.07 | 9.76 | 12.52 | 12.31 | 11.95 | 12.52 | 11.93 | 12.05 | 11.21 | 10.77 | 10.96 | 11.18 | 11.83 |
| Nitrogen, % | 0.008 | 0.026 | 0.053 | 0.16 | 0.18 | 0.22 | 0.24 | 0.24 | 0.34 | 0.36 | 0.40 | 0.51 | 0.62 |
| Sulfur, % | 0.31 | 1.88 | 0.27 | 0.36 | 0.67 | 0.21 | 0.22 | 0.93 | 2.26 | 2.44 | 2.22 | 1.63 | 1.05 |
| Ash, % | <.001 | <.001 | <.001 | 0.023 | 0.012 | 0.02 | 0.036 | 0.033 | 0.067 | 0.027 | 0.081 | 0.034 | 0.038 |
| Oxygen, % | 0.62 | 0.24 | 0.36 | 0.61 | 0.41 | 0.46 | 1.04 | 0.83 | 1.3 | 1.78 | 1.10 | 0.61 | 0.71 |
| Conradson Carbon Residue, % |  |  |  | 2.1 | 6.0 | 4.4 | 3.98 | 5.1 | 12.4 | 14.8 | 6.8 | 12.9 |  |
| Asphaltene, % |  |  |  | 0.34 | 3.24 | 0.94 | 0.74 | 2.59 | 4.04 | 7.02 | 8.4 | 5.6 |  |
| Flash Point, °F |  |  |  | 205 | 350 | 325 | 210 | 176 | 275 | 155 | 210 | 215 |  |
| Pour Point, °F |  |  |  | 50 | 48 | 105 | 61 | 48 | 66 | 40 | 58 | 38 |  |
| API Gravity at 60°F | 33.1 | 18.3 | 32.6 | 24.9 | 19.8 | 25.1 | 21.8 | 23.3 | 15.4 | 13.2 | 14.1 | 15.6 | 19.5 |
| Viscosity, SSU, at 140°F | 33.0 | 32.0 | 30.8 | 131.2 | 490 | 222.4 | 199 | 113.2 | 1049 | 835 | 742 | 1,071 | 246.1 |
| at 210°F | 29.5 | 28.8 | 29.5 | 45 | 131.8 | 69.6 | 65 | 50.5 | 240 | 181 | 196.7 | 194 | 70.00 |
| Heat of Combustion: |  |  |  |  |  |  |  |  |  |  |  |  |  |
| Gross Btu/lb |  |  | 19,330 | 19,260 | 19,070 | 19,110 | 19,070 | 18,400 | 18,520 | 18,240 | 18,240 | 18,470 |  |
| Net Btu/lb |  |  |  | 18,140 | 17,980 | 17,970 | 17,980 | 17,300 | 17,500 | 17,260 | 17,400 | 17,580 |  |
| Calcium, ppm |  |  |  | 7.1 | 1.2 | 9.52 | 14 | 8.7 | 9.2 | 4.4 | 9.1 | 6.9 |  |
| Iron, ppm |  |  |  | 16 | 2.6 | 123.6 | 16 | 6.5 | 13.2 | 19 | 11 | 24 |  |
| Maganese, ppm |  |  |  | 0.09 | 0.02 | 0.46 | 0.13 | 0.09 | 0.10 | 0.13 | 0.09 | 0.06 |  |
| Magnesium, ppm |  |  |  | 3.7 | 0.08 | 2.23 | 3.6 | 3.6 | 3.3 | 0.4 | 3.8 | 1.4 |  |
| Nickel, ppm |  |  |  | 6.7 | 13 | 14.10 | 19 |  | 32.7 | 29 | 52 | 50 |  |
| Sodium, ppm |  |  |  | 37 | 0.98 | 3.74 | 15 |  | 64.5 | 3.6 | 32 | 37 |  |
| Vanadium, ppm |  |  |  | 14 | 25 | 3.11 | 101 |  | 81.5 | 45 | 226 | 67 |  |

## TABLE 2-1. DETAILED FUEL ANALYSES (Concluded)

| | R11 | R12 | R13 | R14 | A1 | A2 | A3 | A4 | A5 | A6 | A7 | A8 | A9 |
|---|---|---|---|---|---|---|---|---|---|---|---|---|---|
| | California | California | California | California (Kern County) | Shale-Derived DFM | Synthoil | Crude Shale | SRC II Blend | Shale Residual | SRC II | Shale Fraction (520-850°F) | Shale Fraction (+850°F) | SRC II Heavy Distillate |
| | ○ | ◇ | ✥ | ⬯ | ◥ | ■ | ● | ▲ | ◣ | ◆ | ◗ | ◓ | ☗ |
| **Ultimate Analysis:** | | | | | | | | | | | | | |
| Carbon, % | 85.4 | 85.33 | 86.66 | 86.61 | 86.18 | 86.30 | 84.6 | 89.91 | 86.71 | 85.91 | 85.39 | 85.92 | 88.98 |
| Hydrogen, % | 11.44 | 11.23 | 10.44 | 10.93 | 13.00 | 7.44 | 11.3 | 9.27 | 12.76 | 8.74 | 11.53 | 10.61 | 7.64 |
| Nitrogen, % | 0.77 | 0.79 | 0.86 | 0.83 | 0.24 | 1.36 | 2.08 | 0.45 | 0.46 | 0.96 | 1.92 | 2.49 | 1.03 |
| Sulfur, % | 1.63 | 1.60 | 0.99 | 1.16 | 0.51 | 0.80 | 0.63 | 0.065 | 0.28 | 0.30 | 0.72 | 0.63 | 0.39 |
| Ash, % | 0.043 | 0.032 | 0.20 | 0.030 | 0.003 | 1.56 | .026 | 0.004 | 0.009 | 0.04 | 0.002 | 0.24 | 0.058 |
| Oxygen, % | 0.71 | 1.02 | 0.85 | 0.44 | 1.07 | 2.54 | 1.36 | 0.30 | 0.03 | 4.08 | 0.44 | 0.11 | 1.90 |
| Conradson Carbon Residue, % | 8.72 | 9.22 | 15.2 | 8.3 | 4.1 | 23.9 | 2.9 | 6.18 | 0.19 | 0.51 | 0.07 | 9.3 | |
| Asphaltene, % | 5.18 | 5.18 | 8.62 | 3.92 | 0.036 | 16.55 | 1.33 | 4.10 | 0.083 | | 0.12 | 4.24 | |
| Flash Point, °F | | 150 | 180 | 225 | 182 | 210 | 250 | 70 | 235 | 1.73 | 255 | 370 | 265 |
| Pour Point, °F | 38 | 30 | 42 | 65 | 40 | 80 | 80 | <−72 | 90 | −55 | 70 | 95 | 8 |
| API Gravity at 60°F | 15.4 | 15.1 | 12.6 | 12.3 | 33.1 | S=1.14 | 20.3 | 10.0 | 29.0 | | 22.3 | 12.0 | 1.3 |
| Viscosity, SSU, at 140°F | 854 | 748.0 | 720 | 4630 | 36.1 | 10,880 | 97 | 40.6 | 54.3 | 39 | 62.9 | 3050 | 67.2 |
| at 210°F | 129 | 131.6 | 200 | 352 | 30.7 | 575 | 44.1 | 32.5 | 37.3 | | 41.8 | 490 | 41.3 |
| **Heat of Combustion:** | | | | | | | | | | | | | |
| Gross Btu/lb | 18,470 | 18,460 | 18,230 | 18,430 | 19,430 | 16,480 | 18,290 | 17,980 | 19,350 | 17,100 | 18,520 | 18,000 | 17,120 |
| Net Btu/lb | 17,430 | 17,440 | 17,280 | 17,430 | 18,240 | 15,800 | 17,260 | 17,130 | 18,190 | | 17,470 | 17,030 | 16,240 |
| Calcium, ppm | 21 | 14 | 90.6 | 4.4 | 0.13 | 1,670 | 1.5 | 0.33 | 4.20 | | <0.5 | 238 | |
| Iron, ppm | 73 | 53 | 77.2 | 15 | 6.3 | 109 | 47.9 | 3.9 | <0.5 | | 2.9 | 86 | |
| Manganese, ppm | 0.8 | 0.1 | 0.87 | 0.15 | 0.06 | 6.2 | 0.17 | <0.5 | <0.5 | | 0.033 | 1.3 | |
| Magnesium, ppm | 5.1 | 3.8 | 31.4 | 1.1 | | 170 | 5.40 | 0.17 | 0.15 | | 0.021 | 51 | |
| Nickel, ppm | 65 | 82 | 88.0 | 68 | 0.43 | 2.6 | 5.00 | <0.5 | <0.5 | | <0.5 | 7.4 | |
| Sodium, ppm | 21 | 2.6 | 22.3 | 3.4 | 0.09 | 148 | 11.71 | 0.31 | 2.51 | | <0.1 | 11 | |
| Vanadium, ppm | 44 | 53 | 66.2 | 39 | <.1 | 6.5 | <.3 | <1.0 | <1.0 | | <0.2 | 1.1 | |

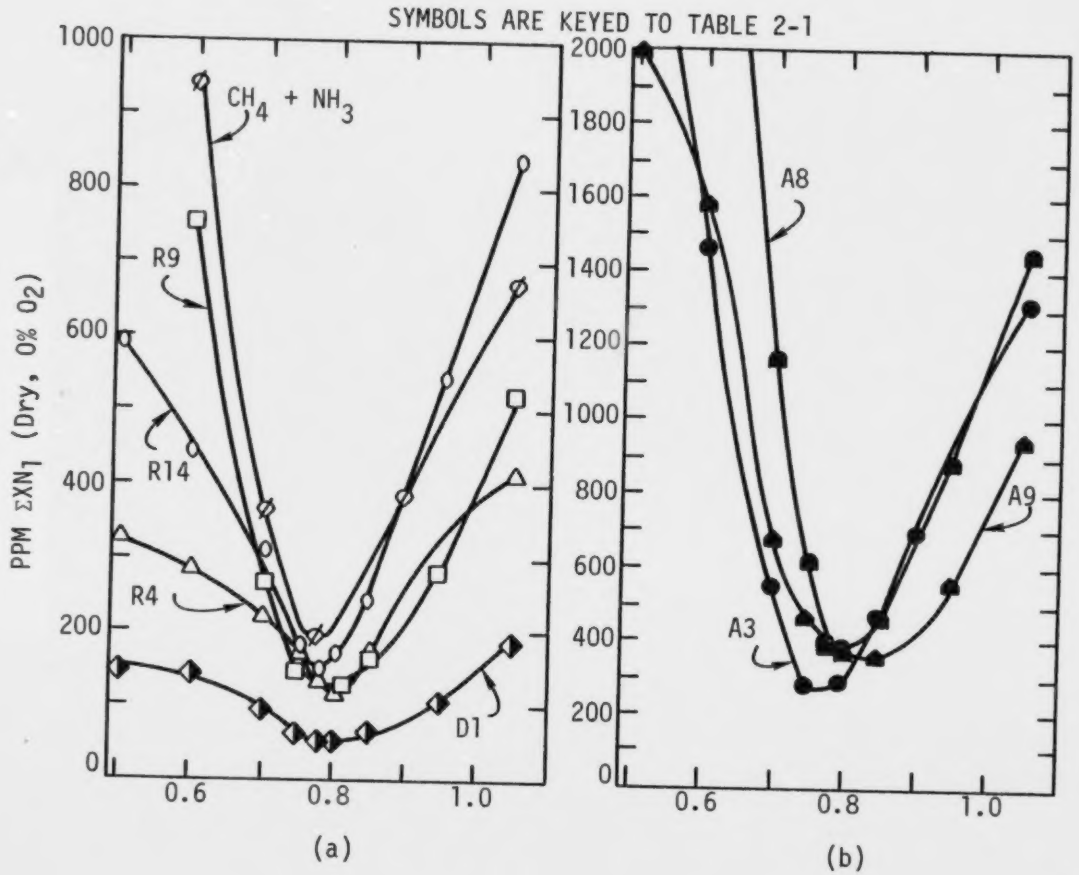

Figure 2-9. The effect of fuel type and stoichiometry on the production of TFN ($\Sigma XN$) for (a) petroleum oils, and (b) alternate fuels.

Symbols are keyed to Table 2-1

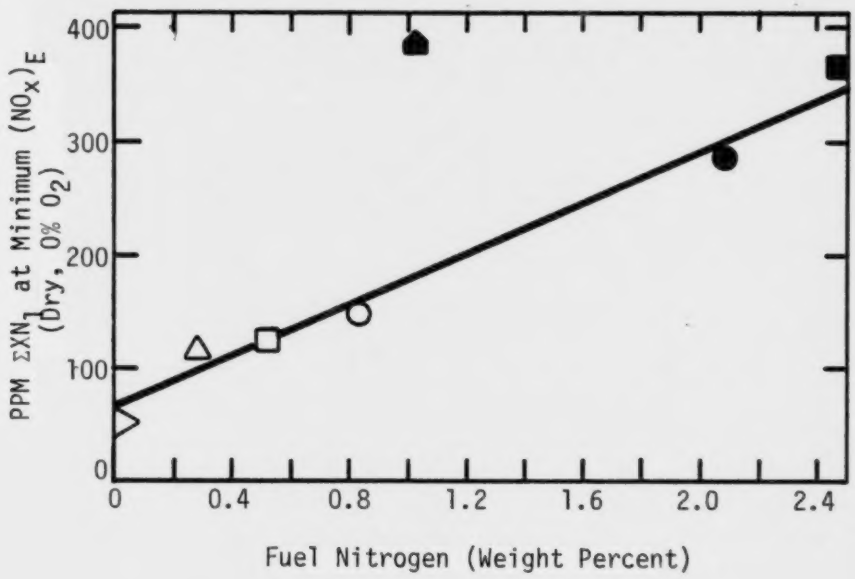

Figure 2-10. Relationship between fuel nitrogen content and first-stage TFN.

$NO_x$ concentration occurred at $SR_1 = 0.78 \pm 0.02$). Under these optimum staged conditions, TFN correlates well with total fuel nitrogen content. Only the SRC-II heavy distillate (☗) exhibited an unusually high TFN yield. NO, $NH_3$, and HCN were all substantially higher for this fuel than with comparable fuels at the minimum stoichiometry (0.78). The increased TFN may be the result of basic chemical bonding differences between the parent coal from which the SRC-II was derived and petroleum liquids.

A summary of the partition of the TFN compounds is shown in Figure 2-11 as a function of the first-stage stoichiometric ratio. Data for the six liquid fuels and the 0.79 weight-percent nitrogen (as $NH_3$) in methane gas are presented as the percentage of the original fuel nitrogen existing as HCN, $NH_3$, or NO at the end of the fuel-rich first stage. In each case, the missing fuel nitrogen has either been converted to $N_2$ or still exists in some partially oxidized fuel fragment, which is unlikely. All of the liquid fuels exhibited the same general trends:

- Above approximately $SR_1 = 0.8$, NO was the dominant TFN species.
- Below $SR_1 = 0.75$, the major TFN species was HCN and under very fuel-rich conditions HCN usually accounted for more than 50 percent of the initial fuel nitrogen.
- First-stage $NH_3$ levels were always low, generally less than 20 percent of the fuel N.

The fraction of fuel nitrogen converted to HCN was somewhat less for the $CH_4/NH_3$ mixture (◇) than for most of the liquid fuels tested (Figure 2-11a); however, as expected, conversion to $NH_3$ (Figure 2-11b) and NO (Figure 2-11c) was higher than the liquid fuels. This is in agreement with the kinetic model results for methane/$NH_3$ flames. The light (API = 21.8) Indonesian/Malaysian residual oil (△) produced consistently higher conversion of fuel nitrogen to HCN, $NH_3$, and NO than the much heavier (API = 12.3) Kern County crude oil (○). Conversely, conversion of HCN and $NH_3$ for the +454°C shale residuum (■) was higher than for the light parent crude shale (●); however, conversion to NO was lower. The exact relationship of simple fuel properties to the conversion of fuel nitrogen to intermediate XN species is not apparent at this time.

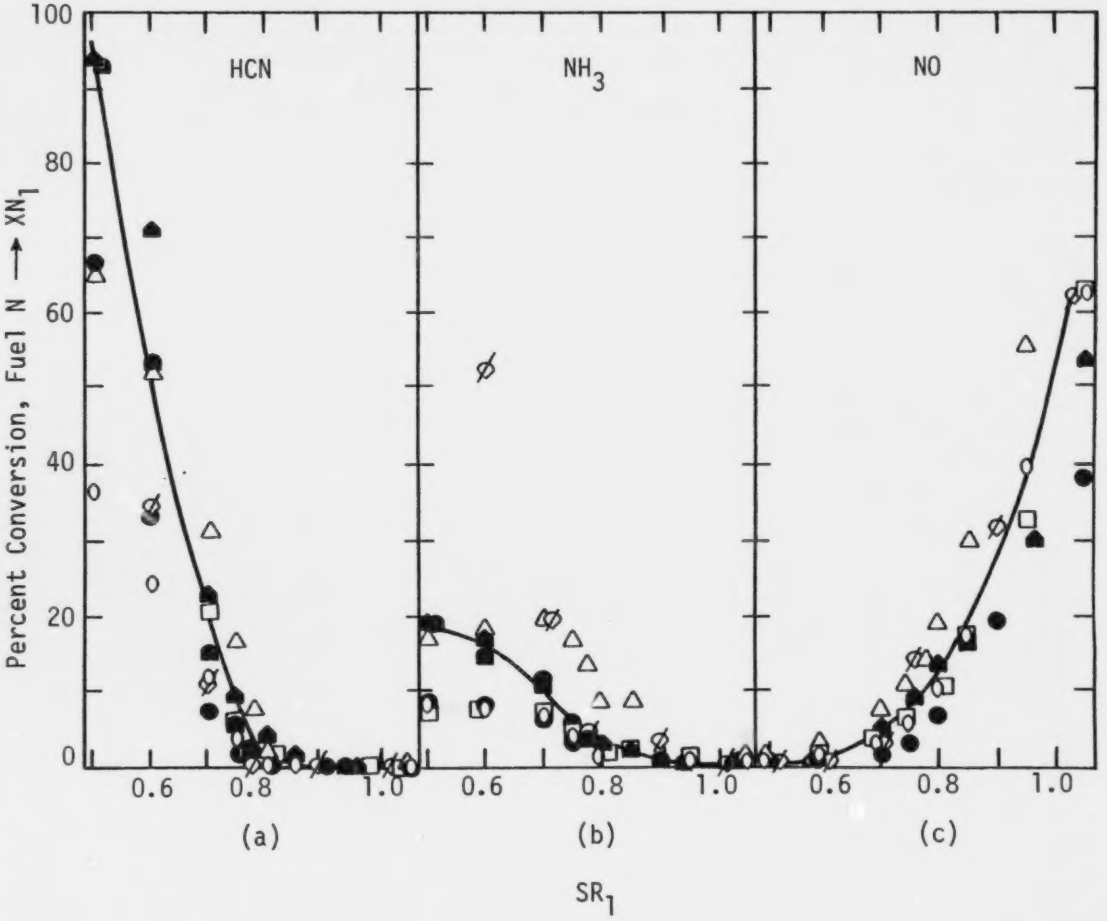

Figure 2-11. The conversion of fuel-bound nitrogen to XN species.

Figure 2-12 shows the minimum exhaust NO concentration at optimum fuel-rich first-zone conditions. The minimum emissions occurred at $SR_1 = 0.78 \pm 0.2$ and under these conditions it appears that NO emissions are a function of the original fuel nitrogen content. Only the SRC-II distillate (☗) exhibited unusually high emissions.

## 2.3 Pilot-Scale Studies

The low-$NO_x$ combustor concepts were evaluated at two scales (England et al., 1982). Two prototype low-$NO_x$ burners, shown in Figure 2-13, were constructed with nominal design firing rates of $2 \times 10^6$ Btu/hr (small pilot scale or SP) and $10 \times 10^6$ Btu/hr (intermediate pilot scale or IP). Each of the two test burners contains three major elements:

- An Air/fuel injection system
- A fuel-rich holdup zone
- A secondary air injection section

The first stage was constructed from high temperature refractories and insulation to minimize heat loss through the walls and permit near-adiabatic conditions in the primary zone. Fuel and primary air are injected at the entry of a divergent which forms the initial section of the fuel-rich holdup zone. The residence times in the fuel-rich zone calculated at a first-stage stoichiometric ratio of 0.7 were approximately 0.50 sec for the SP burner and 0.43 sec for the IP burner. The primary products were directed through a convergent section which serves to minimize radiative heat loss, ensure complete mixing of the primary products, and minimize backmixing of secondary air into the primary zone. Secondary air was injected parallel to the burner axis annularly around the primary exit.

Two different commercial atomizers were used, an ultrasonic, air-assist atomizer and an internal mixing steam-assist atomizer. The ultrasonic atomizer produced droplets with a narrow size distribution about a mean diameter of 20 μm and the internal mixing atomizer produced droplets with a much broader size distribution about a mean diameter of 40 μm.

The tests were conducted in two different combustors:

- Firetube Simulator (FS). The combustion chamber is 10.5 feet long

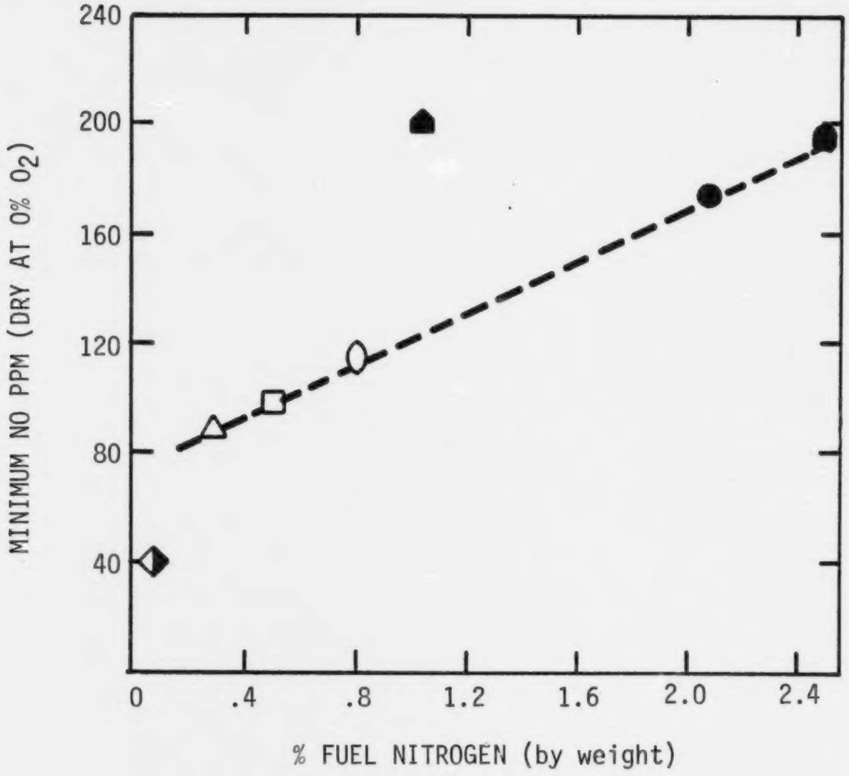

Figure 2-12. Effect of fuel bound nitrogen content on exhaust NO (3% excess $O_2$, 21 kW).

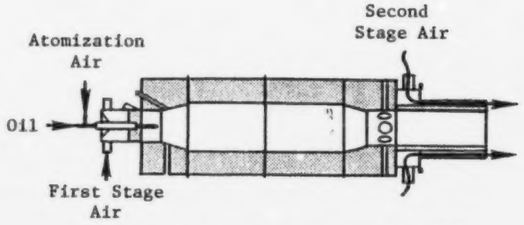
Atomization Air
Second Stage Air
Oil
First Stage Air

(a) Small Prototype Burner (0.6 MW)

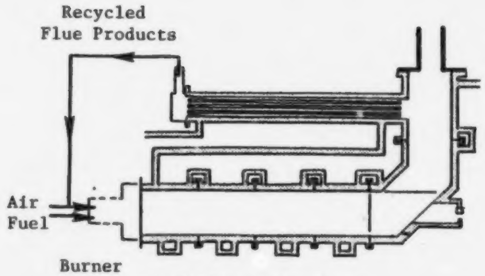
Recycled Flue Products
Air
Fuel
Burner

(b) Firetube Simulator

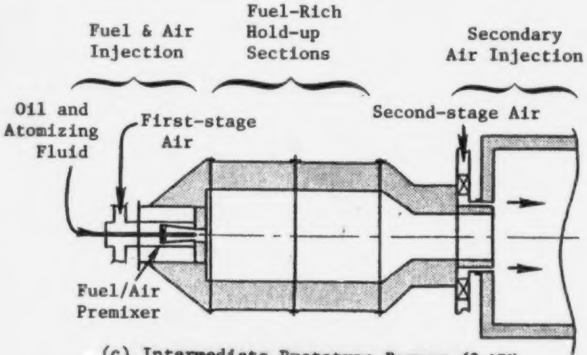
Fuel & Air Injection
Fuel-Rich Hold-up Sections
Secondary Air Injection
Oil and Atomizing Fluid
First-stage Air
Second-stage Air
Fuel/Air Premixer

(c) Intermediate Prototype Burner (3 MW)

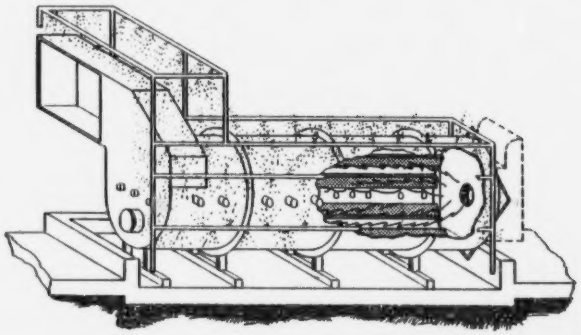

(d) Small Watertube Simulator

Figure 2-13. Prototype burners and experimental test furnaces.

with an internal diameter of 0.60 m. The chamber is composed of calorimetric sections cooled by heat transfer fluid and has a nominal wall temperature of 230$^{o}$C. Only the SP burner was tested in this facility.

- Small Watertube Simulator (SWS). The furnace is 5.2 m in length and 1.8 m inside diameter and is externally spray-cooled with a partial refractory lining. The total heat extraction is controlled by varying the percentage of internal surface which is covered by refractory. Both the SP and IP burners were tested in this facility.

### 2.3.1 First-Stage Parameters

Figure 2-14 shows the influence of the first-stage stoichiometric ratio on exhaust emissions from the prototype tests with different residual oils containing approximately 0.6 percent nitrogen. As $SR_1$ decreased, $NO_x$ emissions decreased rapidly until a minimum was reached and then increased. Smoke and CO emissions from the SP burner were low for $SR_1 > 0.7$, but under more fuel-rich conditions emissions increased sharply. CO was less than 100 ppm and smoke number was generally less than 5 at the point where the minimum $NO_x$ level occurred. CO and smoke emissions from the IP burner were also low for $SR_1$ greater than the point where minimum $NO_x$ occurred; however, for many of the configurations tested, the sharp increase in emissions below this point was not observed. Differences in second-stage thermal environment between the 0.6 MW firetube simulator and 3 MW small watertube simulator may contribute to the observed difference in burnout of CO and smoke.

The residence time in the fuel-rich zone which is required to achieve the desired TFN concentration is an important practical design parameter. Figure 2-15 summarizes minimum exhaust $NO_x$ and TFN data for the bench- and pilot-scale tests. At both scales, increasing the first-stage residence time significantly decreased exhaust $NO_x$ because of an associated decrease in TFN. Both the exhaust $NO_x$ and the TFN from the SP burner were lower than from the tunnel furnace because of the increased rich-zone temperature associated with the increase in scale. Variations in first-stage residence time were achieved in the SP burner/firetube simulator tests by altering the

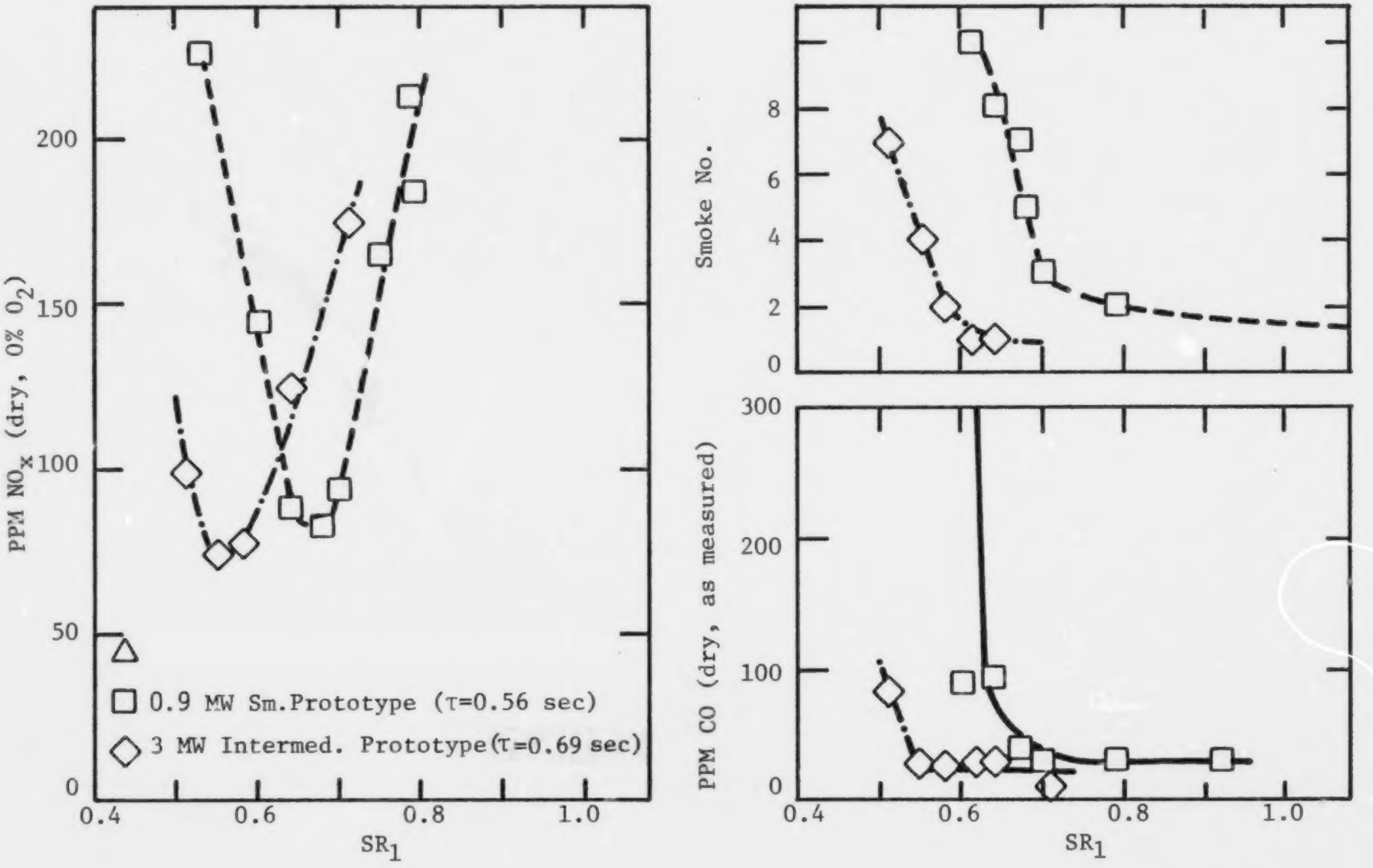

Figure 2-14. Influence of first-stage stoichiometry on $NO_x$, CO and smoke emissions (bench scale and pilot scale, California residual fuel oil).

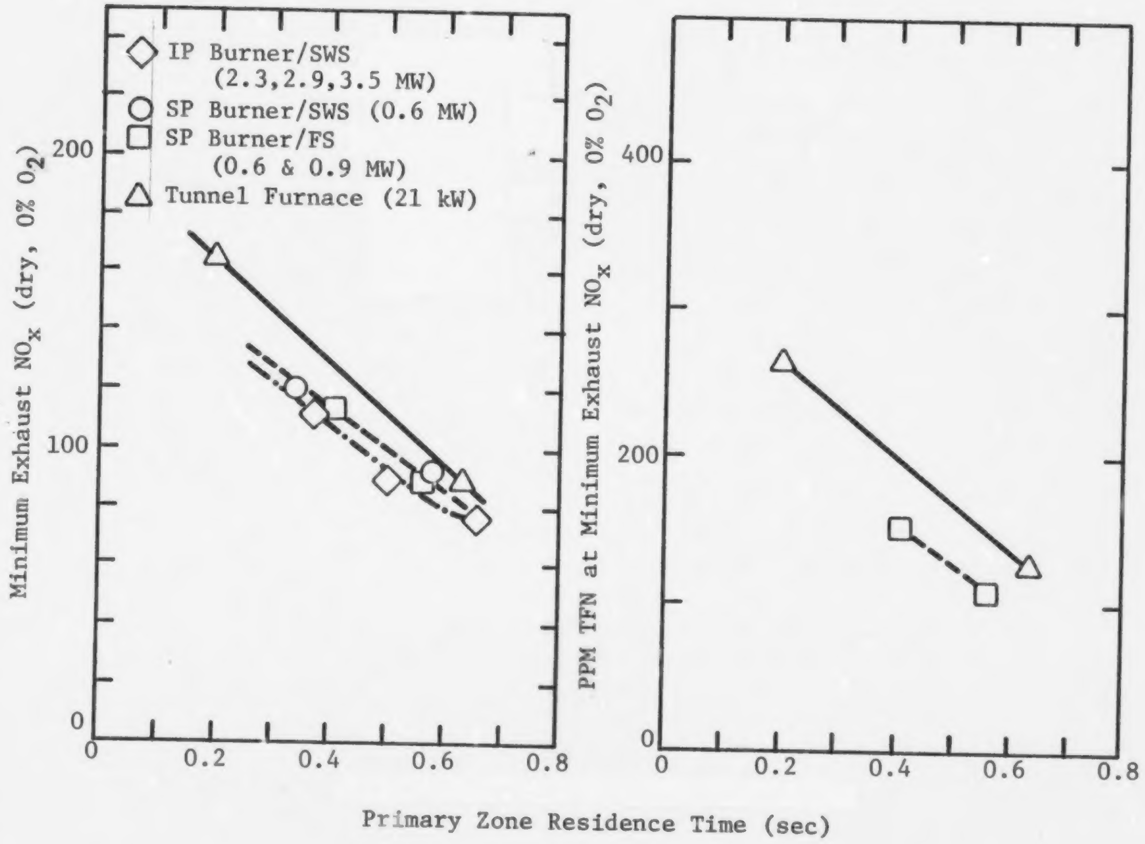

Figure 2-15. Second-stage $NO_x$ production and first-stage TFN decay for bench scale and pilot scale.

firing rate (0.6 and 0.9 MW) and in the SP burner/watertube simulator tests by changing the reactor length (2.7 m to 1.9 m) at 0.6 MW. A strong correlation between the two sets of experiments suggests that the controlling processes are dominated by kinetic effects (time and temperature) and not by aerodynamics and that the principle influence of firing rate is on residence time. Clearly, increasing firing rate also increases first-stage temperature, but this effect is small because even at 0.6 MW heat losses were low. First-stage exit temperatures measured at $SR_1$ of 0.7 were 1621°C compared to adiabatic flame temperature of 1750°C.

As indicated by the bench-scale studies fuel preparation is an important part of the process. In the pilot-scale systems this zone was not separated physically from the fuel-rich first zone. As first-stage residence time was decreased, the importance of the fuel injection system design became more apparent. Figure 2-16 compares data obtained with a premixed burner to that obtained with the standard axial fuel nozzle arrangement. Both were fired in the SP burner mounted on the watertube simulator. The premixer was based on a high-swirl gas-turbine design which utilized ultrasonic atomization. In the short first-stage residence time configuration (350 msec at $SR_1 = 0.7$), the premixer slightly reduced the exhaust NO emissions, and broadened the $SR_1$ for minimum emissions. A similar conclusion was reached by comparing data for a propane/$NH_3$ fuel (which represents a limit of instant fuel vaporization) to the California residual with the standard fuel nozzle.

### 2.3.2 Second-Stage Parameters

All the TFN which exists in the fuel-rich first stage does not form NO in the combustion products of the second stage. Thus, it is important to design the second-stage air injection system to minimize NO formation from TFN species. In addition, thermal NO formation must be minimized which requires that second-stage flame temperatures must be maintained below some critical level. Heat extraction between the fuel-rich zone and the secondary air injection system allows some control over temperature in the second stage. Figure 2-17 presents SP burner/SWS results obtained when water cooling tubes were placed around the periphery of the second-stage throat. This cooling removed approximately 35 kW (6 percent of the heat input) and decreased the minimum exhaust $NO_x$ by approximately 20 ppm. Exactly analogous results were

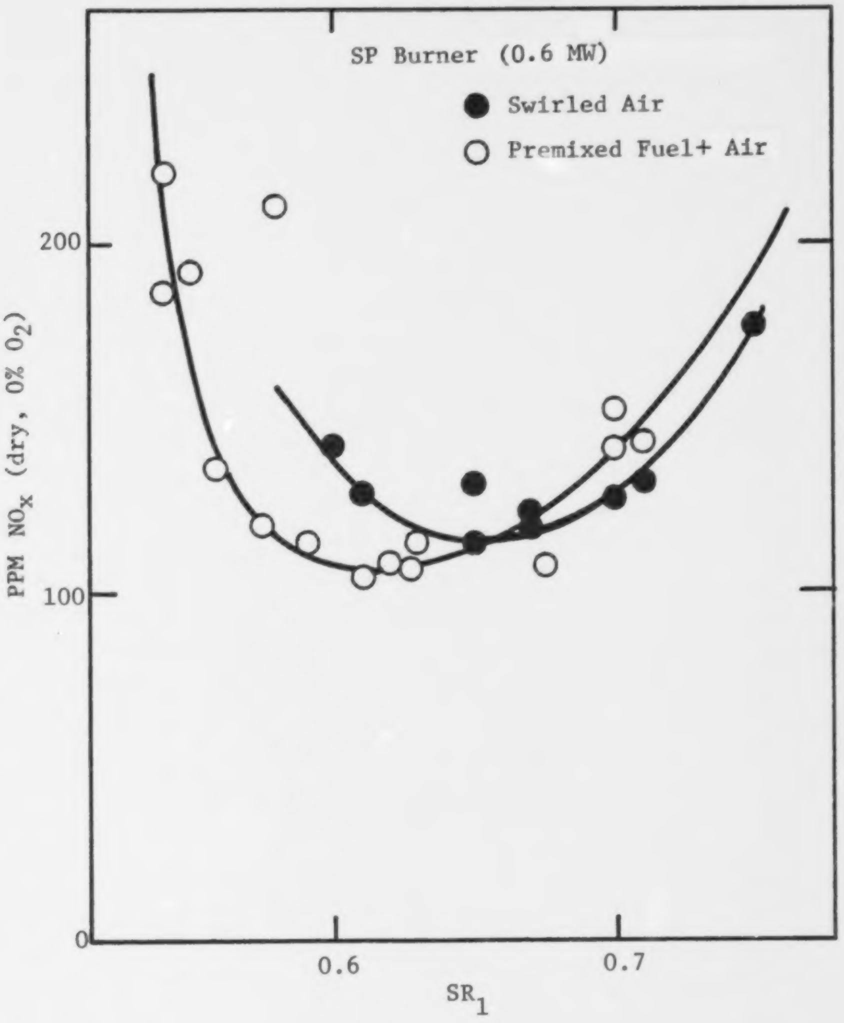

Figure 2-16. Pilot-scale second-stage $NO_x$ emissions for premixed and non-premixed first-stage reactants (0.6 MW; California residual oil; 350 msec first-stage residence time at $SR_1$ = 0.7).

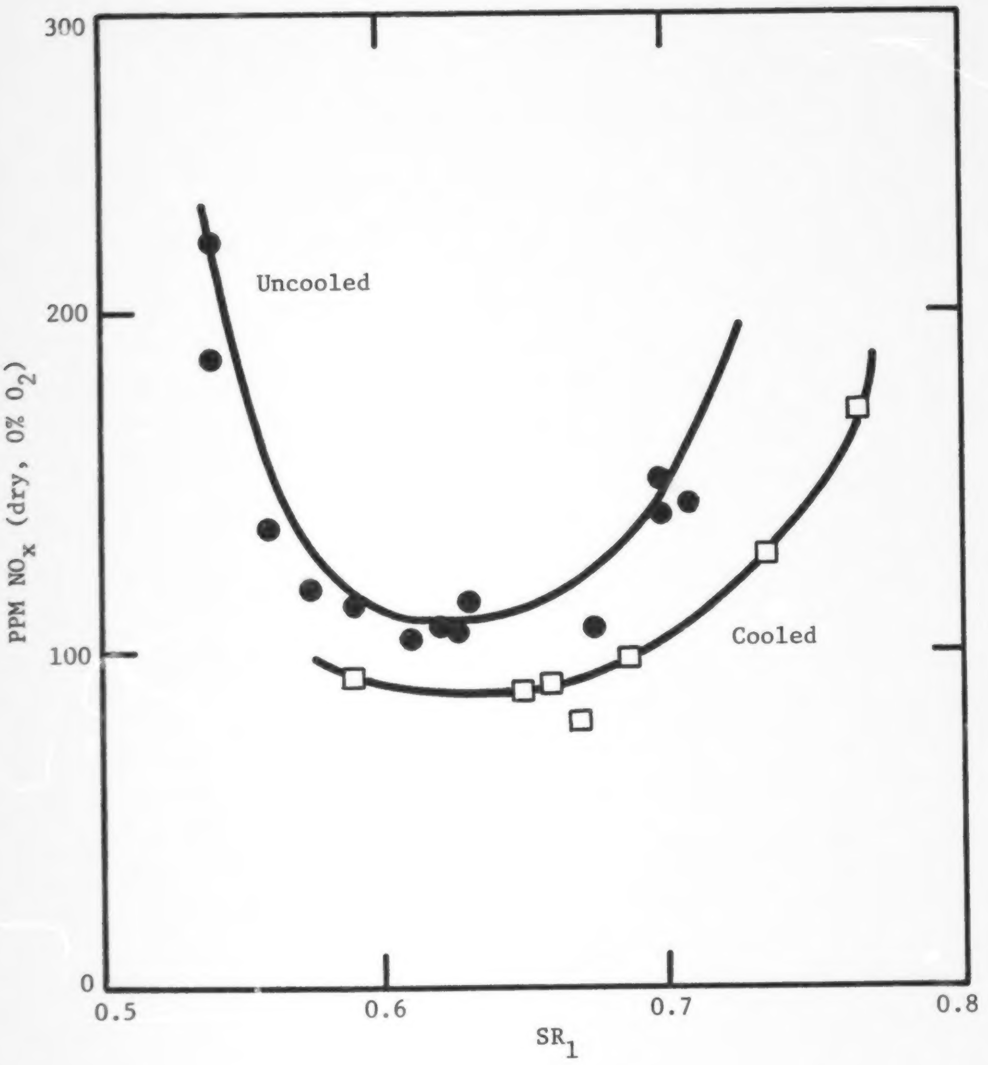

Figure 2-17. Pilot-scale second-stage NO$_x$ emissions with and without inter-stage heat extraction (0.6 MW, 35 kW interstage heat removal in cooled case).

achieved when 40 percent flue gas recycle was introduced with the second-stage air ($\Delta$NO = 18 ppm). In both tests there was a minor impact on smoke emissions; thus, it appears that at the optimum operating conditions, second-stage thermal NO formation accounts for approximately 20 percent of the exhaust emissions with the burner.

The method of secondary air injection could impact exhaust NO levels and two different methods were investigated to determine the sensitivity of emissions to changes in secondary fuel/air mixing in the pilot-scale burner systems. The standard annular (parallel) air injector provided a relatively slow mixing rate; rapid mixing was obtained by injecting the second-stage air radially through a water-cooled boom inserted along the firetube axis from the rear. $NO_x$ emissions remained essentially constant when the ratio of air between the axial and radial injectors was varied; however, smoke emissions were substantially decreased as secondary air was transferred from the parallel injector to the radial injector. Similar results were obtained when swirl vanes were added to the second-stage air injection system.

Figure 2-18 shows the effect of overall excess oxygen on $NO_x$ emissions from the IP burner firing at 2.3 MW ($SR_1$ = 0.56) and at 3.5 MW ($SR_1$ = 0.62). $NO_x$ increased by approximately 12 ppm at 2.3 MW and by 15 ppm at 3.5 MW in varying excess oxygen from 0.5 to 5.0 percent, which again points to the importance of the first-stage parameters in determining final emissions. Bacharach smoke number ranged from 1 to 4 and CO emissions were less than 50 ppm (except at 3.5 MW and 0.3 percent excess $O_2$) for the data shown in Figure 2-18.

## 2.4 Summary

Data obtained at bench and pilot scales indicate that low-$NO_x$ combustors with emission levels of less than 100 ppm can be designed for fuels which contain high quantities of fuel-bound nitrogen. In essence, the design requires the formation of a fuel-rich zone with sufficient residence time at high temperatures to maximize $N_2$ formation. The influence of fuel-nitrogen content on the performance of the low-$NO_x$ concept was established by conducting tests with a distillate oil, residual oils, a coal-liquid, and propane/$NH_3$. Data obtained in these tests are shown in Figure 2-19 which indicates that with the SP burner minimum NO emissions are only weakly dependent upon

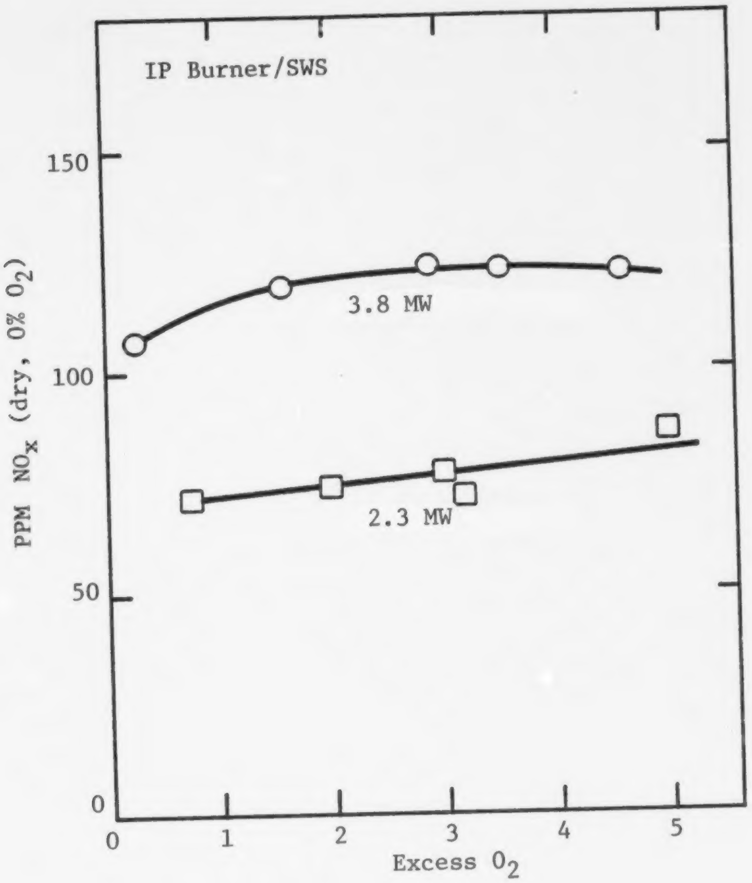

Figure 2-18. Influence of excess air on second-stage $NO_x$ IP burner.

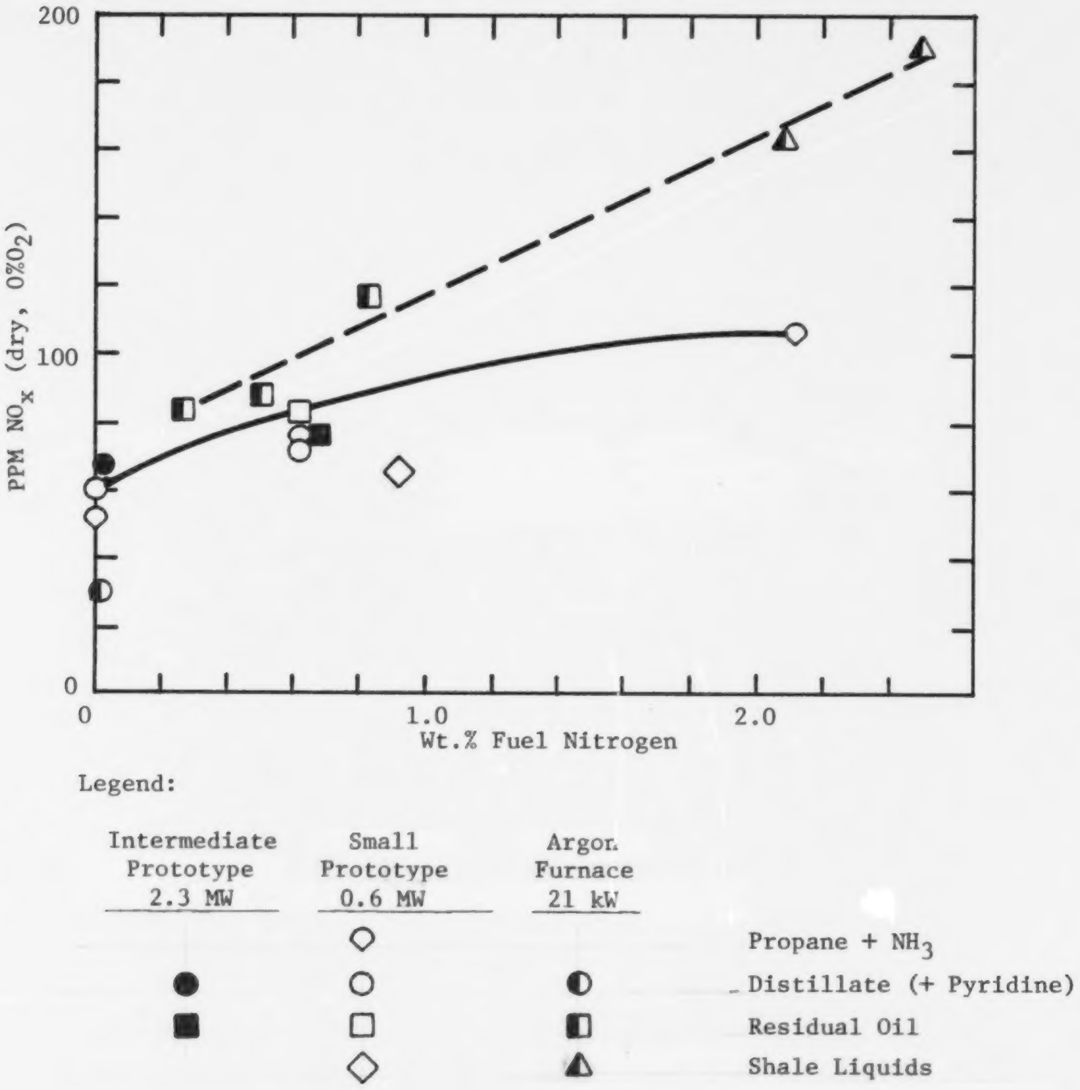

Figure 2-19. Influence of fuel nitrogen on second-stage $NO_x$- bench-scale and pilot-scale data.

total fuel nitrogen content. Figure 2-19 also summarizes similar data obtained in the bench-scale tunnel furnace. Concept scaleup reduced the dependence on fuel-nitrogen; this is probably because of the increased temperature in the fuel-rich zone. Thus, this low-$NO_x$ concept should be capable of producing $NO_x$ emissions less than 100 ppm at 0 percent $O_2$ (85 ppm at 3 percent $O_2$) even when firing the high nitrogen crude oils typical of Kern County oil-fields.

# 3.0 CONCEPTUAL DESIGN DEVELOPMENT

Scale-up of the low-$NO_x$ combustion concept has been successfully accomplished up to a 3 MW pilot-scale experimental burner. Consistent performance trends among the 21 kW, 1 MW, and 3 MW experiments confirmed the basic scaling criteria; i.e., residence time and temperature. The 1 MW and 3 MW studies indicated that as scale increases, mixing becomes increasingly important, and "good" mixing is increasingly difficult. The objective of these tests was to address the questions relative to direct scale-up to 18 MW; i.e.:

- Can premixing of fuel and primary air be achieved?
- Can plug flow be achieved?
- How important is atomizer performance?

It is known in the burner industry that flame stability and turndown do not follow a general scaling law and are usually obtained by trial and error. Transient performance of the burner was also an unknown factor in completion of the previous work.

This phase of the program examined these areas to verify and refine the scaling criteria necessary for successful scale-up from 3 to 18 MW, and to assist in translating the design requirements to practical hardware designs. Two experimental efforts were involved. Additional tests in the 3 MW pilot-scale burner were directed toward effects of burner parameters and design on emissions performance and flame shape. Isothermal (noncombusting) tests were also conducted to screen mixing performance of various first-stage throat geometries.

## 3.1 3 MW Pilot-Scale Experiments

The emphasis of these experiments was to derive specific hardware design information regarding atomizer selection, first-stage throat design, swirl level, and second-stage mixing. Conventional atomizer designs were investigated and performance was compared to the ultrasonic atomizer used in previous tests. First-stage air throat design parameters (velocity, swirl, geometry) were also investigated. A series of secondary air injection variations explored the degree of $NO_x$ and flame shape control possible through these variations. The sensitivity of burner performance to operating parameters (load, excess air, air preheat level) was also investigated. Table 3-1 summarizes the variables investigated in these tests.

### 3.1.1 Experimental Hardware

The 3 MW pilot-scale burner is illustrated in Figure 3-1. The burner's first-stage chamber is a horizontal cylinder constructed from high temperature and insulating castable refractories. Internal diameter is 102 cm and length is approximately 203 cm prior to a convergent section which reduces to the exit diameter of 51 cm. First-stage air and fuel enter through an interchangeable injection section. Second-stage air passes through a swirl register and then through an annulus surrounding the first-stage exit. Second-stage air normally enters the burnout zone via the annulus; however, some tests were run where secondary air was injected through a series of ports immediately downstream of the exit. Further details of the burner construction can be found in a report by England, et al (1983).

The SWS furnace is illustrated in Figure 3-2. The furnace is a horizontal cylinder 1.8 meters internal diameter by 5.2 meters long. It is externally cooled by water and has a partially-insulated interior surface to control heat extraction. Nominal firing rate range is 2.9 to 8.0 MW. Nominal firing characteristics for the furnace are given in Table 3-2. Emissions from the furnace are measured after cooling the gases in the exhaust ducting to approximately 500°C. Samples are drawn through a water-cooled, stainless steel probe and an ice bath condensor before entering the emissions monitors listed in Table 3-3. Smoke number is determined using a manual Bacharach smoke meter.

Several hardware changes were investigated during the testing. Table 3-4 summarizes the first-stage hardware variations which were evaluated. Most of the configurations were variations on the fuel/air premixer concept with different exit geometries. The premixer design (Figure 3-3) is scaled up on the basis of constant velocity and swirl numbers from the 0.9 MW design utilized in the small pilot-scale prototype (England et al., 1983). Four atomizers were included in these tests (Figure 3-4): a commercial "ultrasonic" atomizer, a commercial internal-mixing atomizer, and two experimental

TABLE 3-1. VARIABLES INVESTIGATED IN 3 MW STUDIES

| Vaporization Zone | Hold-Up Zone | Burnout Zone |
|---|---|---|
| • Atomizer Type/Atomizing Fluid<br>— Ultrasonic/Air/Steam<br>— Internal Mixing/Steam<br>— Y-Jet/Air/Steam<br>• Atomizing Fluid Pressure<br>• Throat Geometry<br>— Parallel Exit<br>— Divergent Exit<br>• First-Stage Air<br>— Velocity<br>— Swirl<br>— Distribution<br>• Air Preheat | • Stoichiometry (TV)<br>• Residence Time<br>— Load | • Air Injectors<br>— Annulus<br>— Ports<br>• Air Mixing (Ports)<br>— Radial<br>— Axial<br>— Inboard/Outboard<br>• First-Stage Exit Velocity<br>— Diameter<br>• Furnace Heat Extraction<br>— Insulation<br>• Excess Air<br>• Air Preheat |

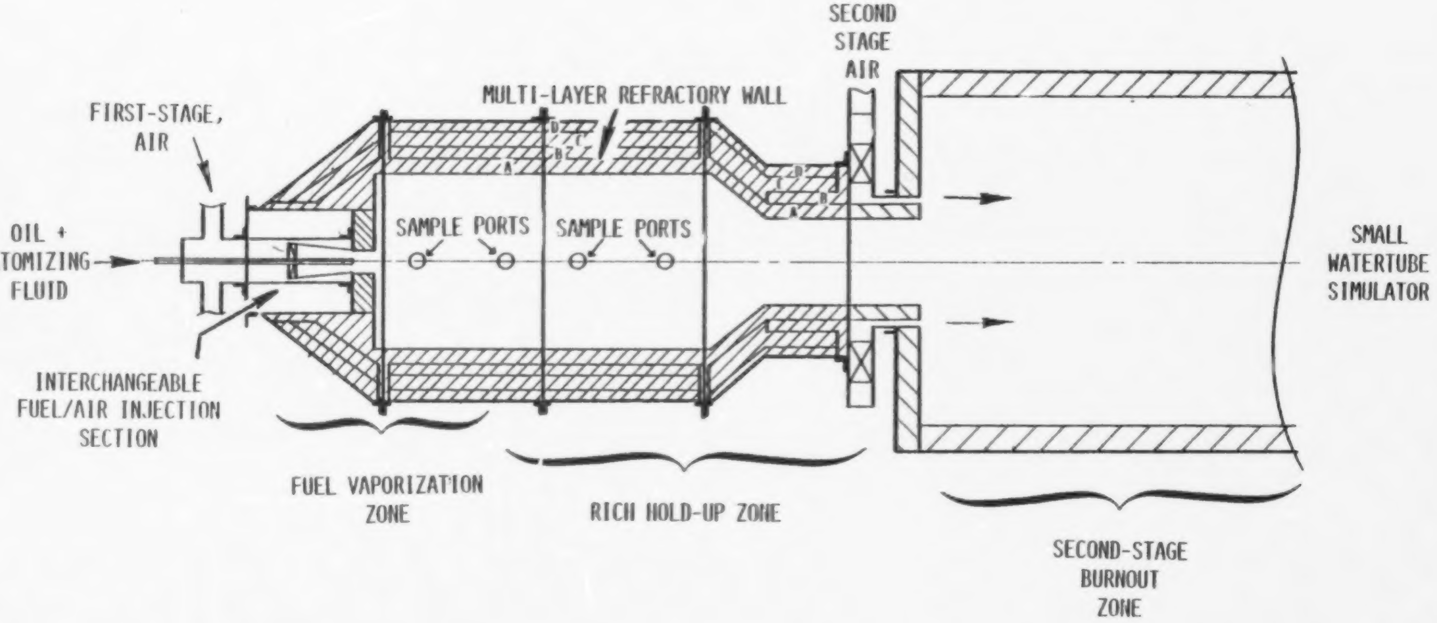
FIRST-STAGE, AIR
OIL + ATOMIZING FLUID
INTERCHANGEABLE FUEL/AIR INJECTION SECTION
MULTI-LAYER REFRACTORY WALL
A
B
C
D
SAMPLE PORTS
SAMPLE PORTS
SECOND STAGE AIR
SMALL WATERTUBE SIMULATOR
FUEL VAPORIZATION ZONE
RICH HOLD-UP ZONE
SECOND-STAGE BURNOUT ZONE

Figure 3-1. 3 MW pilot-scale test burner.

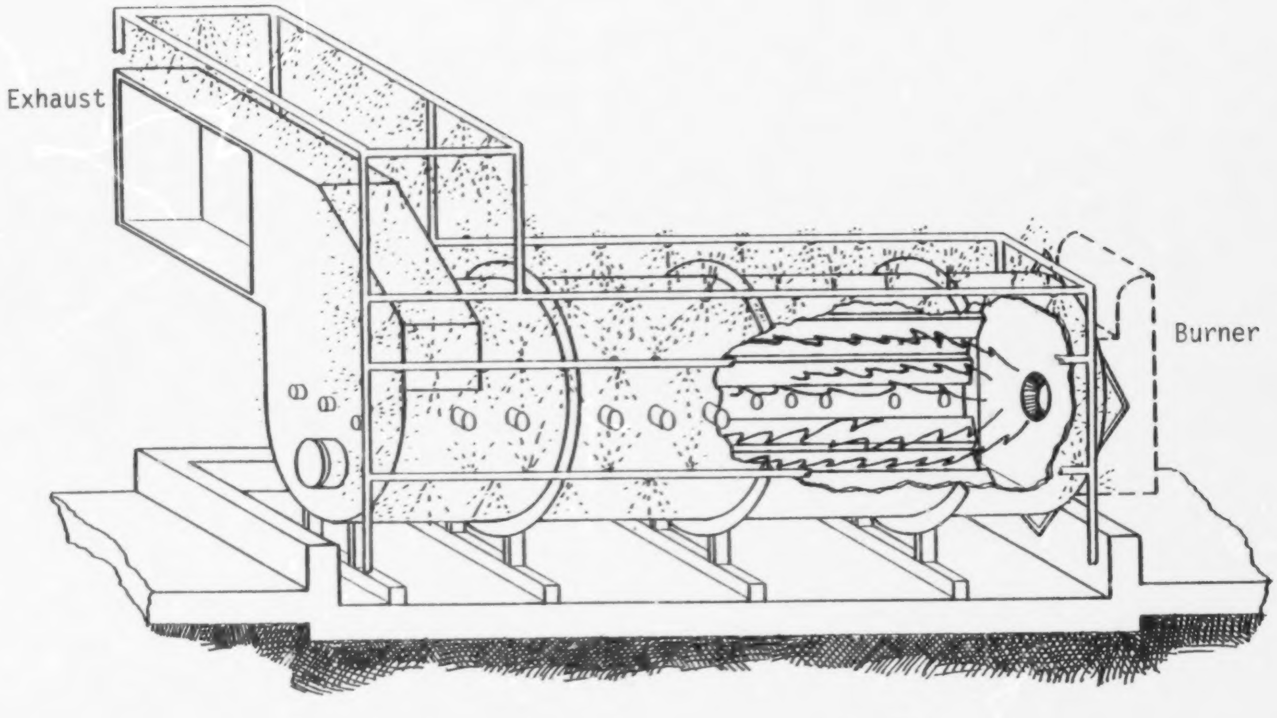
Exhaust
Burner

Figure 3-2. Small Watertube Simulator (SWS) test furnace.

## TABLE 3-2. SWS FURNACE CHARACTERISTICS

| Parameter | | Value |
|---|---|---|
| Firing | | |
| Configuration | | Single Wall |
| Firing Rate | Minimum | 2.9 MW (10 x $10^6$ Btu/hr) |
| | Maximum | 8.8 MW (30 x $10^6$ Btu/hr) |
| Dimensions | | |
| Shape | | Cylinder |
| Diameter | | 1.8 m (6 ft) |
| Length | | 5.2 m (17 ft) |
| L/D | | 2.8 |
| Surface Area | | |
| Total | | 42 $m^2$ (450 $ft^2$) |
| Insulated (Axial Strips Around Circumference and Rear Wall) | | 19 $m^2$ (45 Percent) |
| Cooled | | 23 $m^2$ (55 Percent) |
| Volume | | 19.7 $m^3$ (696 $ft^3$) |
| Cooling | | Spray-Cooled on All Surfaces |
| Thermal Environment* | | |
| Heat Release/Cooled Surface | | 0.38 $MW/m^2$ (121,951 $Btu/hr/ft^2$) |
| Heat Release/Volume | | 1.26 $MW/m^3$ (43,103 $Btu/hr/ft^3$) |

*In burner zone at maximum firing rate.

TABLE 3-3. SWS CONTINUOUS MONITORS

| Gas Measured | Detection Principle | Manufacturer | Model No. | Full Scale Range |
|---|---|---|---|---|
| NO/$NO_x$ | Chemiluminescence | TECO | 10 AR | 2.5 to 10,000 ppm |
| $CO_2$ | Nondispersive Infrared (NDIR) | Anarad | AR500R | 1% to 25% |
| CO | Nondispersive Infrared (NDIR) | Anarad | AR500R | 250 ppm to 5% |
| $O_2$ | Paramagnetic | Taylor | OA272 | 5% to 25% |
| $SO_2$ | Ultraviolet (NDUV) | DuPont | 400 | 50 ppm to 10,000 ppm |
| HC | Flame Ionization Detector | Beckman | 402 | 0.05 ppm to 10% |

TABLE 3-4. FIRST-STAGE HARDWARE CONFIGURATIONS TESTED IN 3 MW TESTS

| CONFIGURATION | FIRST-STAGE | SECOND-STAGE |
|---|---|---|
| 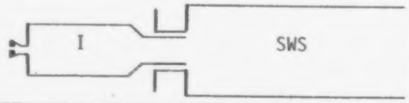 | – PREMIXER<br>– SWIRL (S=0.4)<br>– PARALLEL EXIT | – AXIAL AIR INJECTION<br>– ANNULUS INJECTOR<br>– 51 CM FIRST-STAGE EXIT DIAMETER |
| 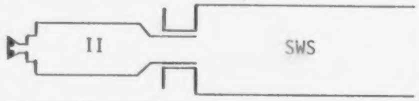 | – PREMIXER<br>– SWIRL (S=0.4)<br>– SET BACK PARALLEL EXIT | – AXIAL AIR INJECTION<br>– ANNULUS INJECTOR<br>– 51 CM FIRST-STAGE EXIT DIAMETER |
| 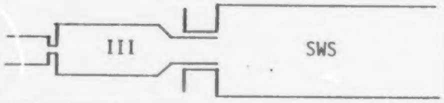 | – PREMIXER<br>– NO SWIRL<br>– PARALLEL EXIT | – AXIAL AIR INJECTION<br>– ANNULUS INJECTOR<br>– 51 CM FIRST-STAGE EXIT DIAMETER |
| 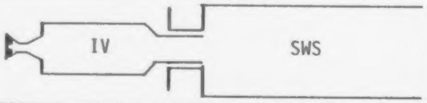 | – PREMIXER<br>– SWIRL (S=0.4)<br>– DIVERGENT EXIT (L/D=2.6) | – AXIAL AIR INJECTION<br>– ANNULUS INJECTOR<br>– 51 CM FIRST-STAGE EXIT DIAMETER |
| 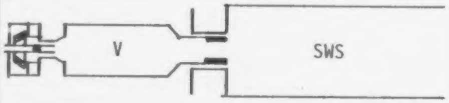 | – ℄ CHANNEL (LOW VELOCITY)<br>– SWIRL<br>– DIVERGENT EXIT (L/D=1.1) | – AXIAL AIR INJECTION<br>– ANNULUS INJECTOR<br>– 36 CM FIRST-STAGE EXIT DIAMETER |
| 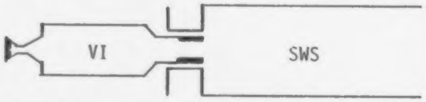 | – PREMIXER<br>– SWIRL (S=0.4)<br>– DIVERGENT EXIT (L/D=2.6) | – AXIAL AIR INJECTION<br>– ANNULUS INJECTOR<br>– 36 CM FIRST-STAGE EXIT DIAMETER |
| 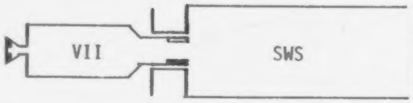 | – PREMIXER<br>– SWIRL (S=0.4<br>– PARALLEL EXIT | – AXIAL AIR INJECTION<br>– ANNULUS INJECTOR<br>– 36 CM FIRST-STAGE EXIT DIAMETER |

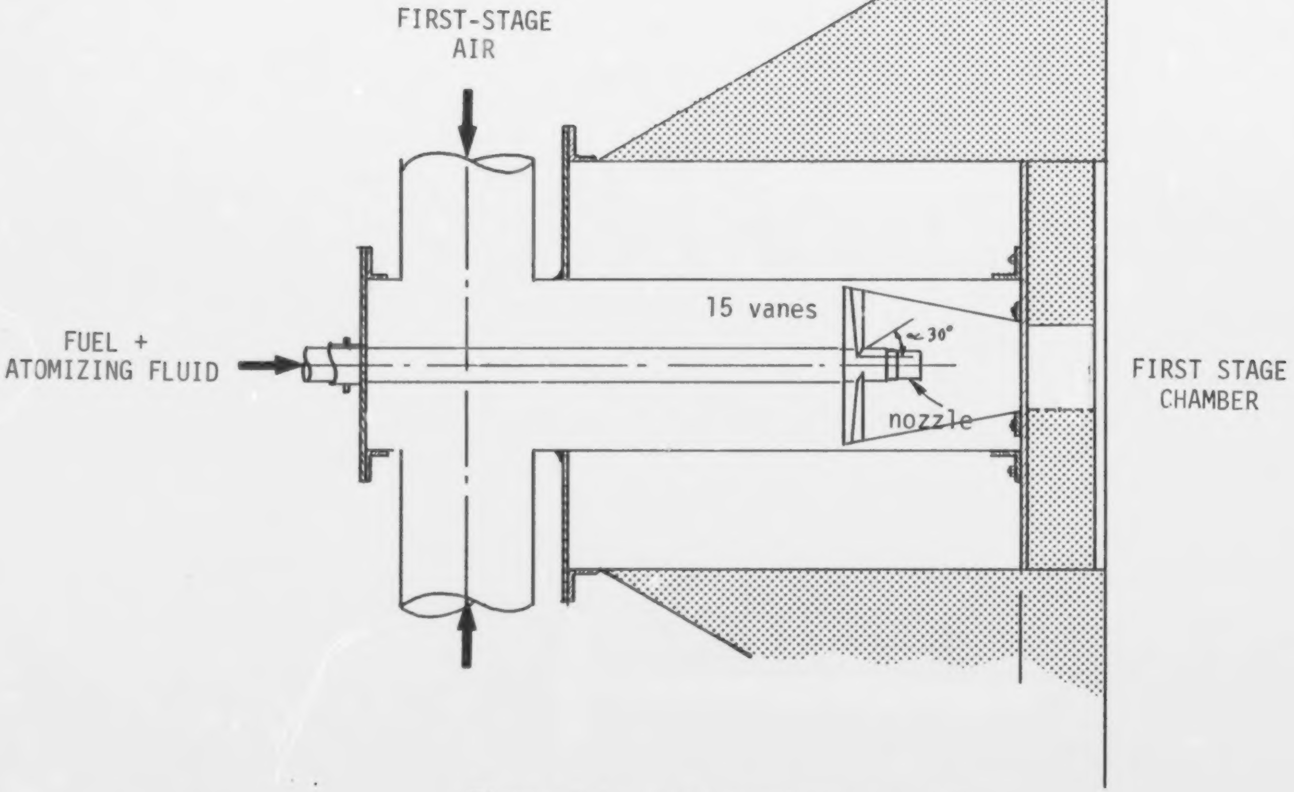
FIRST-STAGE AIR
FUEL + ATOMIZING FLUID
15 vanes
≈30°
nozzle
FIRST STAGE CHAMBER

Figure 3-3. 3 MW premixer assembly.

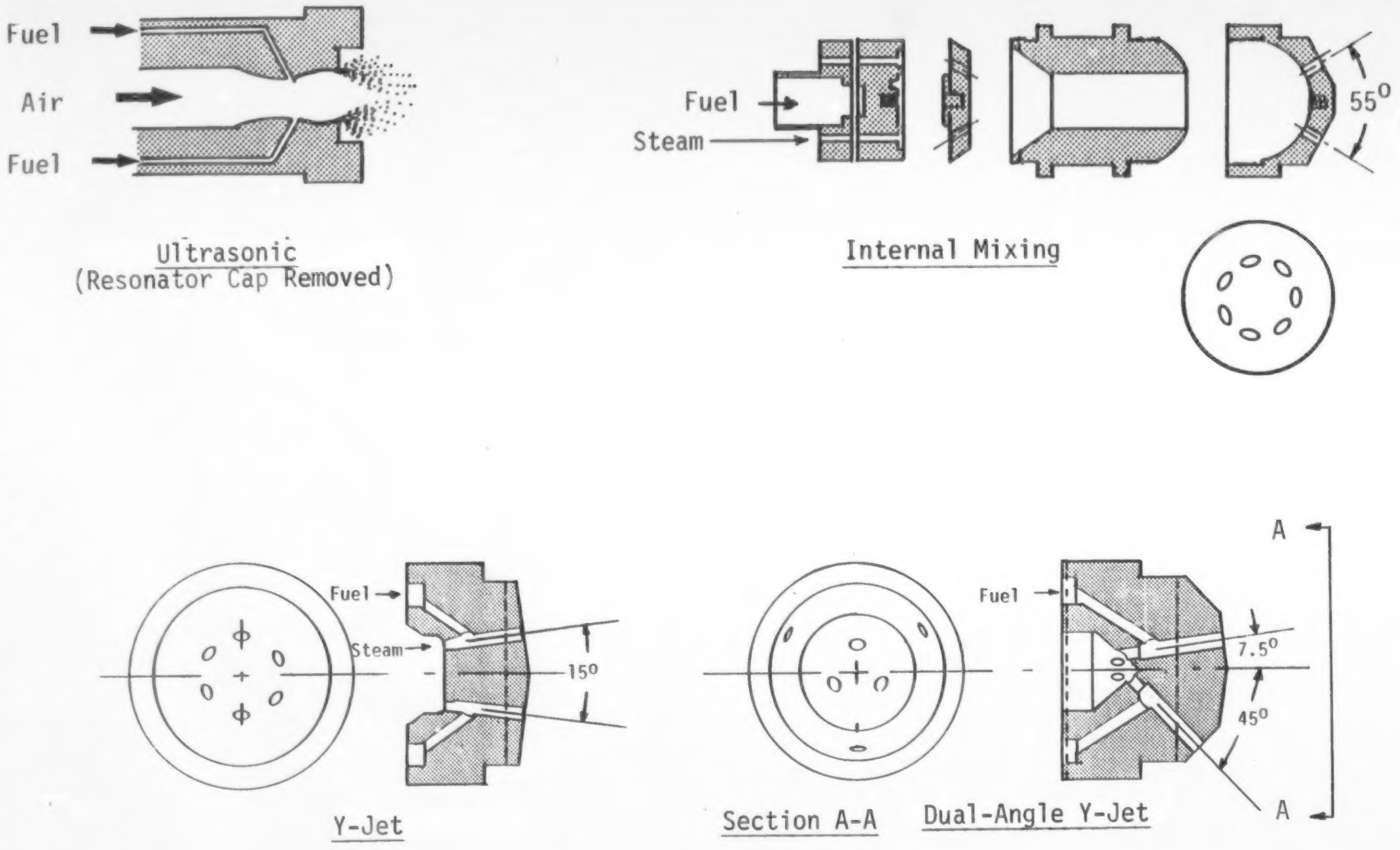
Fuel
Air
Fuel
Fuel
Steam
55°
Fuel
Steam
15°
Fuel
7.5°
45°
A
A

Ultrasonic
(Resonator Cap Removed)

Internal Mixing

Y-Jet

Section A-A

Dual-Angle Y-Jet

Figure 3-4. Atomizers tested in 3 MW pilot-scale burner.

Y-jet atomizers. The commercial ultrasonic atomizer was modified for these tests by removing the resonator cap normally used in order to produce a very narrow spray angle. The two Y-jet atomizers were similar in design except for spray angle, as shown in the figure.

A 2-channel swirl register was also investigated. This experimental 3.5 MW register was designed under another program for low-$NO_x$ operation, but with all air supplied through the register. When operated deeply staged in these tests, throat velocity was quite low--approximately 10 meters/second. Some of the first-stage configurations were tested with a sleeve insert in the first-stage exit, which approximately doubled the exit velocity. The configuration numbers assigned in this table are used throughout the discussion of test results in this section.

Second-stage air injection variations are summarized in Table 3-5. In addition to the first-stage exit sleeve shown in the previous table, several air injection port configurations were tested to vary second-stage mixing. The number of ports, diameter (yielding two velocity levels), and distance from centerline were varied. Figure 3-5 illustrates the different hardware configurations used.

The majority of the tests were conducted using No. 6 residual fuel oil of California origin. A brief series of tests was also conducted using No. 2 fuel oil and a Kern County crude oil. Analyses of the heavy fuels is given in Table 3-6.

### 3.1.2 Results: First-Stage Effects

#### 3.1.2.1 Baseline Conditions

The burner conditions corresponding to Table 3-7 were chosen as the baseline. Data was obtained both with and without preheat over the duration of the tests (Figure 3-6). The lack of scatter in these data indicates the overall reproducibility of experimental conditions and measurements. $NO_x$ data was generally reproducible to better than 5 ppm within the same day's trial, but day-to-day reproducibility within one standard deviation was ± 5.7 ppm near the minimum $NO_x$ point.

TABLE 3-5. SUMMARY OF SECOND-STAGE AIR VARIATIONS

Annular Air Injector

| | |
|---|---|
| First-State Exit Velocity: | 20, 40 m/s |
| Secondary Air Swirl Number: | 0 to 2 |
| Secondary Air Velocity: | 15 m/s |

Discrete Port Injectors

First-Stage Exit Velocity: 20 m/s

Port Variations:

| Port Orientation | Secondary Air Velocity (Port Diameter) | | | |
|---|---|---|---|---|
| | Outboard Ports | | | Inboard Ports |
| | 4 Ports | 8 Ports | 16 Ports | 8 Ports |
| Axial | 25 m/s<br>(8 cm) | 12,28 m/s<br>(8,5 cm) | 14,36 m/s<br>(5,3.2 cm) | 28 m/s<br>(5 cm) |
| Radial | 25 m/s<br>(8 cm) | 12 m/s<br>(8 cm) | 36 m/s<br>(3.2 cm) | 28 m/s<br>(5 cm) |

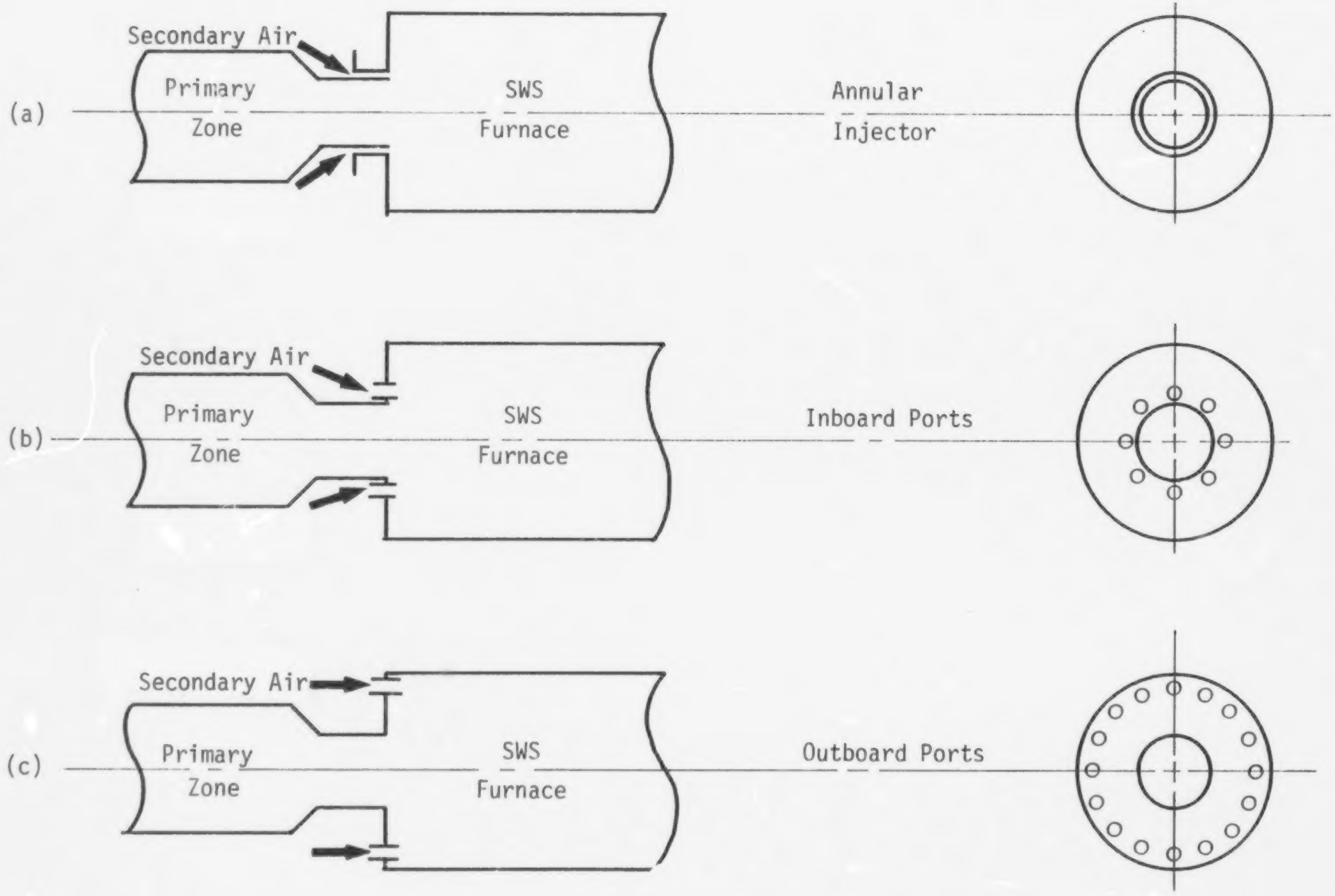
(a)
Secondary Air
Primary Zone
SWS Furnace
Annular Injector
(b)
Secondary Air
Primary Zone
SWS Furnace
Inboard Ports
(c)
Secondary Air
Primary Zone
SWS Furnace
Outboard Ports

Figure 3-5. Secondary air injection configurations investigated with 3 MW pilot scale burner (ports shown in axial orientation).

## TABLE 3-6. ANALYSIS OF HEAVY FUELS TESTED IN PILOT-SCALE TESTING

| | No. 6 Oil | Kern Front Crude Oil |
|---|---|---|
| Specific Gravity | 0.96 | - |
| Ultimate Analysis | | |
| % C | 86.4 | 86.3 |
| % H | 11.7 | 11.4 |
| % N | 0.69 | 0.81 |
| % S | 0.84 | 1.06 |
| % O | 0.36 | 0.46 |
| % Ash | 0.05 | 0.04 |
| Viscosity (CP) | 142 (@ 60°C)<br>28 (@ 99°C) | 205 (@ 71°C)<br>45 (@ 99°C) |
| Heat of Combustion | | |
| Net kJ/g | 40.8 | 40.3 |
| Gross kJ/g | 43.3 | 42.6 |

TABLE 3-7. BASELINE TEST CONDITIONS

| | |
|---|---|
| Configuration | I |
| Fuel | No. 6 |
| Atomizer | Ultrasonic |
| Primary Air Temp | Ambient, High |
| Load | 2.9 MW |
| Secondary Air Swirl | Zero |
| Atomizing Air Pressure | 69-83 kPa |

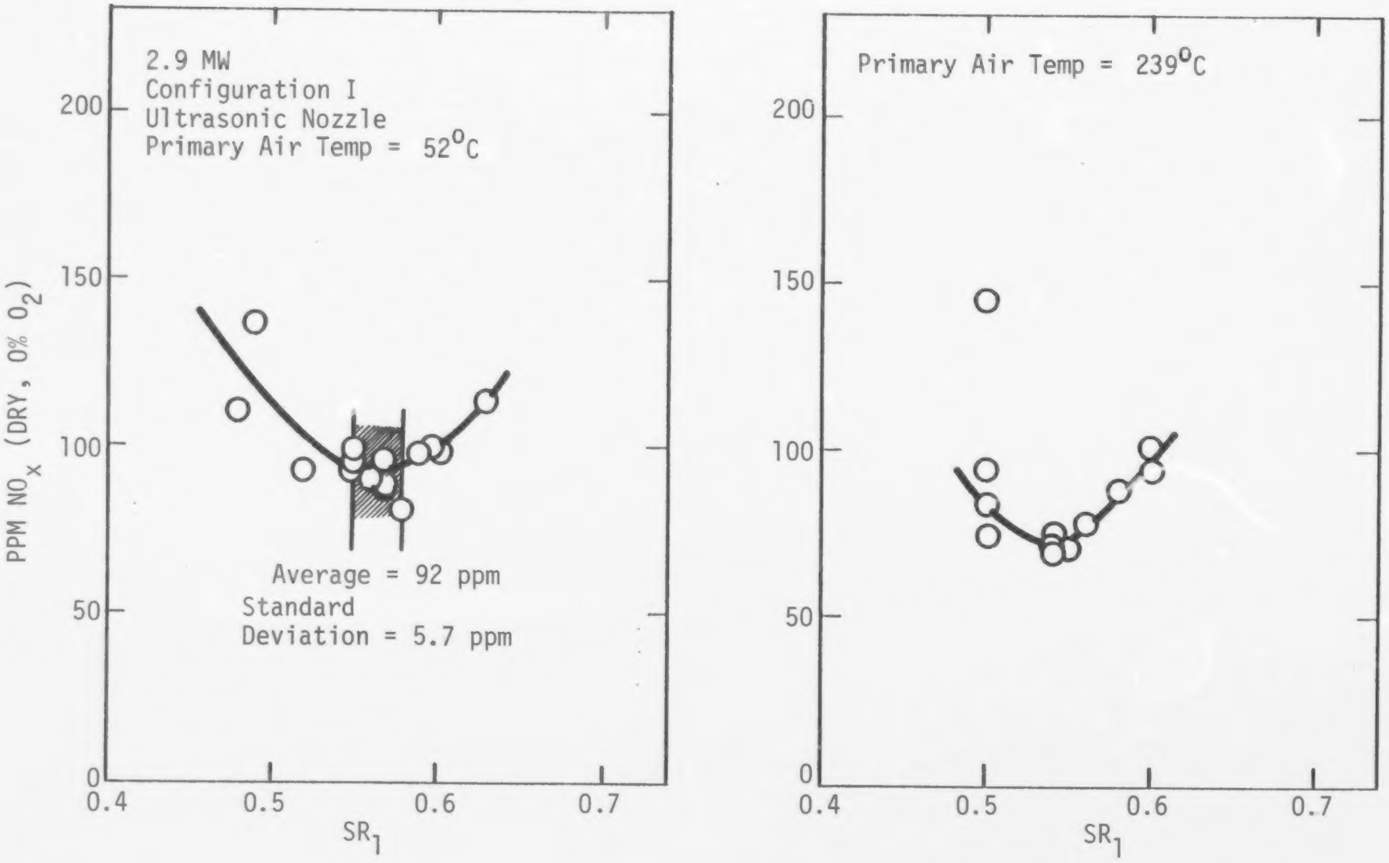

Figure 3-6. Baseline $NO_x$ emissions (2.9 MW).

$NO_x$ levels reached a minimum of approximately 92 ppm, corrected to zero percent oxygen (all data presented in this report are taken at 3 percent overall excess oxygen and corrected to zero percent oxygen unless otherwise noted) with no first-stage air preheat. This would correspond to 79 ppm at 3 percent oxygen. Increasing first-stage air preheat to 239°C (± 17°C) but maintaining ambient temperature second-stage air decreased $NO_x$ emissions to approximately 73 ppm (63 ppm at 3 percent oxygen). The optimum stoichiometric ratio decreased slightly with the increase in air temperature, from 0.56 to 0.54.

Smoke emissions were similar with and without primary air preheat (Figure 3-7). Smoke was generally low at the minimum $NO_x$ condition (Bacharach smoke numbers 2 to 4) and increased sharply as stoichiometry was further reduced below optimum.

The influence of burner load is shown in Figure 3-8, with and without air preheat. Fuel flowrate was varied above and below the baseline load from 2.3 MW to 3.5 MW throughput. Minimum $NO_x$ emissions increased with load, ranging from 95 ppm to 77 ppm at 3.5 to 2.3 MW load, respectively, without first-stage air preheat. With first-stage air preheat, minimum $NO_x$ ranged from 88 to 63 ppm at the same loads, respectively. The optimum stoichiometry in the first-stage was not shifted significantly. Optimum $SR_1$ varied from 0.54 to 0.56 with preheat and from 0.55 to 0.57 without preheat. Smoke emissions were insensitive to load, as seen in Figure 3-9.

#### 3.1.2.2 First-Stage Variations

$NO_x$ emissions increased substantially from baseline emissions when the swirl vanes were removed from the premixer assembly (configuration III), Figure 3-10. Optimum stoichiometry was also shifted to higher $SR_1$ than in the baseline configuration. The steep dependence of $NO_x$ on $SR_1$ was somewhat reduced at high primary air preheat for configuration III; however, only limited data was obtained. Observation of the flame from the rear of the SWS indicated a rather bright, narrow jet flame was formed in the first-stage chamber. Utilization of available volume for residence time is probably very poor in this configuration, accounting for the increased $NO_x$ emission.

In Figure 3-11, the effect of adding a divergent throat quarl to the baseline configuration can be seen. The quarl is a 30-degree half-angle

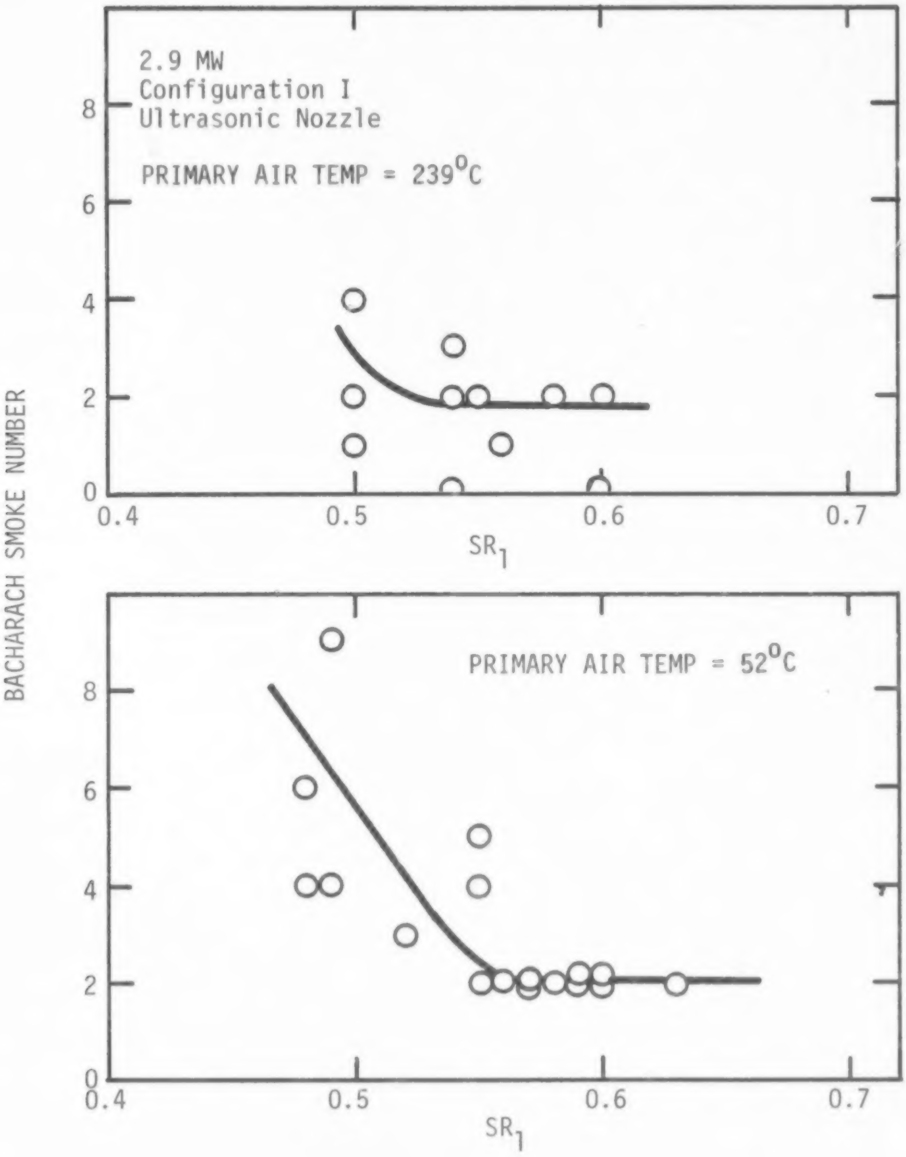

Figure 3-7. Baseline Smoke Emissions (2.9 MW).

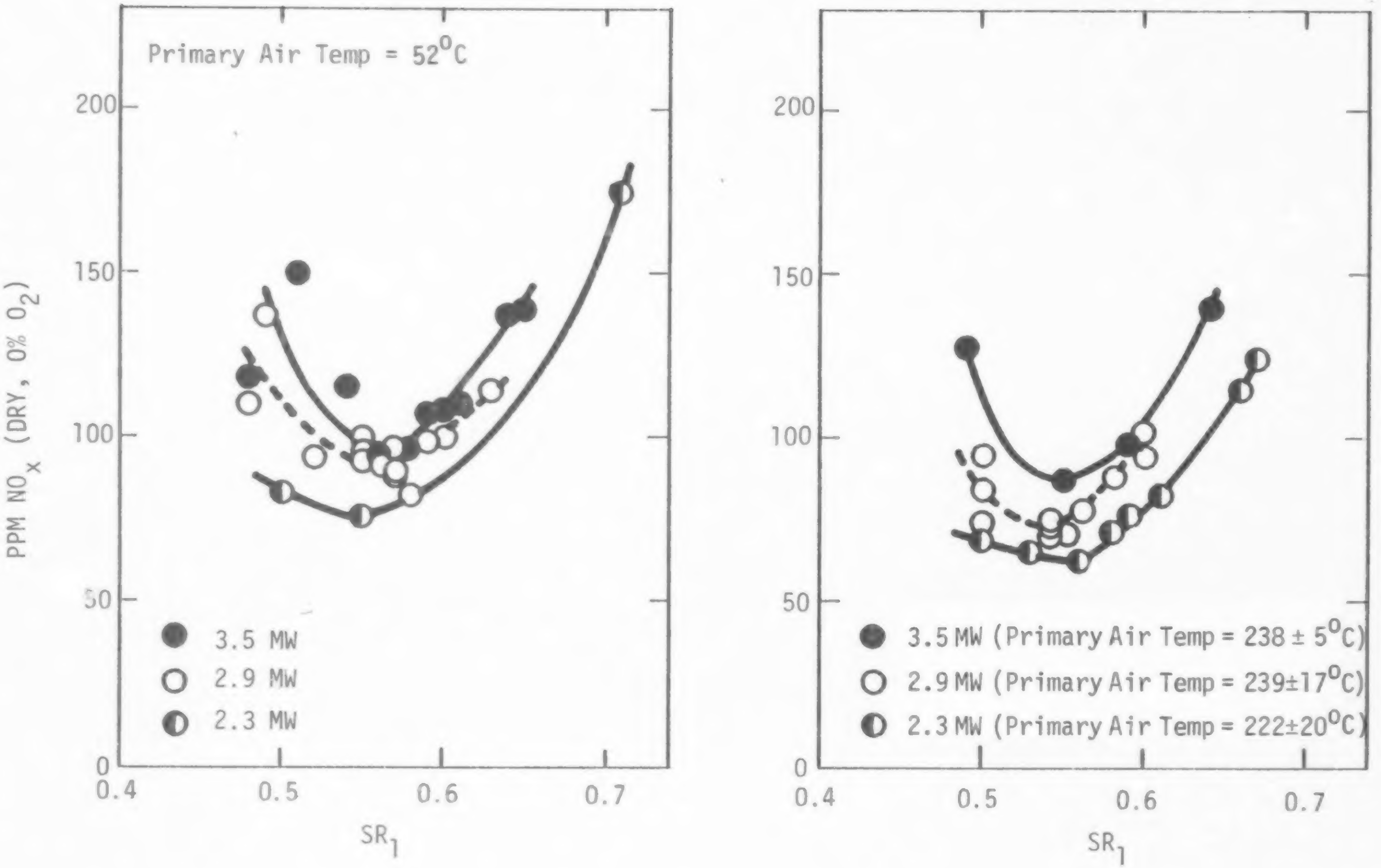

Figure 3-8. Effect of load - baseline configuration.

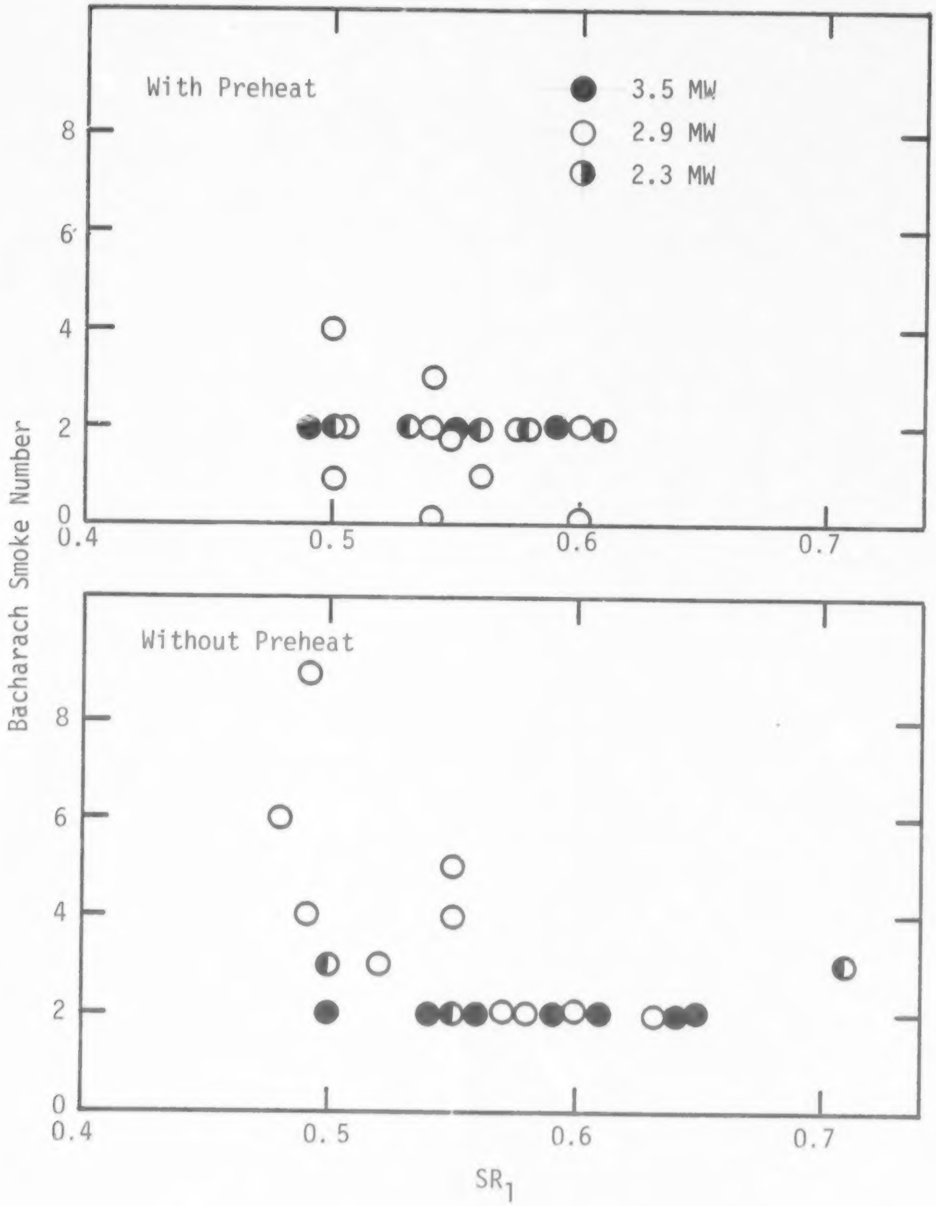

Figure 3-9. Effect of load on smoke emissions.

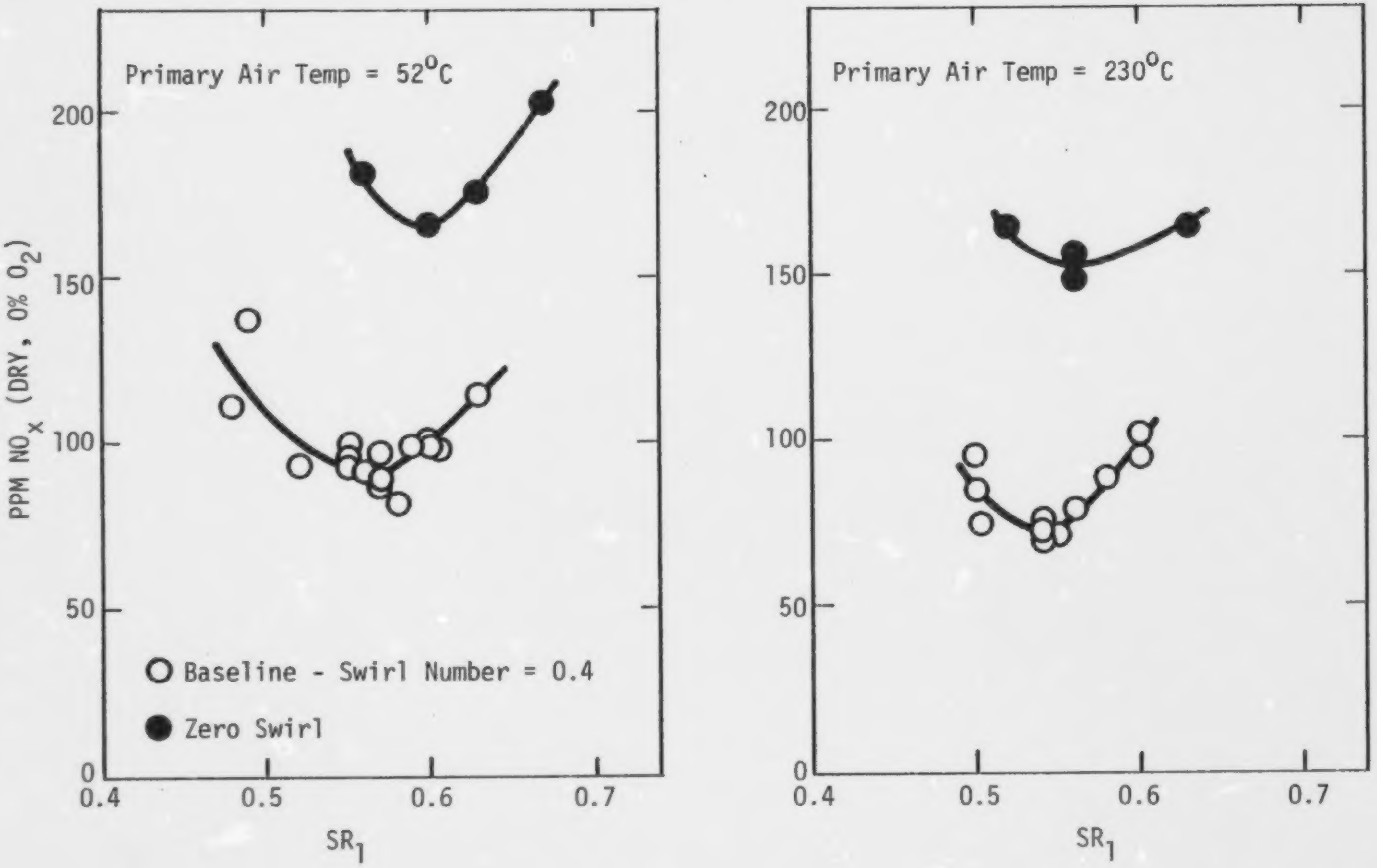

Figure 3-10. Effect of Swirl - Premixer (2.9 MW; Configuration I).

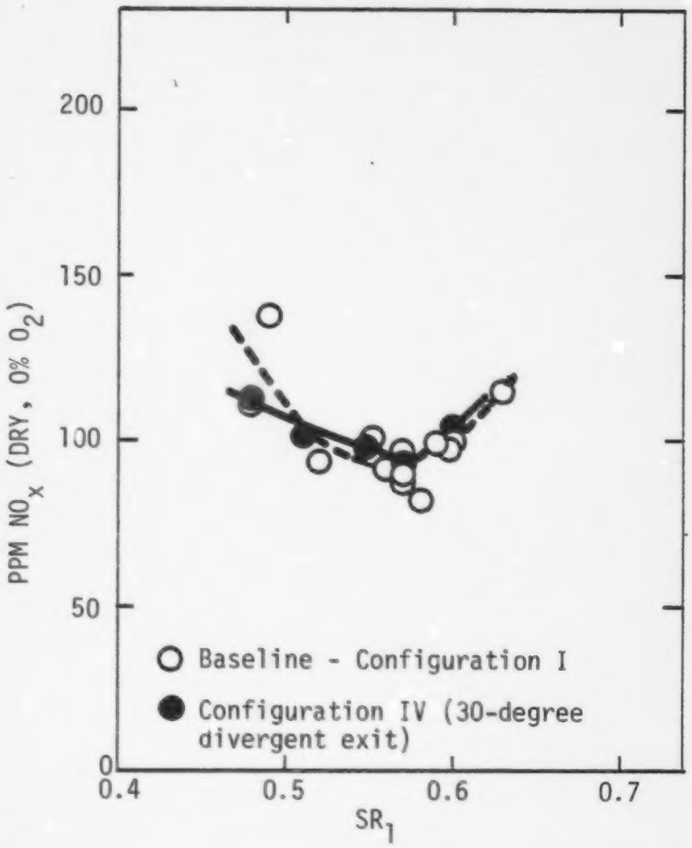

Figure 3-11. Effect of first-stage throat geometry (2.9 MW; ultrasonic atomizer; primary air temp = 52°C).

truncated cone attached to the exit of the premixer assembly, and has a length:diameter ratio of 2.6. The swirl vanes were in place producing a swirl number of 0.4. $NO_x$ emissions were similar with and without the quarl, although sensitivity to $SR_1$ seemed slightly reduced with the quarl.

Further variation of the first-stage air distribution was attempted by replacing the premixer assembly with a more conventional swirl-register type air inlet. The register is adapted from an experimental coal burner designed for low-$NO_x$ operation with outboard air ports. Throat velocity was therefore only 8-11 meters per second when operated under deeply staged conditions. The burner has two air channels, a central core and a surrounding annular air passage. Swirl is variable in the annulus and fixed in the core. Figure 3-12 shows the range of $NO_x$ emissions possible with this burner as the first-stage air register. The data includes variations in core and annular swirl, air split, and both atomizer type and atomizing fluid/ pressure. This data was taken late in the test series with a sleeve installed in the first-stage exit to double the velocity of the first-stage combustion products entering the second-stage burnout zone. The effect of this sleeve is discussed in the next subsection. Data is shown for the baseline first-stage configuration (i.e., premixer plus parallel throat) for comparison. The minimum $NO_x$ level achievable with the 2-channel register is approximately the same with and without air preheat, and was 15 ppm higher than with the premixer configuration. Smoke number for this configuration was similar to the baseline emissions, and in general was insensitive to the first-stage conditions.

Several atomizer variations were investigated with the premixer to determine whether more conventional atomizers were suitable for the full-scale application. Figure 3-13 shows $NO_x$ emissions obtained in the baseline configuration with the commercial internal-mixing atomizer and the 15-degree Y-jet atomizer using steam for atomization. The narrow spray angle of the Y-jet was chosen to match the angle of the ultrasonic nozzle and avoid spray impingement on the premixer throat. Both the experimental and ultrasonic atomizers produced similar $NO_x$ emissions under equivalent conditions, although slightly higher than baseline in both cases. Smoke number from both the Y-jet and internal-mixing atomizer was two for all data shown in the figure. The effect of varying atomizing fluid and pressure is shown in

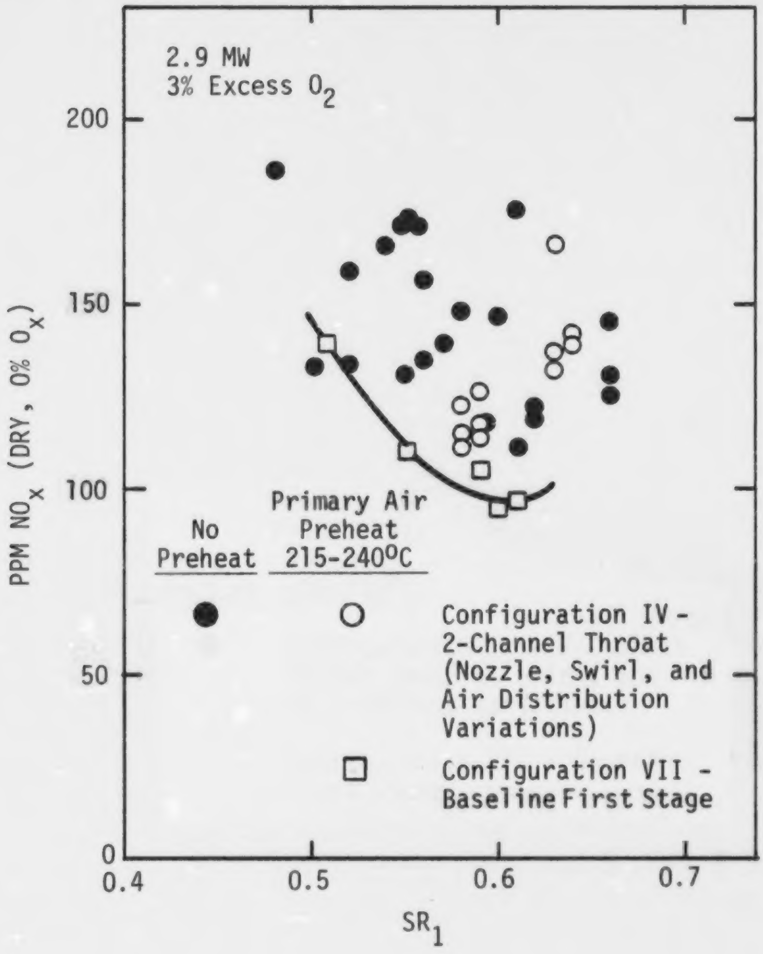

Figure 3-12. Effect of first-stage air distribution.

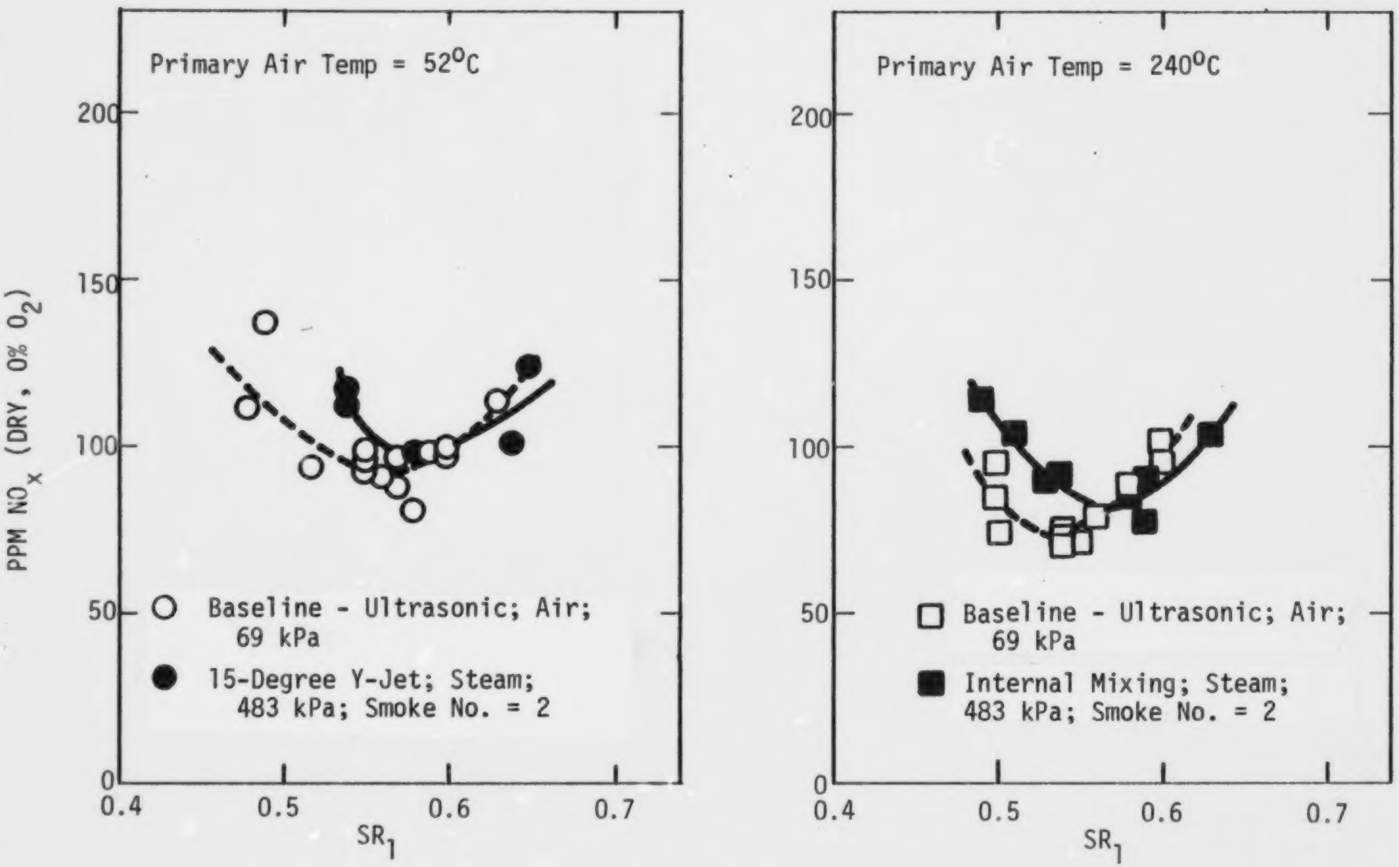

✓Figure 3-13. Effect of atomizer type on baseline NO$_x$ emissions (2.9 MW; Configuration I).

Figure 3-14. The 15-degree Y-jet was tested in configuration IV ($30^o$ divergent throat) with both air and steam atomization and at two atomizing steam pressures. $NO_x$ emissions were insensitive to atomizing pressure, although optimum $SR_1$ was shifted by changing from air to steam. Increasing steam pressure on the dual-angle Y-jet atomizer did produce a significant increase in $NO_x$ emissions, however. Compared to the ultrasonic atomizer with air atomization, minimum $NO_x$ was slightly lower with the dual-angle Y-jet. The shift to higher optimum $SR_1$ is consistent with the results from the 15-degree Y-jet. Some coking around the premixer throat was observed after extended operation with the dual-angle Y-jet, but these data suggest that further optimization of the atomizer spray pattern could lead to slightly lower $NO_x$ emissions.

### 3.1.3 Second-Stage Effects

This series of tests was conducted to determine limits of additional $NO_x$ reduction through variations in the second-stage mixing. Practical information on the tradeoffs between $NO_x$/smoke emissions and flame shape was necessary to finalize the design of the full-scale burner.

The effect of inducing swirl on the secondary air with the annular injector was small (Figure 3-15) producing a decrease in minimum $NO_x$ of 10 ppm over the baseline condition. Although the swirl register was designed to yield a high swirl number for secondary air, the swirl induced to the total stream is much less. A very minor change in flame shape was observed with the the addition of swirl. The importance of second-stage air on $NO_x$ emissions was discovered when the annulus was distorted by heat during a series of tests, producing an unsymmetric air flow from the annulus. This maldistribution of air could be seen in the unsymmetric flame produced and in an upward shift in the $NO_x$ emissions (Figure 3-15). This also pointed out deficiencies in the annular injector design.

Figure 3-16 shows the results of doubling the velocity of first-stage combustion products entering the second stage. This was accomplished by adding a sleeve to the first-stage exit. The flame produced by this configuration was very short without a visible smoky trail. The increase in velocity by a factor of two decreased flame length by a factor of 3 to 4, and increased $NO_x$ emissions to 95 ppm from 72 ppm. Entrainment rate of unconfined jets increases approximately as the square of velocity, hence the flame length

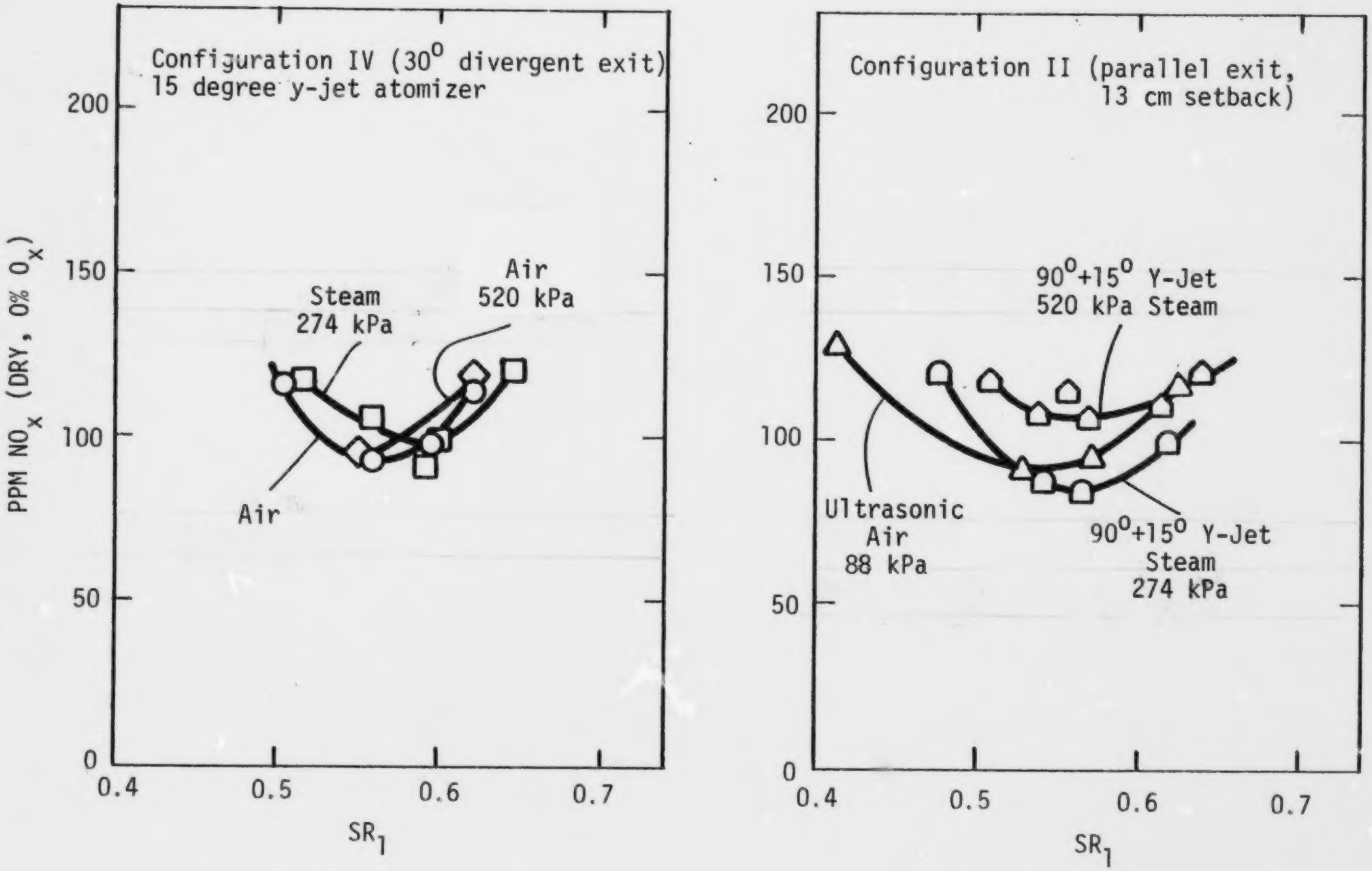

Figure 3-14. Effect of atomizing fluid and pressure on $NO_x$ emissions (2.9 MW; primary air temp = 52°C).

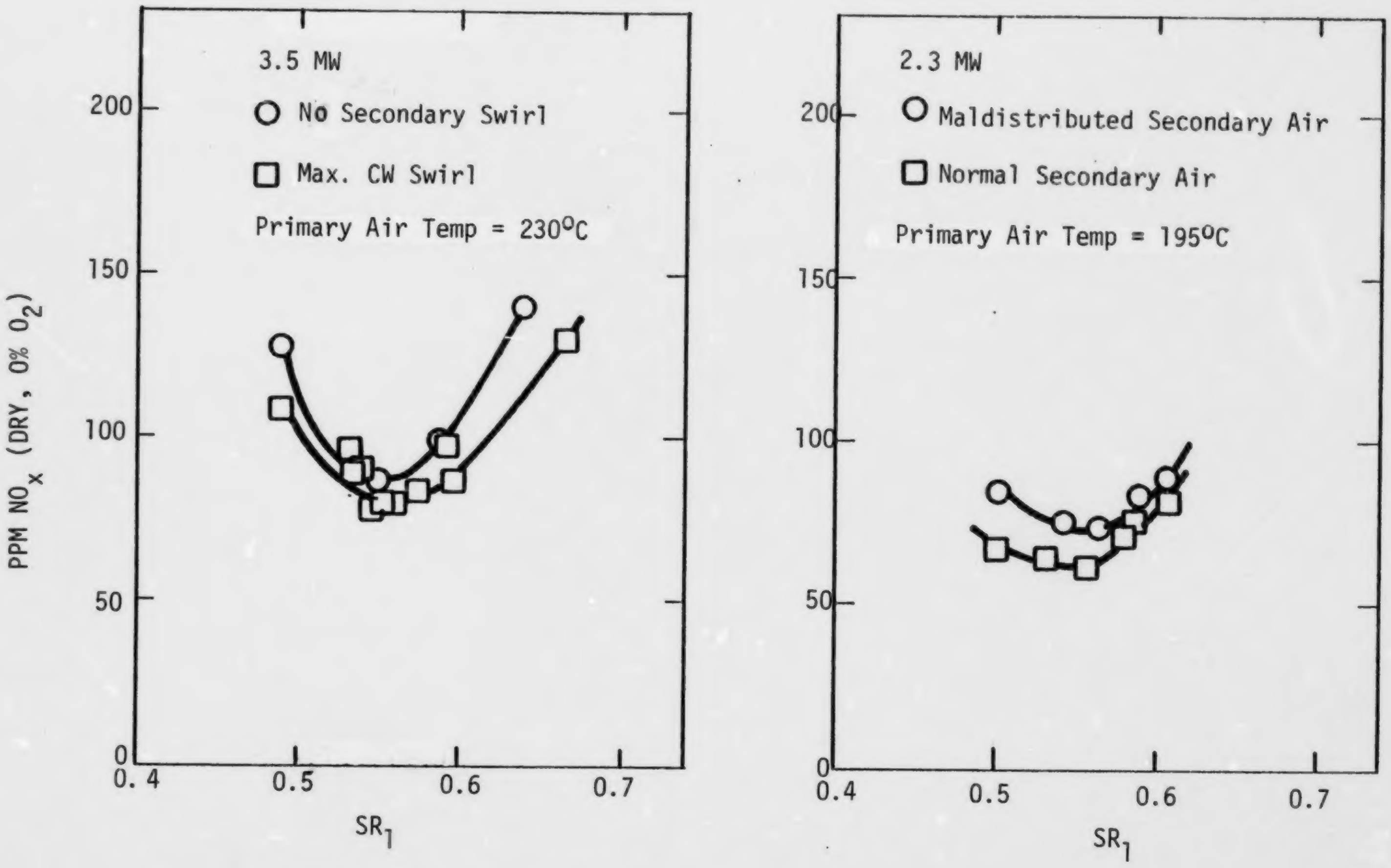

Figure 3-15. Effect of annular air swirl and air distribution.

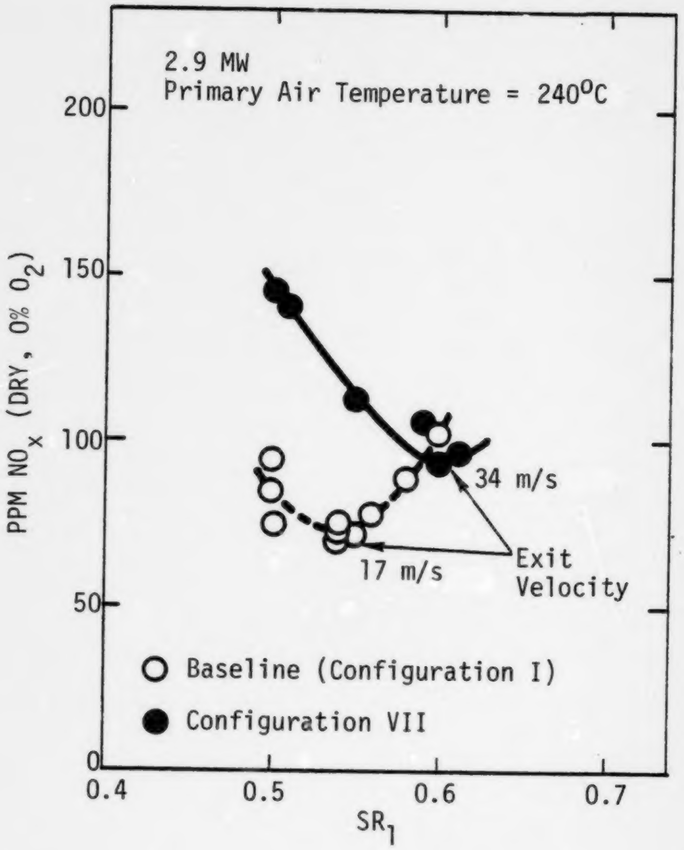

Figure 3-16. Second Stage Mixing - Effect of First-Stage Exit Velocity.

seems to be proportional to entrainment rate. The increase in $NO_x$ emissions with decreasing flame volume is qualitatively in the right direction based on experience with oil flames of various sizes (Payne and Akiyama, 1979). Further optimization of exit velocity and swirl level could improve $NO_x$/flame shape characteristics with the annular air injector.

Discrete ports for second-stage air injection were also investigated as an alternative to the annulus for the full-scale burner. Figure 3-17 shows details of the two hardware configurations which were used for discrete port injection. The tests were conducted in two phases. The first series of tests covered a screening of port number (4,8,16 ports), size (velocity), and distance from burner centerline. The outboard port configuration was chosen for the initial tests due to physical limitations of the burner refractory. Outboard radius was 69 cm from burner centerlines or 44 cm from the edge of the first-stage exit. The inboard ports were 33 cm from burner centerline, or 8 cm from the first-stage exit. The annular air injector was removed for these tests.

The second series of tests utilized a ring manifold injector which was used to obtain a direct comparison of air injection through the annulus and through the axial ports. The port size was chosen based on the results of the initial screening tests. Maximum secondary airflow through these axial ports was 60 to 80 percent for most tests, as some annular airflow was maintained for annulus cooling.

$NO_x$ emissions data obtained with 16 low-velocity (15 m/s) outboard axial ports and with 8 high-velocity (30 m/s) inboard axial ports are compared to baseline emissions in Figure 3-18. At this load, $NO_x$ emissions with either port configuration were substantially higher than baseline emissions, and optimum first-stage stoichiometry was shifted towards slightly higher $SR_1$. Both port configurations produced similar minimum $NO_x$ emissions of approximately 120 ppm, compared to baseline $NO_x$ of 95 ppm. Smoke emissions (not shown) were higher than baseline with the 16-port configuration but were similar to baseline with the 8-port configuration.

Secondary air mixing characteristics are likely to be more critical at higher load since furnace temperature and mean velocities are higher. Table 3-8 compares minimum $NO_x$ emissions, corresponding smoke number, and

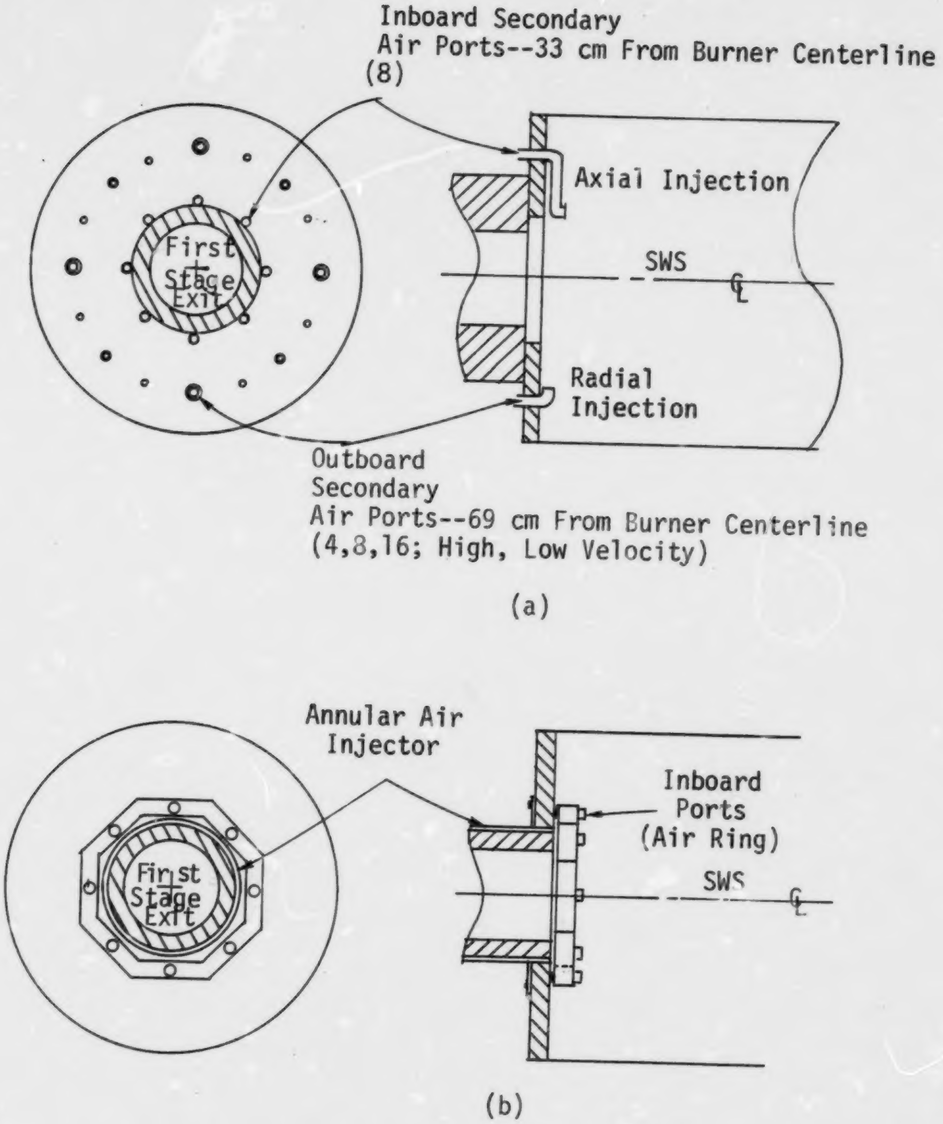
Inboard Secondary
Air Ports--33 cm From Burner Centerline
(8)
First Stage Exit
Axial Injection
SWS
℄
Radial Injection
Outboard Secondary
Air Ports--69 cm From Burner Centerline
(4,8,16; High, Low Velocity)
(a)
Annular Air Injector
First Stage Exit
Inboard Ports (Air Ring)
SWS
℄
(b)

Figure 3-17. Second-stage air port injectors.

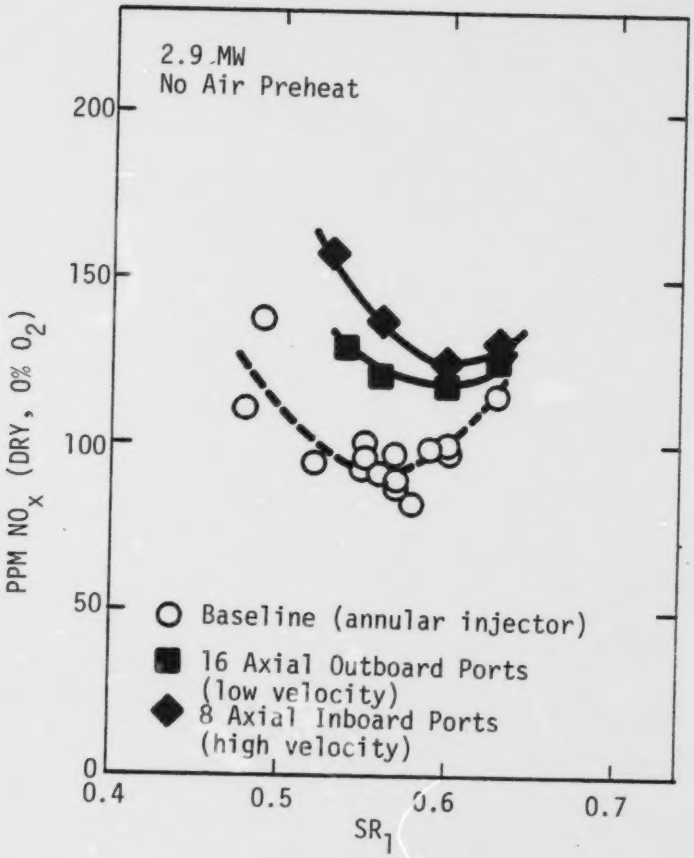

Figure 3-18. Effect of port geometry on $NO_x$ emissions.

TABLE 3-8. RESULTS OF SECOND-STAGE AIR PORT VARIATIONS (3.6 MW; NO AIR PREHEAT)

| Port Orientation | Secondary Air Injection Velocity | ● Minimum $NO_x$ (ppm, dry, 0% $O_2$)<br>● Smoke Number<br>● Optimum Stoichiometric Ratio | | | | | |
|---|---|---|---|---|---|---|---|
| | | Without Annular Air (Figure 3-17a) | | | | With 20% Annular Air (Figure 3-17b) | With 80% Annular Air (Figure 3-17b) |
| | | Outboard | | | Inboard | Inboard | Inboard |
| | | 4 Ports | 8 Ports | 16 Ports | 8 Ports | 8 Ports | 8 Ports |
| Axial | High (30 to 45 m/s) | 124<br>8<br>0.58 | 110<br>8<br>0.57 | 139<br>9<br>0.57 | 139<br>2<br>0.59 | 143<br>1<br>0.64 | 144<br>2<br>0.62 |
| | Low (15 to 20 m/s) | * | 140<br>5<br>0.60 | 146<br>6<br>0.56 | * | * | * |
| Radial | High (30-45 m/s) | 133<br>-<br>0.62 | * | 187<br>3<br>0.57 | * | 187<br>2<br>0.55 | * |
| | Low (15-20 m/s) | * | 146<br>-<br>0.61 | * | * | * | * |

*Not Tested

optimum first-stage stoichiometry for various secondary air port configurations at 3.6 MW load. $NO_x$ emissions ranged from 110 ppm to 187 ppm, smoke number ranged from 1 to 9, and optimum first-stage stoichiometry ranged from 0.56 to 0.62 over the range of port configurations shown in Figure 3-17. $NO_x$ emission for the baseline configuration (annular air injector) at this load [illegible] 95 ppm with a smoke number of 2 (Figure 3-8).

The results of the secondary air port configuration variations at 3.6 MW load can be summarized as follows:

- Axial versus radial ports: secondary air injection through radial ports always increased $NO_x$ compared to axial ports; the increase with 16 ports was greater than with 4 ports in the outboard configuration;
- Inboard versus outboard ports: $NO_x$ emissions were higher for the inboard port configuration but smoke emissions were much lower;
- Velocity: increasing axial air velocity increased $NO_x$ emissions and decreased smoke emissions;
- Annulus versus ports: $NO_x$ emissions produced with 80 percent of the secondary air injected through the annulus (20 percent through 8 axial ports) were similar to $NO_x$ with 80 percent secondary air through the 8 axial ports. Smoke number was slightly higher with annular air injection. $NO_x$ emissions with the ring manifold configuration (Figure 3-17b) were higher than baseline emissions at 3.6 MW load even when most of the air was injected through the annulus.

Radial and axial port injection is compared to the baseline configuration at base load (2.9 MW) in Figure 3-19. Similar $NO_x$ and smoke levels were obtained with annular and axial port injection at both 2.9 and 2.3 MW. Radial air injection produced a much shorter second-stage flame, and $NO_x$ emissions rose accordingly. The flame produced at 2.9 MW with radial injection appeared to neck down approximately where the secondary air jets would theoretically reach the burner centerline and then expanded outward rapidly between the jets, giving the impression of 8 "fingers" of flame.

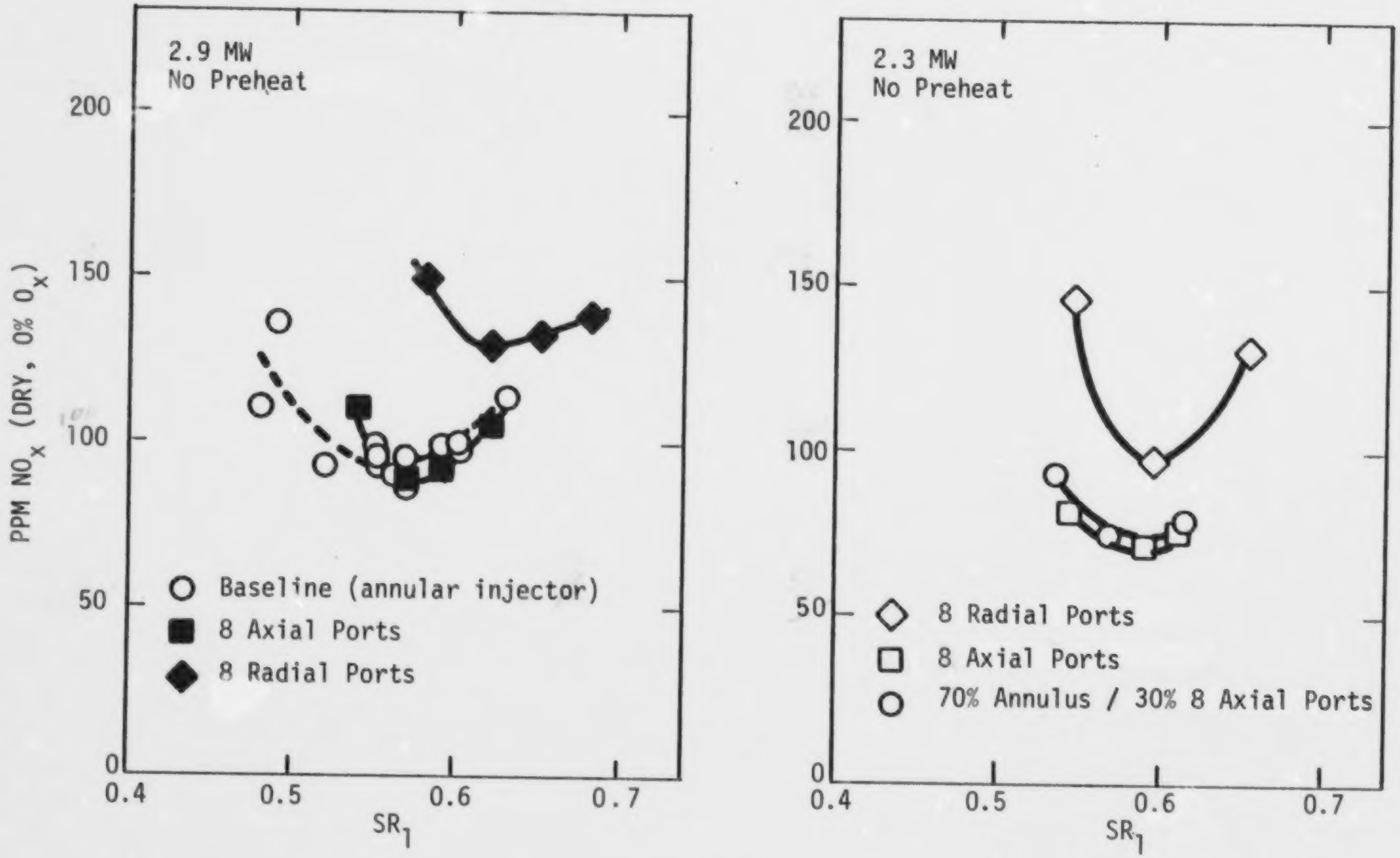

Figure 3-19. Optimized $NO_x$ emissions using ports and annular secondary air injectors.

### 3.1.4 Optimized Burner Performance

The best emissions performance for the IP burner was achieved with configuration I (Table 3-4) and primary air preheat of 240°C. $NO_x$ emissions were 73 ppm, corrected to zero percent oxygen (63 ppm corrected to 3 percent oxygen), firing residual fuel oil containing 0.68 percent fuel-bound nitrogen. First-stage residence time in this configuration was approximately 0.5 seconds. Figure 3-20 compares $NO_x$ and smoke emissions from the Kern Front crude oil which will be burned in the full-scale burner (see Chapter 4.0--Field Retrofit). The crude oil produced higher $NO_x$ emissions than the residual oil, however smoke emissions were approximately the same. This difference may be due to the higher nitrogen content of the crude oil, although previous tests indicate the burner performance should be insensitive to fuel properties. A limited quantity of this fuel was available for testing; hence, a complete assessment could not be made. The previous results suggest it may be possible to reduce emissions to baseline levels by minor operating adjustments (fuel temperature, atomizing pressure).

A brief series of measurements firing No. 2 oil were also made in order to assess performance on a nitrogen-free fuel. $NO_x$ emissions under baseline test conditions (without preheat) were approximately 70 ppm, compared to 92 ppm with the residual fuel oil. This suggests that greater than 60 percent of final $NO_x$ emissions may be due to thermal NO formation. Bench-scale experiments show that even with a nitrogen-free fuel, a significant amount of oxidizable nitrogen species are present at the exit of the first-stage, hence $NO_x$ emissions from No. 2 oil cannot be attributed to thermal NO in the conventional sense.

After the burner was optimized for $NO_x$ emissions, particulate mass and size distribution were measured firing residual fuel oil. Figure 3-21 presents the size distribution and mass loading under baseline conditions with preheat. Total particulate loading was 0.26 grams per cubic meter. Examination of the catch revealed some matter from the furnace ducting was present in the large size fraction so this measurement may be artificially high. Size distribution indicates that 50 percent of the mass is below 4 microns in diameter and approximately 90 percent is less than 100 microns.

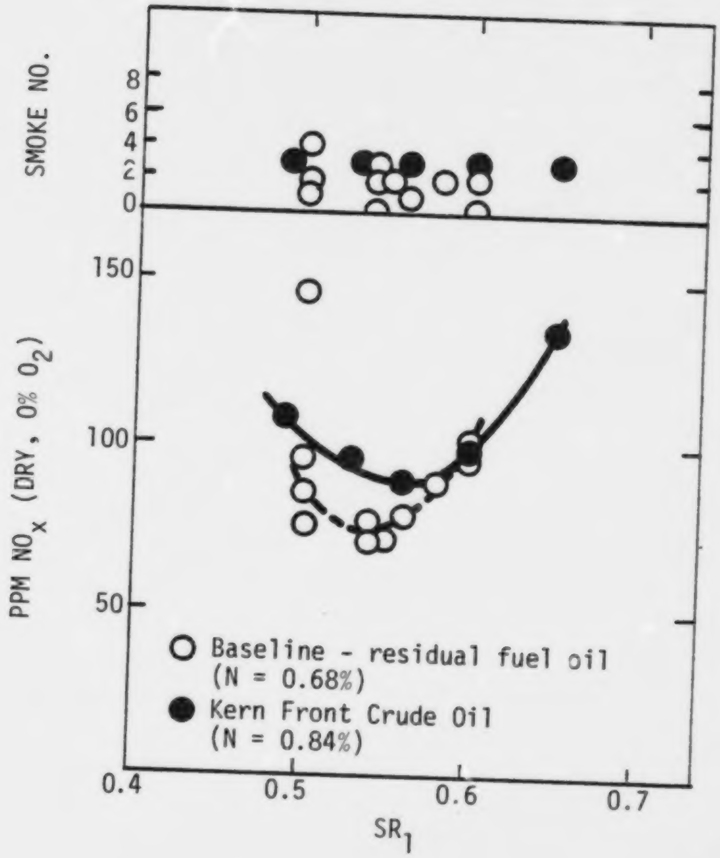

Figure 3-20. Emissions from crude oil and residual oil (baseline conditions).

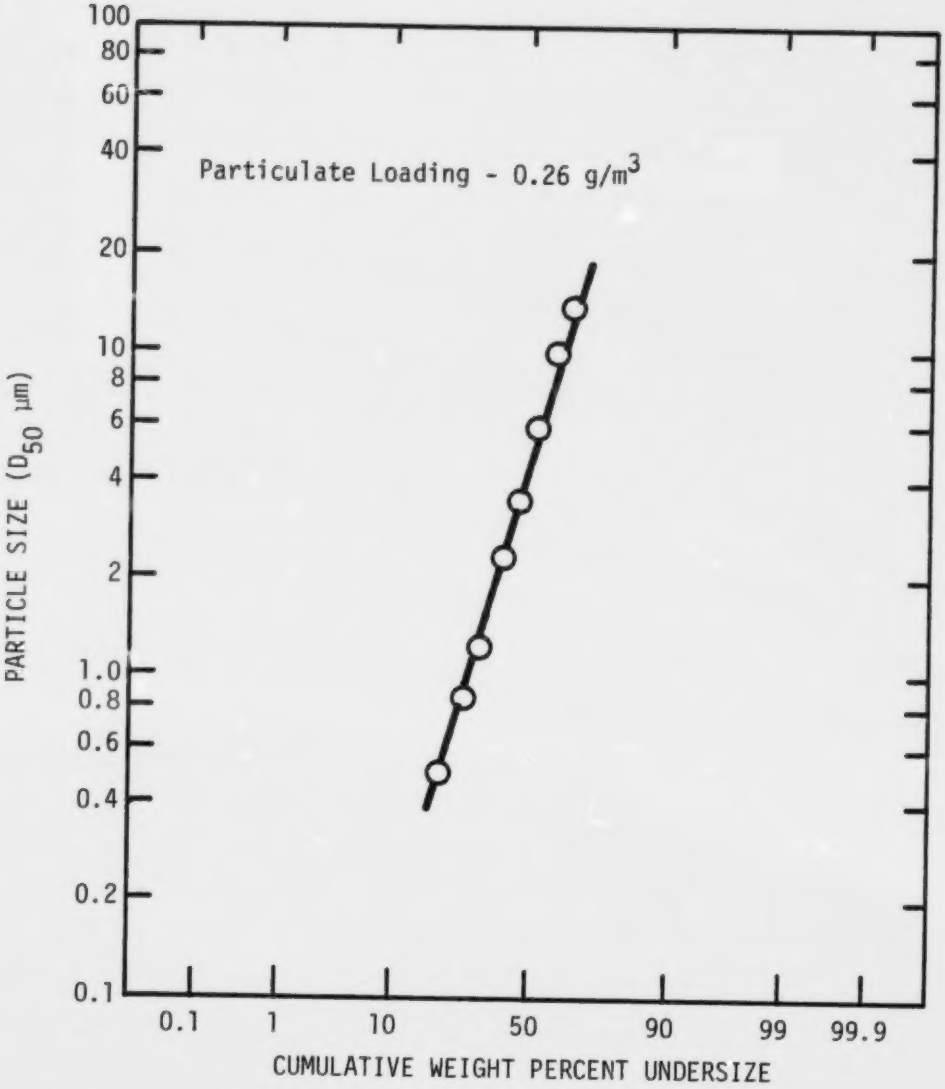

Figure 3-21. Particulate measurement - baseline conditions (residual oil).

## 3.2 Isothermal Screening

The results of the isothermal nozzle screening experiments are presented in this section. The tests were conducted at two scales: 1 MW-equivalent and 18 MW-equivalent. The smaller scale experiment evaluated nozzle and throat configurations which were used in the small prototype burner tests. Comparisons could then be drawn between isothermal results and actual combustion performance. The 18 MW-equivalent tests evaluated full-scale atomizers and throat concepts which were considered as potentially attractive for the commercial prototype.

### 3.2.1 Experimental Equipment

*Small Spray Rig*

Two spray chamber facilities were used. A detailed description of the small spray rig, shown in Figure 3-22, has been given elsewhere (Seeker, et al, 1982). The main body of the spray chamber consisted of a vertical-oriented plexiglass cylinder about 2 meters high and 0.61 meters inner diameter, and could accommodate a variety of inlet geometries and swirl generators. The primary air was supplied by a blower (0.38 $m^3/s$ @ 3.7 kPa) and flow was controlled by a blower exit damper. Air flowrate was measured using a venturi flowmeter. A low-velocity screen airflow was provided across the chamber cross-section with a maximum flow of 0.18 $m^3/s$ corresponding to a velocity of 0.64 m/s. The screen air was used mainly to minimize the recirculation of fine droplets which developed around the central spray. Atomizing air was supplied from a central facility air compressor. Water was used for the small spray rig tests and was delivered to the nozzle by a gear pump from a reservoir located at the bottom of the spray rig. The system is also capable of pumping light oil. The exhaust mixture was evacuated from the spray chamber by an induced draft blower, maintaining slight negative pressure in the chamber, and then passed through a mist eliminator to separate most of the liquid from air. The liquid then recycles to the spray chamber reservoir.

Five different burner configurations were tested in the small spray rig (SSR). General descriptions of these configurations are presented in Table 3-9. In Configuration I, primary air flow was directed axially into a $30^{0}$ half-angle divergent burner quarl without swirler. The ratio of chamber

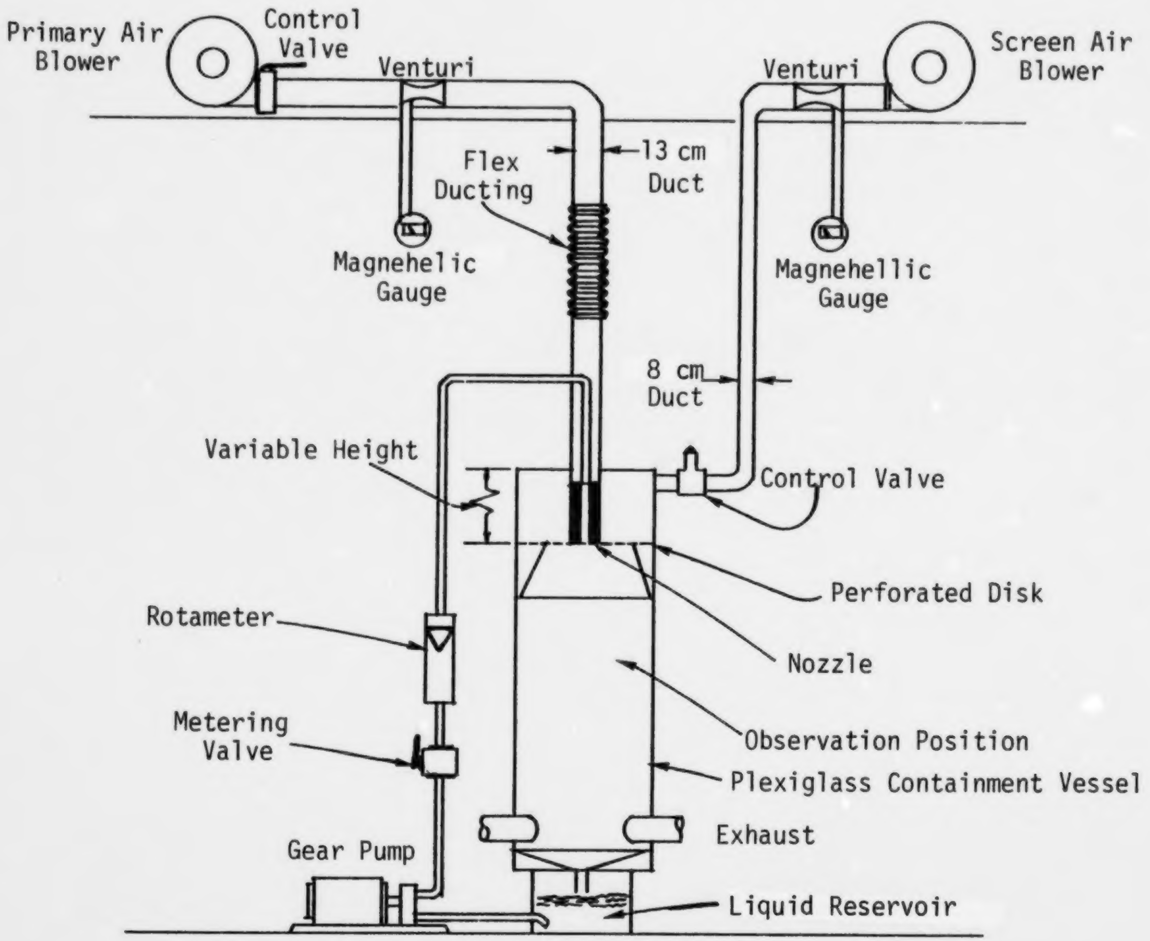
Primary Air Blower
Control Valve
Venturi
Venturi
Screen Air Blower
Flex Ducting
13 cm Duct
Magnehelic Gauge
Magnehellic Gauge
8 cm Duct
Variable Height
Control Valve
Perforated Disk
Rotameter
Nozzle
Metering Valve
Observation Position
Plexiglass Containment Vessel
Exhaust
Gear Pump
Liquid Reservoir

Figure 3-22. Small spray characterization rig (SSR).

## TABLE 3-9. BURNER CONFIGURATIONS TESTED IN SMALL-SCALE SPRAY RIG

| Configuration | Geometry | Swirl Generator | Throat Diameter | Nozzle | Remarks |
|---|---|---|---|---|---|
| 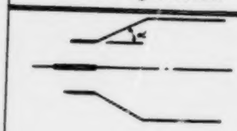 I | Divergent<br>$\alpha = 30^0$ | No<br>$S = 0$ | 30 cm | Sonicore<br>250T | |
| 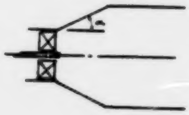 II | Divergent<br>$\alpha = 30^0$ | Yes<br>$S = 0.39$ | 30 cm | Sonicore<br>250T | Tested in<br>SS-SWS<br>$NO_x$(@ $SR_1$=0.6)<br>= 128 ppm<br>@ 0% $O_2$ |
| 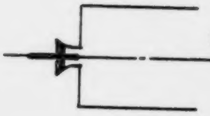 III | Cylindrical<br>$\alpha = 90^0$ | Yes<br>$S = 0.39$ | 6.9 cm | Sonicore<br>250T | |
| 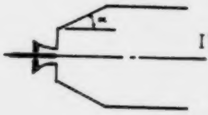 IV | Divergent<br>$\alpha$ $30^0$ | Yes<br>$S = 0.39$ | 6.9 cm | Sonicore<br>250T | Tested in<br>SS-SWS<br>$NO_x$(@ $SR_1$=0.6)<br>= 104 ppm<br>@ 0% $O_2$ |
| 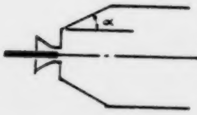 V | Divergent<br>$\alpha = 30^0$ | No<br>$S = 0$ | 6.9 cm | Sonicore<br>250T | |

diameter to burner exit diameter (Dc/De) was 2.0. Air velocity at the throat of the burner was approximately 1.4 m/s at 60 percent of theoretical air for 0.6 MW load. A commercial ultrasonic atomizer was used in all tests. Rated nozzle capacity for a light oil was 62 g/s at 276 kPa liquid pressure.

Configuration II was a duplicate of Configuration I but with a swirl generator placed at the inlet of the divergent section. The swirler used in this configuration and shown in Figure 3-23a, was a guide vane cascade in an axial tube flow with six vanes mounted on a hub which extend to the tube wall. The swirl number corresponding to this annular swirler was calculated to be approximately 0.40.

The swirl number is calculated using the expression (Beer and Chigier, 1972):

$$S' = \frac{G_\phi}{G_x' R} = \frac{2}{3}\left[\frac{1 - (R_h/R)^3}{1 - (R_h/R)^2}\right] \tan \alpha$$

where

$G_\phi$ = axial momentum of flow

$G_x'$ = axial momentum of flow

R = outer radius of the burner duct that contained the swirl vanes

$R_h$ = outer radius of the hub

$\alpha$ = vane angle

Configuration III consisted of a primary zone fuel/air premixer (Figure 3-23b) mounted on a ninety-degree quarl. The premixer which was tested under EPA Contract 68-02-3125, is described in detail elsewhere (England et al, 1982). An annular swirler was mounted at the inlet of the convergent section to generate swirling flow. The swirl number was calculated to be approximately 0.39. Throat diameter was 6.8 cm which produced an exit velocity of approximately 28 m/s at 60 percent of theoretical air for 0.6 MW load. The ratio of chamber diameter to throat diameter was 8.9.

Configuration IV and V were essentially the same with the exception that configuration V did not have a swirler. Both configurations used the same

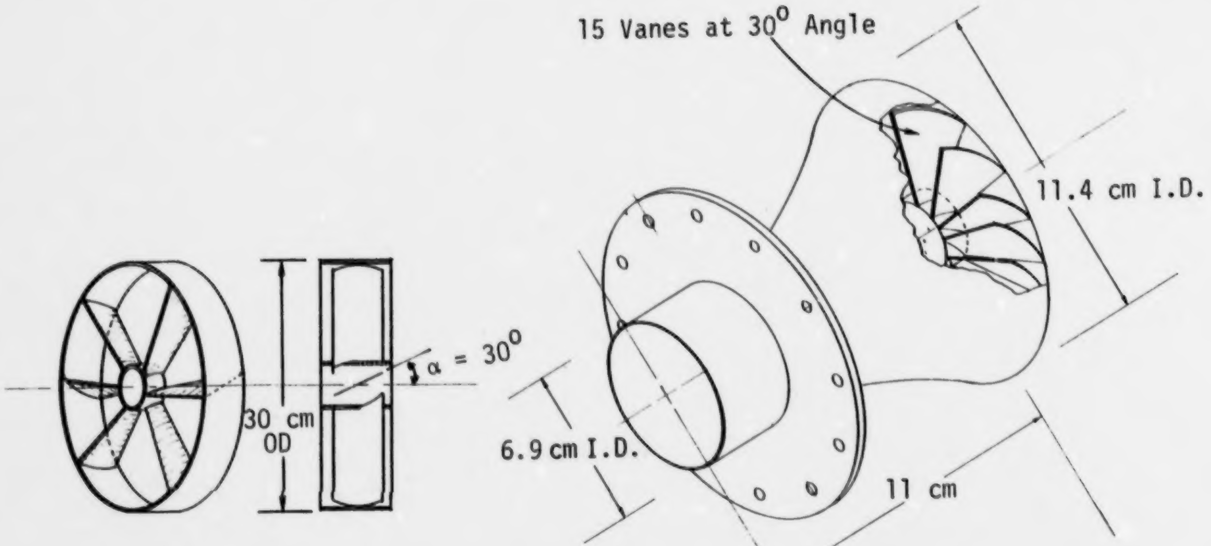
15 Vanes at 30° Angle
11.4 cm I.D.
α = 30°
30 cm
OD
6.9 cm I.D.
11 cm

(a) (b)

Figure 3-23. (a) Annular swirler used in Configuration II (SSR); (b) Primary zone fuel/air premixer (SSR).

premixing device described in Configuration III, and were mounted on a 30° half-angle divergent burner quarl.

*Large Spray Rig*

The large spray rig (LSR) shown in Figure 3-24 had essentially the same features as the small spray rig but the chamber design was octagonal in cross-section. The chamber is about 1.47 m at the smallest dimension, 2.44 m tall and was constructed of aluminum with cutouts for visual and measurement access. The chamber was mounted in an exhaust plenum which distributed exhaust to four 15.3 cm ID ducts and also served as a liquid reservoir. The fluid transport devices used in the system consisted mainly of a forced draft blower, an induced draft blower, an auxilliary fan and a gear pump. Table 3-10 summarizes the capacity of these devices.

The primary air, supplied by a forced draft blower, was fed to the burner air box through four 15.3 cm flexhoses. A butterfly valve located at the intake of the blower was used to regulate flow rate, which was measured using a pitot tube placed downstream of the blower exit. The differential pressure drop then was measured using a manometer.

The atomizing air was supplied by a central facility air compressor and flowrate was measured using a venturi. The pressure drop measured with a differential pressure gauge. The atomizing air pressure at the nozzle was set using a pressure regulator valve. Maximum atomizing air flow was 45 g/s and the maximum air pressure available at the nozzle was 550 kPa.

Water was used for the flow characterization tests in the LSR. A light oil , Hyvis 04 (BP Chemicals, Ltd), was used for the dropsize characterization tests. Table 3-11 gives manufacturer's specifications for this oil. This particular oil was chosen because of its high flash point and low volatility, which reduces the risk of accidental explosion. The viscosity of this oil closely simulates real preheated heavy oils.

Oil or water was supplied to the nozzle using a rotary gear pump. Flowrate was monitored using a rotameter and was controlled using a pressure regulator. The chamber was maintained under slightly negative pressure in order to reduce the risk of explosion or health hazard due to leakage of oil droplets into the laboratory. Screen air was to be used to prevent the

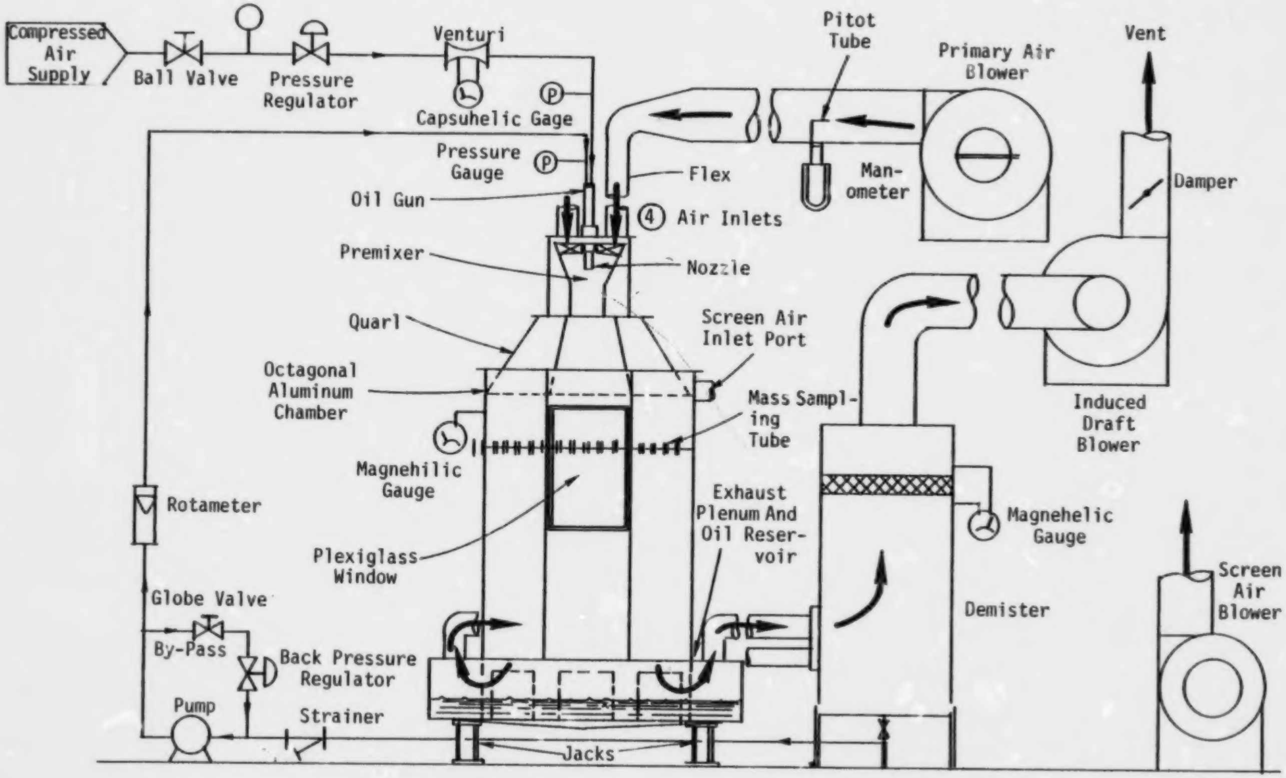
Compressed Air Supply
Ball Valve
Pressure Regulator
Venturi
Capsuhelic Gage
Pressure Gauge
Oil Gun
Flex
④ Air Inlets
Premixer
Nozzle
Quarl
Screen Air Inlet Port
Octagonal Aluminum Chamber
Mass Sampling Tube
Magnehilic Gauge
Plexiglass Window
Exhaust Plenum And Oil Reservoir
Rotameter
Globe Valve
By-Pass
Back Pressure Regulator
Pump
Strainer
Jacks
Pitot Tube
Manometer
Primary Air Blower
Vent
Damper
Induced Draft Blower
Magnehelic Gauge
Demister
Screen Air Blower

Figure 3-24. Schematic of LSR facilities.

TABLE 3-10. CAPACITY OF LSR FLUID TRANSPORT DEVICES

| Device | Type | Maximum Flow Delivery* | | | Motor Capacity | | |
|---|---|---|---|---|---|---|---|
| | | Flow* | Pressure | RPM | kW | RPM | Voltage (AC) |
| Forced Draft Blower | Radial Blade (Belt Drive) | 3.2 $m^3/s$ | 3.6 kPa | 1770 | 18.6 | 1770 | 460 |
| Induced Draft Blower | Radial Blade (Belt Drive) | 3.1 $m^3/s$ | 2.0 kPa | 2250 | 14.9 | 1765 | 460 |
| Screen Air Blower | Forward Curve (Belt Drive) | 3.1 $m^3/s$ | 0.3 kPa | 553 | 2.2 | 1745 | 460 |
| Pump | Rotary Gear (Direct Drive) | 1.02 kg/s | 690 kPa | 1725 | 2.2 | 1725 | 460 |

*Flow delivery at speed and pressure shown.

TABLE 3-11. PROPERTIES OF HYVIS 04 OIL

| | |
|---|---|
| Molecular Mass | 300 (number average) |
| Kinematic Viscosity | |
| at 98.9°C | 4.8 cSt (42 SSU) |
| at 37.8°C | 27 cSt (128 SSU) |
| Flash Point | 115°C |
| Pour Point | -50°C |
| Specific Gravity | 0.835 |
| Refractive Index | 1.471 |
| Color (Hazen) | 50 |
| Acid Number | 0.02 |
| Inorganic Chloride | <2 ppm |
| Organic Chloride | 50 ppm |
| Bromine Number | 55 |
| Water | 40 ppm |
| Sulfur | <1 ppm |
| Iron | <1 ppm |

smaller droplets from recirculating back into the spray and biasing droplet size distribution measurements.

Table 3-12 presents a general description of the three burner configurations tested in the large spray rig. Configuration I was a scaled-up version of the fuel/air premixer tested in the small spray rig, mounted onto a $45^{0}$ half-angle octagonal quarl (Figure 3-25). The calculated swirl number for this assembly is 0.39. This premixer was scaled from 1 MW to 18 MW by maintaining the same axial exit velocity of the small premixer, approximately 20 m/s at 60 percent of theoretical air flow. The swirl generator was scaled up based on geometric similarity criteria; therefore, the swirl number was similar.

Configuration II is similar to Configuration I except that swirl level was reduced by removing some of the vane blades from the original swirler. The swirl number for Configuration II was approximately 0.29. Configuration III has the same swirl configuration as Configuration I but was attached to a zero-angle (parallel exit) quarl.

Two full-scale twin-fluid atomizers were tested in the LSR, a commercial ultrasonic nozzle (similar to the atomizer which proved most successful in terms of atomization quality at small scale), and an experimental Y-jet nozzle (Figure 3-26).

In the ultrasonic nozzle, the atomizing air is conveyed down the axis of the nozzle and the liquid is introduced downstream of the throat of a converging-diverging section. The atomization occurs in the high-shear region where the sheet of liquid and high-velocity air stream come into contact. The ultrasonic nozzle design incorporates a hollow cap placed downstream of the nozzle exit which, according to the manufacturer's claims enhances atomization by creating a standing shock wave which breaks up large droplets as they pass through. Dropsize measurements conducted on small-capacity nozzles (up to 21 g/s capacity) of similar design showed only a minor change in dropsize when the resonator cap was removed (Seeker et al, 1982; Payne et al, 1979). The measurements of dropsize with the ultrasonic nozzle reported in this section are without the resonator cap. The design of the full-scale experimental Y-jet nozzle was based on the twin-fluid atomizer design criteria suggested by Mullinger et al (1974). The atomization process

TABLE 3-12. BURNER CONFIGURATIONS TESTED IN LSR

| Configurations | Geometry | Swirl Generator | Throat Diameter | Nozzle | Remarks |
|---|---|---|---|---|---|
| 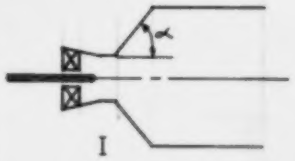 | Divergent<br>$\alpha = 45^0$ | Yes<br>S = 0.39 | 35 cm | 1) Sonicore 375-T<br>2) $60^o$ Y-Jet | |
| 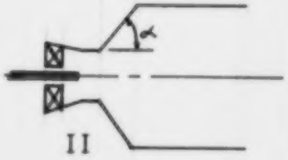 | Divergent<br>$\alpha = 45^0$ | Yes<br>S = 0.29 | 35 cm | 1) Sonicore 375-T<br>2) $60^0$ Y-Jet | |
| 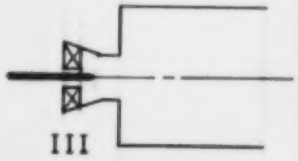 | Cylindrical | Yes<br>S = 0.39 | 35 cm | 1) Sonicore 375-T<br>2) $60^0$ Y-Jet | |

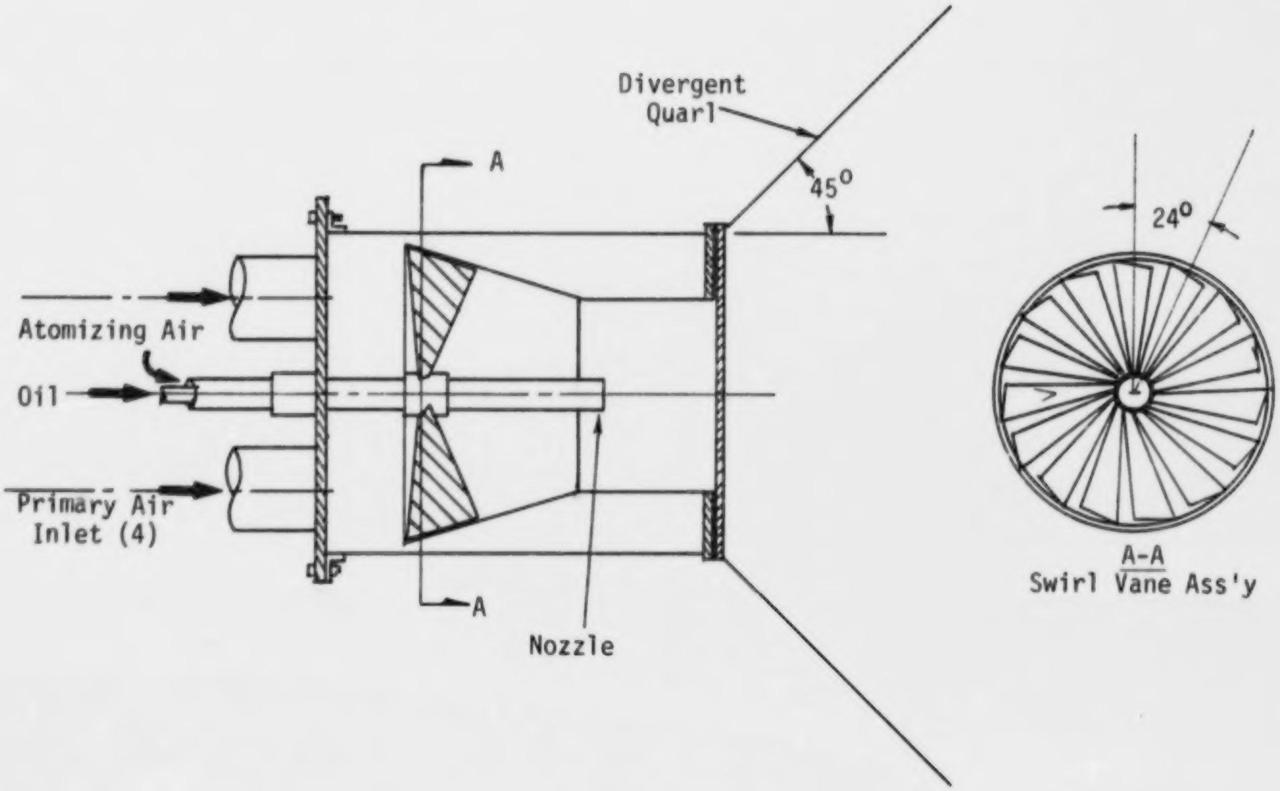
Divergent Quarl
45°
A
A
24°
Atomizing Air
Oil
Primary Air Inlet (4)
Nozzle
A-A
Swirl Vane Ass'y

Figure 3-25. 18 MW-equivalent premixer used in LSR tests.

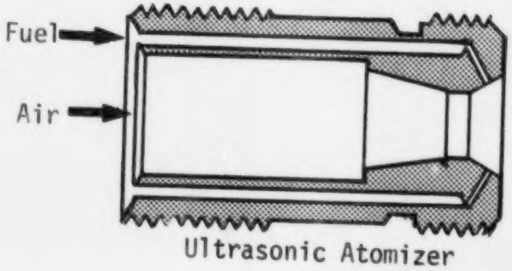
Fuel
Air
Ultrasonic Atomizer

| Nozzle | Max. Flow | kPa |
|---|---|---|
| Ultrasonic | 0.47 kg/s | 413 |
| Y-Jet | 0.47 kg/s | 620 |

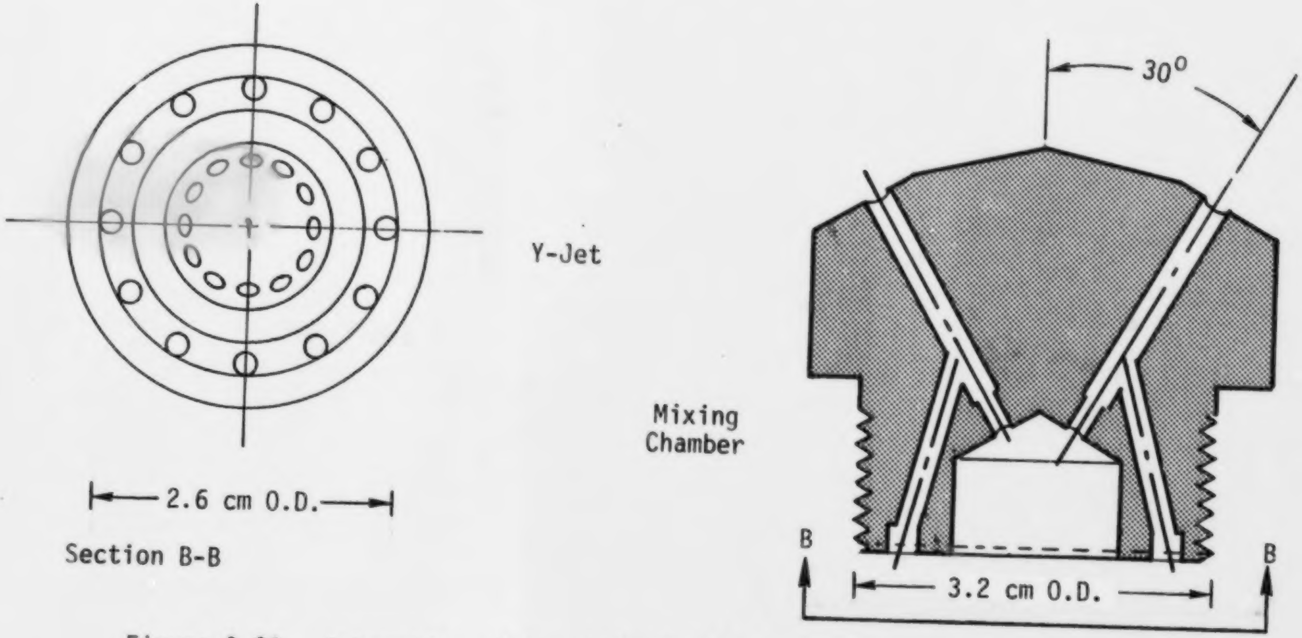
2.6 cm O.D.
Section B-B
Y-Jet
30°
Mixing Chamber
B
B
3.2 cm O.D.

Figure 3-26. Schematics of two twin-fluid nozzles characterized.

takes place in a Y-jet nozzle at the point where an oil jet and steam (or air) jet impinge at less than a 90-degree angle (hence the name). The oil and atomization fluid are emulsified in a mixing passage and exit the nozzle. The critical design parameters are the diameters of the atomizing fluid, oil, and mixing passages, and the intersection angle of the oil and atomizing fluid passages. The nozzle used in these experiments was designed approximately according to the criteria giving by Mullinger et al and has 12 passages drilled to give a 60-degree included spray angle.

### 3.2.2 Measurements

Three types of measurements were made to gain a qualitative assessment of overall mixing characteristics: flow visualization, radial spray mass distribution, and droplet size distribution.

The flow visualization measurements allowed the general mixing characteristics (spray trajectory, size of recirculation zones, etc.) of the near-burner region to be qualitatively determined. Various techniques have been developed for visualizing and quantifying the characteristics of a complex flow field. Quantitative flow mapping measurements using pitot tubes and hot-wire anemometers (McEwan, 1971) can yield information of value but tend to be very time-consuming, as a large number of measurement points are usually required. Simple flow-field visualization was achieved in these experiments by injecting tracers, such as smoke or other fine particles small enough to follow flow streamlines, and illuminating a plane across the spray chamber normal to the cross-section using a slit light. Boron trifloride was used as a tracer in the 1 MW-equivalent studies, and was injected with a lance at various points. A combination of the atomized water spray from the nozzle (at reduced flow rates) and streamers on the end of a piece of wire was used for flow mapping. The emphasis of the measurements was on defining the boundaries of reverse-flow zones. The measurements were recorded through sketches, presented in these results.

The second measurement normally taken was radial spray mass distribution. Sampling the distribution of spray mass in the complex flow field is not possible through physical sampling, and optical techniques are limited, typically by spray density. A relative impression of the spray pattern was obtained in these tests by placing an array of sampling tubes across the spray. A mass balance of input and sampled liquid could not consistently be closed (sampled liquid flowrate was generally less than input) because of nonisokinetic sampling and the presence of strong recirculation zones; however, results for a given configuration were reproducible within expected accuracy.

The sampling array for the 1 MW-equivalent spray tests consisted of seven 25-milliliter beakers evenly spaced on a support. Sampled liquid was collected and measured directly in these beakers. The 18 MW-equivalent sampling array consisted of 15 evenly spaced 1.3-cm diameter tubes attached to a support and connected by flexible tubing to a series of graduated cylinders located outside the chamber.

The results of the spray distribution measurements are presented graphically in this section as actual sampled liquid volume and area-integrated sampled volume versus radius. For comparison purposes, the ideal distribution which would result from uniformly distributing the sampled mass over the cross-section of the chamber is also shown.

Atomizer performance was determined using a commercial Malvern dropsize analyzer which is based on a laser diffraction technique (Figure 3-27). The operating principle and limitations of this instrument are discussed in detail by Swithenbank, et al (1977) and Payne, et al (1979).

The size analysis technique is based on the diffraction pattern produced as particles move through a collimated beam of monochromatic light produced by a low-power laser. The droplet cloud causes a deflection of a portion of the collimated beam and produces a conical pattern of diffracted light. Since there is a direct relation between the diameter of the particle (assumed spherical) and the solid angle of the light diffracted by this particle, it is possible to evaluate the diffracted light energy distribution, and thereby calculate the size distribution of a cloud of particles.

Droplet size distribution is given for this particular instrument in terms of the Rosin-Rammler law,

$$R = e^{-\left(\frac{X}{PE}\right)^{W}}$$

where R is the weight or volume fraction of droplets greater than size X, PE is the Rosin-Rammler mean diameter and W is the Rosin-Rammler exponent. As W

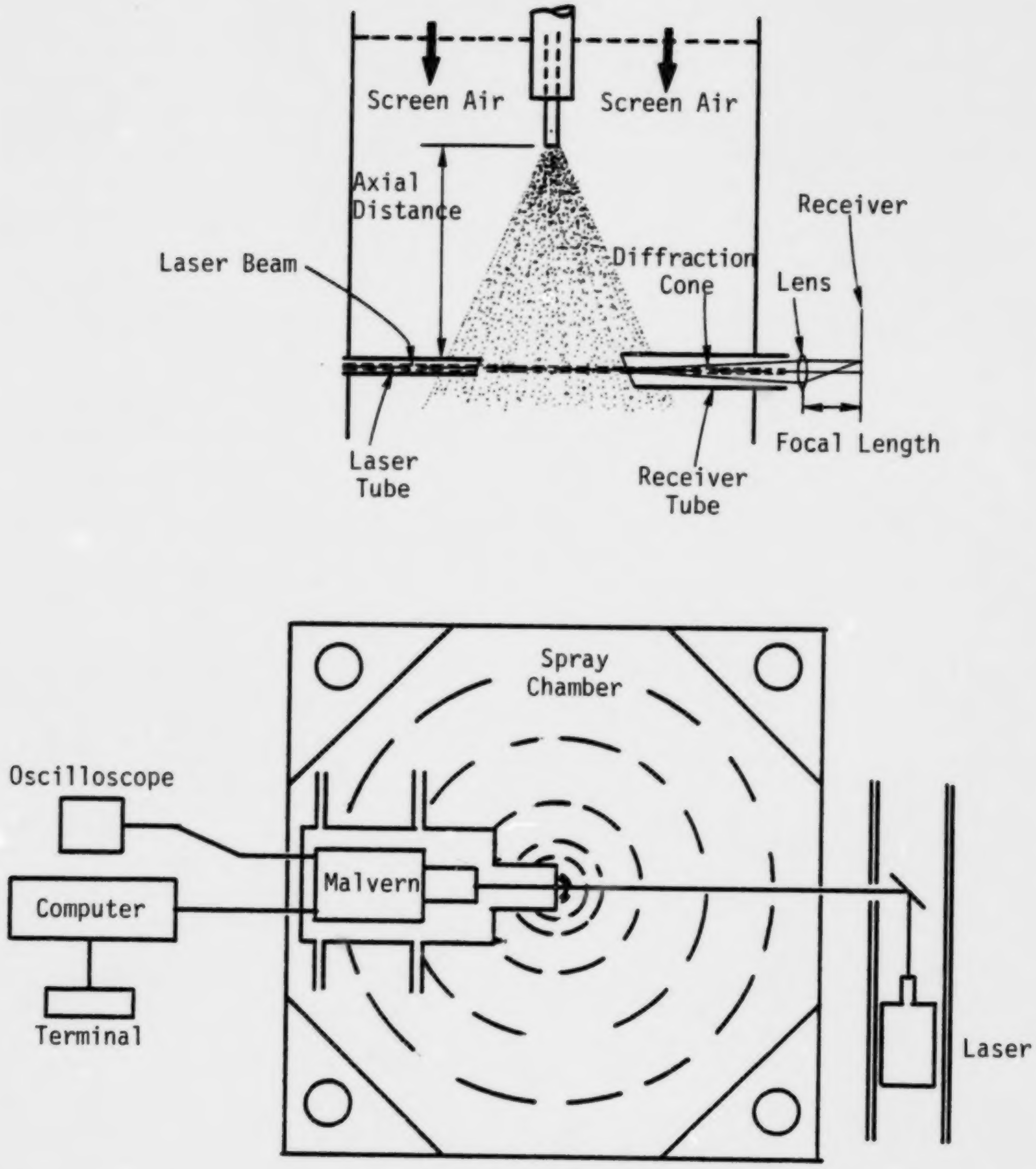
Screen Air
Screen Air
Axial Distance
Receiver
Laser Beam
Diffraction Cone
Lens
Laser Tube
Focal Length
Receiver Tube
Spray Chamber
Oscilloscope
Malvern
Computer
Terminal
Laser

Figure 3-27. Installation of laser diffraction system.

increases the breadth of the size distribution decreases. The primary limitations to the technique are a minimum dropsize threshold (5.7 μm for the present arrangement), and spray density where the scattered signal is weak. The instrument provides a line-of-sight average size along the measurement axis and does not provide velocity information.

### 3.2.3 Flow Test Results

The test conditions were designed to match selected operating conditions of the 1 MW prototype low-$NO_x$ burners. The conditions ranged from primary air flow equivalent to 55 percent to 70 percent of theoretical air required for 0.6 MW load, at which minimum $NO_x$ emissions were obtained. The test conditions for each burner configuration are summarized in Table 3-13.

#### 3.2.3.1 1 MW Equivalent

Flow patterns measured at two swirl levels for a low exit velocity divergent burner configuration are compared in Figure 3-28. The axial exit velocity at the burner throat was 1.8 m/s. At zero swirl, only mild external recirculation at the end of the divergent was observed, the major feature being a fairly uniform, gentle flow. The rate of mixing is apparently very slow for this configuration. Adding swirl (swirl number = 0.4) increased the strength of external recirculation eddies near the divergent exit. No central recirculation was seen.

The flow pattern produced with a cylindrical burner quarl, high exit velocity (approximately 28 m/s), and swirl is presented in Figure 3-29. An annular recirculation zone was clearly visible and the central air stream was rapidly entrained into the recirculation stream. At the very top of the burner, strong circular motion flow was observed. No central reverse zone was found for this particular configuration.

Figure 3-30 compares the effect of swirl level with a $30^o$ half-angle divergent burner quarl and high-exit velocity. The axial exit velocity was about 27 m/s. At zero swirl (Figure 30a), the central jet penetrated far into the chamber, much as a free jet. Mild external recirculation was induced surrounding the jet.

When swirl was applied, a central recirculation zone was induced (Figure 30b). The central air stream rapidly expanded and eddies were formed

## TABLE 3-13. TEST CONDITIONS INVESTIGATED IN SMALL-SCALE SPRAY RIG (SSR)

| | | Test Conditions | | | | |
|---|---|---|---|---|---|---|
| | Configuration | I | II | III | IV | V |
| Flow Visualization Tests | Primary Air Flow ($m^3/s$) | 0.093;0.1;0.12 | 0.093;0.1;0.12 | 0.093;0.1;0.12 | 0.093;0.1,0.12 | 0.093;0.1;0.12 |
| | Atomizing Air Pressure (kPa) | 1.45 | 1.45 | 1.45 | 1.45 | 1.45 |
| | Nozzle Position (cm)* | 0 | 0 | 0 | 0 | 0 |
| Spray Distribution Tests | Primary Air Flow ($m^3s$) | 0.093;0.1;0.12 | 0.093;0.1;0.12 | 0.093;0.1;0.12 | 0.093;0.1;0.12 | 0.093;0.1;0.12 |
| | Liquid Flow (kg/s) | $1.47 \times 10^{-2}$ | $1.47 \times 10^{-2}$ | $1.47 \times 10^{-2}$ | $1.47 \times 10^{-2}$ | $1.47 \times 10^{-2}$ |
| | Sampling Location (cm)† | 40.6 | 40.6 | 20.3;25.4;40.6 | 40.6 | 40.6 |
| | Atomizing Air Pressure (kPa) | 1.45 | 1.45 | 1.45 | 1.45 | 1.45 |
| | Nozzle Position (cm)* | 0 | 0 | 0;-3.8 | 0;-3.8 | 0;-3.8 |

*Position relative to burner throat exit.

†Axial distance from burner throat exit.

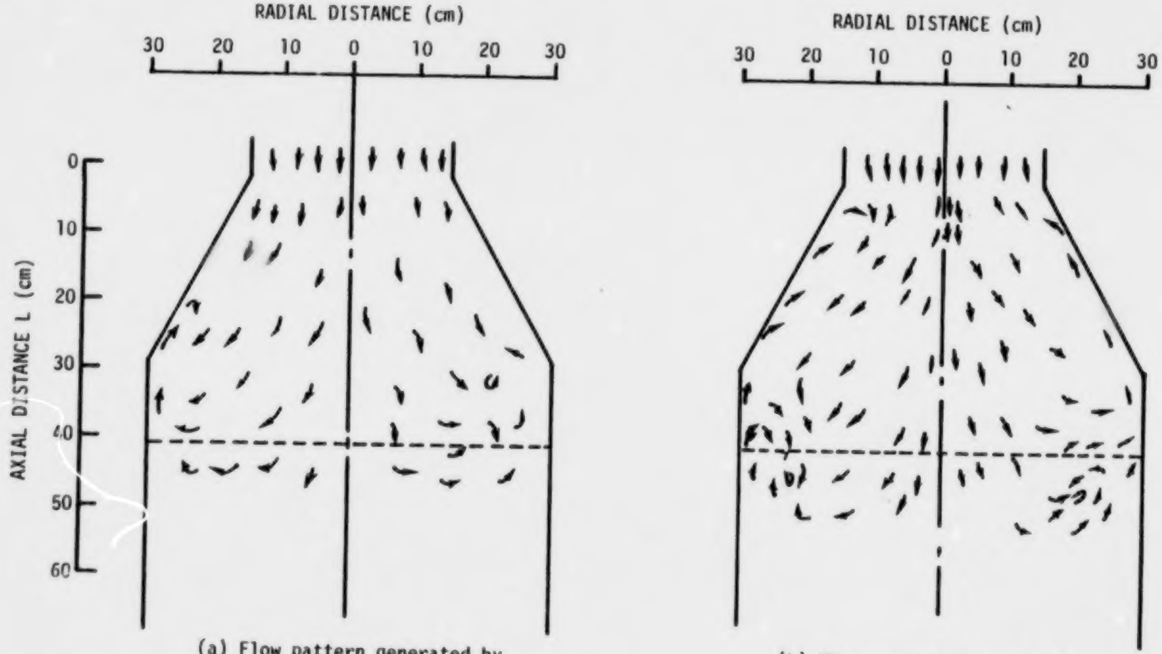

(a) Flow pattern generated by Configuration I (S=0)

(b) Flow pattern generated by Configuration II (S=0.4)

Figure 3-28. Effect of swirl levels on flow pattern generated by low exit velocity divergent burner quarl (SSR).

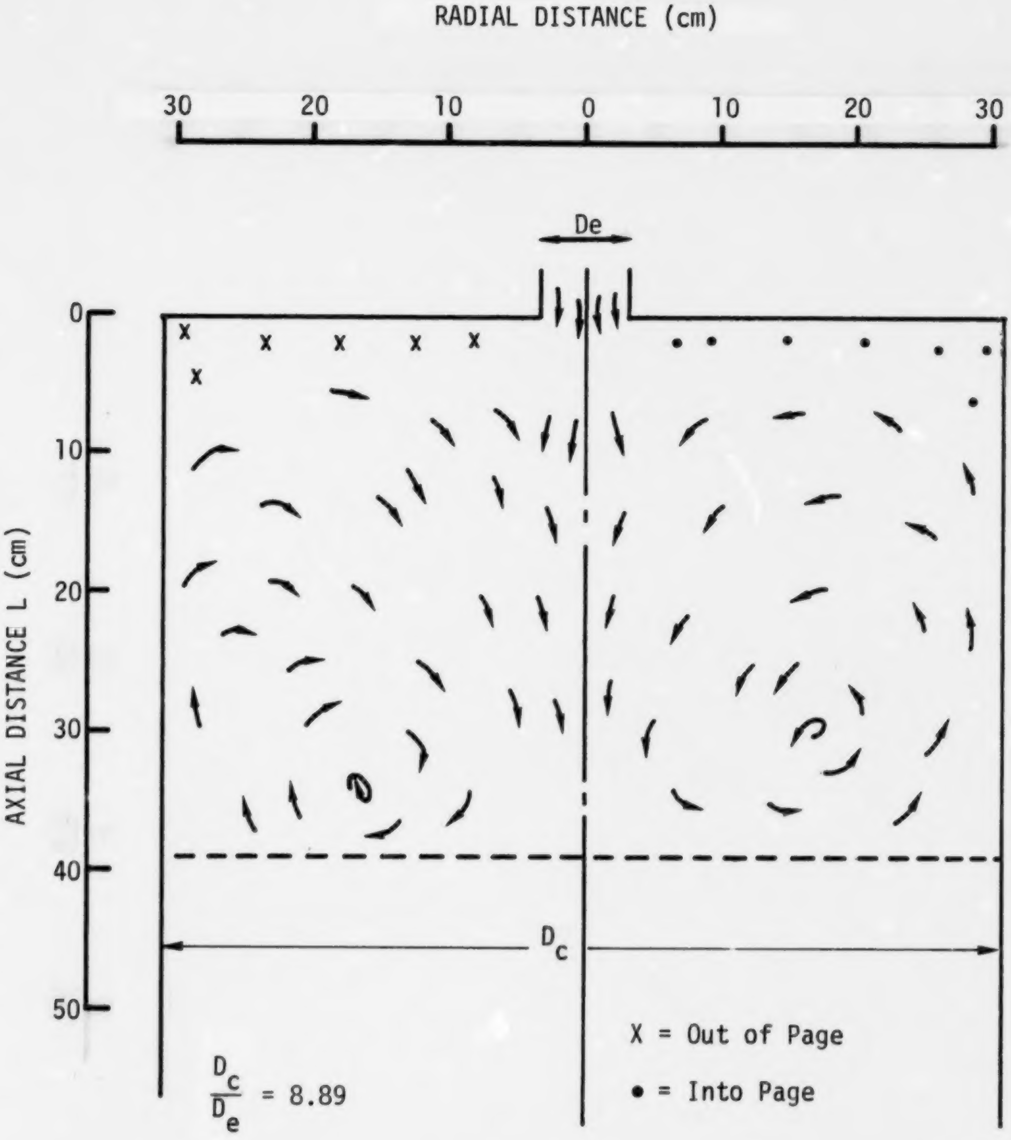
RADIAL DISTANCE (cm)
30
20
10
0
10
20
30
De
AXIAL DISTANCE L (cm)
0
10
20
30
40
50
$D_c$
$\frac{D_c}{D_e} = 8.89$
X = Out of Page
• = Into Page

Figure 3-29. Effect of the premixer on flow pattern in a cylindrical burner quarl (SSR, Configuration III).

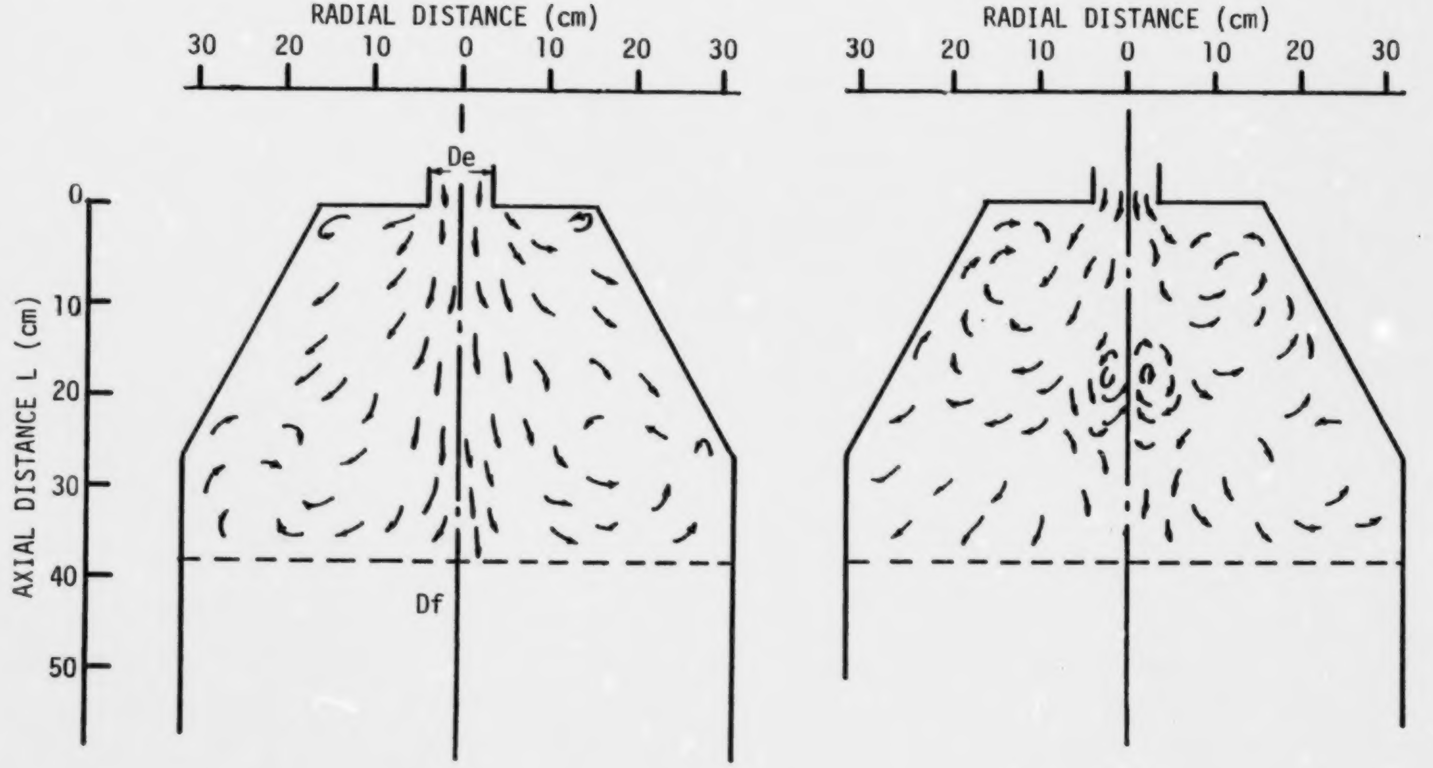
RADIAL DISTANCE (cm)
30
20
10
0
10
20
30
RADIAL DISTANCE (cm)
30
20
10
0
10
20
30
De
Df
AXIAL DISTANCE L (cm)
0
10
20
30
40
50

(a) Configuration V (S=0)

(b) Configuration IV (S=0.39)

Figure 3-30. Effect of swirl level on flow pattern generated in a high exit velocity divergent burner quarl (SSR).

near the top corner of the quarl. The flow immediately downstream of the divergent exit was much more uniform than other configurations.

All the results described above were obtained with primary air only. A second set of experiments assessed the effect on flow pattern for different burner geometries when atomizing air was also introduced. The atomizing air mass flowrate was approximately 14 g/s at 69 kPa constant pressure throughout the entire experiment.

Figure 3-31 shows the flow patterns produced by the low-velocity burner quarl at two swirl levels. It can be seen in Figure 31a that atomizing air produced very little effect on the bulk flow pattern compared to Figure 28a. In Figure 31b, when swirl was applied, the central air stream produced external recirculation zones in the narrow region of the quarl.

Figure 3-32 presents the flow pattern produced by Configuration III when atomizing air was added. It shows little difference compared to the case with no atomizing air (Figure 3-29) except that the central stream appears to push the center of the annular recirculation zones further radially away from the center line. Flow patterns produced by the addition of atomizing air for two levels of swirl in a high exit velocity divergent burner quarl are presented in Figure 3-33. The nonswirling flow case (33a) produced small eddies at the top corner of the quarl and mild annular recirculation zones near the mass sampling location. The central recirculation zone for the swirling flow (Figure 3-33b) has been displaced close to the exit of the divergent section, and the air from external recirculation is rapidly entrained into the central stream.

Variations in primary air flowrate were investigated and found to have a negligible effect on the major features of the flow pattern, but increased or decreased the intensity and sometimes the size of recirculation eddies.

Results of mass distribution measurements for the ultrasonic atomizer tested in five different burner configurations are presented in Figures 3-34 through 3-36. Measurements with the diverging quarl were made with the sampling rack positioned 41 cm from the burner exit. Measurements from the parallel exit were made 20 and 41 cm from the exit. Liquid flowrate was 14 g/s, atomizing air pressure was 69 kPa, and air flow was 6.1 $m^3/s$.

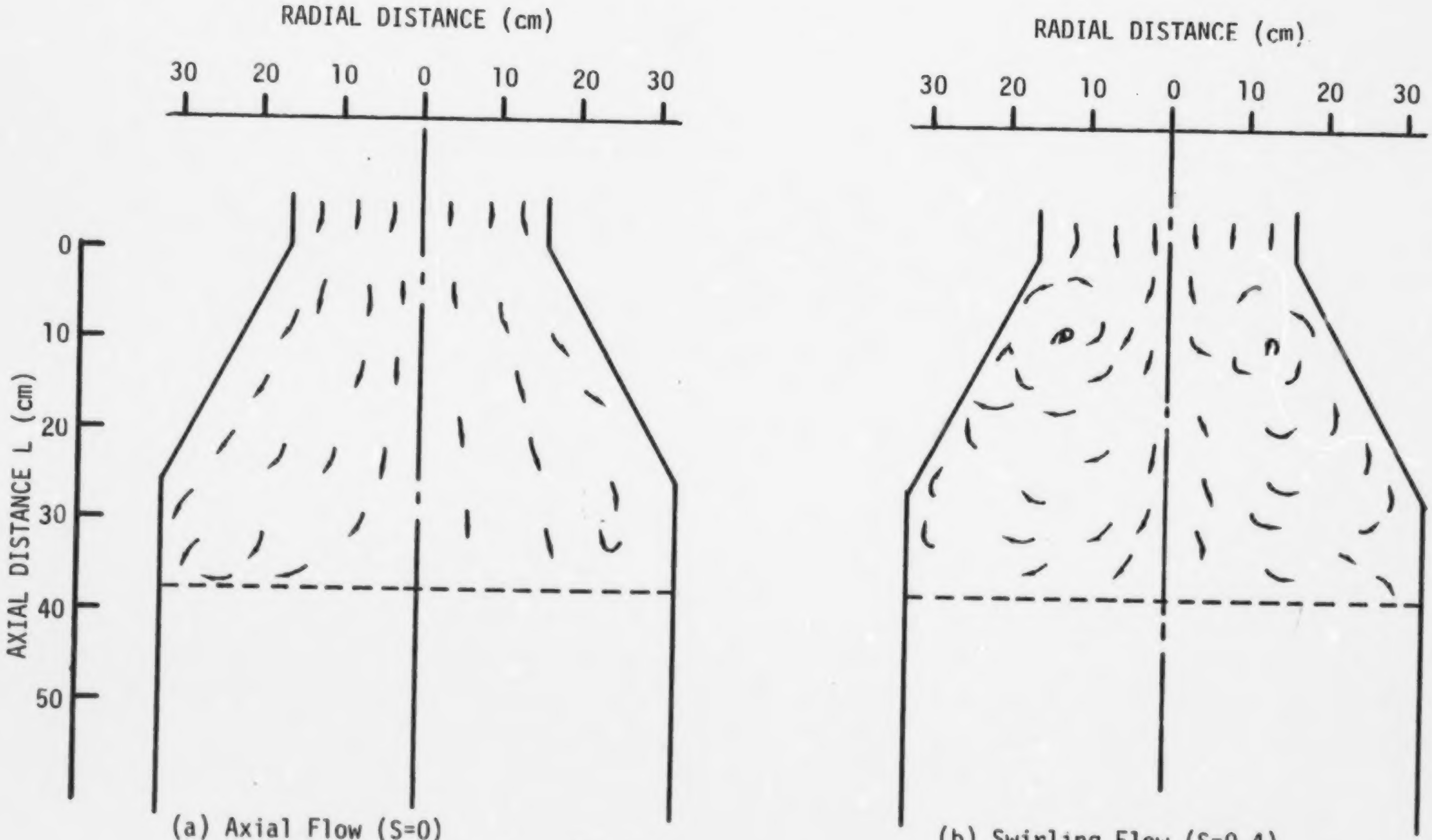
RADIAL DISTANCE (cm)
30
20
10
0
10
20
30
AXIAL DISTANCE L (cm)
0
10
20
30
40
50
RADIAL DISTANCE (cm)
30
20
10
0
10
20
30

(a) Axial Flow (S=0)
Atomizing Air Pressure = 69 kPa

(b) Swirling Flow (S=0.4)
Atomizing Air Pressure = 69 kPa

Figure 3-31. Effect of swirl level on flow pattern generated with the addition of atomizing air in a divergent burner quarl (SSR Configuration I).

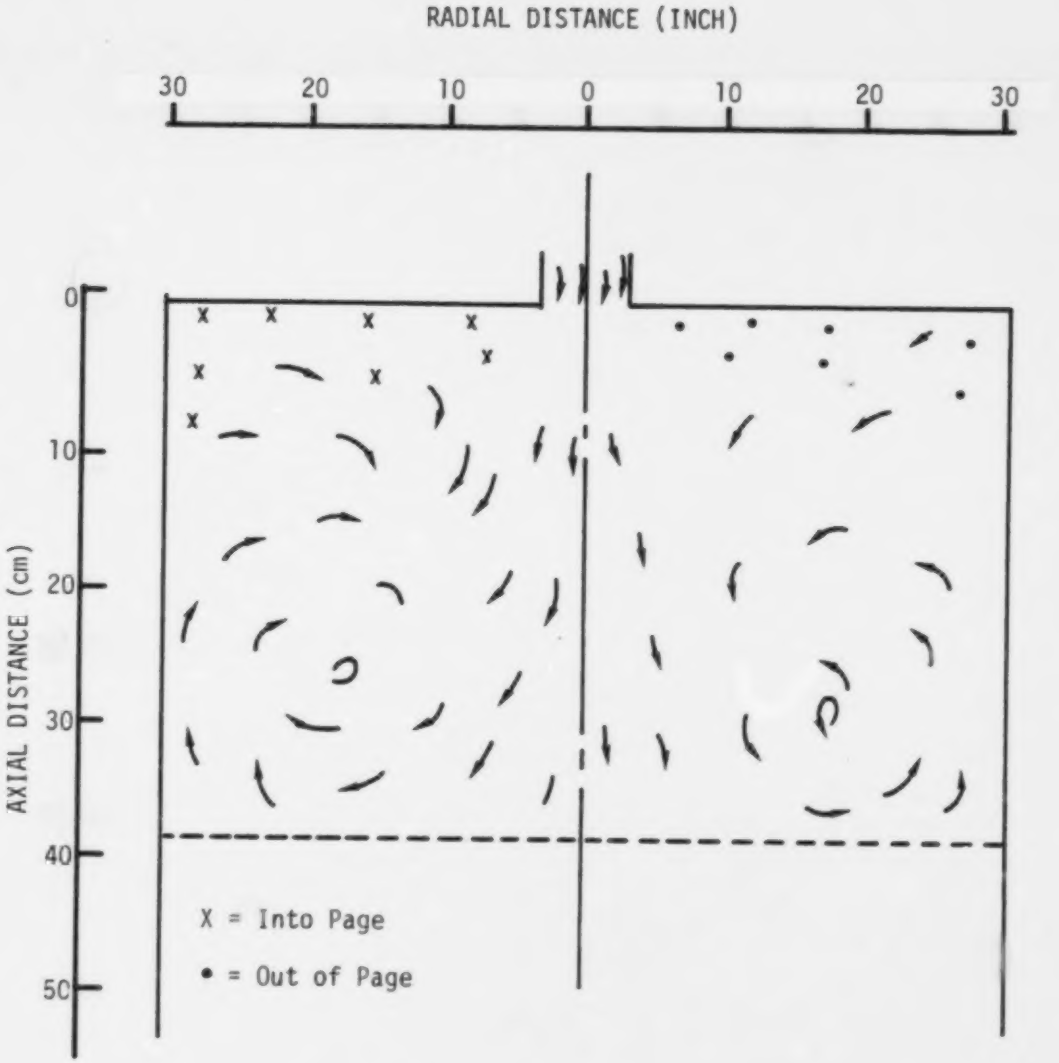
RADIAL DISTANCE (INCH)
30
20
10
0
10
20
30
AXIAL DISTANCE (cm)
0
10
20
30
40
50
X = Into Page
• = Out of Page

Figure 3-32. Flow pattern produced in a cylindrical burner quarl with the addition of atomizing air jet (SSR Configuration III).

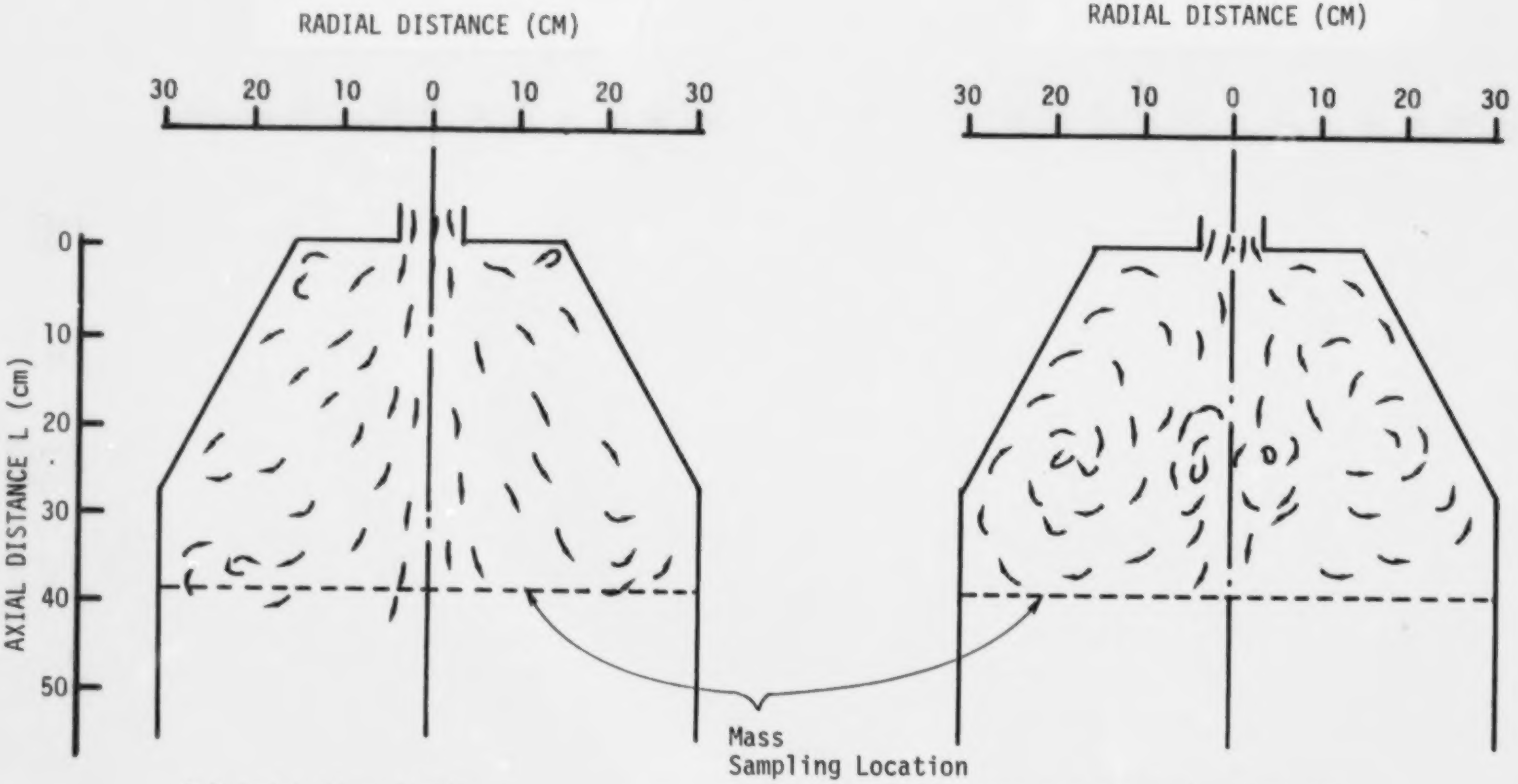
RADIAL DISTANCE (CM)
30
20
10
0
10
20
30
RADIAL DISTANCE (CM)
30
20
10
0
10
20
30
AXIAL DISTANCE L (cm)
0
10
20
30
40
50
Mass
Sampling Location

(a) Axial Flow (S=0)
Atomizing Air Pressure = 69 kPa
(SSR Configuration V)

(b) Swirling flow (S=0.39)
Atomizing Air Pressure = 69 kPa
(SSR Configuration IV)

Figure 3-33. Effect of swirl level on flow pattern with the addition of atomizing air stream in a high exit velocity divergent burner quarl (SSR).

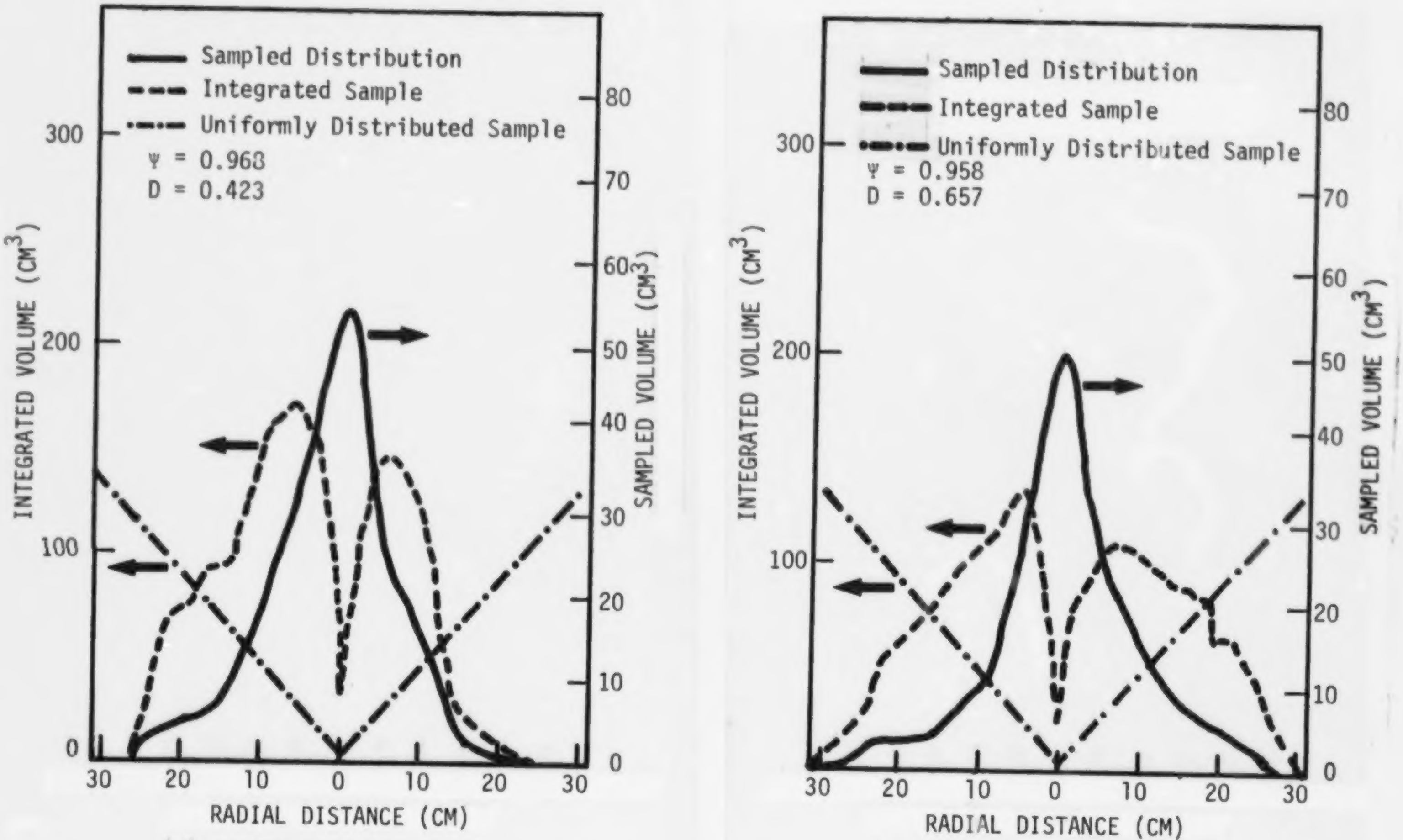

(a) Configuration I (S=0)

(b) Configuration II (S=0.4)

Figure 3-34. Influence of swirl level on spray distribution in a low exit velocity burner (SSR).

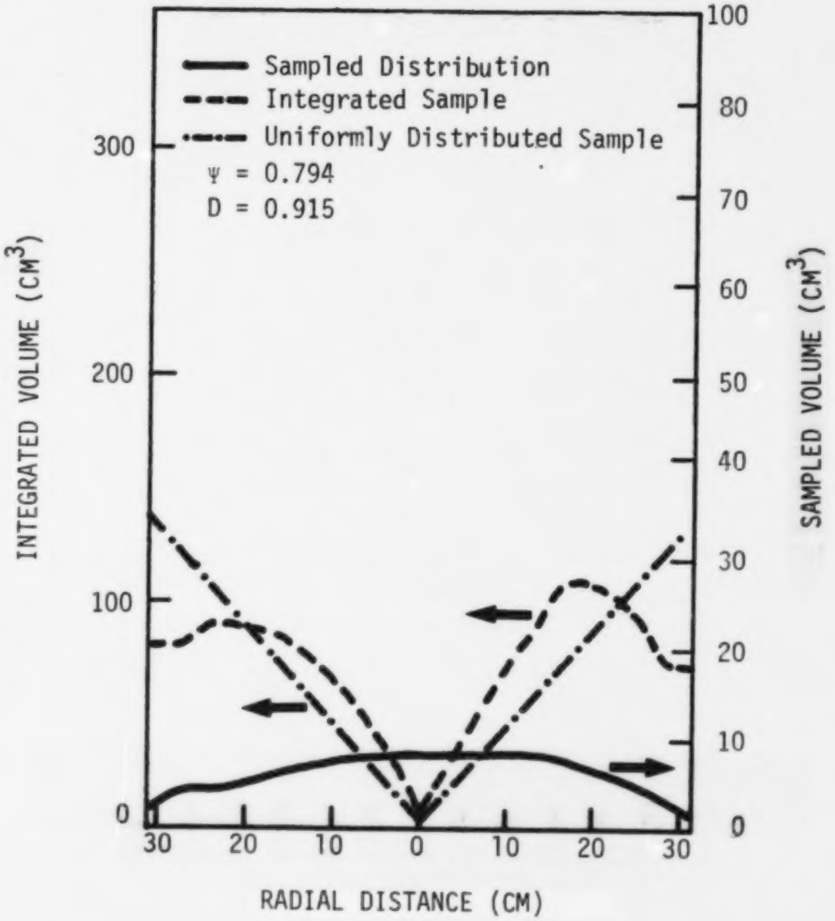

Figure 3-35. Spray distribution for a cylindrical burner quarl (SSR Configuration III).

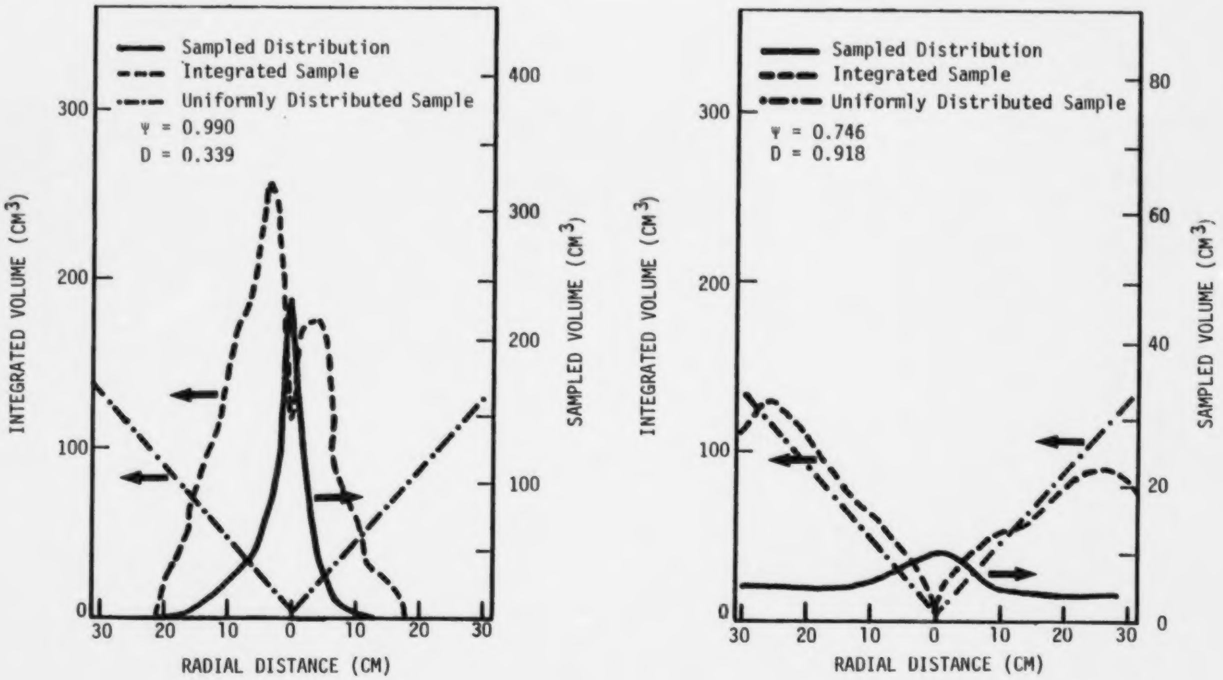

(a) Configuration V (S=0)

(b) Configuration IV (S=0.39)

Figure 3-36. Effect of swirl level on spray distribution in a high exit velocity divergent burner quarl (SSR).

Sample distribution data were normalized to account for discrepancies in input versus collected sample volume. The normalized integrated distribution is generated by integrating the measured liquid volume over the cross-sectional area (1/2 annular section) at the sampling location as a function of radial distance. The integrated curve is normalized by a factor $\psi$

$$\psi = \frac{V_c}{V_l}$$

where $V_c$ is the volume of liquid collected in the sample tubes per unit time integrated over cross-sectional area and $V_l$ is the input liquid flowrate.

The integrated distribution which results if the sample were uniformly distributed over the chamber cross-section is also shown in the figures. A "dispersion index" D was calculated to enable comparisons between configurations, which is given by

$$D = \frac{A_m}{A_I}$$

where $A_m$ is the area of the measured distribution which lies under the ideal distribution, and $A_I$ is the area of the ideal distribution. This index provides a simple relative measure of the uniformity of the spray distribution for different configurations, where a uniformly distributed spray corresponds to D = 1.

Figure 3-34 shows mass distribution from Configurations I and II. In the zero swirl and low throat velocity case (Configuration I) the nozzle spray remained as a concentrated jet from the exit of the burner throat to an axial distance of about 25 cm. Beyond that axial distance, the fine droplets around the spray cone began to leave the main jet stream forming a skirt-shaped spray. The sampled distribution is very narrow (Figure 3-34a); the entire spray concentrated within a diameter of about 20 cm. The normalized integrated distribution shows that the main mass flow of the spray is concentrated within a radius of 13 cm. Calculated dispersion index is approximately 0.42. The normalization factor (fraction of input mass flow recovered) for this configuration is calculated to be 0.97. Appreciable improvement in the spray distribution was obtained when swirl was applied (Figure 3-34b). The integrated distribution is slightly more spread out and tended to cover the whole chamber area. The dispersion index of 0.66 indicates that the mass is indeed more evenly distributed. The central spray jet appeared to break up and mix with the bulk flow very rapidly.

Spray distribution from the high-velocity premixer assembly with moderate swirl and the cylindrical exit geometry (Configuration III, Figure 3-35) was much more uniform than the divergent exit, low-velocity case (Configuration II--Figure 3-34b). Both sampled and integrated volumes indicated much faster radial mixing than the previous configuration. The dispersion factor D for this case was 0.92, which means the distribution is close to being uniform. The normalization factor was low, since much of the spray collected on the walls of the chamber in this case.

In Figure 3-36 (high-velocity, divergent quarl) it can be seen that when the swirl vanes were removed from the premixer assembly (Figure 3-36a, Configuration V) the uniformity of the spray decreased dramatically. The jet issuing from the throat penetrated far into the chamber without mixing into the surrounding stream. This is evident from the high sample concentration along the radial centerline. Hence it would appear that the optimum primary configuration (i.e., the one with "D" closest to unity) was Configuration IV, consisting of the premixer assembly with swirl vanes and with moderate swirl. It should be noted, however, that the mass balance was also poor in this configuration, and this was attributed to spray impingement on the walls of the spray rig.

### 3.2.3.2 18 MW-Equivalent Test Results

The test conditions for this series of tests are summarized in Table 3-14. The tests investigated the primary air/fuel mixing with 50 percent to 60 percent theoretical air flow required at 18 MW load. The effect of atomizing air pressure and liquid flowrate was also investigated.

Figure 3-37 shows the flow patterns produced by three configurations tested with throat exit velocity of 27 m/s. The divergent quarl with swirl number = 0.39 (Figure 3-37a) shows that the flow from the throat was rapidly entrained in the external recirculation zones. A small internal recirculation zone was observed at this swirl level. The mild internal recirculation zone was eliminated by decreasing swirl number to 0.29 (Figure 3-37b), and the external recirculation eddies were replaced by an almost purely tangential

## TABLE 3-14. TEST CONDITIONS INVESTIGATED IN LARGE-SCALE SPRAY RIG (LSR)

a) Flow Visualization

| Burner Configuration | Air Velocity at Throat (m/s) | Atomizing Air Pressure (kPa) |
|---|---|---|
| I, II, III | 24.4 to 27.4 | 5.8 |

b) Spray Distribution (measured 41 cm from throat exit)

| Burner Configuration | Atomizer | Air Velocity at at Throat (m/s) | Atomizing Air Pressure (kPa) | Water Flowrate (kg/s) | Nozzle Position* (cm) |
|---|---|---|---|---|---|
| I, II, III | Sonicore 375-T (without resonator) | 24.4 to 27.4 | 5 to 8.7 | 0.41 | -44.5 |
| I, II, III | Y-Jet $60^{0}$ Spray Angle | 24.4 to 27.4 | 5 to 8.7 | 0.41 | -25.4 |

*Nozzle position relative to burner throat exit.

c) Nozzle Characterization

| Nozzle | Atomizing Air Pressure (kPa) | Oil Flowrate (kg/s) | Axial Distance From Nozzle Tip (cm) | Radial Distance From Centerline (cm) |
|---|---|---|---|---|
| Sonicore 375T | 3.6 to 9.1 | 0.27 | 91 | 0 |
| $60^{0}$ Y-Jet | 3.6 to 9.9 | 0.1 to 0.27 | 46, 64 | 1.27 |

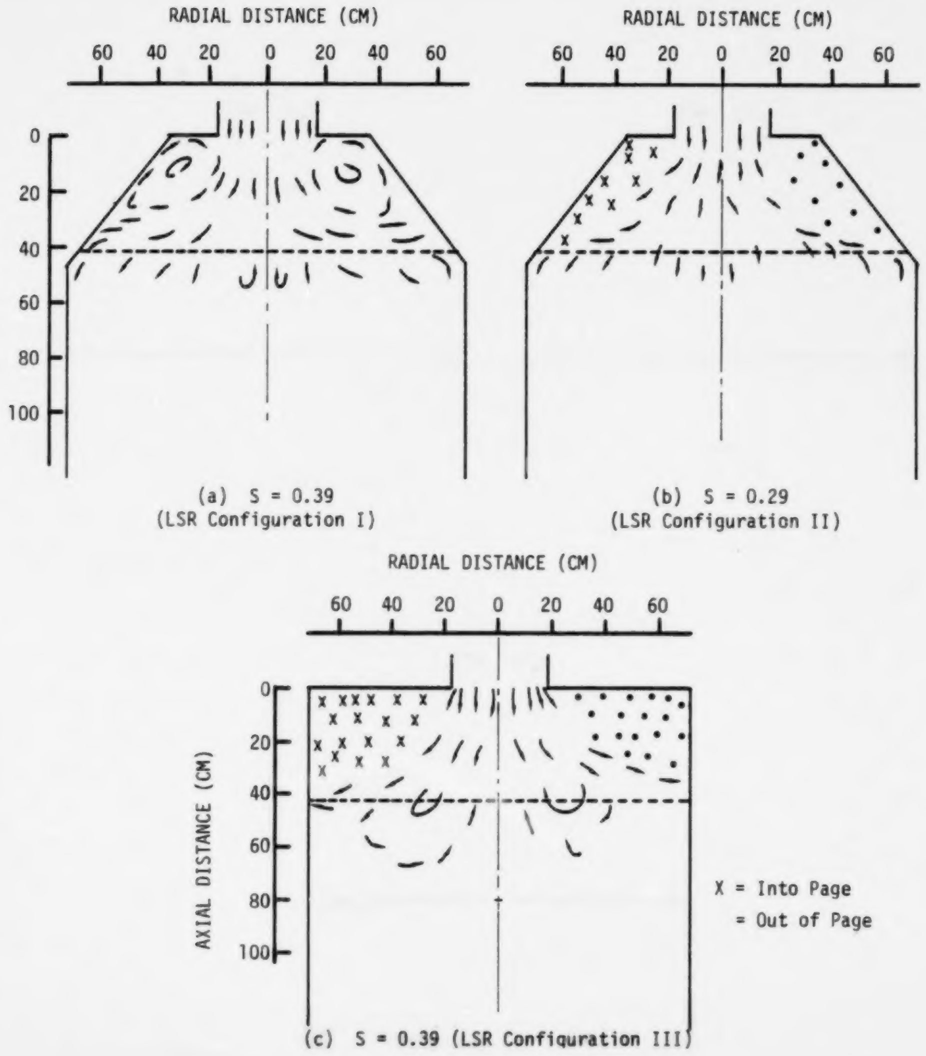
RADIAL DISTANCE (CM)
60
40
20
0
20
40
60
AXIAL DISTANCE (CM)
0
20
40
60
80
100
X = Into Page
= Out of Page

(a) S = 0.39 (LSR Configuration I)

(b) S = 0.29 (LSR Configuration II)

(c) S = 0.39 (LSR Configuration III)

Figure 3-37. EFfect of burner geometry and swirl level air flow pattern (large spray rig).

flow. Changing from divergent to cylindrical quarls caused the central recirculation zone to expand, and tangential motion near the throat is similar to the small-scale observations. Of the three configurations shown, swirl number of 0.29 with a divergent exit appeared to give the most favorable, uniform flow at the exit of the divergent.

The spray distribution using the ultrasonic nozzle corresponding to the flow pattern in Figure 3-37a is given in Figure 3-38. A very narrow, confined jet along the axis of the spray was observed 1 to 1½ throat diameters from the throat exit. Only a few of the fine droplets around the main spray flow appeared to be entrained from the central stream into the swirling flow. This is confirmed by the mass distribution measurement which indicates a strong concentration of mass close to the centerline. The dispersion index calculated is about 0.32 which suggests that relatively poor mixing was achieved with this configuration.

A similar spray pattern was produced at swirl number = 0.29 (Figure 3-39). The calculated dispersion factor was 0.21 indicating very poor premixing due to the low swirl intensity. The spray appears to be confined to a 30-cm radius from the centerline at the measurement point. Changing the exit geometry from divergent to cylindrical seemed to reduce the centerline mass peak due to the expanded central recirculation zone (Figure 3-40).

The Y-jet atomizer previously described was constructed in an attempt to improve the spray distribution over that produced by the ultrasonic nozzle. The nozzle produces a "hollow cone" spray pattern; that is, the spray is formed by a series of jets expanding away from the centerline. This behavior is exemplified by the mass distribution shown in Figure 3-41. The mass appears to peak close to the boundaries of the spray and is not entirely symmetrical. Although the spray mass is moved away from the centerline (compared to the ultrasonic nozzle) the uniformity as measured by dispersion index does not appear to be significantly improved. Figures 3-41 and 3-43 compare Y-jet spray distributions for the divergent and cylindrical exit geometry. At swirl number = 0.39, uniformity is slightly improved over the reduced swirl case shown in Figure 3-42, but the spray boundary is still very sharply defined. The cylindrical exit geometry produced the best apparent distribution using the Y-jet, with a dispersion index of 0.41. Higher atomizing narrowed the spray distribution for the ultrasonic nozzle while,

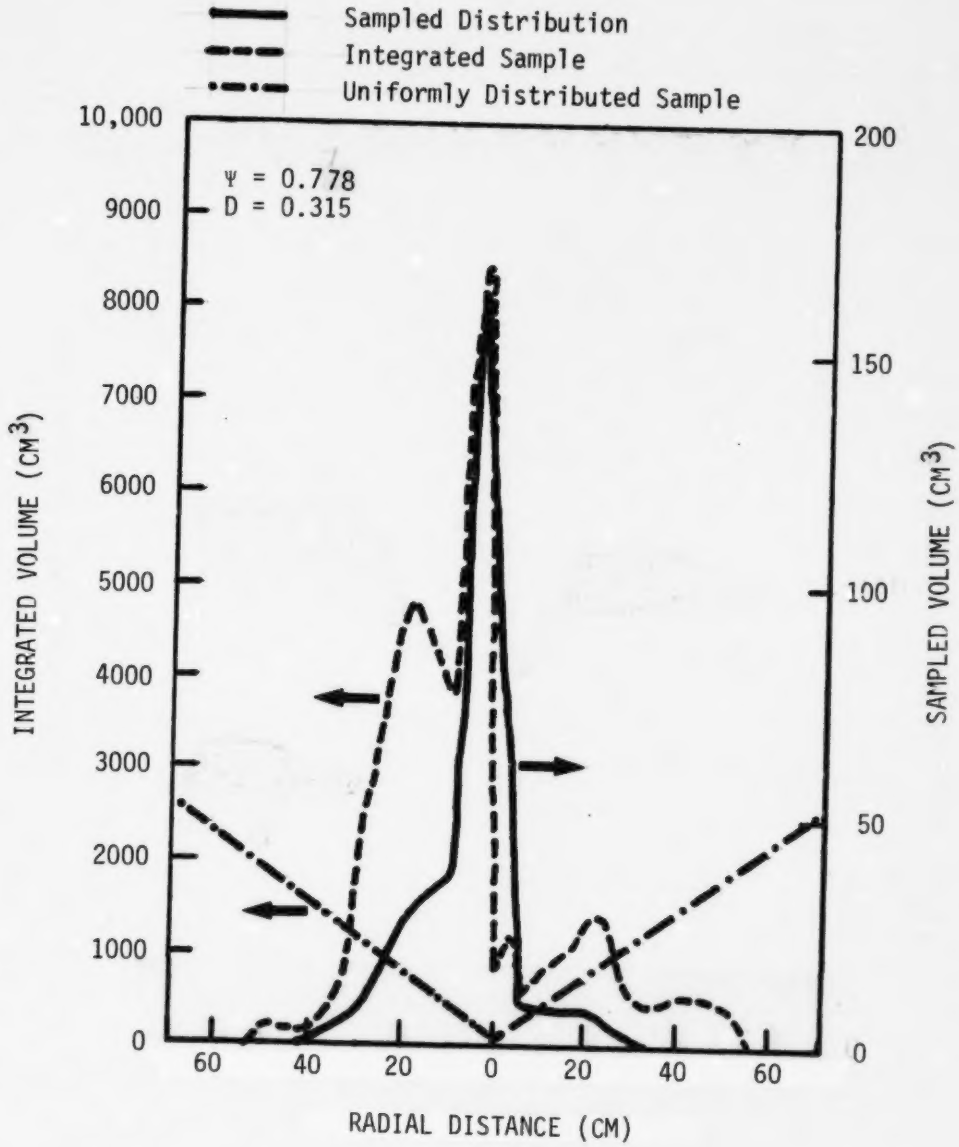

Figure 3-38. Ultrasonic atomizer-spray distribution produced with divergent burner quarl (S = 0.39 - LSR Configuration I).

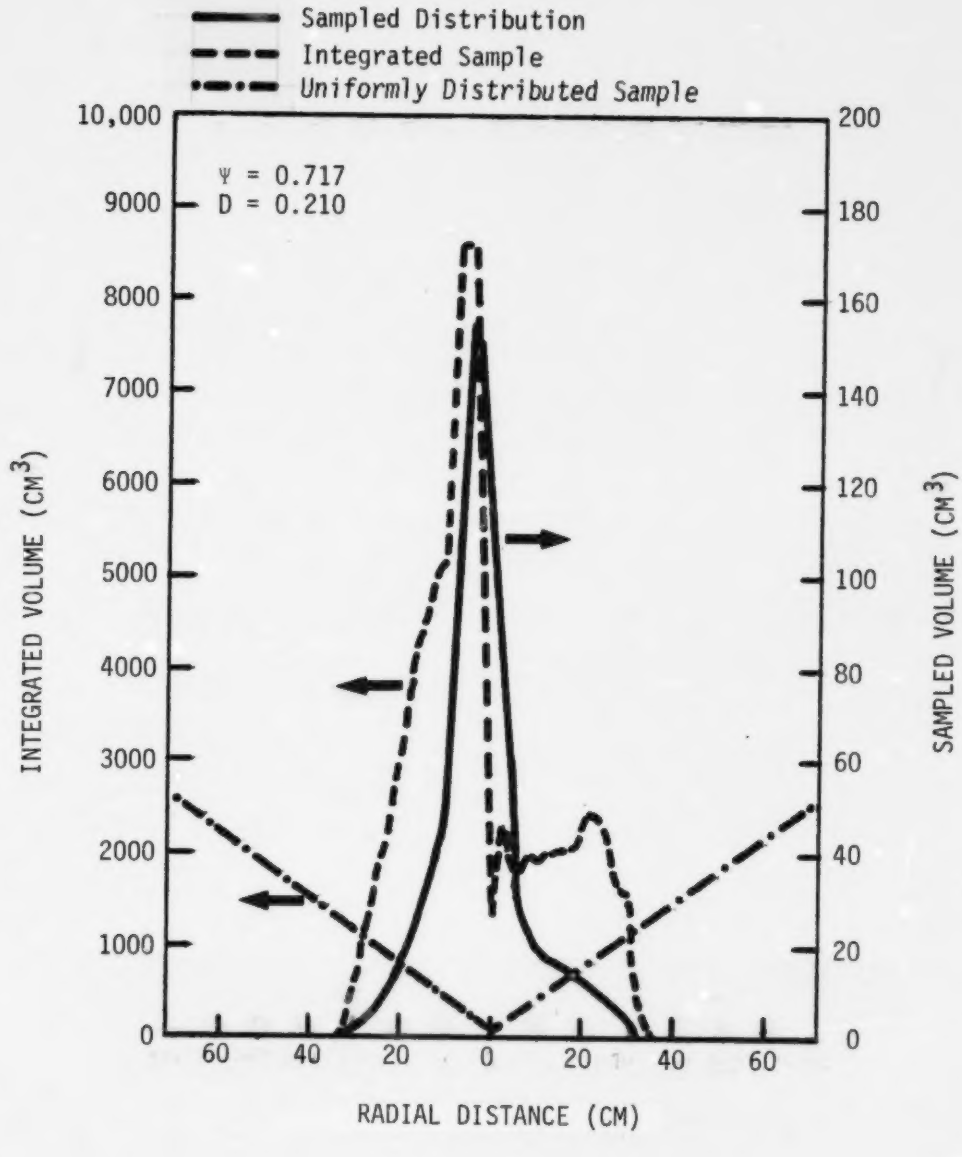

Figure 3-39. Ultrasonic atomizer-spray distribution produced with divergent burner quarl (S = 0.29 - LSR Configuration II).

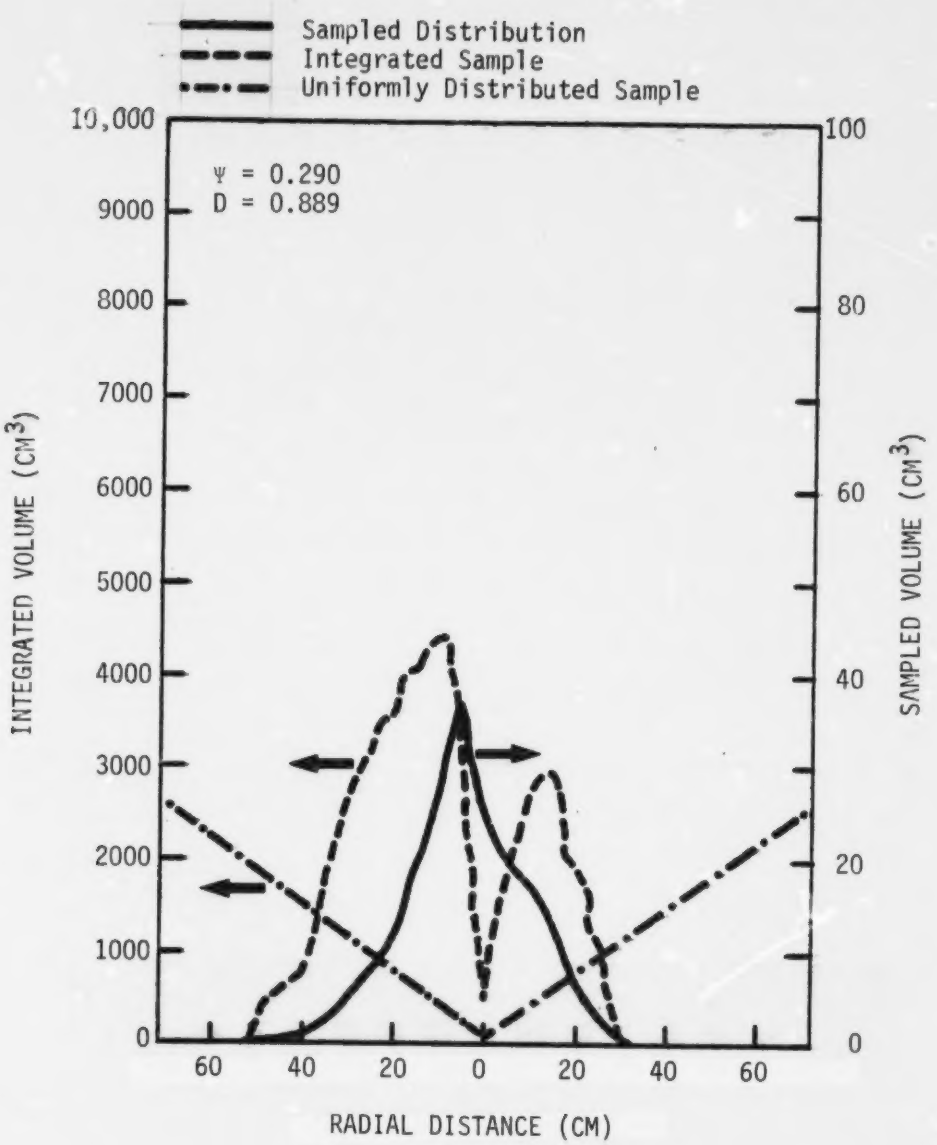

Figure 3-40. Ultrasonic atomizer-spray distribution produced with cylindrical burner quarl (S=0.39-LSR Configuration III).

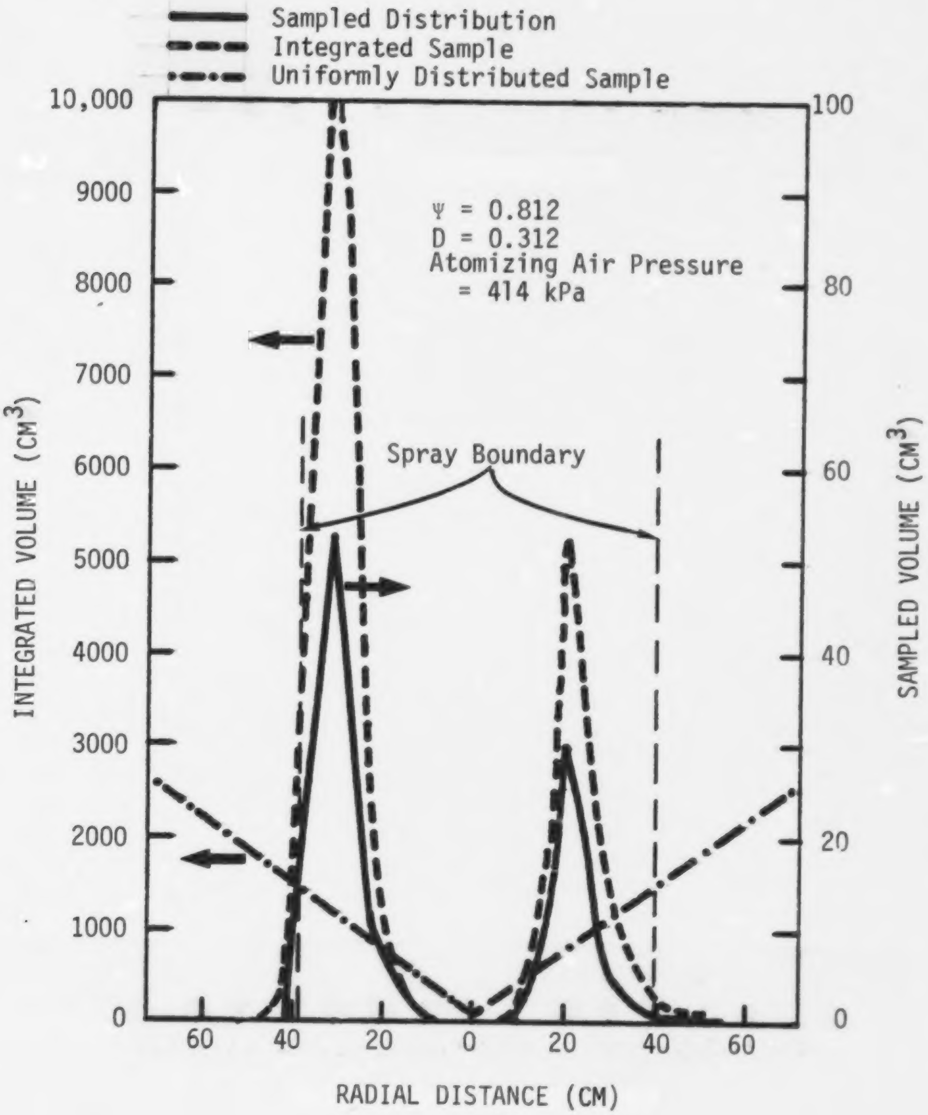

Figure 3-41. Y-Jet-spray distribution produced with divergent burner quarl (S=0.39-LSR Configuration I).

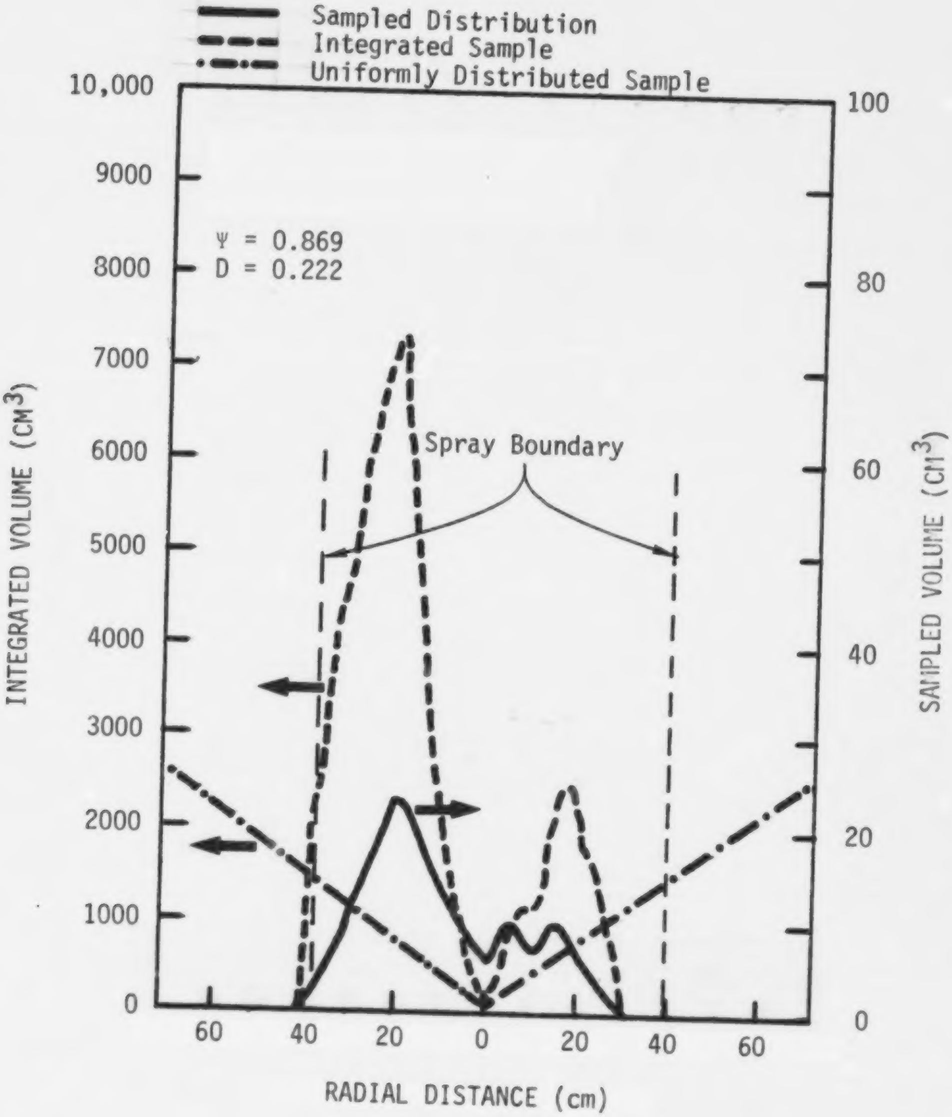

Figure 3-42. Y-Jet-spray distribution produced with divergent burner quarl (S=0.29-LSR Configuration II).

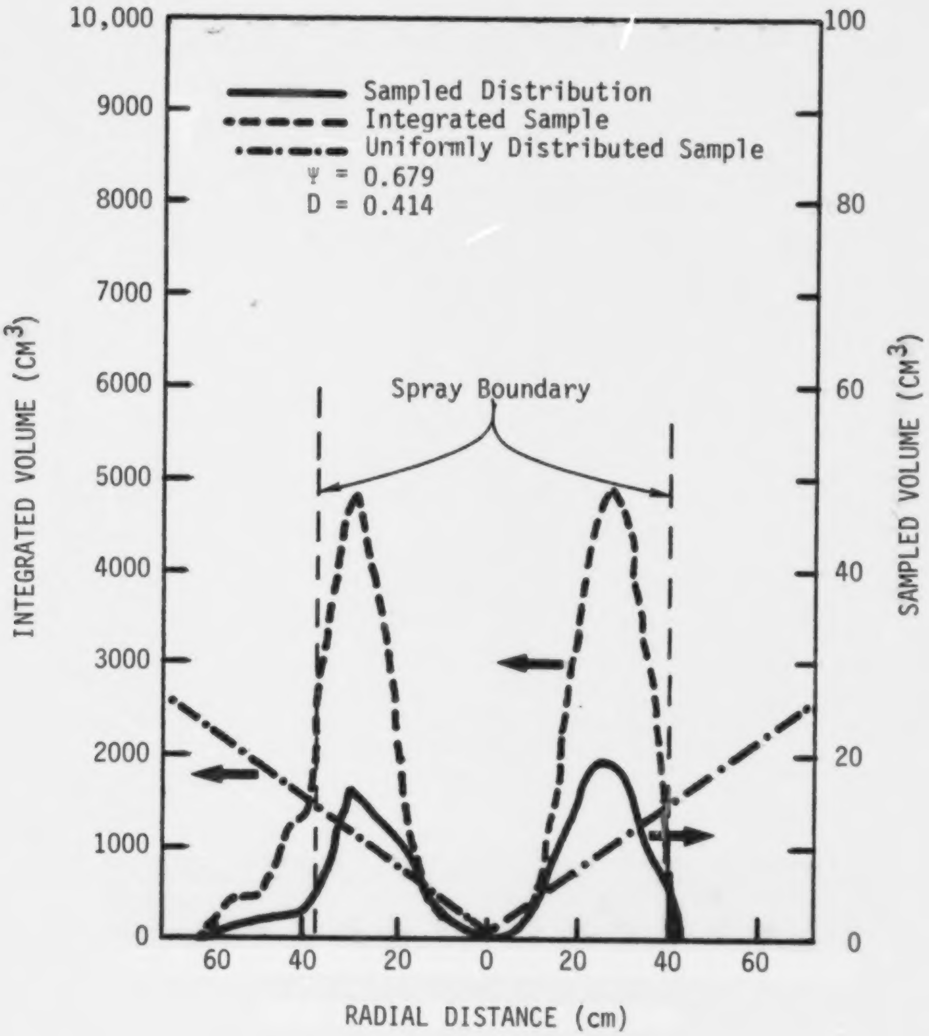

Figure 3-43. Y-Jet-spray distribution produced with cylindrical burner quarl (S=0.39-LSR Configuration III).

conversely, it broadened the spray distribution for the Y-jet (Figures 3-44 and 3-45).

### 3.2.4 Full-Scale Atomizer Performance

The influence of the atomizing air pressure on the Rosin-Rammler mean droplet diameter for the Y-jet nozzle is shown in Figure 3-46. The figure shows the mean droplet diameter measured at the centerline of the spray and 13 cm off center. The mean droplet diameter for the atomizing air pressure range tested is between 150 and 250 microns. Figure 3-47 presents the atomizing air pressure effect for the ultrasonic nozzle. Both nozzles produced similar mean dropsizes and tended to concentrate the larger droplets on the outside of the spray, as indicated by the off-centerline data.

Figure 3-48 is a plot of Rosin-Rammler mean diameter against oil flowrate at constant air pressure for the 12-hole Y-jet nozzle. The mean diameter increased roughly as the square root of the ratio of the liquid to air mass flowrate. The plot also shows calculated mean droplet diameter as a function of oil flowrate for two different viscosity levels using the empirical correlation of Wigg (1964).

### 3.2.5 Discussion

The flow patterns produced in the large scale show some differences from the small scale for equivalent scaled conditions. In the small scale, the degree of fuel/air mixing achieved was considerably higher than the large scale at similar swirl levels, throat exit velocity and burner geometry conditions (e.g., Figure 3-30 and Figure 3-37a). The internal recirculation zone observed in the small scale burner does not appear at large scale. This may be due to differences in confinement between scales. The small spray rig chamber-to-throat diameter ratio is a factor of two higher than that of the large scale rig. A more confined chamber could be expected to reduce the rate of spread of the jet so that the point where the jet boundary reaches the chamber walls moves further down from the burner exit and the axial pressure gradient is reduced. This observation is in good agreement with the observation by Wu et al (1971).

The spray distribution characteristics also exhibit differences between scales. Radial spray distribution produced by the full-scale ultrasonic

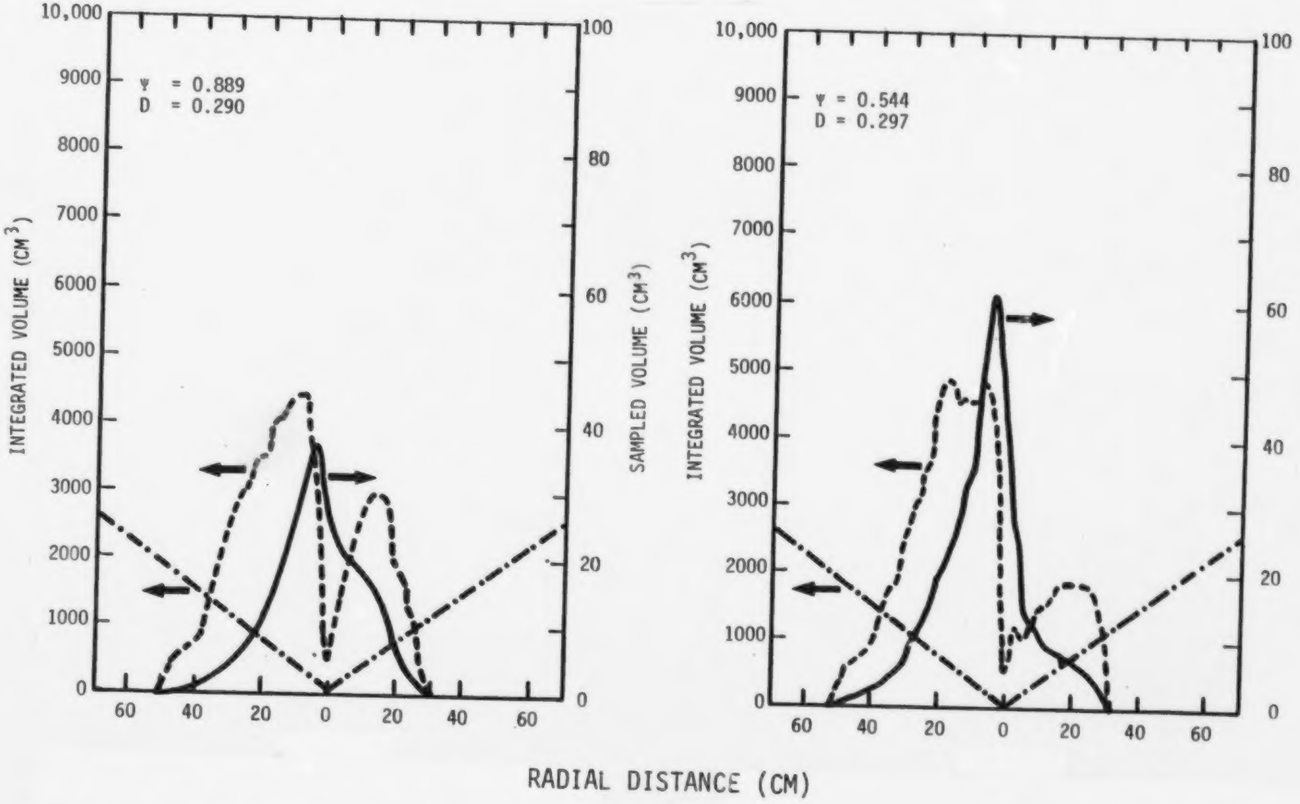

(a) 310 kPa Atomizing Air Pressure

(b) 414 kPa Atomizing Air Pressure

Figure 3-44. Effect of atomizing air pressure on ultrasonic nozzle spray distribution in Configuration III (large spray rig).

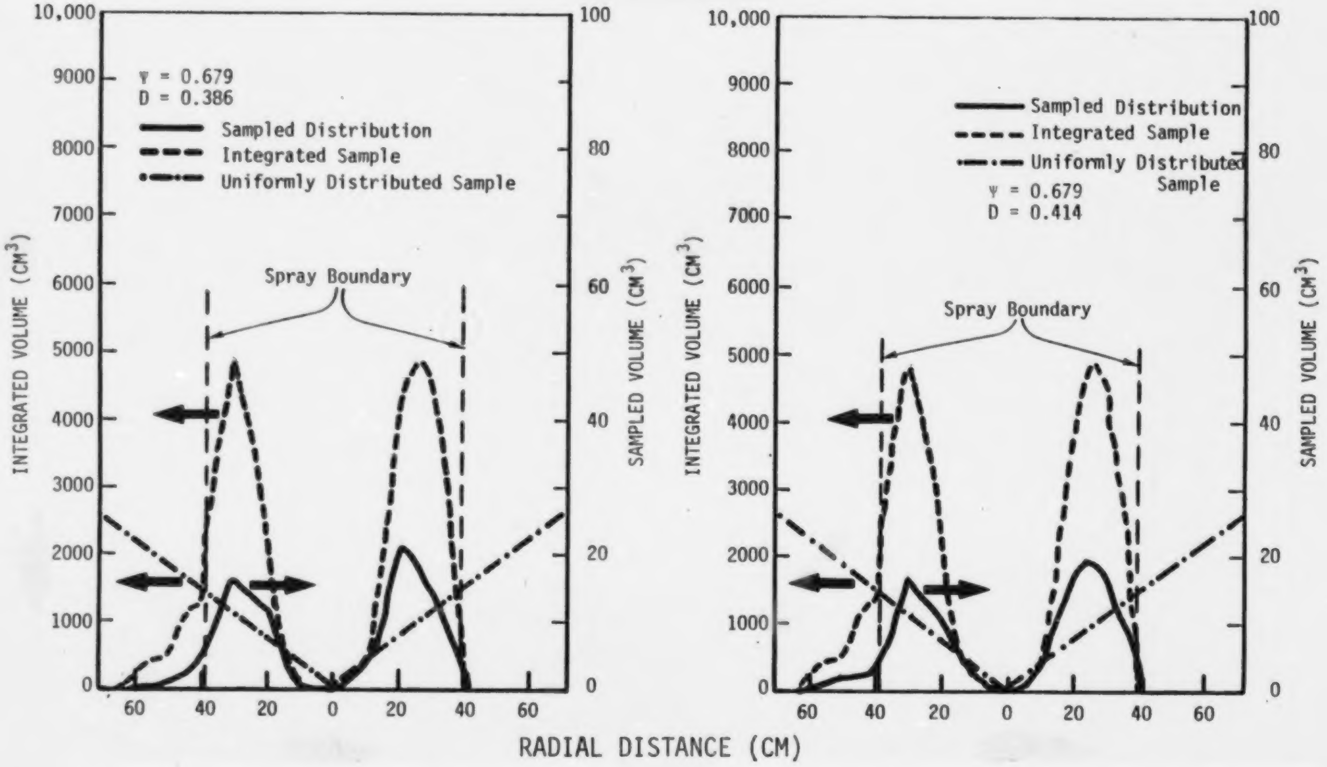

(a) 310 kPa Atomizing Air Pressure

(b) 414 kPa Atomizing Air Pressure

Figure 3-45. Effect of atomizing air pressure on Y-Jet spray distribution in Configuration III (large spray rig).

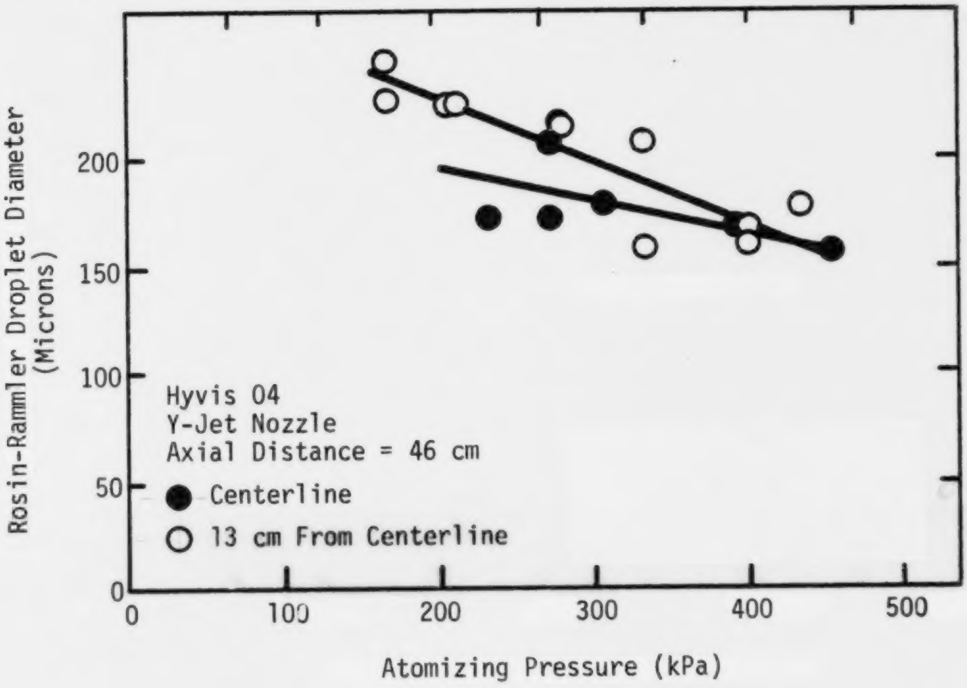

Figure 3-46. Influence of atomizing air pressure on Rosin-Rammler mean diameter from 15 MW Y-Jet nozzle (Hyvis 04, 55 cSt, oil flow = 0.26 kg/s).

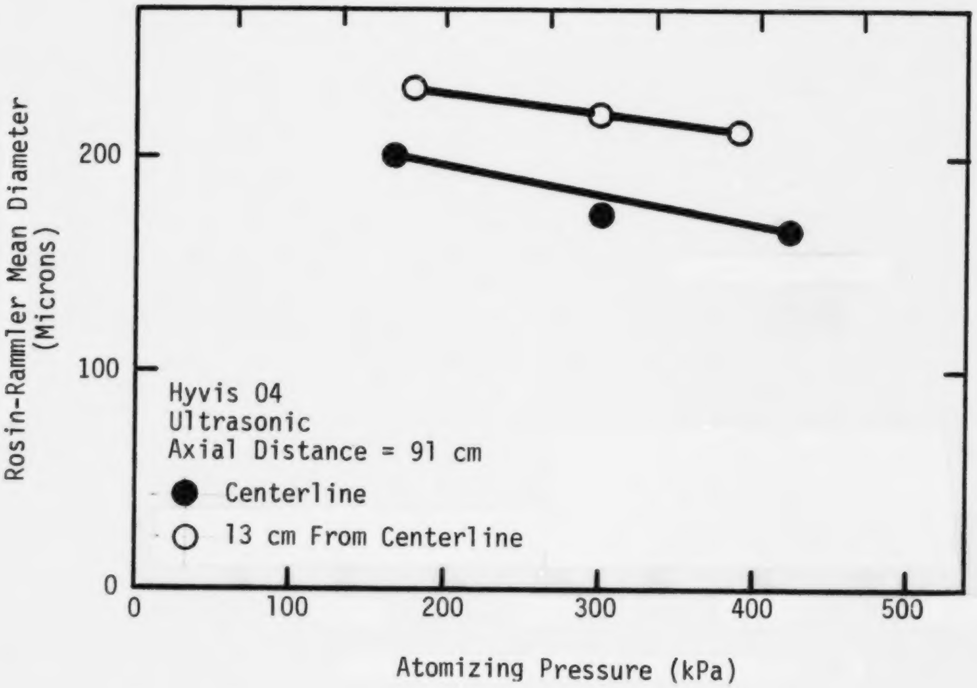

Figure 3-47. Influence of atomizing air pressure on Rosin-Rammler mean diameter from 15 MW ultrasonic nozzle (Hyvis 04, 55 cSt, oil flow = 0.26 kg/s).

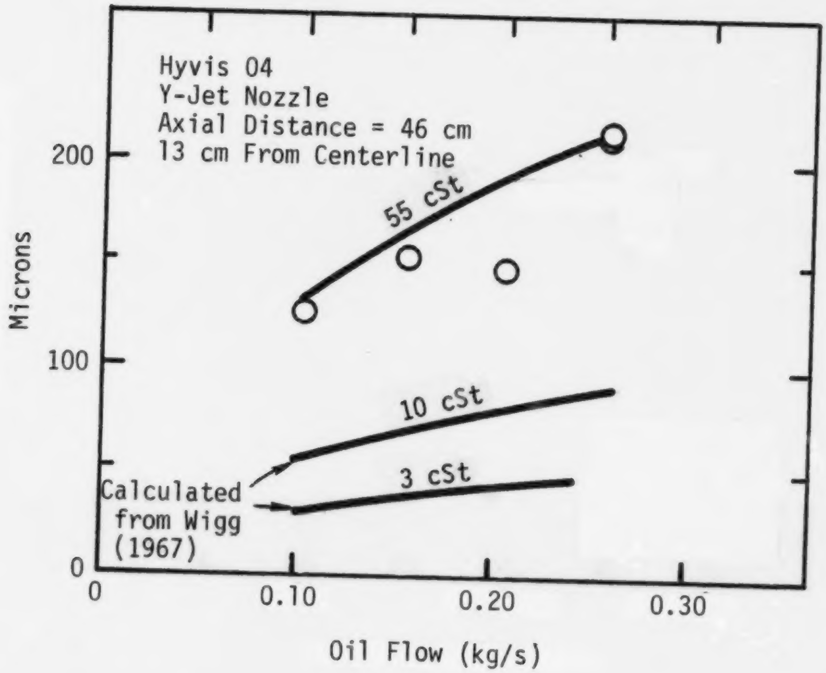

Figure 3-48. Influence of oil flow rate on Rosin-Rammler mean diameter for 12-hole Y-Jet nozzle (Hyvis 04, 55 cSt, atomizing air pressure = 310 kPa).

nozzle (Figure 3-38) was much less uniform than could be achieved with the similar small-scale atomizer. The spray from the full-scale ultrasonic nozzle was confined to an axial region approximately 20 inches diameter at the sampling location, as indicated by the integrated mass distribution. Very little of the spray reached the outer edge of the chamber except for fine droplets entrained in the recirculation flow. The boundaries of the distribution were significantly more confined when swirl level was reduced from 0.39 to 0.29. A slight flow asymmetry was observed in both cases. The flow asymmetry may be due to the tendency of a jet to attach to a nearby wall. The mass distribution produced with the cylindrical exit geometry is very similar to the distribution found in the divergent quarl geometry. Spray distribution produced by the full-scale ultrasonic nozzle (Figure 3-40) was much less uniform than at the small scale (Figure 3-35). The boundaries of the distribution remained unchanged with the increase of atomizing air pressure (Figure 3-44).

Exit geometry appeared to have a relatively minor effect on spray distribution for both small- and large-scale tests in spite of apparently significant flow field variations. This may indicate that the spray momentum is controlling mixing, rather than the aerodynamics in the region close to the nozzle. This is particularly evident at large scale. Exit geometry in actual combustion is likely to affect flame stability since the recirculation of hot gases into the initial mixing region is important for ignition.

In an effort to improve the poor spray distribution at large scale, a Y-jet nozzle (described earlier) with a 60-degree spray angle was used in place of the narrow angle ultrasonic nozzle. The spray produced by this atomizer resulted in a peak mass concentration approximately 30 cm radial distance from the centerline and was roughly symmetrical about the axis at the measurement plane. This is approximately the pattern expected based on the initial fuel jet trajectory. The theoretical jet centerline impinges at the measurement location indicated by the spray boundary in Figure 3-41. At swirl number of 0.39, the mass peaks occurred very close to the theoretical jet centerline. This indicates a "hollow" spray pattern is produced and that the jet direction is not strongly affected (at least radially) by the surrounding air flow. The pattern produced at slightly lower swirl (S = 0.29--Figure 3-42) showed a higher concentration of spray in the center of the pattern but was still contained by the jet centerline. This may indicate that some of the fine droplets in the spray are being deflected axially towards the center of the spray by the surrounding air. It also indicates that the strength of the central recirculation zone is probably weaker (Figure 3-37b) when swirl is lower.

The effect of atomizing air pressure on spray pattern produced by the Y-jet nozzle was also examined. Figure 3-45 compares the spray distribution for two levels of atomizing air pressure produced in a cylindrical burner. Very little enhancement in fuel/air mixing was achieved by reducing spray momentum via a reduction in atomizing air pressure from 414 kPa to 310 kPa.

It should be noted that these mass flux distribution measurements provide only qualitative information regarding spray characteristics. Because of the complex flow field and strong recirculation zones in the plane where measurements are taken, a mass balance cannot be consistently closed on sampled versus input liquid flow. However, the measurements do appear to be reproducible. Also, the flow patterns and mass distributions will be much different in a reacting flow where rapidly vaporizing droplets and strong density gradients are present. These results, therefore, must be interpreted as merely relative indications of the sensitivity of the atomizer spray to variations in burner air distribution.

It is expected that full-scale nozzles will produce relatively large mean droplet diameter sprays since large nozzles are typically operated at relatively low air/oil mass ratios. The large atomizing energy required to achieve high velocities and high air/oil mass ratios is impractical for most applications. Small nozzles can achieve high quality atomization by using high air-to-liquid mass ratios, but these ratios would be restrictively high for larger scales. This observation is consistent with Seeker et al (1982) for prefilming nozzles which indicated that atomization quality decreases with increasing scale. These tests of large-scale atomizers indicated that the air-to-oil mass ratio required to achieve the same atomization quality for the full-scale ultrasonic nozzle is approximatley three times higher than required by the Y-jet nozzle.

The results of these tests can be summarized as follows:

- Significant premixing of fuel and air is difficult to achieve at large scale given the energy levels normally available in conventional burner equipment.
- Throat velocities in the range of 24-30 m/s appear to give adequate mixing under favorable atomization and swirl conditions.
- Swirl level and fuel spray pattern must be optimized for a given throat configuration to achieve uniform mixing.
- Throat geometry has a weak effect on fuel distribution, but is likely to affect flame stability due to entrainment of hot partial combustion products.
- Atomization quality produced with an ultrasonic and a Y-jet atomizer was similar at full scale.

## 3.3 Preferred Conceptual Design

The pilot-scale and isothermal testing identified the following preferred design criteria for the full-scale prototype burner:

- Atomizer
    - Conventional atomizer design
    - Steam or air atomizing fluid
    - Optimize spray angle and distribution
- First-Stage Air
    - Premixer-type register
    - Axial velocity near 25 m/s
    - Variable swirl
    - Preheat (minimum 200°C)
- First-Stage Throat Geometry
    - Design for simple construction (parallel exit)

- First-Stage Chamber
  - Gas temperature > 1540°C
  - 0.5 to 0.7 seconds residence time
- Second Stage
  - Ports for an injection
  - Means to optimize flame shape and $NO_x$/smoke emissions (e.g. combine radial and axial ports).
  - No air preheat
  - First-stage velocity 15 to 25 m/s

# 4.0 FIELD RETROFIT

The ultimate goal of the program is to retrofit a normal 15 MW (thermal output) TEOR steam generator ("steamer") with the prototype commercial low-$NO_x$ burner and demonstrate its performance in the Kern County oilfields. In order to accomplish this, it was necessary to identify a representative steam generator design on which to base the selection criteria, select a steam generator, and determine the impact of the generator design on burner design. This section of the report describes the information acquired in selecting the 14.65 MW (thermal output) steam generator located in the Kern Front oilfield near Bakersfield, California.

## 4.1 Review of Steam Generator Designs

The initial phase in the definition of a typical TEOR steam generator design involved a review of the basic steamer design characteristics. Steamers produce low-quality (approximately 70 to 80 percent) steam for injection into deposits of low-gravity crude oil. Using low quality steam reduces maintenance requirements on the steam tubes since any dissolved impurities in the minimally-treated feedwater remain in solution. Higher quality steam leads to formation of deposits on the inside of the tubes and subsequent tube overheating. Steamers generally burn lease crude (about one-third of the crude produced from the deposit is burned) with from 0.5 to 5 (or higher) percent excess $O_2$, depending upon the design of the burner. This results in generally high $NO_x$ and $SO_2$ emissions due to the high nitrogen and sulfur content of the lease crude.

### 4.1.1 Steam Generator Design

Nearly all of the TEOR steamers in Kern County are manufactured by Struthers Thermo-Flood, Corp., C. E. Natco/National, and Thermotics, Inc., and generally fall into two size ranges: 6 to 9 MW (nominal 7 MW) or 15 to 18 MW (nominal 15 MW). There are a few generators up to 59 MW which are used for TEOR applications. In TEOR applications, 15 MW ($50 \times 10^6$ Btu/hr) steamers far outnumber the smaller units, and most new units purchased are also 15 MW units. Older units are either relocated (if the new units have new operating permits) or are taken out of service (if the new units are covered by a "permit trade" arrangement).

TEOR steamers utilize a single-pass, drumless, once-through design. Feedwater from a high-pressure pump enters a short convective section and then a radiant section, where evaporation occurs. They are normally skid-mounted and shop-assembled and are shipped by rail car or truck to the installation site. The feedwater pump equipment is sometimes installed on a separate skid from the generator skid.

The radiant section designs of steam generators are similar. The radiant section of a 15 MW steam generator is a horizontal refractory-lined steel cylinder approximately 12 m long with an inside diameter of about 3 m (Figure 4-1). Normally 10 to 15 cm of insulating refractory rated for 870 to 1100°C is used. Steaming tubes that extend axially are supported near the refractory on tube hangers and are located around the generator circumference. This design allows for heat transfer from the refractory as well as the flame and combustion products. The burner is located at the center of one end of the cylinder and fires directly along its centerline. Under normal operation, there is no flame impingement on the steaming tubes. The burner typically uses about one percent of the generated steam for atomization.

F4-1

The ends of the steaming tubes are welded to 180 degree bends which direct steam flow from the end of one tube to the beginning of the next adjacent tube. These tube bends are interior to the radiant section shell in most designs; however, in some of the newer generators the steaming tubes at the burner end extend through the burner wall and the bends are located outside the shell. This is done to facilitate replacement or cleaning of the steaming tubes should it (rarely) become necessary.

T4-1

Table 4-1 lists radiant section characteristics for a typical 15 MW steam generator. Steamers typically operate at about 80 to 90 percent overall efficiency. Volumetric heat release (hence mean residence time) is similar for all generator designs. Approximately 55 percent of the total heat is extracted in the radiant section, yielding exit gas temperatures on the order of 1000°C. The refractory insulation normally reduces exterior shell temperature to below 90°C. Steam pressure required for most Kern County wells is generally not greater than $10 \times 10^3$ kPa (1500 psig); however, steam generators for oil fields in other geographic areas may produce steam at pressures as high as $21 \times 10^3$ kPa.

The combustion products exit the radiant section through the end opposite the burner where they enter a transition section that directs the flow through

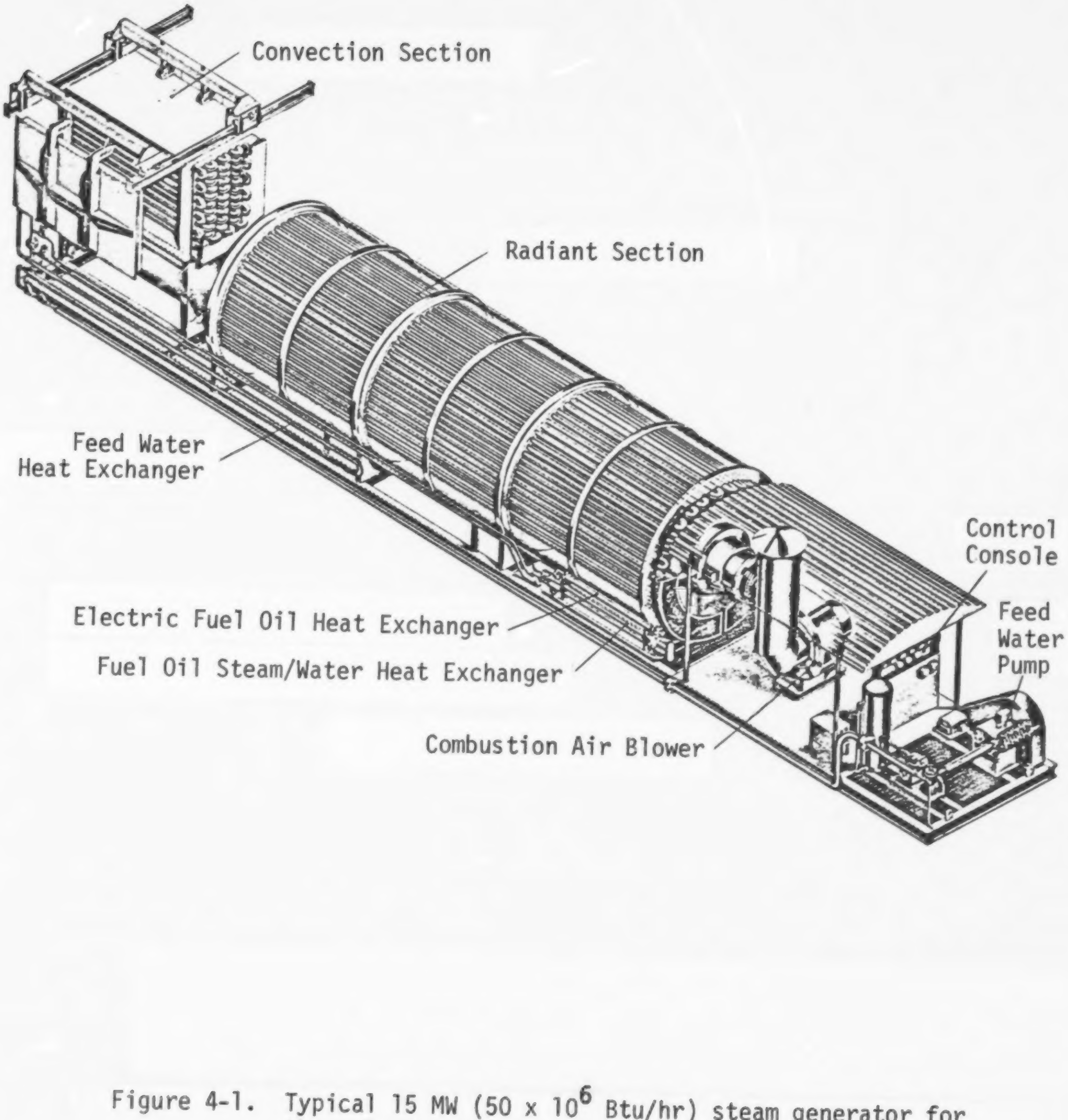
Convection Section
Radiant Section
Feed Water Heat Exchanger
Control Console
Feed Water Pump
Electric Fuel Oil Heat Exchanger
Fuel Oil Steam/Water Heat Exchanger
Combustion Air Blower

Figure 4-1. Typical 15 MW (50 x $10^6$ Btu/hr) steam generator for thermal enhanced oil recovery. The horizontal radiant section is typically about 12 meters long and 3 meters in diameter.

TABLE 4-1. TYPICAL RADIANT SECTION CHARACTERISTICS FOR 14.7 MW (50 x $10^6$ BTU/HR) STEAM GENERATOR

| | |
|---|---|
| Heat Input | 17.2 MW (58.7 x $10^6$ Btu/hr) |
| Combustion Chamber Diameter | 3 meters (10 feet) |
| Combustion Chamber Length | 12 meters (40 feet) |
| Volumetric Heat Release | 0.23 MW/$m^3$ (22,000 Btu/hr/$ft^3$) |
| Tube Heat Flux | 50 kW/$m^2$ (16,000 Btu/hr/$ft^2$) |
| Exit Gas Temperature | 1000°C (1800°F) |
| Tube Surface Temperature | 350°C (660°F) |
| Outside Surface Temperature | Below 90°C (190°F) |
| Steam Pressure | 10.3 MPa (1500 psig) |
| Steam Quality | 80 Percent |
| Steam Flowrate | 6 kg/s (48,000 lb.N/hr) |

a 90-degree bend vertically upward and into the convective section. The specific convective section designs vary, but generally the combustion products pass around and between a bank of tubes situated normal to the flow, transferring further heat to the water/steam mixture in the tubes. The convective section may contain bare or finned tubes or both, depending on the generator. After traversing the convective section, the flue gases either exit through a stack above this section or are channeled to a flue gas scrubber. Exit temperature from the convective section is typically near 200°C.

Steam generators typically operate at between 80 and 100 percent load until the convective section requires cleaning to reduce furnace backpressure. A generator generally has less than 0.13 kPa (0.5 inches of water) furnace backpressure when clean, which typically increases to 0.50 kPa (2.0 inches of water) before cleaning is required. The time between cleaning depends upon available fan pressure but is typically on the order of one month. The convective section is cleaned by water washing. After cleaning, the generator is started from cold firing lease crude typically using steam from nearby generators or compressed air for atomization during startup.

### 4.1.2 Burner Designs

Burners used in Kern County steam generators fall into three categories: conventional, low excess air, and low $NO_x$. It is beyond the scope of this report to fully discuss the design features of every burner currently applied to TEOR steam generators. Several low-$NO_x$ burners and even a complete low-$NO_x$ steam generator system (although to date untested) have been or will be available for application to steamers. Many of those designs have been addressed in a recent study by Nelson and Folsom (1980). Since that study a few additional low-$NO_x$ burners have appeared on the market. The primary purpose of all of these burners is to provide for combustion of a fuel and to produce a flame shape which is compatible with the steam generator radiant section design and efficiency requirements. Steamers equipped with conventional technology burners generally operate in the 3 to 5 percent excess $O_2$ range, but test data have been collected from units operating with more than 10 percent $O_2$ in the stack. When low excess air burners are utilized (to increase the overall thermal efficiency), operation at 0.5 to 1.5 percent $O_2$ is common. Low excess air operation is also a universal characteristic of the current technology low $NO_x$ burners.

The most widely used burner in the oil field generators studied in this report is the North American conventional burner. The basic burner comprises a blower, burner housing, nozzle, diffuser, and throat. The North American throat contains walls that are parallel and the diffuser plate is a flat disk with pie shaped pieces removed from it and a hole in its center. This configuration produces a long and lazy flame which extends approximately 90 percent through the generator without impinging on the steaming tubes (Figure 4-2). This flame pattern is desirable since it spreads the heat transfer over the entire length of the radiant section and prevents excessive temperatures near the throat outlet.

The Coen conventional burner features a divergent throat and a conical diffuser (Figure 4-3). In addition, the louvers within the burner housing produce clockwise swirling flow in the throat core surrounded by counterclockwise swirling flow. This generates high turbulence and the Coen flame is very intense and extends through only about 30 percent of the radiant section. Temperatures in this region are as much as $500^oC$ higher than for the North American burner and much of the heat transfer occurs in this area. In light of the higher temperatures and swirl produced by the conventional Coen burner, it is surprising that the $NO_x$ emissions are comparable for the two-burner designs. Generators firing Coen burners are prone to tube hanger and tube damage at low excess air unless adjustments are made to avoid flame impingement.

The efficiency of steam generators is increased by firing at low excess air conditions. However, conventional burners cannot be operated under these conditions because of high CO, smoke, and particulate matter emissions. For this reason, special burner designs were developed to permit low excess air firing without the problems experienced by conventional burners. These designs rely on rapid mixing of the fuel and air by increasing the energy (relative to conventional burners) imparted to the fuel and air streams at the burner throat.

The North American low excess air burner utilizes the same equipment as the conventional burner with the exception of the diffuser plate and nozzle.

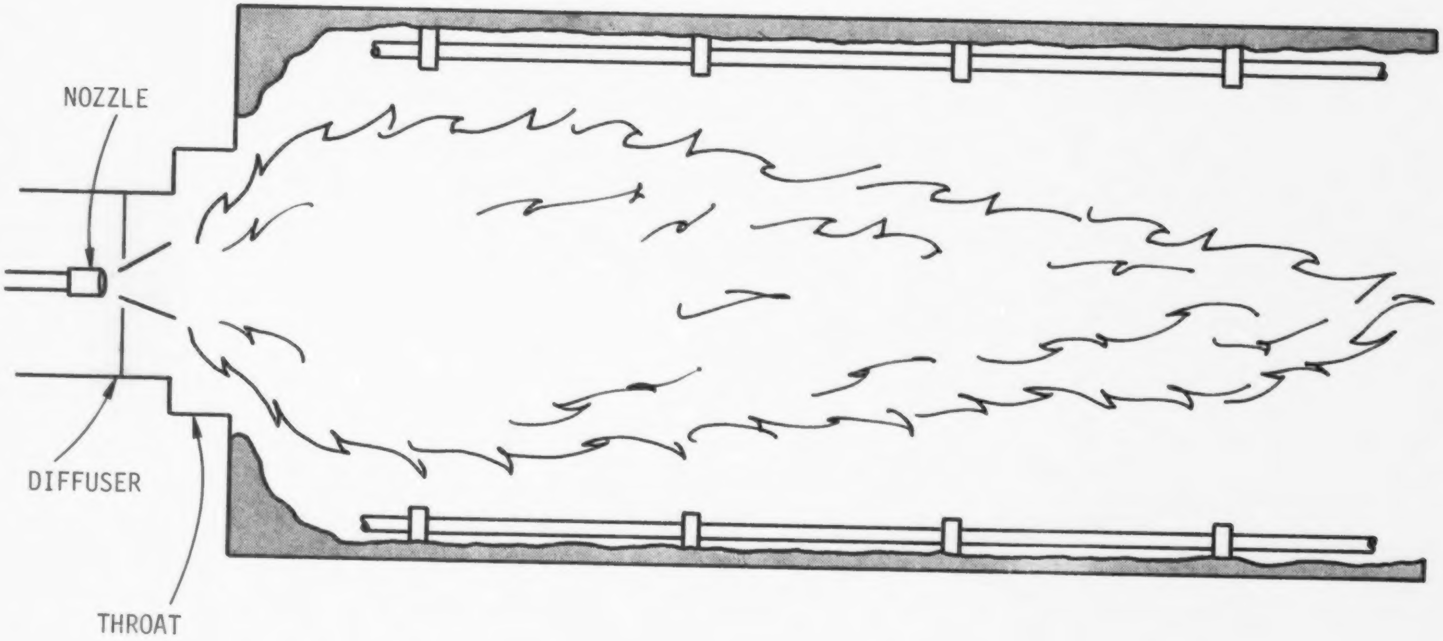
NOZZLE
DIFFUSER
THROAT

Figure 4-2. The conventional North American burner design and flame pattern.

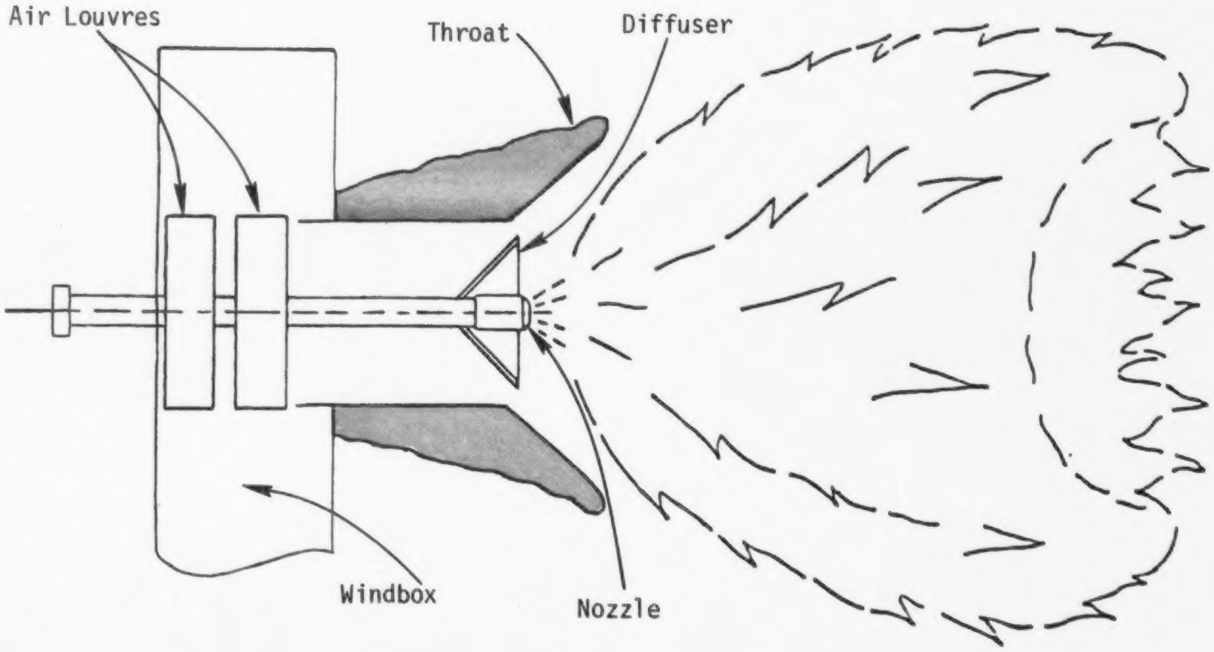
Air Louvres
Throat
Diffuser
Windbox
Nozzle

Figure 4-3. The conventional Coen burner design and flame pattern.

The low excess air nozzle atomizes the fuel more efficiently and the diffuser is equipped with perforations to allow more rapid fuel/air mixing in the early stages of combustion. These changes result in enhanced mixing which offsets the reduced $O_2$ availability. However, they can also result in significantly higher $NO_x$ levels if not operated under low excess air conditions since the fuel and air are mixed before the fuel nitrogen has a chance to form $N_2$.

## 4.2 Steam Generator Selection

The selection of a particular generator for the field retrofit was possible once the typical design characteristics were known. The results of the design survey indicated that only minor differences in combustion chamber design existed among the primary manufacturers. This reduced the problem of selecting the host generator to determining availability of a generator and willingness on the part of the owner to participate in the program. Fuel characteristics were a secondary consideration.

This section describes the selection criteria used in locating an appropriate steam generator, details of the host generator design, and characteristics of the site.

### 4.2.1 Approach to Selection

Once the "typical" steam generator design had been identified, the Kern County oil producers were approached to supply a steam generator which met the typical design requirements and other guidelines. These other guidelines were based on

- fuel characteristics,
- fuel supply, and
- generator availability.

Although the emissions performance of the burner is expected to be insensitive to fuel properties such as nitrogen content, certain properties (viscosity, sediment) may affect the performance of ancillary equipment or atomizers. Thus, the fuel to be used during the field demonstration should be a relatively "difficult" fuel (i.e., high in nitrogen content, viscosity, asphaltenes, and carbon residue) in order to evaluate burner performance under most possible conditions.

The fuels burned at most steam-flood sites are generally very heavy crude oil or residual oil, depending on availability and economy. A few units are fired on natural gas. For instance if the cost of producing and transporting residual oil from a crude is below the value of the lighter crude fractions, then residual oil may be fired. Crude oils ranging in API gravity from 5 to 12 which have a very low yield of light distillates are by far the most common fuels utilized for steam generation. These fuels range in nitrogen content from approximately 0.6 to 0.9 percent and in sulfur content from approximately 1.0 to 1.5 percent.

Fuel supply reliability and consistency was a secondary criteria for site selection. It is desirable but not essential that the same fuel be used throughout the field optimization and evaluation tests. This is generally not a problem at most sites; however, as mentioned above, some sites are subject to fuel changes.

The host site owner was requested to supply the fuel for the testing free of charge to the program since the steam generator would be on-line and injecting steam into the wells. The oil producers suggested that this was a reasonable request and was incorporated into the final agreement for the field demonstration.

The final aspect of the host site which was considered important to the eventual selection was availability of the steam generator for unplanned shutdown. Although the commercial prototype burner will be briefly tested and "debugged" prior to the field installation, it is likely that several unit shutdowns will be necessary during the field test phase. It is very desirable to minimize the impact on oil production of such shutdowns. Two alternatives were suggested for the host generator setting: an isolated generator injecting a single well not yet in the production stage; and a generator whose steam output is manifolded to a common injection distribution network. The current trend in generator installations is moving away from isolated settings and toward centralized, multiple-generator sites. This is primarily due to pollution regulations requiring $SO_2$ control and to the operation efficiency-related trend toward larger generators. $SO_2$ is normally removed from generator flue gases using wet scrubbers. It is desirable to install large capacity scrubbers fed by several generators because of the cost benefit gained in doing so. Large generators are also more difficult to transport than the small 7 to 8 MW units.

The advantage of carrying out the demonstration at a multiple-generator site is that the other generators could make up for lost steam during a shutdown of the host generator. Such installations are, however, more critical to proper operating methods. For instance, if during startup or shutdown unevaporated feedwater is fed to the common steam manifold, severe damage to the injection line can occur as the water flashes to vapor. Therefore, an isolated generator is more desirable because of lower risk of damage to the host owner's equipment.

These criteria for selection were determined largely in conjunction with the oil producers and the Ad Hoc Committee, in order to provide a fair trial of burner performance at minimum risk to field equipment with minimum impact on field operations. This led to the selection of the host generator described in the next section.

### 4.2.2 Description of Host Steam Generator

The host generator is a Struthers Thermo-Flood unit located in the Kern Front field to the north of Bakersfield, California. The host site was volunteered by Standard Oil of California.

Figure 4-4 shows the general layout of the host generator. The mounting skid extends 7.3 meters beyond the burner wall and contains the burner, blower, control console, and feedwater pump. Approximately 4.3 meters is available on the skid between the burner plate and the control console. The existing burner and control console are covered by an overhead roof. The entire unit is 22.5 meters long and 3.5 meters wide. Table 4-2 lists some of the design specifications for the steam generator. The generator specifications are typical for a unit of this size.

Table 4-3 lists some of the general host site characteristics. Standard Oil of California owns and operates the steam generator in the Kern Front oil field 13 kilometers (8 miles) north of Bakersfield. The location close to Bakersfield is ideal in the event supplies are needed. Two steam generators are currently operating at the host site and three more are planned to go into operation. The

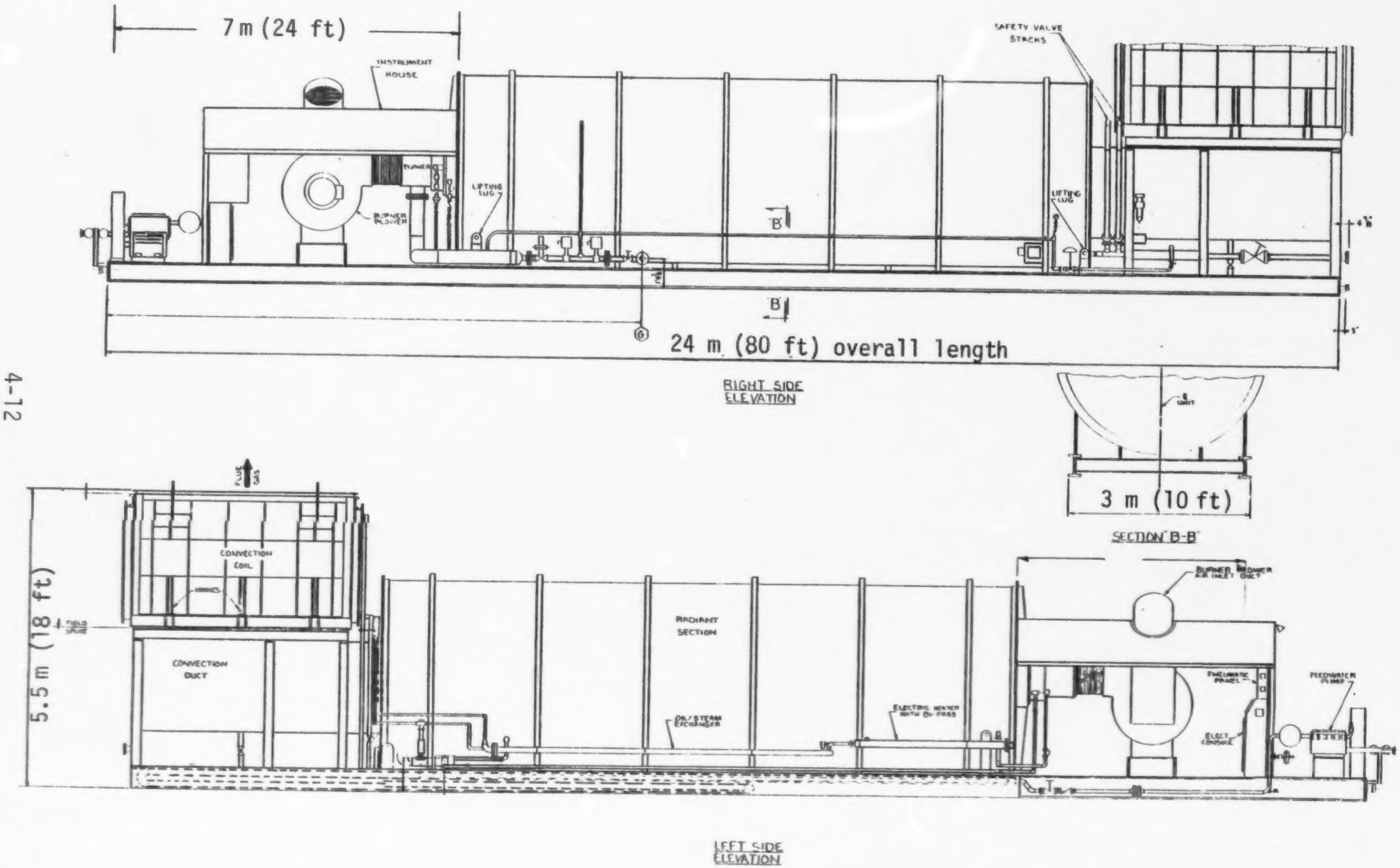
7 m (24 ft)
INSTRUMENT HOUSE
BURNER BLOWER
LIFTING LUG
B
SAFETY VALVE STACKS
LIFTING LUG
B
24 m (80 ft) overall length
RIGHT SIDE ELEVATION
3 m (10 ft)
SECTION B-B
FLUE GAS
CONVECTION COIL
FIELD SPLICE
CONVECTION DUCT
5.5 m (18 ft)
RADIANT SECTION
OIL/STEAM EXCHANGER
ELECTRIC HEATER WITH BY-PASS
BURNER BLOWER AIR INLET DUCT
PNEUMATIC PANEL
ELECT CONSOLE
FEEDWATER PUMP
LEFT SIDE ELEVATION

Figure 4-4. Host steam generator arrangement.

TABLE 4-2. HOST STEAM GENERATOR CHARACTERISTICS

| | |
|---|---|
| Manufacturer/Model: | Struthers Thermo-Flood OH50 |
| Burner: | North American 6131G-62.5 |
| Date of Manufacture: | 1981 |
| Steam Output: | 14.5 MW (6.2 kg/s at 7.6 MPa) |
| Fuel Input: | 16.2 MW |
| Overall Unit Efficiency: | 89.6% (Based on lower fuel heating value) |
| Exit Flue Gas Temperature: | 204°C (at 18 percent excess air) |
| Radiant Section: | Internal Tube Bend Design |
| Inside Diameter: | 2.91 Meters |
| Inside Length: | 11.3 Meters |
| External Diameter: | 3.4 Meters |
| Volumetric Heat Release: | 0.23 $MW/m^3$ |
| Tube Surface Heat Flux: | 51 $kW/m^2$ |
| Atomizing Steam Supply: | 170 kg/hr |
| Fuel Preheat Capacity: | 150°C |
| Pilot: | Spark-Ignited Natural Gas |

TABLE 4-3. HOST STEAM GENERATOR SITE CHARACTERISTICS

| | |
|---|---|
| Owner: | Standard Oil of California |
| Location: | Kern Front Oil Field |
| Nearest Town: | Oildale--approx. 8 km (5 miles)<br>Bakersfield--approx. 13 km (8 miles) |
| Number of Steam Generators: | 2 (total) Operating<br>5 (total) Planned<br>10 (total) Future |
| Generator Orientation: | Side by Side |
| Space Limitations: | Approximately 5.6 Meters Between Generators<br>Approximately 3 Meters From End of Skid to Road Edge |
| Fuel Storage Capacity: | 2000 Barrels |

units are located side-by-side and are supplied by a common fuel pump from a 2000-barrel tank. The host unit currently exhausts directly to atmosphere; however, a scrubber is planned when the three additional generators come on line. An access road surrounds the site and this forms one space limitation to the field retrofit, as the generator skid is located 3 meters from the edge of the road (Figure 4-5). The adjoining steam generator has a test stack on the exhaust which will be transferred to the host generator during testing.

F4-5

An analysis of the fuel fired in this steam generator is given in Table 4-4. The fuel contains 0.8 percent nitrogen (by micro-Kjeldahl analysis) and 1.06 percent sulfur. The preheat temperature required to reduce viscosity to 21 cp (normally required for atomization) is approximately 135°C.

T4-4

The steam generator is operated by a standard electric flame safety/interlock system and is modulated with a pneumatic drive system. The flame safety/interlock network provides for the correct starting and shutdown sequence including prepurge, pilot and main burner ignition, postpurge, etc. The pneumatic system controls feedwater flow and burner firing rate. The feedwater flow is manually set and burner firing rate follows feedwater flow. The pneumatic system automatically reduces feedwater flow and firing rate if steam pressure exceeds a maximum safe setpoint. A relay logic network controls the pneumatic systems during the startup and shutdown sequence.

## 4.3 Retrofit Constraints

The primary application of the prototype commercial low-$NO_x$ burner is as a retrofit to existing generators. It was necessary to establish limits to the burner design which would ensure that retrofit can be accomplished at minimum cost to the steam generator owner. The constraints imposed on the burner retrofit fall into three categories:

- Physical requirements
- Control system
- Flame pattern

The limitations on physical dimensions are determined by a combination of steam generator external dimensions and the particular manner in which the generator is installed in the field. The control system contains elements

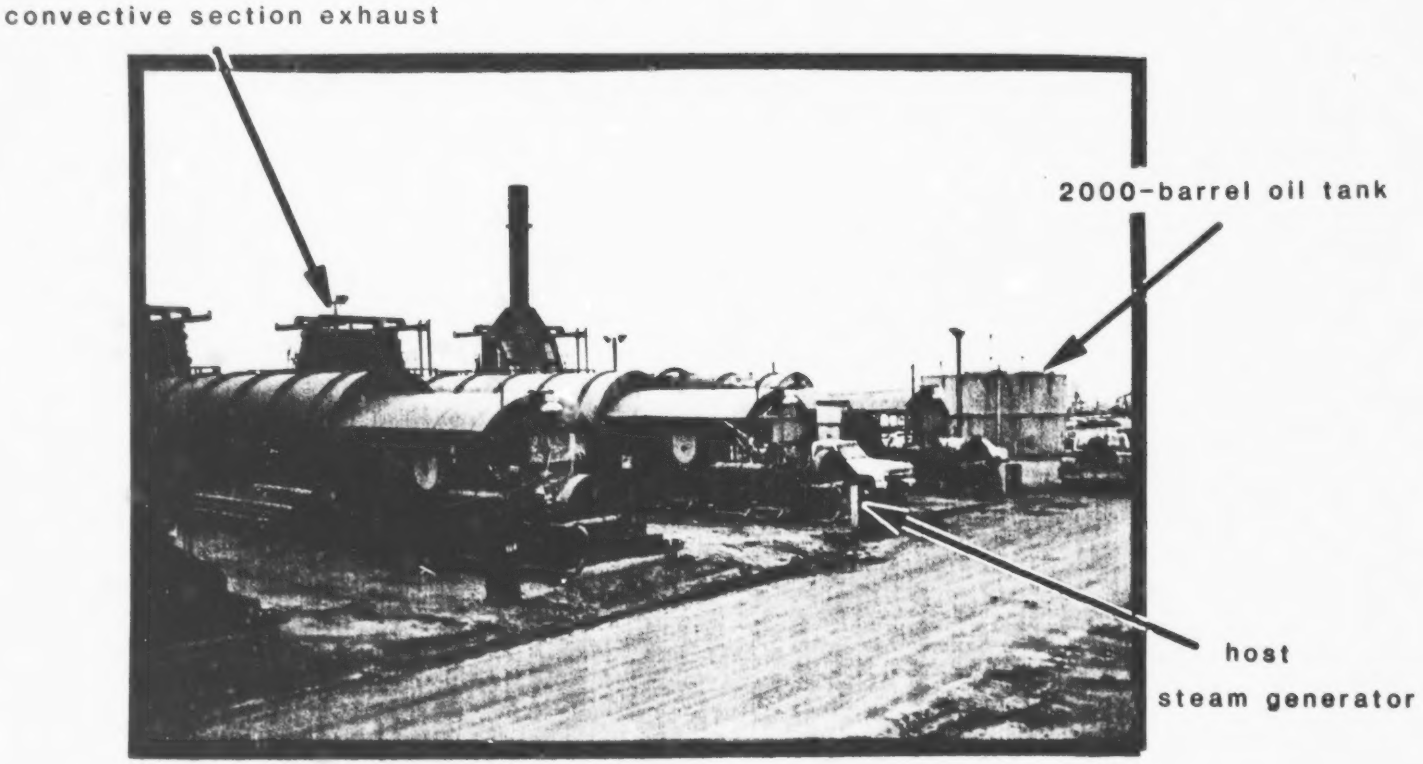
convective section exhaust
2000-barrel oil tank
host
steam generator

Figure 4-5. Kern Front host steam generator site.

TABLE 4-4. HOST STEAM GENERATOR--FUEL CHARACTERISTICS

| KERN FRONT CRUDE OIL | |
|---|---|
| % C | 86.28 |
| % H | 11.35 |
| % N | 0.81 |
| % S | 1.06 |
| % ASH | 0.041 |
| % O | 0.46 |
| **VISCOSITY, CP** | |
| @ 71°C | 205 |
| @ 99°C | 45 |
| HHV | 42.6 kJ/g |
| LHV | 40.3 kJ/g |

which are dedicated to steam generator operation and burner operation; the elements controlling generator operation (and safety) should not be disturbed during retrofit. Flame pattern will impact generator performance and maintenance and is determined by burner design and combustion chamber characteristics. Consideration of all these factors is important to keep the retrofit cost to a minimum. The retrofit constraints imposed by these factors are summarized in Table 4-5.

### 4.3.1 Physical Requirements

The physical constraints to the burner design are primarily diameter and length. Ideally, the retrofit would not require anything more complicated than unbolting the existing burner and bolting on the low-$NO_x$ burner. Most low-$NO_x$ burner retrofits require considerably more than this, specifically: enlargement of the burner opening to accommodate lower air velocities; modification to the skid or cab to accommodate larger burner hardware; installation of additional ductwork and blowers to accommodate multiple air passages or flue gas recirculation; relocation of oil, atomizing steam, and control plumbing.

The constraints to burner diameter and height are determined by shipping requirements. Most steam generators are shipped by truck and/or by rail and must therefore conform to both railway and trucking restrictions to height and width. This is largely what determines the physical layout of oilfield steam generators and accounts for the high L/D of the radiant section; therefore, the retrofit burner should not exceed the overall diameter of the steam generator.

Length restrictions are usually prescribed by the manner in which the generator is installed in the field. In many instances single generators are located in isolated settings where length is not critical. There are many installations where generators are installed near existing roads or hillsides which could restrict the maximum length of the burner/generator assembly. The possible constraints in length vary from no restriction to no allowable increase. The maximum allowable extension of the skid for the host steam generator site is approximately 3 meters, therefore this was used as an approximate guideline for this particular burner design. This placed the maximum allowable skid length beyond the front wall at 10.4 meters. Allowing for the

TABLE 4-5. PRIMARY RETROFIT REQUIREMENTS

| Steam Generator Design/Installation | Impact on burner design. |
|---|---|
| Maximum Diameter 3.5 Meters | Limit burner diameter to 3.5 meters. |
| Distance Available in Front of Generator | Maximum burner length depends on setting (7.7 meters for demonstration host site) |
| Control System | Integrate additional control features without compromising normal operation, safety, reliability of maintenance complexity. |
| Radiant Section Diameter and Length | Minimize impact of flame shape on generator maintenance or reliability. |
| Ancillary Equipment | Minimize additional operating expenses. |

portion of the skid dedicated to the feedwater pump and control console, this restricted the maximum allowable burner length (including room for access to the burner and controls) to 7.7 meters.

There may also be limited space in the burner area for installing additional burner hardware such as control equipment, blowers, ductwork, etc. This equipment must be arranged in such a way so as not to interfere with access to equipment for normal maintenance or repair.

### 4.3.2 Control System Constraints

The existing controls on the steam generator provide for cold startup, on-line operation, and shutdown. Additionally, there are safety interlocks and control overrides which prevent the occurrence of conditions harmful to the steam generator.

The primary retrofit constraints on the control system are that safety elements are not defeated and that operation of the steamer be kept simple.

The control system is based on a pneumatic actuation system with both electric and pneumatic surveillance of steam generator and burner operating conditions. The electric flame safeguard network monitors the burner and safety interlocks. If a limit is exceeded (e.g., high tube temperature, low instrument air, high flue gas temperature) the control system initiates the generator shutdown sequence. A relay logic system sequences the pneumatic and electric elements during startup and shutdown.

The pneumatic controls incorporate valve actuators, controllers, and flow elements. Pneumatic controls are very reliable but do not permit much flexibility of information processing. They are also simple to troubleshoot and repair in the field which is important in a remote environment. It is very desirable not to complicate the control system beyond the point where retraining of maintenance personnel is required. However, there are certain aspects of the prototype commercial low-$NO_x$ burner which require additional complexity and flexibility, and hence certain more sophisticated hardware is required. A hybrid system which incorporates both pneumatic and electronic elements was adopted to provide the reliability inherent in pneumatic systems and the flexibility of a microprocessor-based controller.

The complexity of the burner and controls will affect operating costs through downtime for repair and maintenance. Another factor influencing operating costs is the burner energy consumption for fan power, atomizing steam, fuel preheat and pumping power, etc. For instance, increasing fan power requirements by 22 kilowatts can lead to about 8,000 dollars per year incremental operating cost for electricity. In order for this burner concept to be economically attractive, these costs should not exceed those of the original burner.

### 4.3.3 Flame Shape

Flame shape is critical to extend satisfactory performance of the steam generator. Impingement of the flame directly on the radiant section tubes, refractory, or tube hangers will lead to accelerated deterioration of those components. Excessive flame length may burn out refractory in the transition section or even overheating of convective bank tubes and reduced generator efficiency. The overriding practical concern of the retrofit is to minimize the possibility of damage to the steam generator, and flame shape is a primary factor. Flame shape will be assessed in the preliminary evaluation of the burner at the EER test site; however, certain flexibility is being built into the second stage of the prototype burner to allow for variation of flame shape. It is anticipated that a production phase burner would not require this added degree of complexity.

## 5.0 FULL-SCALE BURNER DESIGN

This chapter of the report deals with the detailed design of the full-scale, commercial-grade prototype burner. Several aspects of the conceptual design dictated that a careful design study be undertaken prior to selecting a final design:

- Maintaining near-adiabatic temperature in the primary zone means high temperature materials will be involved.
- Long residence times at high temperatures mean that a chamber of substantial size is required.
- Steamer startup and shutdown requirements necessitates that the warm-up period be minimized.
- The high L/D of the steam generator radiant furnace means that flame shape is critical to avoid tube and furnace refractory degradation.

The gas temperature in the primary zone at which the low-$NO_x$ concept is favorable necessitates the use of refractory materials (i.e., $Al_2O_3$, $SiO_2$) to form the primary zone lining. Designs similar to gas turbines utilizing high temperature metals as the hot-face material, generally useful up to metal temperatures of approximately 1090°C, were initially considered but quickly discarded due to cost, material availability, and high air pressure drop to maintain shell cooling. Previous experience with refractory materials dramatically demonstrated the importance of correct material selection and construction method. Materials capable of withstanding the combination of 1650°C temperatures and reducing atmospheres are typically low in tensile strength and very brittle. They also tend to have high thermal conductivity which requires a surrounding layer(s) of insulating material to reduce thermal losses. Figure 5-1 shows how a lining fabricated from castable refractories which failed due to insufficient strength in the insulating material to maintain the inner layer in compression during heatup and cooldown. Cracking was so severe that redesign and replacement of the inner linings was required. The brittle nature of these materials also makes linings such as shown in the figure sensitive to rapid temperature changes (thermal shock) so that heating and cooling the lining should be accomplished gradually. The operation of most boiler and

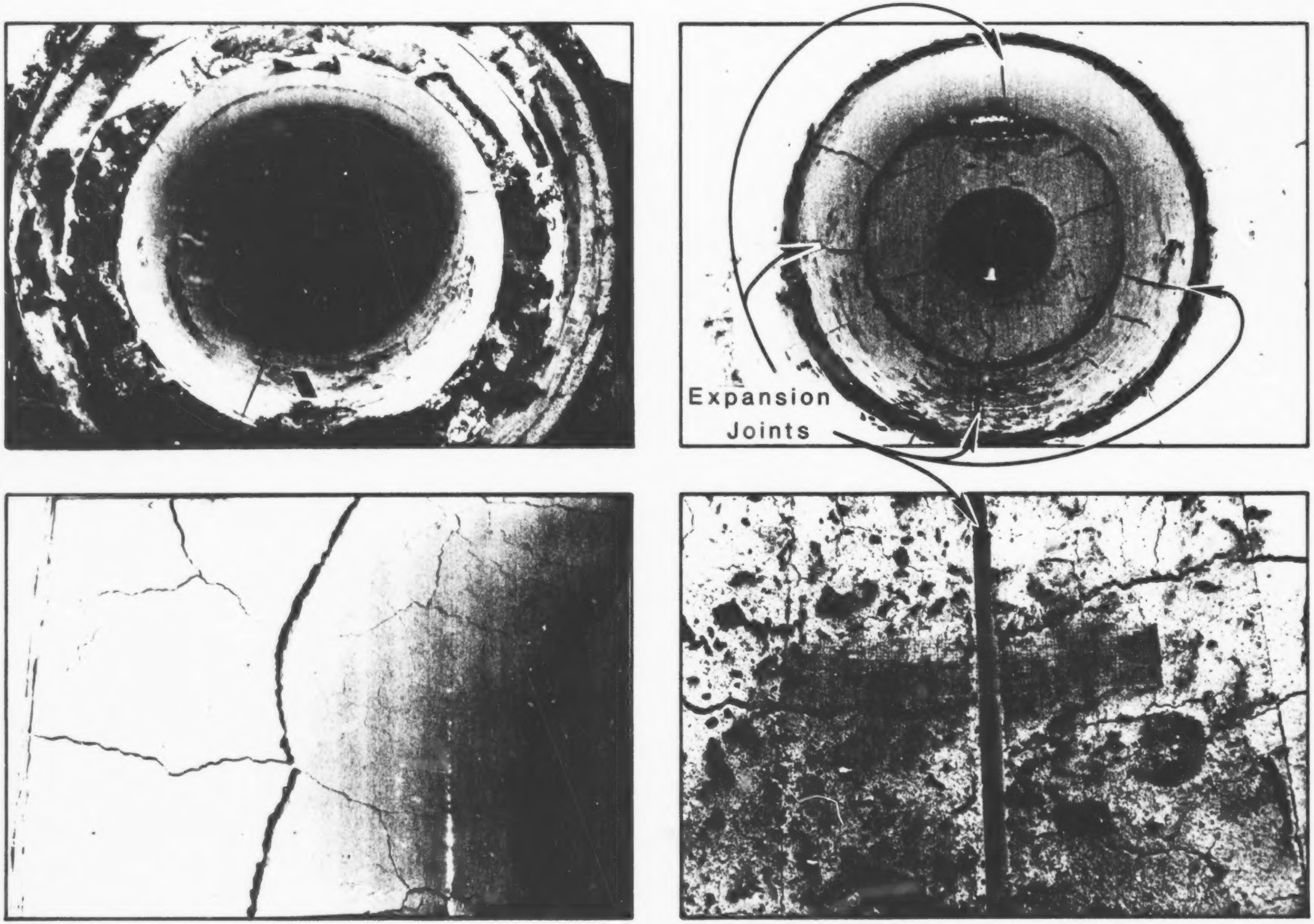
Expansion
Joints

Figure 5-1. Example of refractory lining failure due to inadequate design and thermal shock.

furnace equipment makes this impractical in many cases, where load cycling must occur to follow process demands.

The lining illustrated in Figure 5-1 was a direct scaleup of a lining design successfully used for smaller scale equipment. It is evident that this design approach was not adequate for larger scale equipment. It was realized at the beginning of the detailed full-scale burner design effort that in order to minimize the risk of refractory failure, commercial expertise would be required to arrive at an advanced state-of-the-art design. Several manufacturers, users, and designers of refractory materials were consulted about the design. This initial consultation led to the selection of the following as design consultants:

- Dr. Ross Firestone (Illinois Institute of Technology Research Institute)--a ceramicist with extensive experience in materials technology for slagging coal gasifiers and refractory failure investigations.
- Davy McKee Corporation (Cleveland, Ohio)--an engineering firm engaged in the design of refinery and steel mill equipment.

The two burner manufacturers involved in the program, Coen Company, Inc., and Peabody Engineering Corp., also contributed substantially to the final lining design.

The remainder of this chapter describes the engineering design study which was conducted to select a final full-scale design for the burner lining, shell, control, and air injection. The study began with first defining the requirements of the full-scale burner, then developing the detailed design and analysis. The study was concluded with the selection of one configuration suitable for field retrofit.

## 5.1 Design Definition

The object of this task was to take the conceptual design described in Chapter 3 and develop it into a hardware design. Two design concepts were developed from this study. The first design (Concept A, Figure 5-2) was based on the pilot-scale burner designs, constructing the first stage from multiple layers of castable refractory to insulate the first stage. The thickness and thermal conductivity of each layer were optimized to minimize wall thickness and heat losses while maintaining sufficient thickness to provide necessary

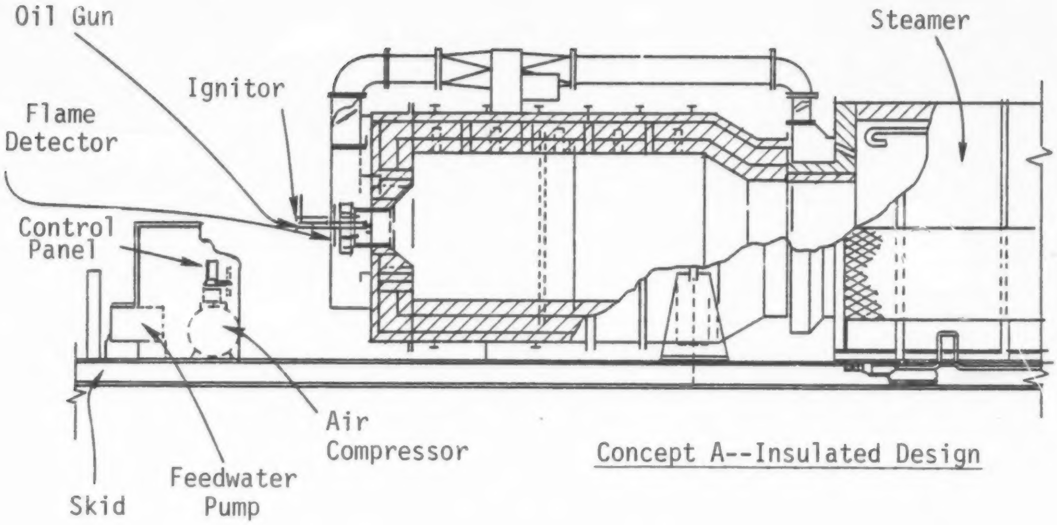
Oil Gun
Steamer
Ignitor
Flame Detector
Control Panel
Air Compressor
Skid
Feedwater Pump

Concept A--Insulated Design

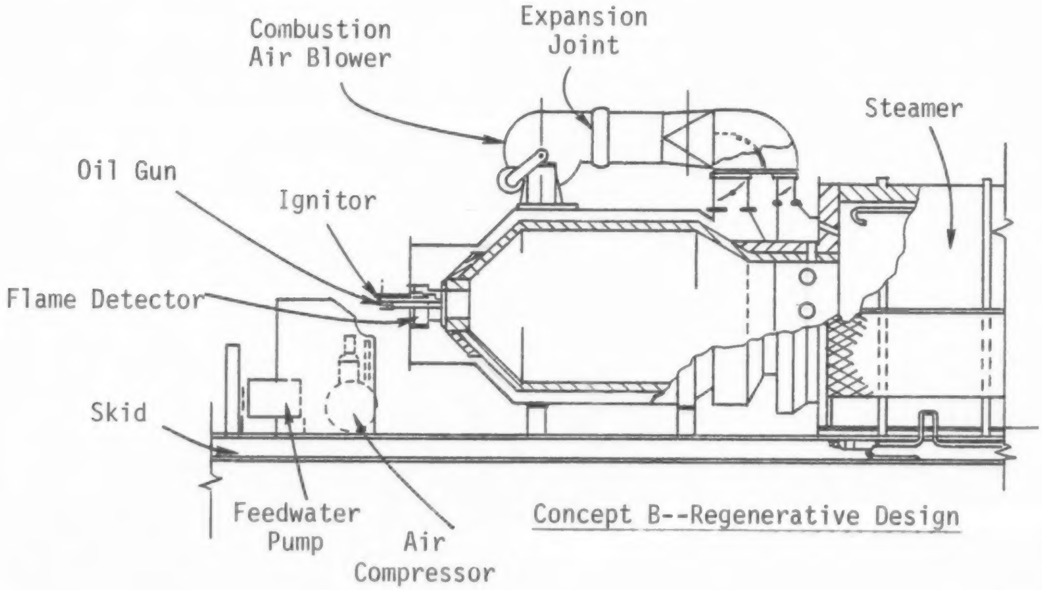
Combustion Air Blower
Expansion Joint
Steamer
Oil Gun
Ignitor
Flame Detector
Skid
Feedwater Pump
Air Compressor

Concept B--Regenerative Design

Figure 5-2. Conceptual burner designs for TEOR steam generators.

strength. Analysis of this design showed that very high stresses would develop in the lining, particularly during transient operation when large temperature gradients are produced. A very slow heatup schedule was recommended in order to keep the temperature gradients small within the large mass of refractory thus keeping thermal stresses low. It would be very difficult to guarantee that this heating/cooling schedule was always maintained in the field, and it is not possible to determine the effects of repeated thernal shock. The analytical studies and practical experience indicated that a substantial risk of lining failure was inherent in this design because uncontrolled heating could occur during an upset condition, so an alternative design was developed.

The alternative design (Concept B, Figure 5-2) minimizes the amount of refractory in the lining by using a "regenerative" double-shell to cool the steel shell using the primary combustion air. This concept has the advantage of transferring heat from the first stage to the primary air, which has been shown to be beneficial to the staging concept. Since there is some heat flow through the refractory, the actual hot-face temperature will be slightly lower than Concept A. Higher thermal stresses could develop because of the large temperature difference across the lining; however, if the diameter is not continuously connected the thermal stresses are limited to the transient stage.

The design task for these two concepts involved translating the conceptual design into a full-scale hardware design, selecting a suitable material for the refractory lining and support shell, and determining the expected performance of the chosen designs. Beyond determining the best shell design for the first stage, the requirements for second stage air addition and burner control also were incorporated into hardware designs. The remainder of this action covers the selection of design points for the two first stage concepts discussed in subsequent sections.

### 5.1.1 First-Stage Dimensions

The conceptual design requirements for the first stage are summarized in Table 5-1. In order to determine the volume of the first-stage chamber to achieve 0.5 to 0.7 seconds residence time, the required air and fuel flowrates must first be established. Table 5-2 lists the expected flowrates for the design point load of 18.3 MW (62.5 x $10^6$ Btu/hr). The expected gas temperature

TABLE 5-1. FIRST-STAGE CONCEPTUAL DESIGN REQUIREMENTS

| | |
|---|---|
| Residence Time | 0.5 to 0.7 sec |
| Gas Temperature | Above 1540°C |
| Stoichiometric Ratio | Rich Optimum |
| Air Inlet Temperature | Maximum Preheat if Possible |
| Bulk Mixing | Plug Flow |

TABLE 5-2. BURNER DESIGN POINT--18.3 MW (62.5 x $10^6$ Btu/hr)

| Parameter | Valve | |
|---|---|---|
| Fuel | | Kern Front Crude Oil |
| Fuel Flowrate | Mass<br>Volume | 1550 kg/hr (3400 lb.m/hr)<br>1.5 $m^3$/min (400 gal/hr) |
| Air Flowrate--First Stage | % TA<br>Mass<br>Volume | 52-77%<br>3.1-4.6 kg/sec (6.8-10.1 lb.m/sec)<br>2.6-3.8 $m^3$/sec (5500-8100 $ft^3$/min) |
| Air Flowrate--Second Stage | % TA<br>Mass<br>Volume | 28-68%<br>1.7-4.1 kg/sec (3.7-8.9 lb.m/sec)<br>1.4-3.4 $m^3$/sec (3000-7200 $ft^3$/min) |

and composition must also be known to calculate density. Equilibrium calculations (Figure 5-3) show that specific gravity of the combustion products (relative to air) varies from approximately 0.85 to 0.95 over the range of expected optimum stoichiometric ratio.

The relationship between first-stage residence time, temperature, and stoichiometry are shown in Figure 5-4 for a fixed first-stage volume of 13.2 $m^3$ (465 $ft^3$) designed to yield a residence time of 0.6 seconds at a first-stage stoichiometric ratio of 0.58 (corresponding to 3 MW pilot-scale results). Calculated flame temperature for these conditions was 1480°C (2700°F). The design point load of 18.3 MW (62.5 x $10^6$ Btu/hr) was used for these calculations.

It can be seen that calculated flame temperature (dashed line) varies steeply with stoichiometric ratio, varying from 1320°C to 1820°C from stoichiometric ratio of 0.5 to 0.75. This temperature variation results in a variation in density (hence residence time) of approximately 30 percent if chamber volume and mass flow is held constant. The temperature variation with stoichiometric ratio is also important to the chemical reaction rate and to material used for the hot-face lining. At the very rich end of this range, the rate of fixed nitrogen species decay may be too slow to reach desired levels within the available residence time (see Chapter 2), therefore very little or no heat loss from the first stage can be tolerated. At the lean end of the range, temperature approaches the practical use limit for the lining material where mechanical strength is jeopardized (see section 5.2). It may be preferable to have some degree of heat extraction from the first stage walls to allow for some margin of safety in this case.

Figure 5-4 shows that first-stage residence time varies substantially from the design point if optimum stoichiometry is unknown. First-stage residence time would be reduced from 0.6 seconds to 0.43 seconds if the minimum in $NO_x$ occurred at a stoichiometric ratio of 0.75 instead of 0.58, chosen as the nominal design point for this case. This would result in an expected increase in $NO_x$ emissions from approximately 73 to 94 ppm (at 3 percent oxygen) according to the pilot-scale data presented in Chapters 2 and 3. Figure 5-4 shows that if some heat loss occurs some residence time is gained; however, if temperature drops below approximately 1430°C (2600°F) fixed nitrogen decay

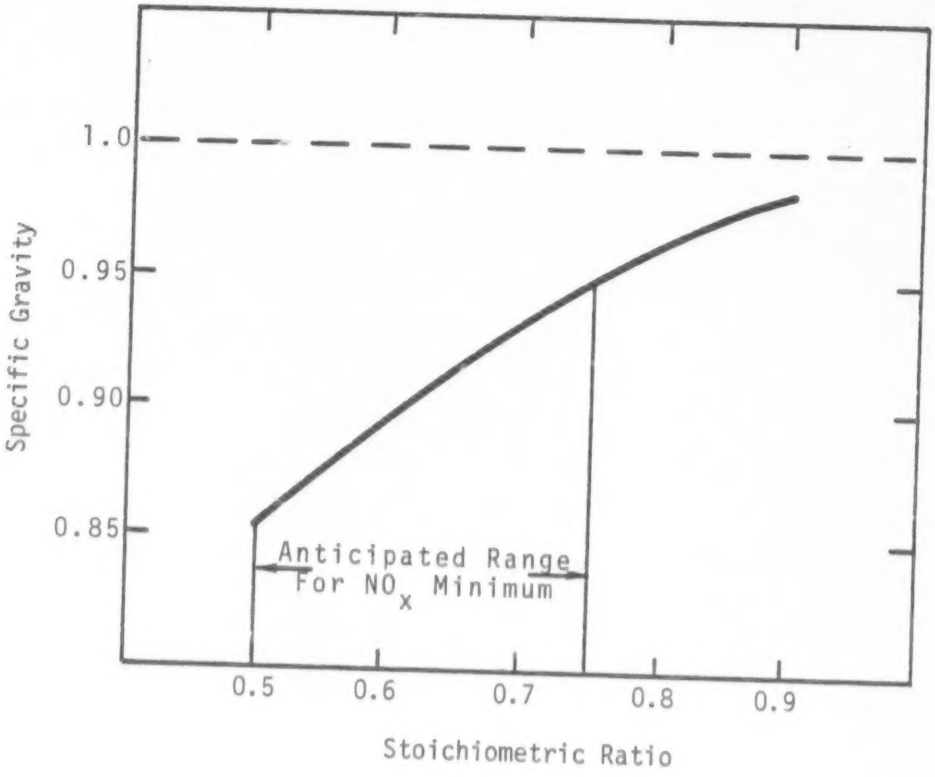

Figure 5-3. Specific gravity of rich equilibrium combustion products.

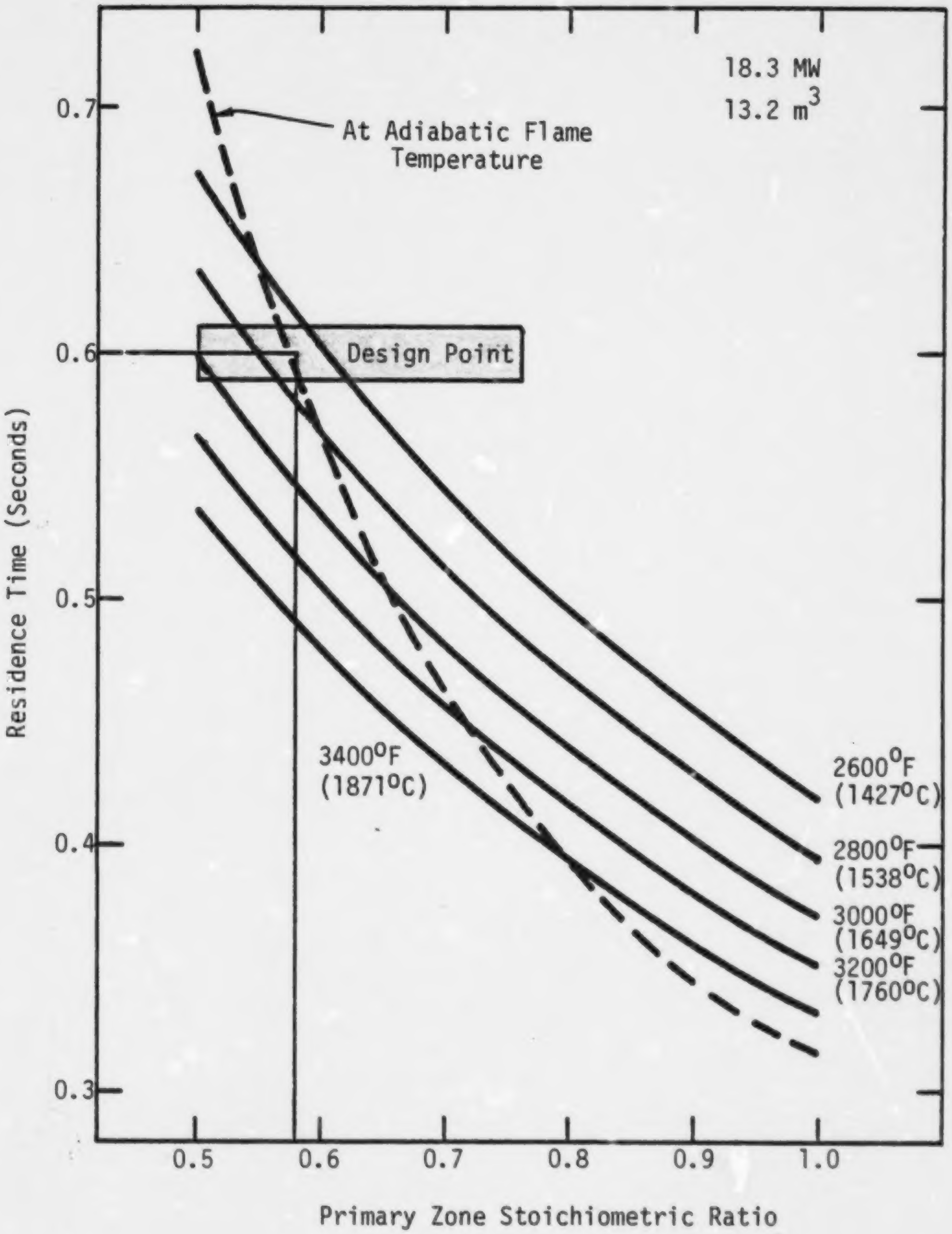

Figure 5-4. Variation of residence time with stoichiometry and temperature.

is expected to be too slow to use the effective first-stage volume, resulting in an increase in $NO_x$ emissions.

The required chamber volume to achieve 0.6 seconds residence time is shown in Figure 5-5 as a function of temperature and stoichiometry. It can be seen that the required chamber volume varies by as much as 50 percent from the case chosen for Figure 5-4. It is obvious that some conservatism must be included in the selection of the design point volume in order to ensure that the residence time requirement can be met. A chamber volume of 18.4 $m^3$ (650 $ft^3$) is required if the optimum stoichiometry is 0.75. This was chosen as an upper level for the minimum acceptable first-stage volume. A chamber volume of 13 $m^3$ (465 $ft^3$) was chosen as a lower level for the minimum acceptable size, corresponding to an optimum stoichiometry of 0.58.

### 5.1.2 First-Stage Geometry

The internal shape of the first-stage could be selected once the requirements for chamber volume had been established. Basic geometries had been evaluated in the conceptual design and cylindrical geometry was chosen to satisfy simplicity and cost requirements. It was necessary to determine cylinder length-to-diameter ratio, entrance geometry, and exit geometry which would satisfy both the retrofit constraints described in Chapter 4 and the conceptual design criteria. A high L/D is desirable to achieve near-plug-flow conditions and thereby maximize the mass-average residence time. The steam generator itself and the installed setting, however, impose constraints on the maximum allowable length and diameter. Wall thickness of the two potential concepts was very different, and therefore the actual constraints on the internal dimensions were not necessarily identical for the two concepts.

The pilot-scale prototype burners have been tested with L/D ratio ranging from approximately 1.2 to 3.0, with no effect on the performance relationship between $NO_x$ and residence time. The implication of these results is that primary-air/fuel mixing and bulk flow patterns within the first stage were sufficiently close to the conceptual design criteria. However, it is more difficult to achieve the same kind of mixing at larger scales, essentially due to the fact that the scale of turbulent mixing does not change. The isothermal tests described in Chapter 3 also confirmed that it is more difficult to achieve similar uniformity of fuel/air mixing with large- and small-scale

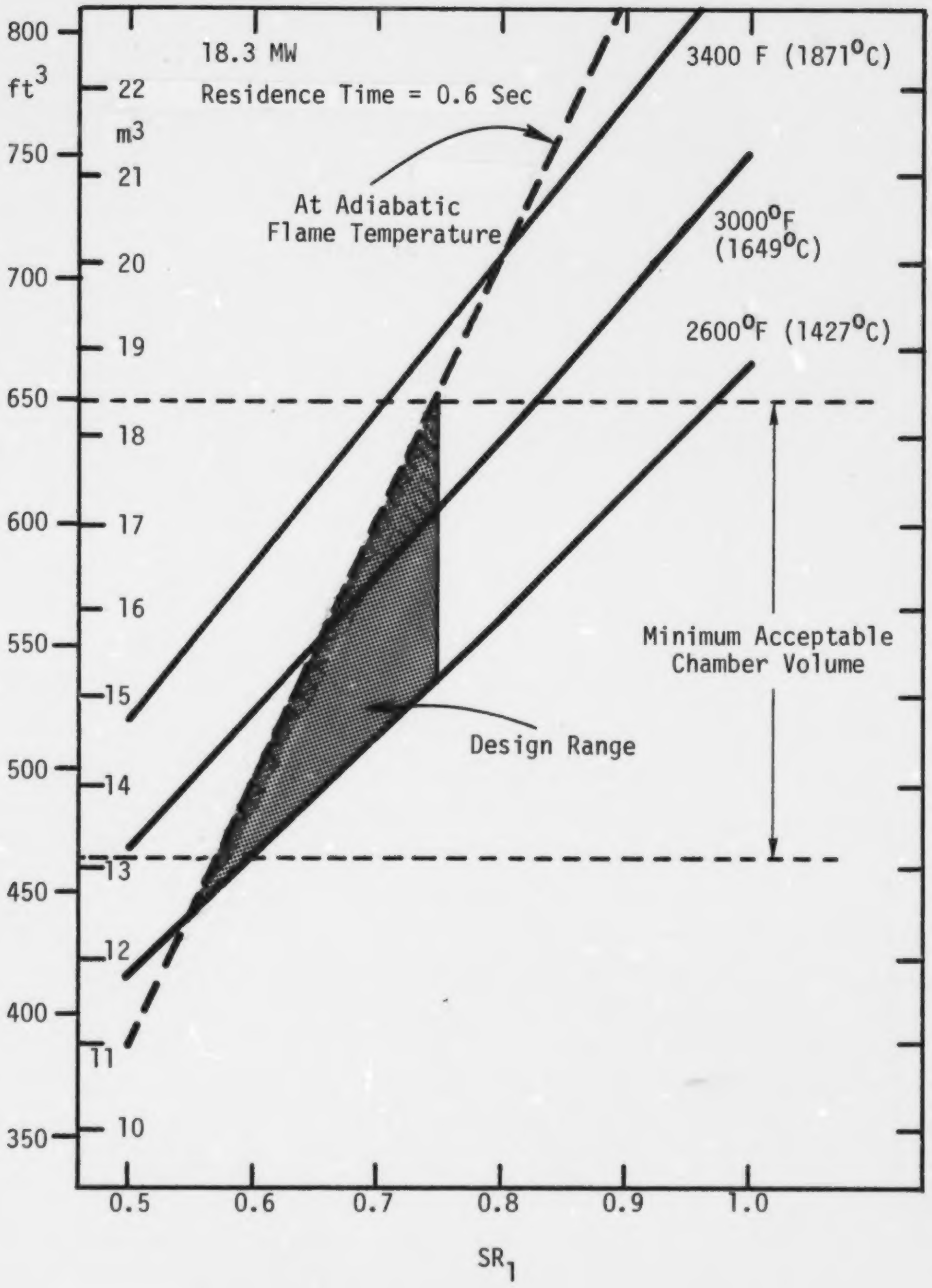

Figure 5-5. Required first-stage volume versus stoichiometry.

burners of the same design. Therefore it was decided to use the highest L/D ratio possible within the constraints imposed by the steam generator.

Figure 5-6 compares internal burner dimensions for L/D ranging from 0.5 to 3.0 for a first-stage volume of 18.4 $m^3$ (650 $ft^3$). It can be seen from the figure that at L/D = 0.5 the internal diameter of the first stage would exceed the external diameter of the steam generator. This would impose unnecessary retrofit and transportation costs as described in Chapter 4. In addition, uniform mixing approaching plug flow would be nearly impossible to achieve.

At L/D = 3, the internal length of the first stage is almost 6 meters (19 feet) long. Although in some instances this would not be unacceptable in terms of the steam generator retrofit, in many cases the overall required extension to the steam generator skid would not be possible.

The host steam generator for the field test is limited to a total skid extension of 3 meters (10 feet) due to a nearby roadway. The maximum allowable first-stage length was determined to be approximately 5.5 meters (18 feet) including windbox and register assemblies. This limits the maximum L/D to approximately 2.3 for a volume of 18.4 $m^3$, neglecting the thickness of the lining.

The choices for entrance configuration were limited to conical geometry as more complicated geometries would be costly to construct. The 3-MW pilot-scale burner was constructed with a flat front wall. A conical transition from the primary air throat could improve mixing across the diameter by causing the flow from the central register to expand thereby reducing recirculation in "dead zones." However, it has been observed that some flows, particularly those with high swirl levels, tend to attach (Coanda effect) to a nearby wall thereby inducing substantial asymmetry in the bulk flow pattern. This had been observed with one of the premixer concepts tested in the 1 MW pilot-scale prototype. It was decided to design the entrance wall of the first-stage flat in order to avoid induced flow asymmetry and simplify construction.

The exit of the first stage must be reduced to achieve the exit velocity prescribed by the conceptual design criteria. This reduction in diameter is also desirable to reduce heat losses from the first-stage by radiation. A conical exit transition was selected in order to minimize "dead zones" and

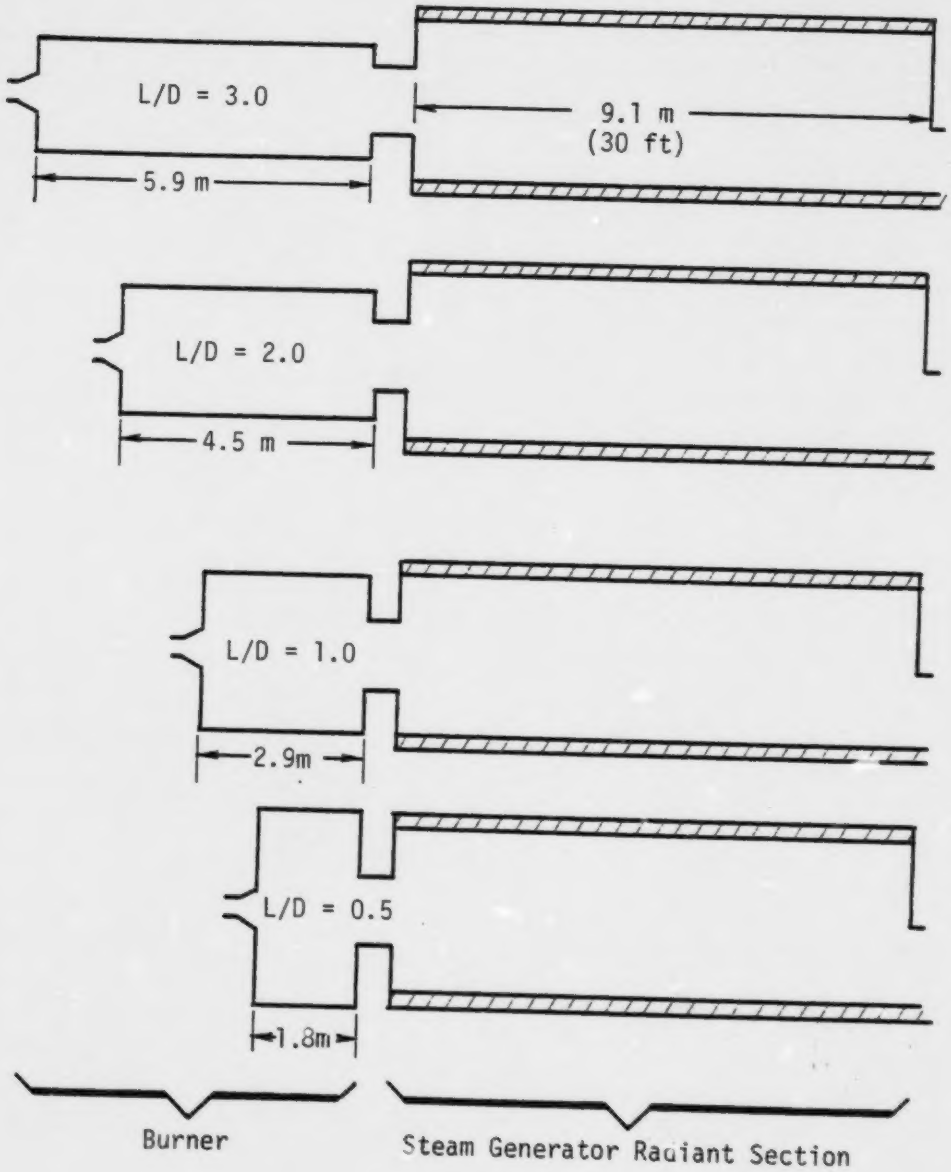
L/D = 3.0
9.1 m
(30 ft)
5.9 m
L/D = 2.0
4.5 m
L/D = 1.0
2.9m
L/D = 0.5
1.8m
Burner
Steam Generator Radiant Section

Figure 5-6. Internal dimensions of burner for different length-to-diameter ratios.

recirculation at the first stage exit. The half-angle of the cone was chosen to be 30 degrees to simplify construction and minimize aggravation of mechanical stresses.

The overall hardware design criteria are summarized in Table 5-3.

### 5.1.3 First-Stage Air/Fuel Mixing

The isothermal screening and pilot-scale combustion tests indicated that although premixing of fuel and first-stage air is desirable, it is difficult to achieve at large scale. Atomizers do not scale and larger mean and maximum dropsizes are produced as capacity increases. It was determined that a conventional commercial twin-fluid atomizer design would suffice, as long as the spray pattern was optimized. The conceptual design development studies indicated that variable primary air swirl and a moderate (25-30 m/sec) throat velocity are necessary. A commercial burner air register and oil gun assembly was selected which satisfied these criteria. Throat diameter is 38 cm and an internal mixing atomizer with interchangeable tips providing spray angles from 50 to 90 degrees is used. Further information is contained in Appendix C.

## 5.2 Refractory Materials

The lining for the first-stage is a key component of the burner hardware design. The properties of various materials and methods of construction must be selected to match the design requirements and evaluated to estimate how durable the lining will be. Refractory materials are required to maintain the high gas temperatures dictated by the conceptual design. The primary objective of the lining design task is to optimize the amount and type of refractory required to minimize the cost and thermal inertia of the lining, but still meet requirements for mechanical strength under the process conditions. The process conditions most significant to the proper material selection are:

- High gas temperatures, approximately 1500-1800°C; with no net heat loss.

TABLE 5-3. OVERALL HARDWARE DESIGN CRITERIA FOR FIRST STAGE

| | |
|---|---|
| Volume | Conservative 18.5 m$^3$ (650 ft$^3$)<br>Minimum 13.2 m$^3$ (465 ft$^3$) |
| Configuration | Horizontal Cylinder |
| L/D | Maximum Within Retrofit Constraints |
| Entrance Configuration | Flat Wall |
| Exit Configuration | Conical--30-Degree Half-Angle |
| Heat Loss | None |
| Expected gas Temperature | 1500-1800°C |

- Fuel-rich (reducing) atmosphere containing as much as 19 percent CO, 12 percent $H_2$, 6 percent $H_2O$, and trace amounts of corrosive gases such as $H_2S$ and $NH_3$.
- Occasional rapid changes in gas temperature.

The most severe mechanical stresses are induced by constraining expansion (external stresses) and by rapid temperature changes (internal stresses). Thus the mechanical environment influences material selection.

### 5.2.1 Refractory Properties

Refractory materials encompass nonmetallic ceramics which are resistant to high temperature and chemical attack. This includes materials such as alumina ($Al_2O_3$), silica ($SiO_2$), magnesia (MgO), zirconia ($ZrO_2$), and graphite. Frequently these pure materials are mixed in varying proportions with hydraulic cements such as lime (CaO), and with stable metal oxides such as chromic oxide ($Cr_2O_3$) and titania ($TiO_2$) and then fired at high temperatures to produce a material which has the combination of strength, porosity, chemical stability, and insulating value desired for a particular application. A staggering number of different materials are available from refractory manufacturers, each suited for a particular application. Many of the materials were developed for specific uses in the iron and steel industry. Refractories of different materials are available from refractory manufacturers, each suited for a particular application. Many of the materials were developed for specific uses in the iron and steel industry. Refractories are also widely used in oil refining, coal gasification, and in glass making.

These materials are generally available in three forms: moldable, brick, and fiber. Moldable materials include castable and gunnable refractories, obtained as a crushed dry material which is mixed with water and then poured into forms or sprayed (gunned) onto a surface. Plastic refractory ("ram mix") is sold as slabs or granules of clay-like material which is pounded (or rammed") into shape using mallets or air hammers.

Refractory materials are also available as bricks, which are mixed, molded and prefired at the factory to controlled sizes and shapes. The bricks are installed masonry-style, often using refractory mortar, to form the desired shape. Refractory brick is available in standard sizes and shapes (straight, arch, wedge, circle, etc) or can be custom-ordered.

Refractory can also be fabricated into fibers which are then formed into a matrix and can be obtained in board, blanket, and bulk form. Fiber matrices are generally useful because of their high insulating value. Generally it is necessary to first consider the service temperature limit when selecting which refractory material is best suited for particular applications. The temperature ranges of typical high temperature refractories is shown in Figure 5-7 and Table 5-4. Several materials appear to have the required temperature resistance; however, resistance to chemical attack must also be considered. Slagging environments, such as in coal gasifiers or the throats of coal-fired burners, are particularly severe for most refractory. Slag penetrates into the refractory pores, and when the refractory is cooled and heated, high stresses develop due to different thermal expansion coefficients in the penetration layer, leading to a phenomenon known as spalling. Spalling is the cracking or rupturing of refractory which usually results in detachment of a surface layer. Slag can also react chemically with some refractory components to lower the fusion point leading to thermal failure below the rated service temperature.

Reasons for spalling can be loosely categorized into three categories. Thermal spalling is due to an uneven temperature gradient which sets up internal stresses in excess of the failure stress. Mechanical spalling is due to compressive stresses resulting from constrained thermal expansion. Structural spalling is caused by slag penetration or chemical changes in a surface layer resulting in a different coefficient of thermal expansion at the surface than in the body of the lining. The prototype commercial burner will not be subjected to high levels of slag since the crude oil contains relatively low levels of ash, therefore slagging resistance is not of primary concern. Spalling resistance to thermal transients is, however, very important because of the potential for uncontrolled upsets when rapid temperature changes may occur. The problem of mechanical constraint is primarily a design problem and is dealt with in a later section.

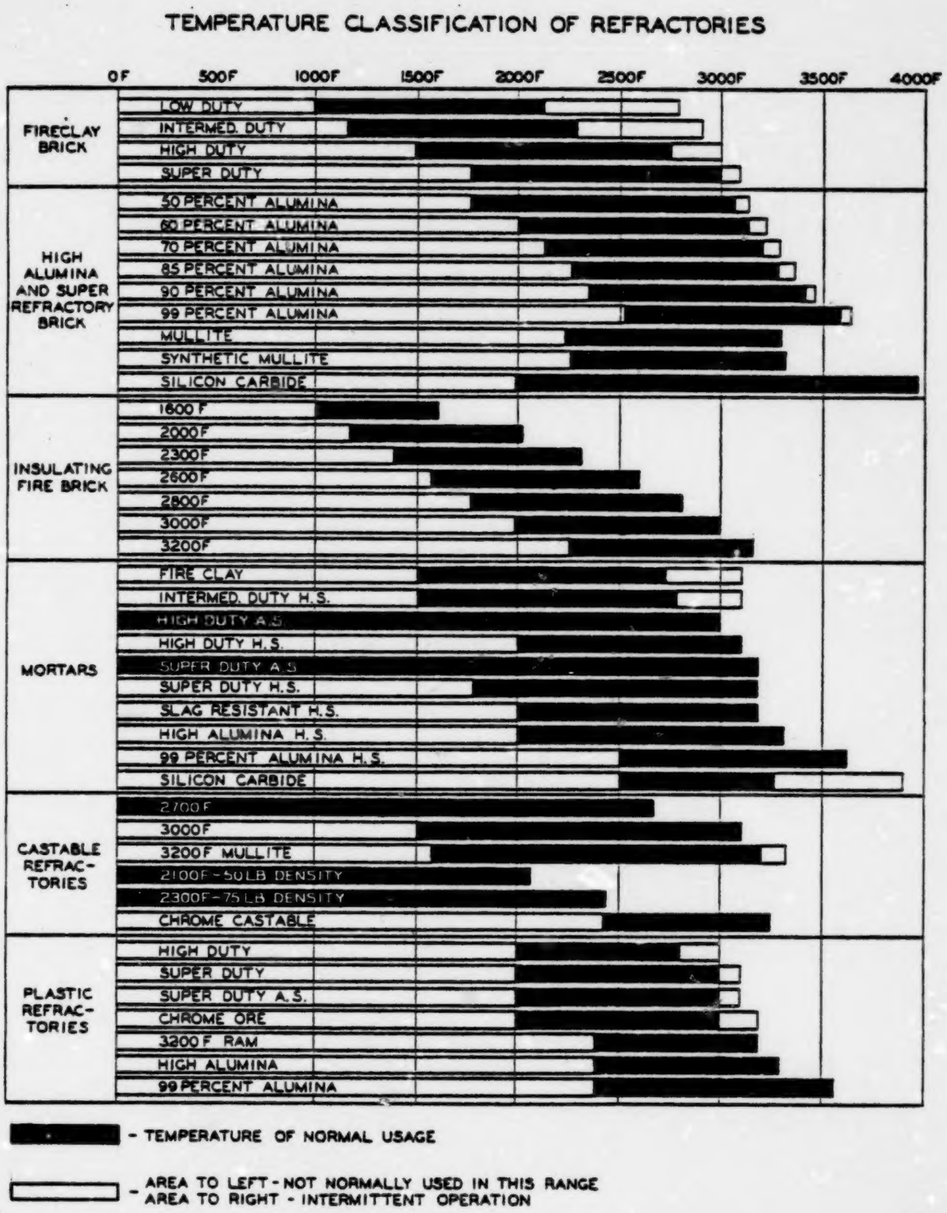

Figure 5-7. Temperature ranges for various refractory materials (from Fryling, 1966, published by permission from Combustion Engineering)

## TABLE 5-4. GENERAL PHYSICAL AND CHEMICAL CHARACTERISTICS OF REFRACTORY BRICK (FROM PERRY, J. H., AND C. H. CHILTON, "CHEMICAL ENGINEER'S HANDBOOK." 5th ED., MC GRAW-HILL, N.Y., 1973. REPRODUCED WITH PERMISSION OF MC GRAW-HILL BOOK COMPANY)

| Type of brick | Typical composition | Approx. bulk density, lb./cu.ft. | Fusion point, °F. | Chemical nature | Deformation under hot loading | Apparent porosity, % | Permeability | Hot strength | Thermal shock resistance | Chemical resistance | |
|---|---|---|---|---|---|---|---|---|---|---|---|
| | | | | | | | | | | To acid | To alkali |
| Silica | $SiO_2$, 95% | 115 | 3100 | Acid | Excellent | 21 | High | Excellent | Poor[‡] | Good | Good at low temperatures |
| High-duty fire clay | $SiO_2$, 54%<br>$Al_2O_3$, 40% | 134 | 3125 | Acid | Fair | 18 | Moderate | Fair | Fair | Good | Good at low temperatures |
| Superduty fire clay | $SiO_2$, 52%<br>$Al_2O_3$, 42% | 140 | 3170 | Acid | Good | 15 | High | Fair | Good | Good | Good at low temperatures |
| Acid-resistant (type H) | $SiO_2$, 59%<br>$Al_2O_3$, 34% | 142 | 3040 | Acid | Poor | 7 | Low | Poor | Good | Insoluble in acids except HF and boiling phosphoric | Very resistant in moderate concentrations |
| Insulating brick | Varies | 30–75 | Varies | ... | Poor | 65–85 | High | Poor | Excellent | Poor | Poor |
| High-alumina | $Al_2O_3$, 50–85% | 170 | 3200–3400 | Slightly acid | Good | 20 | Low | Good | Good | Good except for HF and aqua regia | Very slight attack with hot solutions |
| Extra-high-alumina | $Al_2O_3$, 90–99% | 185 | 3000–3850 | Neutral | Excellent | 23 | Low | Excellent | Good | | |
| Mullite | $Al_2O_3$, 71% | 153 | 3290 | Slightly acid | Excellent | 20 | Low | Good | Good | Insoluble in most acids | Slight reaction |
| Chrome-fired | Chrome ore, 100% | 195 | Varies | Neutral | Fair | 20 | Low | Good | Poor | Fair to good | Poor |
| Magnesite-chrome bonded[§] | MgO, 50–80%<br>$Cr_2O_3$, 5–18%<br>$Fe_2O_3$, 3–13%<br>$Al_2O_3$, 6–11%<br>$SiO_2$, 1.2–5% | 190 | Varies | Basic | Good | 12 | Very low | Good | Excellent | Fair except to strong acids | Fair resistance at low temperatures |
| Magnesite-chrome fired | | 180 | | | Excellent | 20 | High | Good | Excellent | | |
| Magnesite-chrome high-fired | | 180 | | | Excellent | 18 | High | Excellent | Excellent | | |
| Magnesite-bonded[§] | MgO, 95% | 181 | 3900 | Basic | Good | 11 | Low | Good | Good | Soluble in most acids | Good resistance at low temperatures |
| Magnesite-fired | | 178 | | | Good | 19 | Moderate | Good | Good | | |
| Zircon | $ZrO_2$, 67%<br>$SiO_2$, 33% | 200 | 3100[†] | Acid | Excellent | 25 | Very low | Excellent | Good | Very slight | Very slight |
| Zirconia (stabilized) | $ZrO_2$, 94%<br>CaO, 4% | 245 | 4800 | Slightly acid | Excellent | 23 | Low | Excellent | Excellent | Very slight | Very slight |
| Silicon-carbide | SiC, 80–90% | 160 | 4175 | Slightly acid | Excellent | 15 | Very low | Excellent | Excellent | Slight reaction with HF | Attacked at high temperatures |
| Graphite | C, 97% | 105 | 6400 | Neutral | Excellent | 16 | Low | Excellent | Excellent | Insoluble | Insoluble |

[*] From *Chem. Eng.*, July 31, 1967, p. 100.

[†] Dissociates above 3100 F.

[‡] Good above 1200 F.

[§] Chemically bonded.

Spalling is most often a low-temperature problem. Refractories exhibit substantial creep rates at high temperature and therefore stresses due to thermal expansion are relieved before failure occurs. Creep is dependent upon viscosity, which increases exponentially with decreasing temperature. When the rate of thermal expansion exceeds the rate at which the material relaxes due to creep, stresses can build to the point of failure. This is most likely to occur at low temperatures where creep is negligible. Very little is actually known on the creep behavior of refractory materials.

Thermal stresses and risk of creep failure are minimized by slow heating and cooling, providing allowance for thermal expansion in the design, and avoiding load concentrations.

Service temperature data is usually expressed for oxidizing atmospheres unless otherwise stated. Reducing atmospheres can lead to refractory failure due to the partial pressure of CO and hydrogen. Hydrogen acts to increase the thermal conductivity of a material leading to fusion of surrounding layers. Carbon monoxide will oxidize iron impurities in the refractory and deposit carbon at temperatures near 500°C, which leads to the formation of cracks due to differential thermal expansion rates. Carbon monoxides can also oxidize silica ($SiO_2$) to SiO, which is a vapor at high temperatures, leading to sintering of the material. Carbon dioxide and water vapor attack refractories at high temperatures.

Mechanical strength and ductility must also be considered in selecting an appropriate material. Generally, however, materials for use above 1400°C trade off tensile strength and ductility for temperature resistance. Although compressive strength may be high, the brittleness inherent in very high temperature materials makes them very susceptible to thermal shock. In most cases, once temperature and atmosphere requirements have been specified, there is little choice in terms of mechanical strength. Therefore, the burden is on the designer to create a mechanical design which will accommodate the strength limits of the refractory in addition to the process requirements. This is discussed more completely in later sections dealing with the mechanical design of the two burner concepts.

Thermal shock resistance, a transient operation phenomenon, is critical in selection of materials for both burner linings. The burner is likely to experience rapid temperature changes during light-off and shutdown, or when a power failure or limit trip occurs. This can lead to severe cracking or failure, particularly when the lining heat capacity is large. Several factors contribute to the thermal shock resistance of a refractory material. One factor is those properties which determine the stresses which are induced in the material during thermal transients. These include thermal properties, primarily thermal conductivity and specific heat, which can be and usually are temperature-dependent properties. The important mechanical properties are modulus of elasticity, thermal expansion coefficient, Poisson's ratio, and creep rate. These properties are also very temperature-dependent, thus for a layer of refractory which experiences a large temperature gradient both mechanical and thermal properties are nonisentropic.

A second factor determining thermal shock resistance is the ability of the material to arrest the propagation of cracks. Cracks form when stresses exceed the failure stress of the material. Cracks propagate when the strain (displacement) does not relieve this stress (force). Crack resistance is enhanced in high-alumina bricks, for instance, by the presence of substantial amounts of silica. The silica has a much lower modulus of elasticity than alumina; thus, when a crack reaches a "pocket" of silica stress is relieved and propagation ceases. Pores also act as crack inhibitors, thus increasing porosity increases resistance to crack propagation; however, strength is reduced. Increased porosity is particularly undesirable in slagging environments as it allows for greater slag penetration. Adding silica to high-alumina refractory increases resistance to crack propagation but lowers temperature resistance (silica has a much lower fusion point than alumina), strength, and chemical inertness. Thus the material best suited for either burner concept is necessarily a compromise between temperature/atmosphere suitability, mechanical strength, and thermal shock resistance.

The task of determining the properties of various candidate materials is generally the responsibility of the refractory manufacturer. Typical data published by manufacturers is shown in Tables 5-5 to 5-7. The available data

## TABLE 5-5. PROPERTIES OF HIGH TEMPERATURE REFRACTORIES

(HARBISON-WALKER, 1983)

| BRAND | Refractory A | Refractory B |
|---|---|---|
| Max. Service Temperature °F | 3000 | 3300 |
| ASTM Class C-401 | E | F |
| Approx. % by Wt. Water Added to Cast 100 lbs | 10-12 | 8-10 |
| Lbs. Dry Mix Required/cu.ft. | 137 | 160 |
| Application | C-T-G | C-T-G |
| Bulk Density, lbs./cu.ft. After Drying at 230°F | 139 | 168 |
| MOR, psi, After Drying at 230°F | 400-800 | 1500-2100 |
| Hot MOR, psi at 1500°F | 520 | 1880 |
| Cold Crushing Strength, psi After Drying at 230°F | 1500-3500 | 7000-12,000 |
| Permanent Linear Change % After Drying at 230°F | Negligible | Negligible |
| Permanent Linear Change % After Heating: | | |
| at 1000°F | Negligible | Negligible |
| at 1500°F | 0.0 to -0.5 | Negligible |
| at 3000°F | +1.0 to 3.5 | 0.0 to -0.2 |
| at 3140°F | --- | 0.0 to -0.5 |
| CHEMICAL ANALYSIS | | |
| Silica ($SiO_2$) | 31.5% | 0.2% |
| Alumina ($Al_2O_3$) | 60.5 | 94.0 |
| Iron Oxide ($Fe_2O_3$) | 1.1 | 0.2 |
| Lime (CaO) | 3.5 | 5.3 |

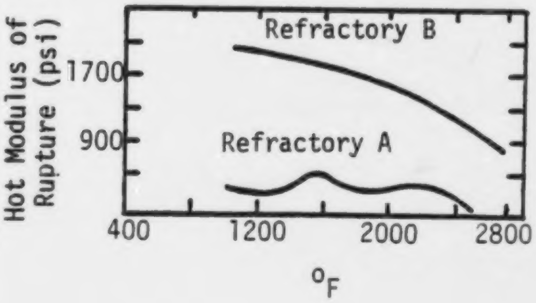

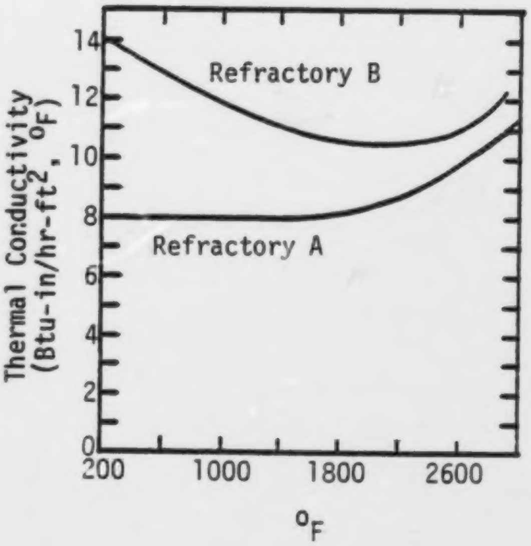

## TABLE 5-6. TYPICAL MATERIAL SPECIFICATION FOR LIGHTWEIGHT HIGH-ALUMINA BRICK

| CHARACTERISTICS | AN 599 |
|---|---|
| Typical Chemical Analysis (%) | |
| $Al_2O_3$ | 99.80 |
| $SiO_2$ | 0.05 |
| $Fe_2O_3$ | 0.06 |
| $K_2O$ and $Na_2O$ | 0.05 |
| $TiO_2$ | 0.04 |
| Maximum Use Temperature | |
| Oxidizing Atmosphere (°F) | 3400 |
| (°C) | 1870 |
| Reducing Atmosphere (°F) | 3300 |
| (°C) | 1815 |
| Bulk Density $(lbs/ft^3)$ | 84 |
| (g/cc) | 1.35 |
| Apparent Porosity (%) | 50 |
| Crushing Strength (psi) | |
| Room Temperature | 1350 |
| 1400°C or 2550°F | 315 |
| Hot Load % Deformation | |
| 25 psi @ 2640°F - 90 min | 0.6 |
| Linear Thermal Expansion | |
| per °C (30-1500°C) | $9.0 \times 10^{-6}$ |
| per °F (86-2732°F) | $5.0 \times 10^{-6}$ |
| Thermal Conductivity (BTU/hr/sq ft/in/F) | |
| @ 1000°F | 9.0 |
| 1500°F | 8.0 |
| 2300°F | 9.0 |
| 2900°F | 10.0 |
| Compressive Creep % Deformation | |
| 10 psi @ 2640°F - 300 hrs. | 4.0 |
| Specific Heat | 0.34 |

TABLE 5-7. TYPICAL MATERIALS SPECIFICATION FOR LIGHTWEIGHT HIGH-ALUMINA BRICK (HARBISON-WALKER INC, 1982, published by permission)

**KXL**

**Classification:** Lightweight High-Alumina Brick

| Physical Properties: (Typical) | English Units | SI Units |
|---|---|---|
| | $lb/ft^3$ | $kg/m^3$ |
| Bulk Density | 114 to 120 | 1,830 to 1,920 |
| Apparent Porosity, % | 40.0 to 45.0 | 40.0 to 45.0 |
| | $lb/in^2$ | kPa |
| Cold Crushing Strength on Flat | 4,000 to 6,000 | 27,600 to 41,400 |
| Modulus of Rupture | 700 to 1,400 | 4,800 to 9,700 |
| Reheat Test<br>Permanent Linear Change %<br>After Heating at 3140°F (1725°C) | +0.2 to +0.8 | |
| Load Test, 1½ Hrs. 25 psi (172 kPa)<br>% Linear Subsidence<br>After Heating at 3200°F (1760°C) | 2 to 5 | |
| Panel Spalling Test<br>% Loss<br>Preheat: 3000°F (1650°C) | 0.0 | |

**Thermal Conductivity:**

| Temperature °F. | Btu/hr. ft.$^2$°F/in. | Temperature °C. | Kcal/hr. m$^2$ °C/m |
|---|---|---|---|
| 500 | 10.40 | 400 | 1.19 |
| 1000 | 9.25 | 600 | 1.13 |
| 1500 | 9.00 | 800 | 1.12 |
| 2000 | 9.45 | 1000 | 1.04 |

**Chemical Analysis:**
(Approximate)

| | | |
|---|---|---|
| Silica | ($SiO_2$) | 17.3% |
| Alumina | ($Al_2O_3$) | 82.0 |
| Iron Oxide | ($Fe_2O_3$) | 0.3 |
| Lime | ($CaO$) | 0.2 |
| Magnesia | ($MgO$) | 0.1 |
| Alkalies | ($Na_2O+K_2O+Li_2O$) | 0.2 |

Protected by U.S. Letters Patent No. 3,269,850.

The above data are typical of the properties of commercial 9" straight brick. The data are subject to reasonable variations and therefore should not be used for specification purposes.

ASTM Test Methods, where applicable, used for determination of data.

is usually limited to service temperature, thermal conductivity, and various ASTM tests to assess strength and durability. Different test procedures generally apply to brick and castable refractories. Some manufacturers also have special test procedures which they have developed to determine other properties.

Table 5-8 lists the commonly employed ASTM tests for which data are available from manufacturers. In general, these tests indicate relative material performance under controlled environment and test conditions. Significant variations in the reported properties are often found in practice due to several reasons. Typically, a range of values is given for material properties as can be seen in Tables 5-5 to 5-7. This range is generally attributed to lot-to-lot variations in material composition, preparation, and firing. The range of variation for castable materials is typically much greater than for brick, since brick is molded and fired to controlled factory tolerances, whereas castable materials are prepared and fired in the field where control over mixture consistency and application is much more difficult.

It is desirable to determine certain fundamental material properties in certain instances where an engineering analysis of the design is desired. Such data as modulus of elasticity (reversible), coefficient of thermal expansion, Poisson's ratio, surface emissivity, and specific heat is often not available or difficult to measure. Some manufacturers use a rule-of-thumb approach to determining these properties. For instance, A. P. Green recommends estimating modulus of elasticity by multiplying modulus of rupture data by a constant. This is a crude estimate at best but may indicate the actual uncertainty due to production variations. Data for various high-alumina brick tested by Larson, et al (1974) is shown in Table 5-9. It can be seen from the table that nearly a five-fold variation in Young's modulus (modulus of elasticity) was observed among several brick containing 90 percent alumina. Modulus of elasticity and coefficient of thermal expansion are typically $2 \times 10^{11}$ Pa ($30 \times 10^6$ psi) and $3.6 \times 10^{-6}$ per degree centigrade ($6.5 \times 10^{-6}$ per degree F), respectively, for mild steel. It is also seen that the data for mixtures vary significantly from pure materials by comparison with Table 5-10. These properties are also temperature-dependent. In Table 5-11, surface emissivity data is summarized for alumina and silica materials and it is evident that there is a strong dependence on temperature, grain size, and composition.

TABLE 5-8. TYPICAL ASTM TESTS FOR REFRACTORY MATERIALS

| Test | ASTM # | Data Produced | Qualitative Interpretation | Application |
|---|---|---|---|---|
| Hot Load Deformation | C16 | Percent deformation under 25 psi load at temperatures near service temperature limit. | Dimensional stability under 25 psi load at operating temperature; creep rate. | |
| Hot Modulus of Rupture | C268 | Point load force required to break a sample, supported near the ends and loaded at the center, at elevated temperature. | Changes in tensile failure strength with temperature. | Castable |
| Cold Crushing Strength | C133 | Force required to break evenly loaded test specimen in compression. | Compressive failure strength of fired but unheated material. | Brick<br>Castable |
| Reheat Test | C113 | Percent permanent linear change of brick after heating to specified temperature and coded. | Dimensional stability of brick under no external lead after heating. | Brick |
| Permanent Linear Change | C269 (Discontinued) | Percent linear change of test specimen upon initial heating to specified temperature and subsequent cooling. | Expected shrinkage or expansion of castable refractory upon first heating cycle. | Castable |
| Thermal Conductivity | C201 or Other | Thermal conductivity at various mean sample temperatures. | Insulating value of material samples under controlled conditions. | Brick<br>Castable |

## TABLE 5-9. PROPERTIES OF VARIOUS HIGH-ALUMINA BRICK

| Refractory No. | $Al_2O_3$ (%) | Modulus of Rupture (psi) | Young's Modulus ($10^6$ psi) | Coeff. of th. exp. ($10^{-4}$ $^oC^{-1}$) |
|---|---|---|---|---|
| 1 | 99 | 3600 ± 300 | 17.0 | 9.3 |
| 2 | 99 | 2060 ± 300 | 8.5 | 9.4 |
| 3 | 90 | 3230 ± 500 | 12.2 | 7.5 |
| 4 | 90 | 2830 ± 240 | 11.5 | 8.1 |
| 5 | 90 | 2470 ± 590 | 9.0 | 8.2 |
| 6 | 90 | 2760 ± 380 | 8.1 | 8.0 |
| 7 | 90 | 2020 ± 200 | 2.7 | 8.1 |
| 8 | 85 | 1980 ± 230 | 8.9 | 7.8 |
| 9 | 85 | 2940 ± 300 | 9.4 | 7.6 |
| 10 | 85 | 4400 ± 310 | 10.1 | 7.6 |
| 11 | 85 | 1793 ± 200 | 5.0 | 7.6 |
| 12 | 85 | 2170 ± 180 | 7.5 | 7.4 |
| 13 | 85 | 1540 ± 90 | 9.0 | 7.3 |

### TABLE 5-10. PHYSICAL PROPERTIES OF PURE REFRACTORIES

(FROM BANNISTER, ET AL., 1958)

| Material | Density, per cm$^3$ | Modulus of rupture, $10^3$ lb/in$^2$ at 70$^0$F | Modulus of rupture, $10^3$ lb/in$^2$ at 1800$^0$F | Modulus of elasticity, $10^6$ lb/in$^2$ at 70$^0$F | Fusion point, $^0$F | Linear coeff. of expansion, $10^{-6}$ in/in $^0$F between 65 and 1800$^0$F | Thermal conductivity, Btu/(in)(ft$^2$)(h)($^0$F) at 212$^0$F | Thermal conductivity, Btu/(in)(ft$^2$)(h)($^0$F) at 1800$^0$F | Specific heat, Btu/(lbm)($^0$F) | Thermal stress resistance |
|---|---|---|---|---|---|---|---|---|---|---|
| $Al_2O_3$ | 3.97 | 100 | 60 | 53 | 3690 | 5.0 | 210 | 55 | 0.26 | Good |
| BeO | 3.03 | 20 | 10 | 45 | 4660 | 4.9 | 1450 | 130 | 0.50 | Very good |
| MgO | 3.58 | 14 | 12 | 31 | 5070 | 7.5 | 240 | 47 | 0.25 | Poor |
| $ThO_2$ | 10.00 | 12 | 7 | 21 | 5520 | 5.0 | 62 | 20 | 0.06 | Fair |
| $ZrO_2$ | 5.60 | 20 | 15 | 22 | 4600 | 5.5 | 15 | 15 | 0.14 | Fair |
| $UO_2$ | 10.96 | 12 | -- | 25 | 5070 | 5.6 | 58 | 20 | 0.06 | Fair |
| SiC | 3.22 | 24 | 24 | 68 | 5000+ | 2.2 | 390 | 145 | 0.20 | Excel. |
| BC | 2.52 | 50 | 40 | 42 | 4440 | 2.5 | 200 | 145 | 0.36 | Good |
| BN | 2.25 | 7 | 1 | 12 | 5000 | 2.6 | 150 | 130 | 0.39 | Good |
| $MoSi_2$ | 6.20 | 100 | 40 | 50 | 3890 | 5.1 | 220 | 100 | 0.11 | Good |
| C | 2.22 | 3 | 4 | 2 | 7000 | 2.2 | 870 | 290 | 0.34 | Good |

TABLE 5-11. NORMAL TOTAL EMISSIVITIES OF VARIOUS SURFACES

| Surface | t, °F | |
|---|---|---|
| Alumina (99.5-85 $Al_2O_3$; 0-12 $SiO_2$; 0-1 $Fe_2O_3$). Effect of mean grain size, microns (μ) | 1850-2850 | --- |
| 10 μ | | 0.30-0.18 |
| 50 μ | | 0.39-0.28 |
| 100 μ | | 0.50-0.40 |
| Alumina-silica (showing effect of Fe) | 1850-2850 | --- |
| 80-58 $Al_2O_3$; 16-38 $SiO_2$; 0.4 $Fe_2O_3$ | --- | 0.61-0.43 |
| 36-26 $Al_2O_3$; 50-60 $SiO_2$; 1.7 $Fe_2O_3$ | --- | 0.73-0.62 |
| 61 $Al_2O_3$; 35 $SiO_2$; 2.9 $Fe_2O_3$ | --- | 0.78-0.68 |
| Silica (98 $SiO_2$; Fe-free), effect of grain size, microns (μ) | 1850-2850 | --- |
| 10 μ | --- | 0.42-0.33 |
| 70-600 μ | --- | 0.62-0.46 |

The uncertainty or unavailability of data required for engineering analysis make such analysis only qualitative at best. The impact of this uncertainty is treated in later sections.

### 5.2.2 Materials for Prototype Commercial Burner Concepts

The selection of materials compatible with the design concepts was based on consideration of:

- Thermal and chemical environment
- Refractory life
- Construction method
- Mechanical design

Thermal and chemical environment has been extensively discussed; construction method and mechanical design constrain the practical extent to which refractory weakness can be allowed for; and these factors interact to determine the refractory lifetime. A secondary consideration for the prototype was cost. Reasonable effort was expended to ensure that the lining cost was commensurate with the degree of conservatism in the design.

Concept A, described in detail in the next section, utilizes a multilayer castable refractory design. Thermal and chemical environment dictated that a high-alumina material with 85 percent or greater alumina content be used. Pilot-scale prototype experience showed that a 99 percent alumina lightweight castable gave the best combination of temperature, chemical, and thermal shock resistance. After consultation with several refractory manufacturers and completing a survey of available materials, this same material was recommended for the full-scale prototype. Selection of the subsequent insulating materials was based on minimizing thickness to achieve an external shell temperature below 100°C.

Table 5-12 lists the known properties of these materials. A lightweight "bubble" alumina castable was chosen for the inner layer primarily because of enhanced crack resistance over dense high-alumina castable linings. This material is made by blowing steam through a sheet of molten alumina to form hollow alumina spheres ranging in size from about 1 to 5 mm diameter. These are then

TABLE 5-12. KNOWN PROPERTIES OF MATERIALS SELECTED FOR CONCEPT A, MULTILAYER CASTABLE REFRACTORY LINING

| Type | Lightweight "Bubble" Alumina Insulating Castable | Lightweight Insulating Castable | Insulation Block |
|---|---|---|---|
| Maximum Service Temp. | 1815°C | 1430°C | 870°C |
| Composition: | | | |
| $SiO_2$ | 0.4% | 37.4 | |
| $Al_2O_3$ | 92.6% | 52.8 | |
| $Fe_2O_3$ | 0.03% | 0.6 | |
| CaO | 6.8% | 7.0% | |
| Bulk Density After Drying $kg/m^3$ | 1585 | 881 | 336 |
| Modulus of Rupture After Drying, Pa | $3.7x10^6$ | $0.6x10^6$ to $1.1x10^6$ | $0.2x10^6$ to $0.4x10^6$ |
| Cold Crushing Strength After Drying, kPa | $2x10^4$ | $1.8x10^3$ to $3x10^3$ | $3.9x10^6$ to $5.9x10^2$ |
| Permanent Linear Change After Drying, After Heating to: | Negligible | Negligible | Negligible |
| 540°C | | -0.2 to -0.5% | Negligible |
| 815°C | -0.2% | -0.2 to -0.5 | Negligible |
| 1370°C | | +1.0 to +3.0 | |
| 1760°C | -0.6% | - | - |
| Thermal Conductivity $kcal\text{-}m/hr\text{-}m^2\text{-}^oC$: | | | |
| 260°C | 0.71 | 0.20 | 0.05 |
| 540°C | 0.66 | 0.22 | 0.08 |
| 815°C | 0.63 | 0.24 | - |
| 1095°C | 0.63 | 0.26 | - |
| 1370°C | 0.67 | 0.33 | - |
| Application | Inner Layer | Backup Layer (Intermediate) | Backup Layer (External) |

mixed with finely-ground conventional alumina and hydraulic cements which produces a lightweight castable of high porosity and low thermal conductivity. The bubbles act to stop the propagation of cracks through the lining. Secondary advantages of this material are that it has low density and relatively low thermal conductivity. It contains 92 percent alumina and is therefore inert to chemical attack. The primary disadvantage of this material is its low mechanical strength compared to dense castables.

The materials selected for the backup layers are conventional insulating refractory. The intermediate layer is a 1430°C insulating castable which contains 37 percent silica and 57 percent alumina. The high silica content of this material makes it unsuitable for direct contact with 1800°C reducing gases; however, it has very good insulating value and thermal shock resistance. Insulating castables such as this one are typically low in strength but are much more ductile than high-alumina meterials. The external layer is block insulation, fireclay mixture which is preformed and fired. This material has very low thermal conductivity and therefore is a good insulator. This material was chosen instead of castable because the castable equivalent has a high (1.5 percent) shrinkage on firing. The block insulation does not shrink on firing, which is desirable from the mechanical design aspects.

Several properties of these materials required to conduct an engineering analysis are not available from the manufacturer or other sources. A literature survey conducted by Davy McKee Corporation produced the estimated properties shown in Table 5-13.

The design for Concept B utilizes a single thin layer of refractory surrounded by a double-shell arrangement which is air-cooled. Certain aspects of this design make castable refractories unsuitable. This design requires that a large thermal gradient exist across the thin lining. This would produce very high tensile stresses in a continuous monolithic lining as described in the design report in Appendix A. A castable lining could be formed with construction joints, resulting in a segmented lining which would prevent tensile stresses from building up. This method of construction could tend to undermine the overall strength of the lining, particularly in consideration of the shrinkage the castable material undergoes during firing. Fiber-based materials

TABLE 5-13. ESTIMATED MATERIAL PROPERTIES USED IN ENGINEERING ANALYSIS OF CONCEPT A

| Material | | "Bubble" Alumina (Inner Layer) | Insulating Castable (Intermediate Layer) | Castable Insulation Block (External Layer) |
|---|---|---|---|---|
| Specific Heat | $C_p$ | 0.24 | 0.23 | 0.22 |
| Modulus of Elasticity (Young's Modulus) (Pa) | E | $5.5 \times 10^{10}$ | $4.5 \times 10^{10}$ | $3.4 \times 10^{7}$ |
| Poisson's Ratio | $\nu$ | 0.15 | 0.15 | 0.15 |
| Coefficient of Thermal Expansion: | $\alpha$ | | | |
| 240°C | | $2.7 \times 10^{-6}$ | $4.0 \times 10^{-6}$ | $10 \times 10^{-6}$ |
| 1800°C | | $5.5 \times 10^{-6}$ | | |

would be ideal for this application from a mechanical point of view. They are extremely shock-resistant, very lightweight, and have very low thermal conductivity; therefore, a very thin lining could be used. The maximum service temperature for these materials is typically only 1540°C, however, and tend to collapse rapidly above this temperature; also, abrasion resistance is very low and direct flame impingement could lead to failure. A single layer of high-alumina, mullite-bonded brick was therefore chosen for this application based on recommendations from the refractory manufacturers. Properties of this material are shown in Table 5-14.

## 5.3 First-Stage Concept A--Insulated Lining Design

The first ot two designs which emerged from the conceptual design study is based on a multilayer castable insulating refractory construction. The essential features of this design are shown in Figure 5-8. The cross-section of the chamber is circular, with a flat wall at the inlet end and a conical exit wall. Chamber L/D is approximately 2, neglecting the conical exit section. The inner layer of refractory consists of 20 cm of "bubble" alumina insulating castable, described in the previous section. This layer is backed up by two insulating layers, the first of which is 1400°C insulating castable 23 cm thick, the second of which is a 1000°C insulating block 10 cm thick. The entire assembly is contained in a 9.5 mm thick carbon steel rolled shell. The shell is reinforced with rolled I-beam to add rigidity. Refractory anchors are attached to the shell with stainless steel links, and extend through to the inside diameter in order to prevent the inner layer of refractory from failing catastrophically. The anchors are widely spaced around the top two-thirds of the shell circumference, as shown in the section view.

The thickness of each refractory layer was determined by prescribing the interface temperatures to be near the maximum use limit of the backup material, and the external shell temperature to be below 100°C, preferably below 65°C. Total lining thickness is minimized by judicious selection of material thermal conductivity. Total lining thickness of the final design was 53 centimeters (21 inches).

The internal dimensions of the chamber were determined by limiting the total external diameter to 3.4 meters (11 feet), roughly corresponding to the

TABLE 5-14. MANUFACTURER'S DATA ON MATERIAL SELECTED FOR REGENERATIVE LINER

TECHNICAL DATA

GREENAL-90

Pressed, 90% Alumina, Mullite Bonded Brick
Manufactured at Philadelphia, Pennsylvania

REHEAT (Permanent Linear Change)--A.S.T.M. C113
Contraction or Expansion at 3200°F ---------- 0.5-2% Exp.

HOT LOAD TEST--A.S.T.M. C16
Deformation at 3101°F ----------------------- 0.2% Dev.-0.5% Exp.

PANEL SPALLING TEST--A.S.T.M. C122
Preheat at 3000°F--Spalling Loss ------------ 0-1%

APPARENT POROSITY--A.S.T.M. C20 --------------- 12-25%

BULK DENSITY--A.S.T.M. C20
Grams per Cubic Centimeter ------------------ 2.96-3.02
Pounds per Cubic Foot ----------------------- 185-189

MODULUS OF RUPTURE--A.S.T.M. C133 -------------- 3000-4500 psi

COLD CRUSHING STRENGTH--A.S.T.M. C133 ---------- 12000-18000 psi

CHEMICAL ANALYSIS
Silica - $SiO_2$ ------------------------------- 9.0-11.0%
Alumina - $Al_2O_3$ ----------------------------- 89.0-91.0%
Iron Oxide - $Fe_2O_3$ ------------------------- 0.03-0.2%
Lime - CaO ------------------------------------ Trace
Magnesia - MgO -------------------------------- Trace
Titania - $TiO_2$ ------------------------------ Trace
Alkalies - $Na_2O + K_2O$ ---------------------- 0.15-0.25%

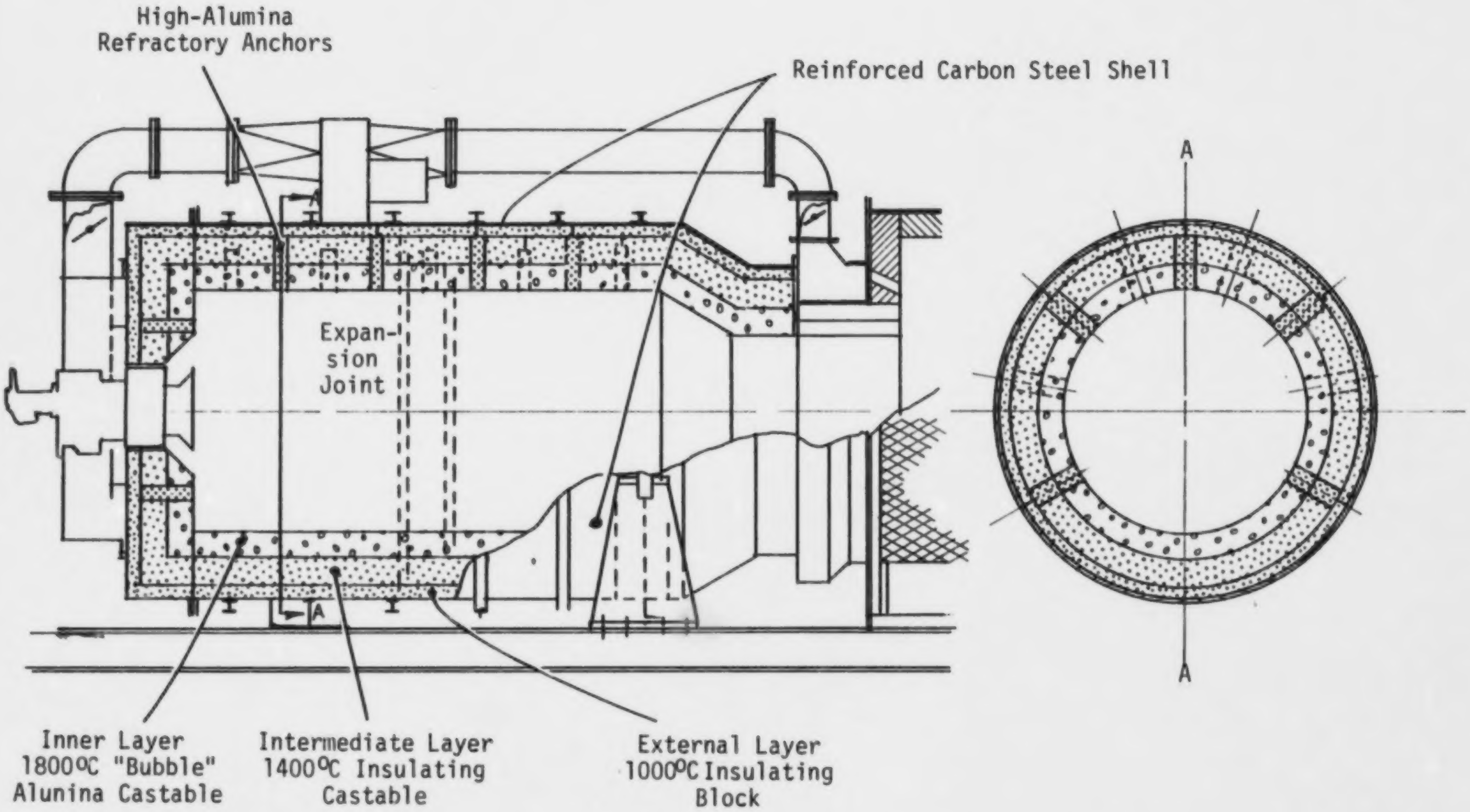
High-Alumina
Refractory Anchors
Reinforced Carbon Steel Shell
A
A
Expan-
sion
Joint
A
A
Inner Layer
1800°C "Bubble"
Alunina Castable
Intermediate Layer
1400°C Insulating
Castable
External Layer
1000°C Insulating
Block

Figure 5-8. Features of insulated first-stage lining design (Concept A).

diameter of the steam generator. The final external diameter, including reinforcing beams, was 3.3 meters. This produced a maximum internal diameter of 1.98 meters. Length was chosen to face within the constraints of the host steam generator and required volume. Total volume of the first-stage is 14 cubic meters, which is within the acceptable design range but on the low end. The 30-degree half-angle of the conical exit section was chosen to reduce stresses at the juncture of the cylinder and cone.

The detailed hardware design and analysis of this lining concept were carried out by Davy McKee Corporation. A full report of the study, including construction drawings, is included in this report as Appendix A. The highlights of the Davy McKee design and analysis are summarized in the following sections.

### 5.3.1 Design Considerations

The insulated concept was developed as a conservative approach to achieving high gas temperatures and low heat losses in the first stage. The design was recommended by Davy McKee in part because of their experience with steel mill and refinery equipment, for which this approach is common. The primary gases at the outset of the design were:

- Minimum heat loss to surroundings.
- Gas temperatures above 1450°C.
- 5-7 years refractory life without catastrophic failure or major repair.
- Reasonable cost.

It was realized that, based on pilot-scale prototype burner experience, there was substantial risk of lining failure after only a few thermal cycles which could necessitate complete lining replacement. After reviewing the low-$NO_x$ burner requirements, there appeared to be only scattered practical experience with linings subjected to the temperature and stresses expected in the full-scale burner.

An analytical study was conducted to assess lining performance, in the absence of practical experience. The value of such analysis is dependent upon the accuracy of the material properties and the skill of the engineer in selecting assumptions and test cases. A finite-element computer code was used to determine stress and temperature distributions for certain lining configurations (see Appendix A). Both steady-state and transient cases were examined.

Refractory failure is generally caused by

- chemical attack,
- erosion,
- inadequate dry-out (curing) procedures,
- thermal stresses due to rapid healing of cooling (thermal shock),
- thermal stresses due to load or dimensional constraints,
- poor installation.

Thermal stresses are the most likely cause of failure if the design, installation, and curing have been correctly executed. Thermal stresses due to dimensional or load constraints can be accounted for, to some extent, in the lining design; however, in practice, uncertainty in the material behavior can undermine such design allowances. Thermal stresses due to thermal shock arise due to nonuniform material properties within an unconstrained shape. These are particularly important when a large temperature gradient exists and material properties are temperature-dependent.

Assuming elastic behavior thermal stress $\sigma$ is given by a relationship of the general form

$$\sigma = \frac{E\alpha\Delta T}{2(1-\gamma)} \quad (S)$$

where E, $\alpha$, $\gamma$, and S are Young's modulus, thermal expansion coefficient, Poissan's ratio, and a factor related to shape, respectively. For a material which is constrained from expanding due to a temperature difference $\Delta T$, stress arises which is proportional to the temperature difference and material properties. Material properties are frequently not well known; they can vary with temperature and, for castable materials, with installation technique. Figure 5-9 shows typical expansion characteristics for high alumina brick.

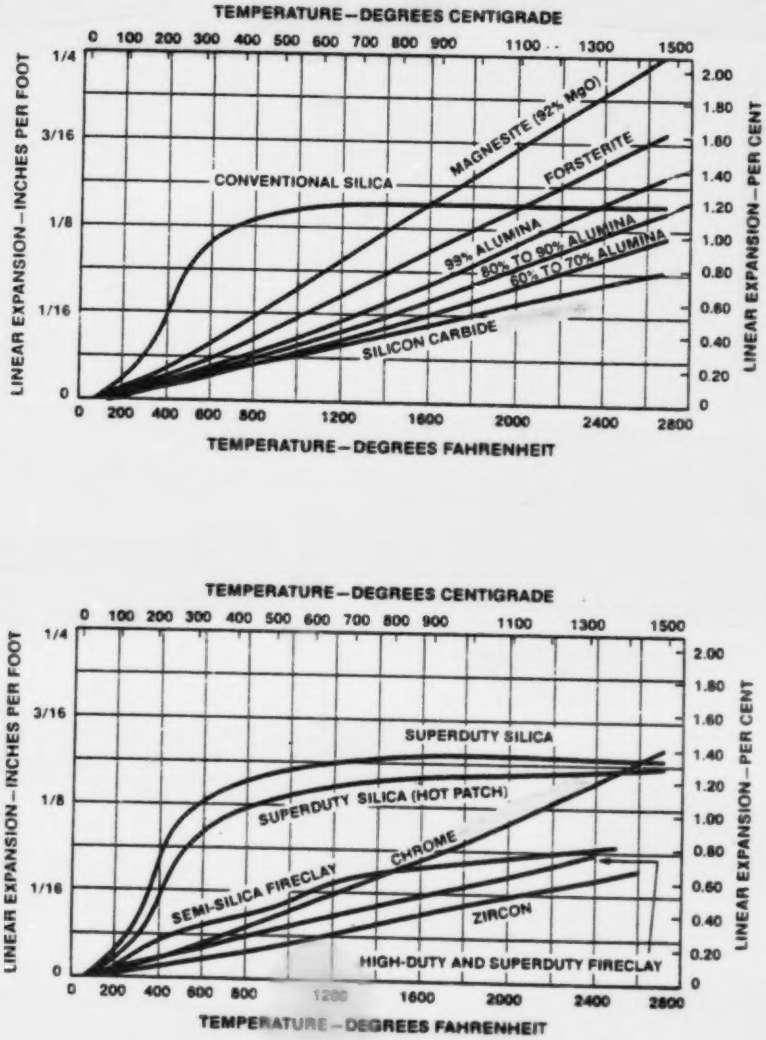

Figure 5-9. Approximate reversible thermal expansion of refractory brick (from Harbison Walker Refractories; 1979, published by permission).

Some of these materials exhibit substantial variation in expansion rate over the illustrated temperature range. Certain properties (E, $\gamma$, Cp) are not routinely determined by refractory manufacturers and therefore can only be estimated.

The thermal stress relationship for elastic materials suggests that there is a maximum temperature gradient which a material can withstand without failure; however, most materials become partially plastic at elevated temperature. This behavior means that the material will creep or deform with time under load. A first approximation to describing creep behavior at elevated temperature can be obtained by assuming Newtonian fluid behavior where shear stress $\tau$ is given by

$$\tau = \eta \frac{\partial \gamma}{\partial t}$$

where $\eta$ and $\gamma$ are apparent viscosity and shear strain (displacement), respectively. The rate of strain will increase as viscosity decreases for a given stress. Viscosity increases exponentially as temperature decreases until eventually approximate elastic behavior again dominates.

Very little is known regarding the properties controlling creep of refractory materials at elevated temperature. It was therefore not possible to include plastic behavior in analyzing liner performance. The stresses calculated by assuming purely elastic behavior are much higher than would actually occur because some relocation of the liner takes place and relieves stresses. For this reason, the transient case is more likely to cause failure since if the rate of temperature rise (and expansion) exceeds the rate of creep then failure stresses can be reached.

### 5.3.2 Preliminary Analysis

A series of lining configurations and boundary conditions were considered in the preliminary analysis to obtain the most favorable temperature distribution within the lining. The analysis was conducted for a one-dimensional infinite cylinder, with fixed internal wall temperature, conduction through the walls, and external convection.

Temperature distributions for various lining configurations is shown in Figure 5-10. The properties of the three materials were given in section 5.2. Hot-face temperature and external convection coefficient (h) were fixed at 1620°C and $15 \frac{\text{kcal}}{\text{hr-cm}^2\text{-}^o\text{C}}$. All of the linings except one are unacceptable because the service temperature of the material is exceeded or maximum shell temperature is exceeded. The three-layer combination of 20 cm 1800°C castable, 23 cm 1400°C castable, and 10 cm 1000°C block insulation was chosen for the final design.

Thin monolayer linings were also considered at this point in the analysis. The effect of varying external convective coefficient $\eta$ on external temperature for an 11-centimeter-thick lining is shown in Figure 5-11a. Free convection corresponds to $h = 29 \frac{\text{kcal}}{\text{hr-m}^2\text{-}^o\text{C}}$. In this case, shell temperature is in excess of 650°C which would be suitable for a mild steel shell. Forced air flow around the exterior at approximately 30 meters per second yields $h = 66$ kcal/hr-$m^2$-°C, and an exterior temperature of approximately 400°C. This is still not recommended for mild steel. Higher convection coefficients would further reduce shell temperature but is impractical for a single-shell design due to energy limitations.

Shell temperature versus lining thickness is shown in Figure 5-11b for $h = 66$ kcal/hr-$m^2$-°C. Doubling the thickness from 11 cm to 23 cm reduces shell temperature to 230°C, but further increases are less effective.

The potential risk of thermal shock during heating and cooling has been addressed. The largest thermal gradients, hence the largest thermal stresses, will occur during heating and cooling cycles. The temperature profiles through a thick-walled (30 cm), 2.1 meter inside diameter cylinder were estimated upon sudden exposure to 1630°C gases. Radiative heat transfer from the gas is prescribed at the inside surface and free convection is prescribed at the exterior surface.

Temperature profiles at 1 hour, 2 hours, and 5 hours are shown in Figure 5-12. The inside surface temperature comes to within 50°C of the gas temperature in the first hour; however, the exterior surface temperature rises very slowly. The temperature gradient after 1 hour in the first 5 cm of

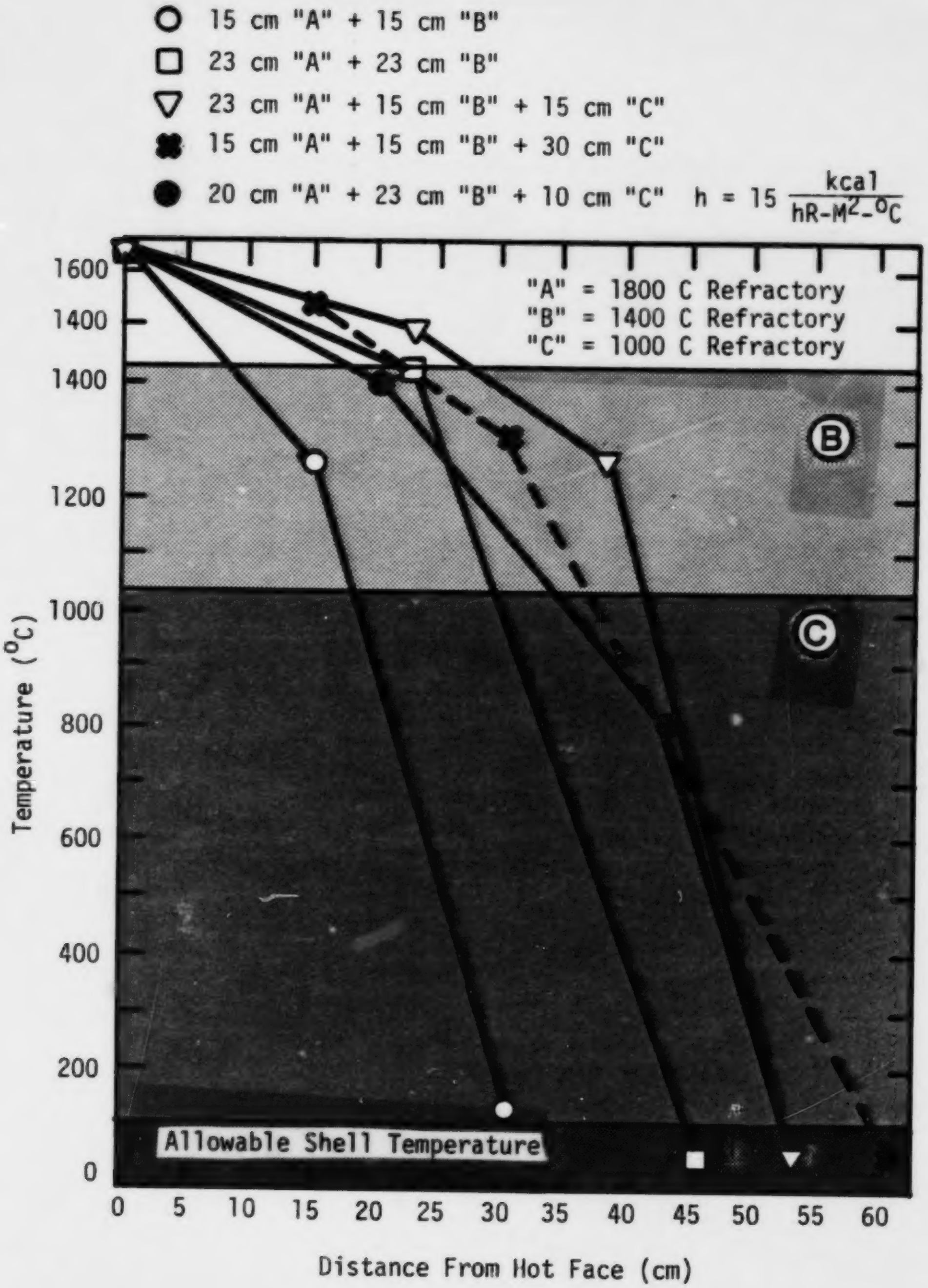

Figure 5-10. Temperature distribution through several lining arrangements.

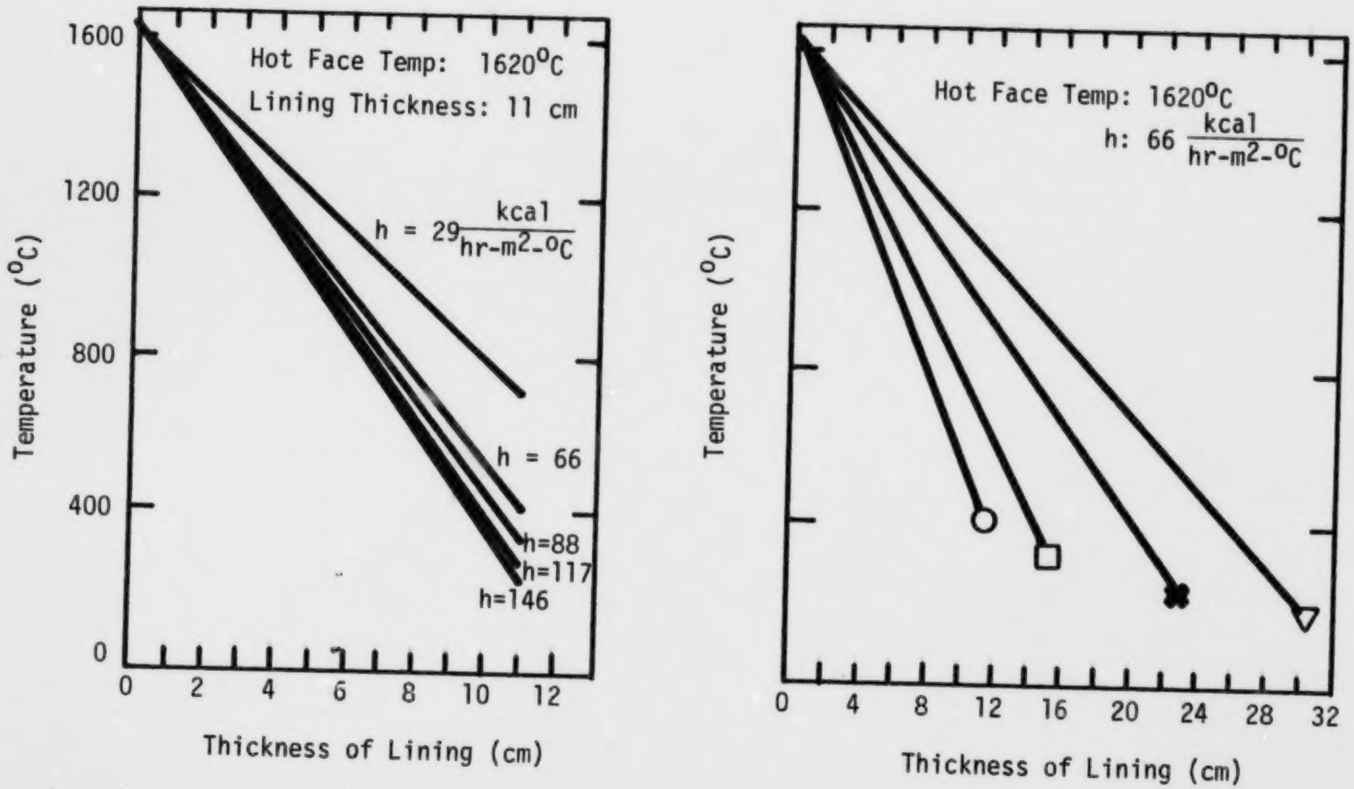

(a)

(b)

Figure 5-11. Effect of external convection and lining thickness for thin refractory linings.

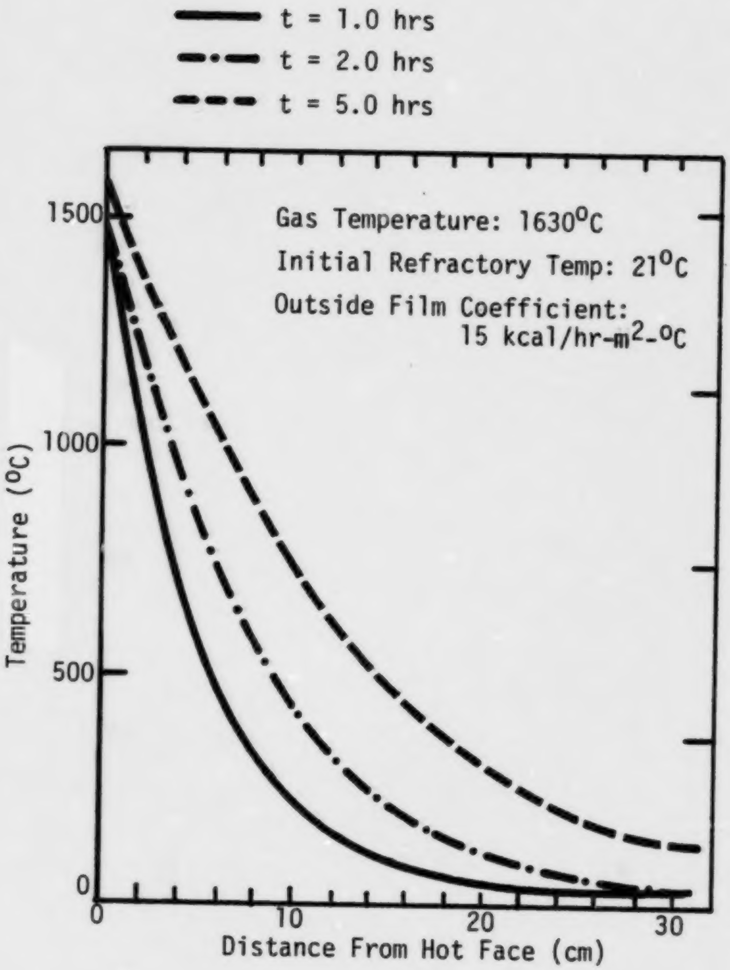

Figure 5-12. Temperature profile through monolayer lining after heating from ambient temperature.

refractory is very steep, approximately 185°C/cm. After 5 hours the gradient is approximately 90°C/cm.

Stresses at steady state temperature were calculated for the 30-cm-thick lining, assuming a semiinfinite thick-walled cylinder (see Appendix A for details). Calculated values at the inner and outer surfaces were:

Inner surface: 400 MPa compression

Outer surface: 340 MPa tension

It is apparent that the lining will crack (assuming no creep) long before these stresses are reached; however, it does indicate that the transient thermal stresses are much greater in magnitude (approximately a factor of 4 after one hour), particularly within the first hour of heating. The most severe stresses during a cooling transient are likely to occur somewhat interior to the inner surface where

$$\frac{\sigma}{\sigma_f} = \frac{E\alpha}{(1-\nu)} \frac{(\bar{T} - T)}{\sigma_f}$$

reaches a maximum due to decreasing strength with increasing temperature. $\bar{T}$ is the mass average temperature between the inner and outer surface, T is the temperature at any point within the lining, and $\sigma_f$ is the ultimate tensile or compressive failure stress. This can be seen in Figure 5-13 which shows transient temperature profiles through a 30-cm-thick cylinder of bubble alumina castable initially at steady state. Temperature profiles are calculated for various times after turning off the flame leaving only a very low flow of air through the burner. Peak temperatures are observed 2-4 cm from the lining hot face after as little as two minutes. It should also be noted that stresses during cooling are tensile, and that refractory tensile strength is much lower than compressive strength.

### 5.3.3 Recommended Design Analysis

Davy McKee Corporation chose the best lining configuration from the foregoing analysis for more detailed calculations. A two-dimensional finite element model of a section of the lining, shown in Figure 5-14, was evaluated. The total lining thickness was 54 cm, including 20.3 cm of bubble alumina castable 22.9 cm of 1430°C insulating castable, 7.6 cm of 1040°C insulating block

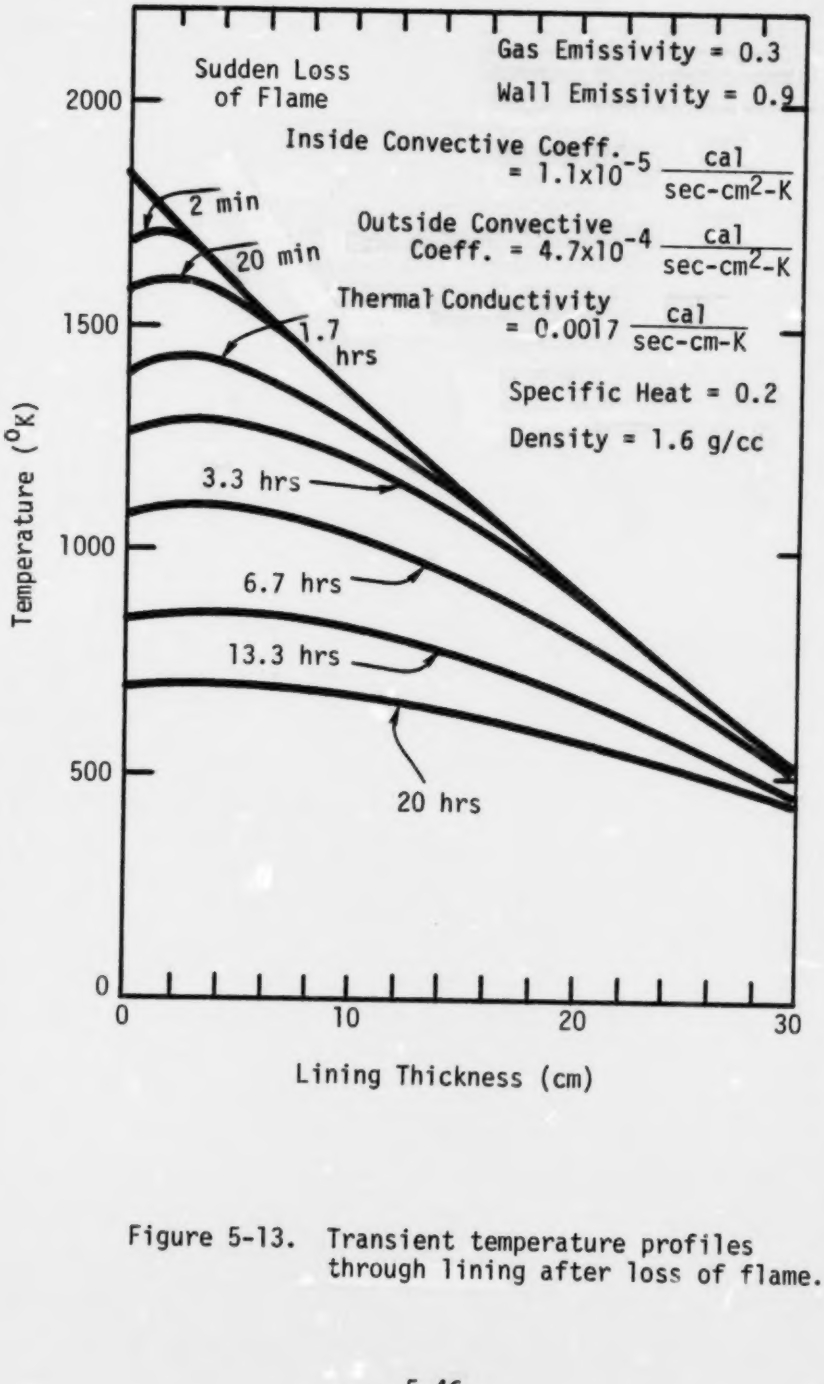

Figure 5-13. Transient temperature profiles through lining after loss of flame.

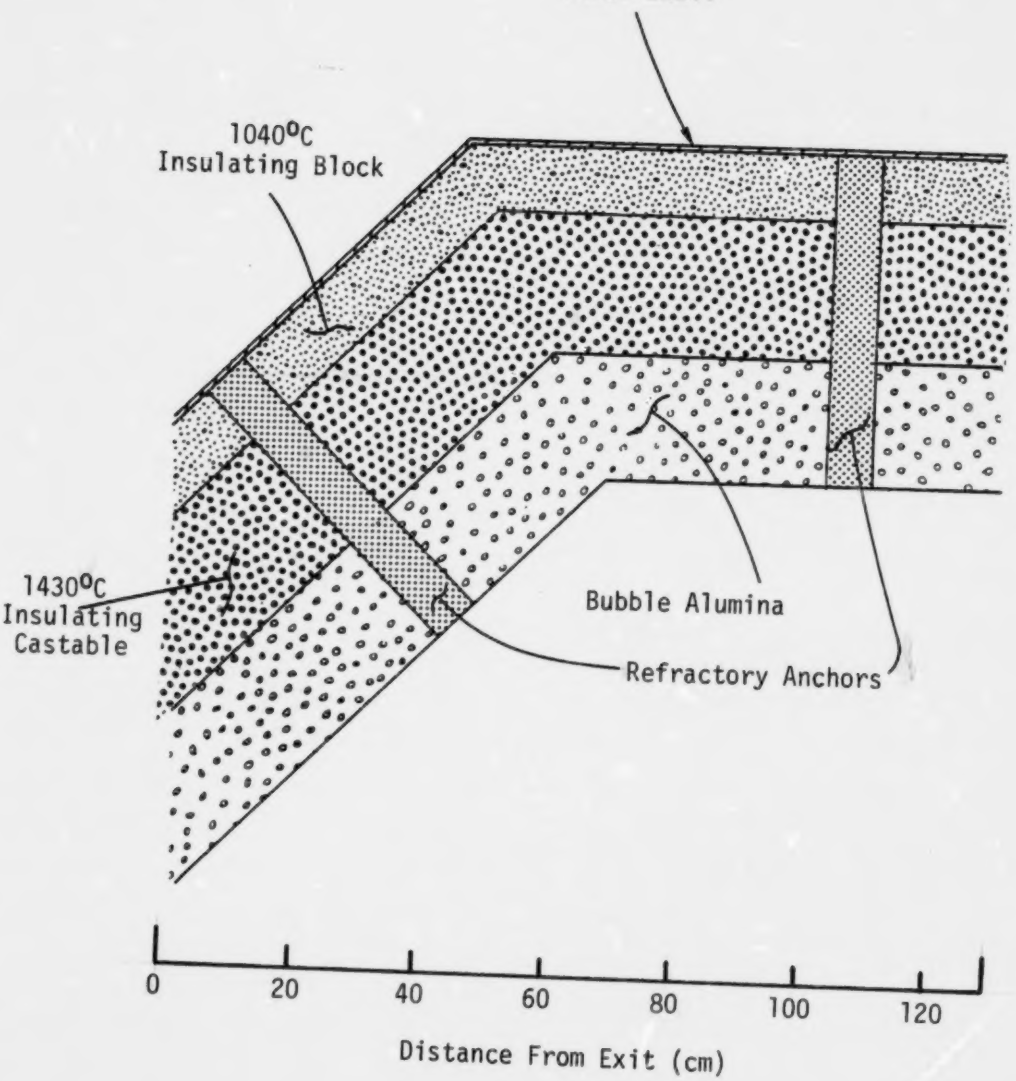
Steel Shell
1040°C
Insulating Block
1430°C
Insulating
Castable
Bubble Alumina
Refractory Anchors
0
20
40
60
80
100
120
Distance From Exit (cm)

Figure 5-14. Recommended design model.

and 6.4 mm of steel shell. Refractory anchors are also included. The interfaces between layers were assumed to be continuous, with radiative heat transfer inside the lining and free convective heat transfer on the outside surface.

The steady-state radial temperature distribution through this lining is shown in Figure 5-15. Each of the materials in the lining is close to its use limit at the interface between layers. The temperature gradient through the brittle bubble alumina layer is fairly modest, while the softer-block insulation experiences a fairly high gradient. Thermal stress in the bubble alumina layer is thus minimized by minimizing the temperature gradient. The figure also shows the expected temperature gradient through a refractory anchor, and it can be seen that the interface temperature between anchor and insulation block is quite high.

Figure 5-16 shows the axial temperature profile through the bubble alumina layer midway through the lining and at the interface with the next layer. The largest temperature difference is seen to be near the juncture between the conical and cylindrical section, indicating a potential problem area.

Figure 5-17 shows the steady-state radial stress distribution through the lining. The bubble alumina layer experiences substantial tangential and axial stresses even for this conservative design. Tangential stress exceeds axial stress by nearly a factor of three at the hot face. Stress switches from compressive to tensile in the insulating castable block. This would imply a high risk of cracking; whether or not complete failure would occur is not discernible.

Figure 5-18 shows the temperature at both surfaces of the bubble alumina layer for a prescribed gas heatup rate of 56$^{o}$C per hour. The hot-face temperature lags behind the gas temperature by only 1 to 2 hours; however, the surface at the insulating castable interface is only 25 percent of its final value after 13 hours. This indicates that the thermal stress after 13 hours is nearly six times greater than at steady state. This large thermal inertia caused Davy McKee Corporation to recommend a heatup schedule which takes 86 hours to complete in order to keep stress at a "reasonable" level.

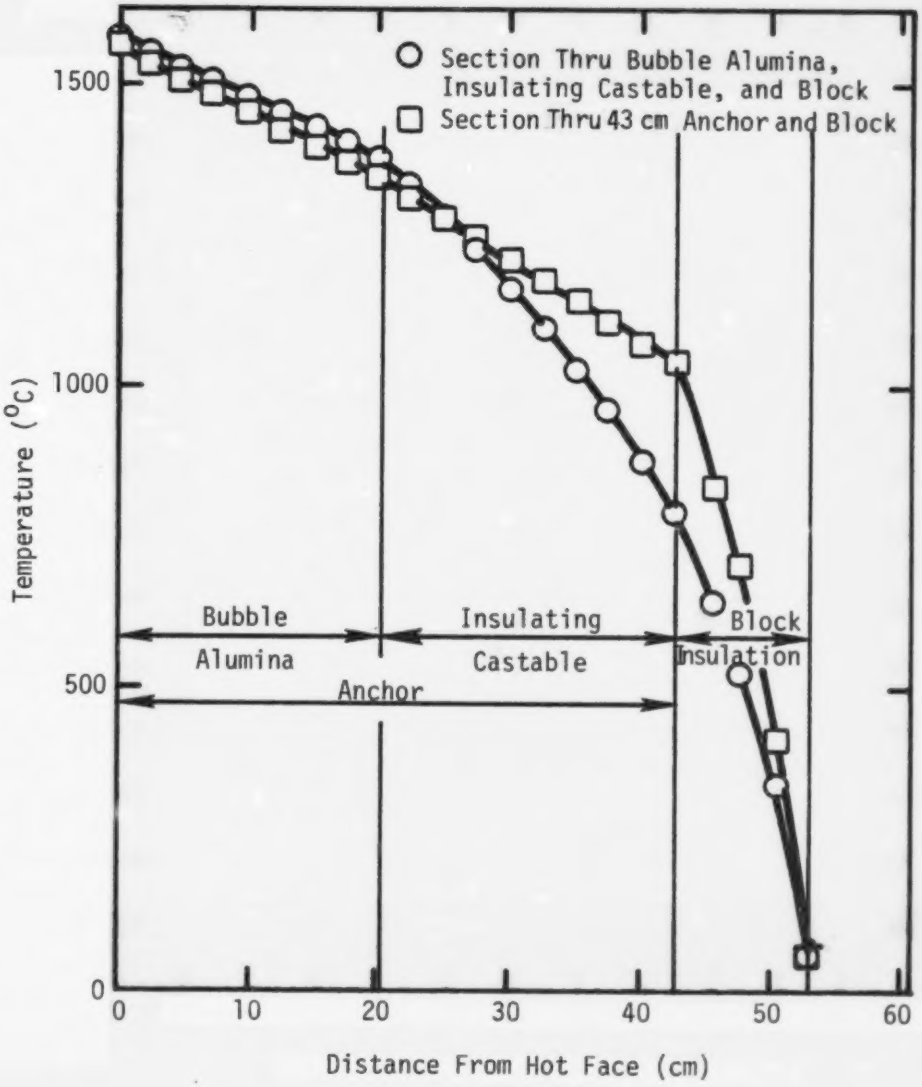

Figure 5-15. Steady state temperature distribution.

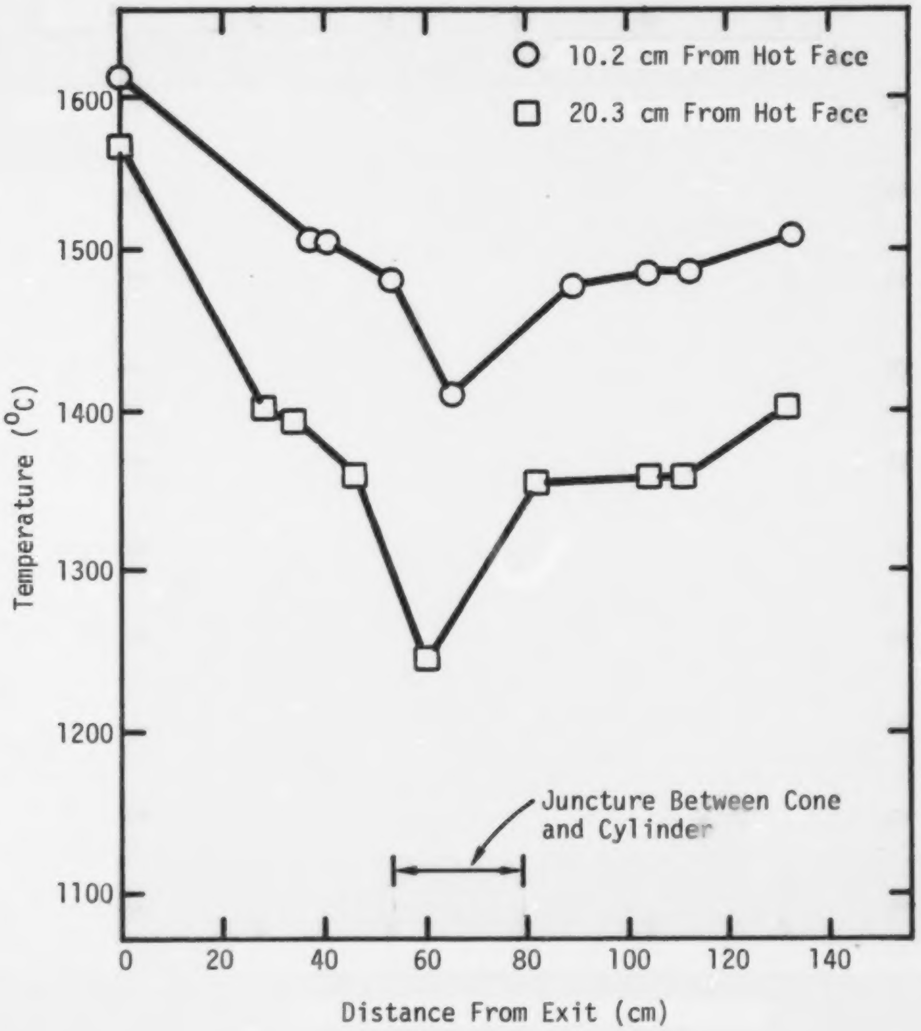

Figure 5-16. Steady state axial temperature distribution.

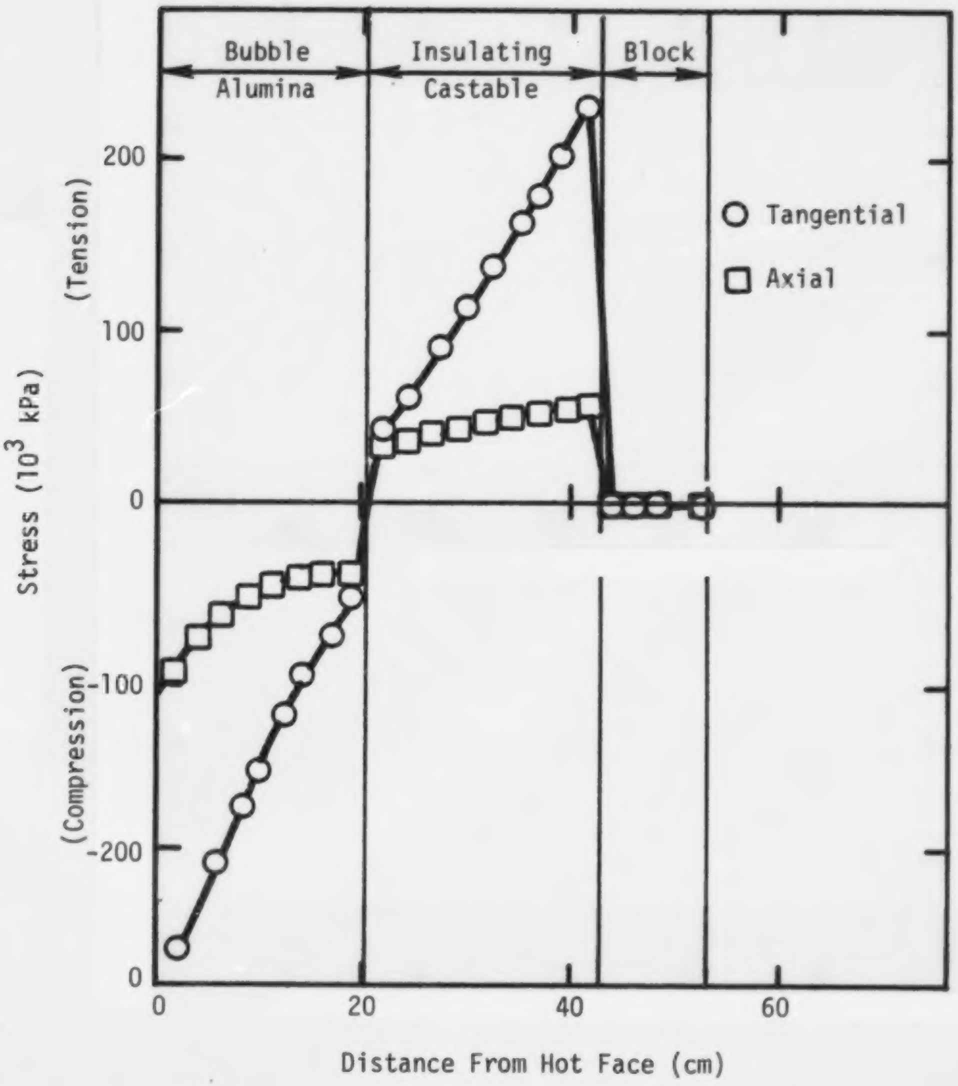

Figure 5-17. Steady state radial stress distribution through multilayer liner (purely elastic).

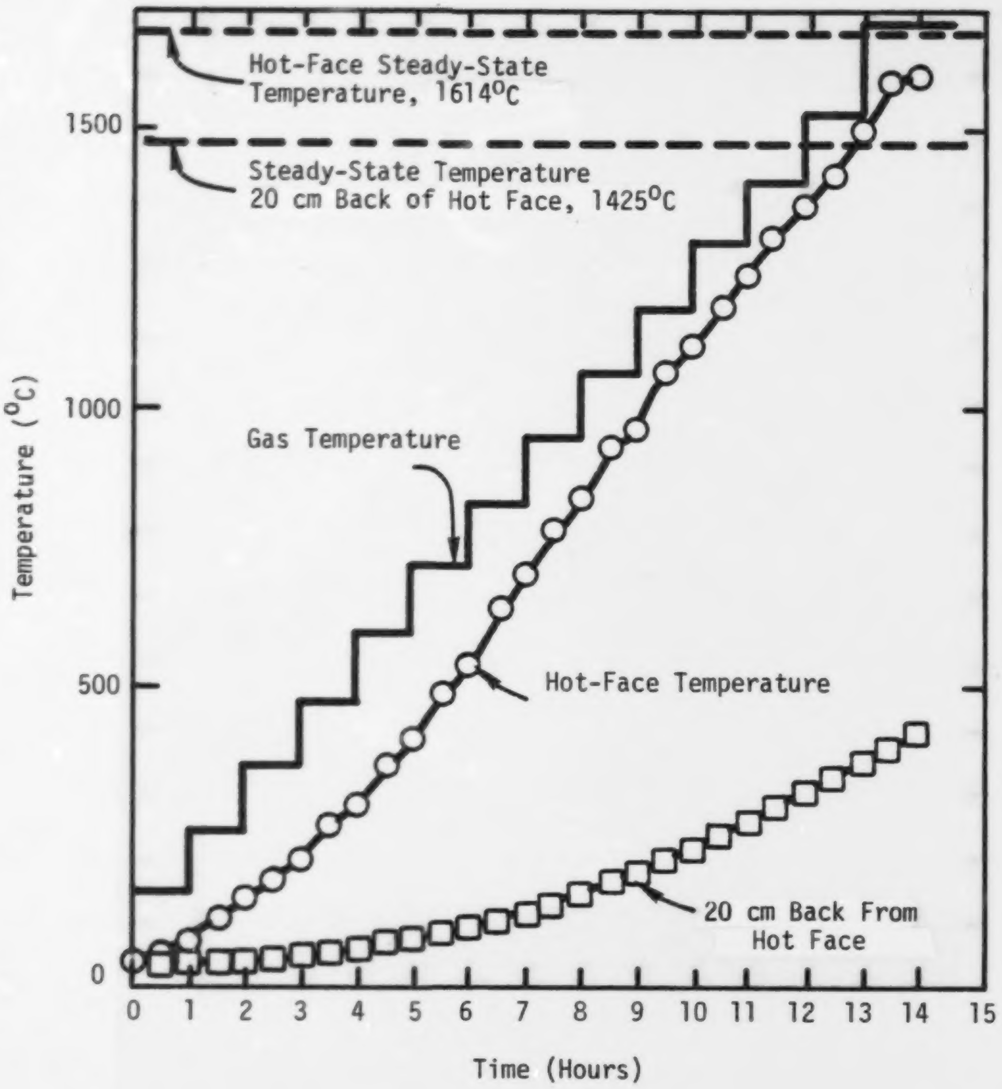

Figure 5-18. Hot face temperature during startup.

## 5.4 First-Stage Concept B--Regenerative Design

The regenerative design was developed as an alternative which would have superior thermal shock resistance and shorter heatup requirements at the risk of being an "unconventional" design. The key to the design is in reducing the mass of refractory required for the inner timing. A thin lining is possible if the shell is cooled by some means, in this case by the primary air.

Figure 5-19 shows the essential features of the regenerative design. Two metal shells form an annulus which is lined on the inside surface with refractory brick and on the outside with ceramic fiber blanket. Primary combustion air enters near the exit of the first stage, is distributed around the circumference of the shell and then passes through the annulus to the burner wind box. The critical parameters for this design are the air velocity in the annulus and the thermal resistance of the brick lining. If the outside ceramic fiber insulation is sufficient to make heat transfer to the surroundings negligible compared to heat transfer from the inner shell, then a substantial amount of heat can be transferred to the primary air. Figure 5-20 illustrates the heat transfer through this lining. Heat is transferred from the gas to the brick lining primarily by radiation. The brick lining conducts heat to the inner shell, which transfers heat to the primary air by convection and to the outer shell by radiation. Most of the heat radiated to the outer shell is transferred to the primary air by convection and a small amount is lost to the surroundings by conduction. Table 5-15 lists the equations which describe this problem to a fair approximation (nomenclature is defined in Table 5-16). Solving these equations allows the thermal performance of the shell to be determined as a function of the lining thickness and air velocity.

### 5.4.1 Results of Thermal Analysis

Figure 5-21 shows the effect of lining thickness and conductivity on temperatures of the various burner surfaces. The lower half of the figure plots outer shell temperature versus inner shell temperature for an air velocity of 13.4 meters per second (at 93°C mean air temperature) in the annulus. This corresponds to 50 percent theoretical air at 16.2 MW. Also shown in the lower half of the figure is the estimated temperature of the primary air after 5 meters length. Since the shell convective heat transfer coefficient is approximately constant for constant product of density and velocity, the heat

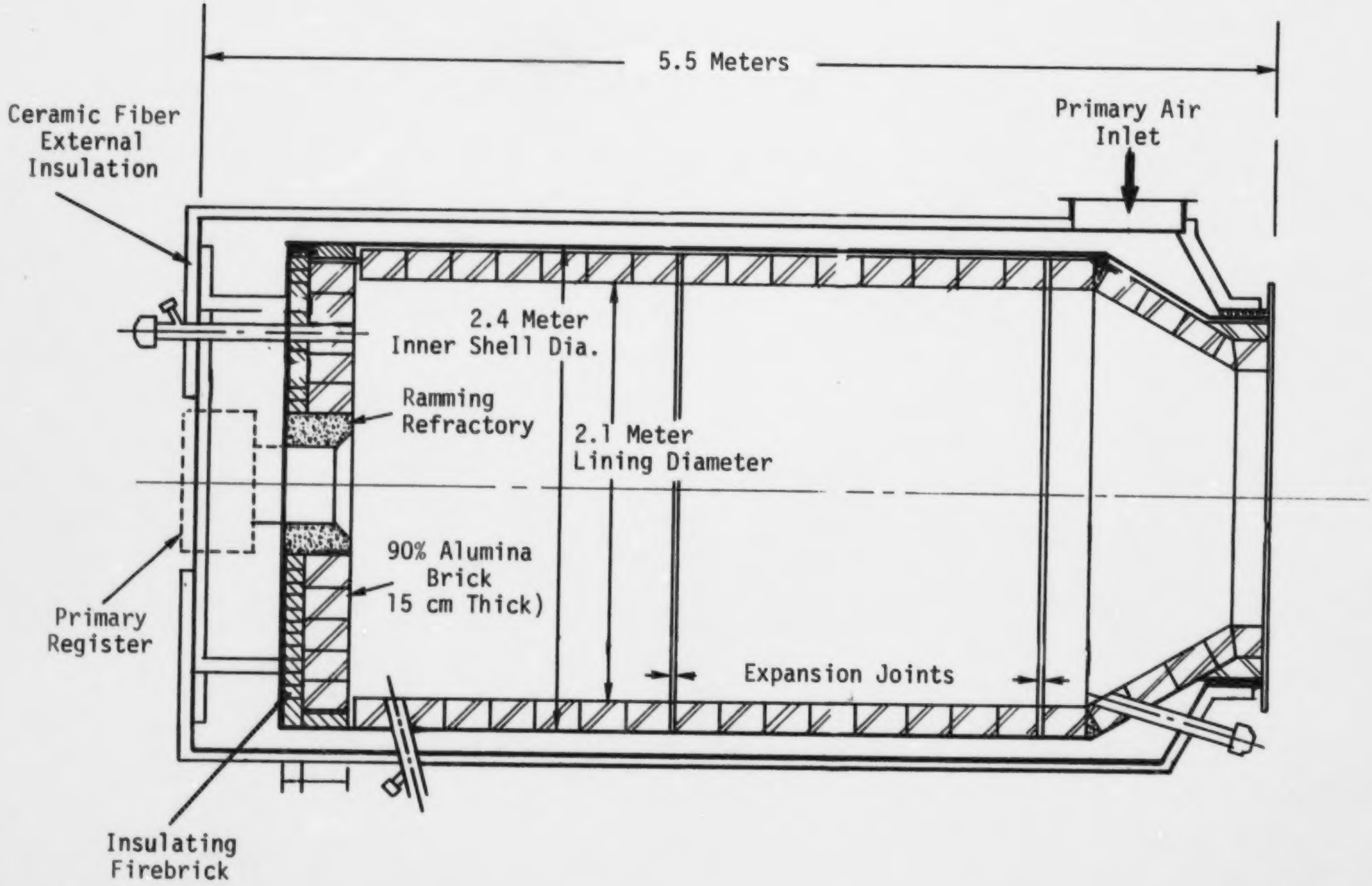
5.5 Meters
Ceramic Fiber External Insulation
Primary Air Inlet
2.4 Meter Inner Shell Dia.
Ramming Refractory
2.1 Meter Lining Diameter
90% Alumina Brick 15 cm Thick)
Primary Register
Expansion Joints
Insulating Firebrick

Figure 5-19. Regenerative first-stage design.

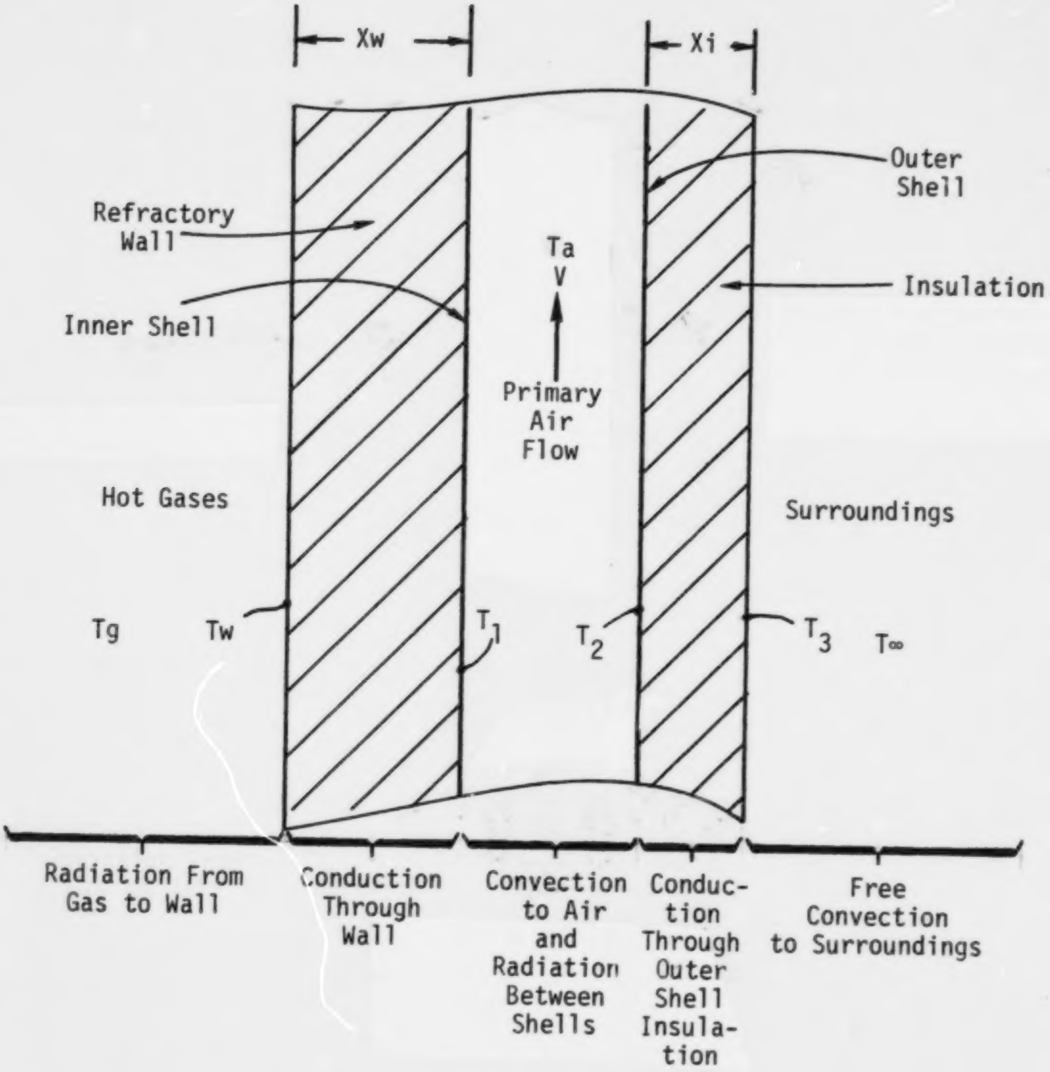
Xw
Xi
Outer Shell
Refractory Wall
Inner Shell
Ta
V
Primary Air Flow
Insulation
Hot Gases
Surroundings
Tg
Tw
$T_1$
$T_2$
$T_3$
T∞
Radiation From Gas to Wall
Conduction Through Wall
Convection to Air and Radiation Between Shells
Conduction Through Outer Shell Insulation
Free Convection to Surroundings

Figure 5-20. Heat transfer through regenerative air-cooled lining.

TABLE 5-15. STEADY-STATE HEAT TRANSFER EQUATIONS FOR REGENERATIVE SHELL DESIGN

| | |
|---|---|
| Radiation from gas to wall: | $q_g \cong h_r A\ (Tg-Tw)$<br>where<br>$h_r = \left[\frac{1+\varepsilon_w}{2}(4+a+b-c)\bar{\varepsilon}_g \sigma \bar{T}^3\right]$<br>$\bar{T} = \left(\frac{T_g{}^4 + T_w{}^4}{2}\right)^{0.25}$<br>a,b,c, = constants |
| Conduction through refractory wall: | $q_w = \frac{k_w Aw\,(T_w - T_1)}{X_w}$ |
| Convection from inner shell to air: | $(q_1)_c = h_1 A_1\ (T_1 - T_a)$ |
| Convection from outer shell to air: | $(q_2)_c = h_2 A_2 (T_2 - Ta)$ |
| Radiation between shells: | $(q_{12})_r = \frac{\sigma A\left(T_1{}^4 - T_2{}^4\right)}{\frac{1}{\varepsilon_1} + \frac{A_1}{A_2}\left(\frac{1}{\varepsilon_2} - 1\right)}$ |
| Conduction through outer shell insulation: | $q_i = \frac{k_i A_i (T_2 - T_3)}{X_i}$ |
| Convection to Surroundings: | $q_\ell = h_o A_o (T_3 - T_\infty)$ |

## TABLE 5-16. NOMENCLATURE FOR FIGURE 5-20 AND TABLE 5-15

| Symbol | Definition |
|---|---|
| $q_g$ | Radiative heat flow from gases to hot face |
| $q_w$ | Conductive heat flow through refractory wall |
| $(q_1)_c$ | Convective heat flow from inner shell to air |
| $(q_2)_c$ | Convective heat flow from outer shell to air |
| $(q_{12})_r$ | Radiative heat flow between shells |
| $q_i$ | Conductive heat flow through outer shell insulation |
| $q_\ell$ | Convective heat flow to surroundings |
| $T_g$ | Gas temperature inside chamber |
| $T_w$ | Hot face temperature of refractory wall |
| $T_1$ | Inner shell temperature |
| $T_2$ | Outer shell temperature |
| $T_3$ | Exterior temperature of outer shell insulation |
| $T_a$ | Air temperature between shells |
| $\overline{T}$ | Mean radiating temperature between gases and hot face |
| $T_\infty$ | Temperature of surroundings |
| $h_r$ | Radiative heat transfer coefficient |
| $h_1$ | Convective heat transfer coefficient, inner shell to air |
| $h_2$ | Convective heat transfer coefficient, outer shell to air |
| $h_o$ | Convective heat transfer coefficient, outer insulation surface to surroundings |
| $k_w$ | Thermal conductivity of refractory wall |
| $k_i$ | Thermal conductivity of outer shell insulation |
| $V$ | Velocity of air between shells |
| $x_w$ | Refractory wall thickness |
| $x_i$ | Outer shell insulation thickness |
| $A_w$ | Area of refractory wall hot face |
| $A_1$ | Area of inner shell |
| $A_2$ | Area of outer shell |
| $A_o$ | Area of exterior insulation surface |
| $\varepsilon_w$ | Emissivity of refractory wall hot face |
| $\overline{\varepsilon}_g$ | Gas emissivity inside chamber at $\overline{T}$ |
| $\varepsilon_1$ | Emissivity of inner shell surface |
| $\varepsilon_2$ | Emissivity of outer shell surface |
| $\sigma$ | Refractory wall thickness |

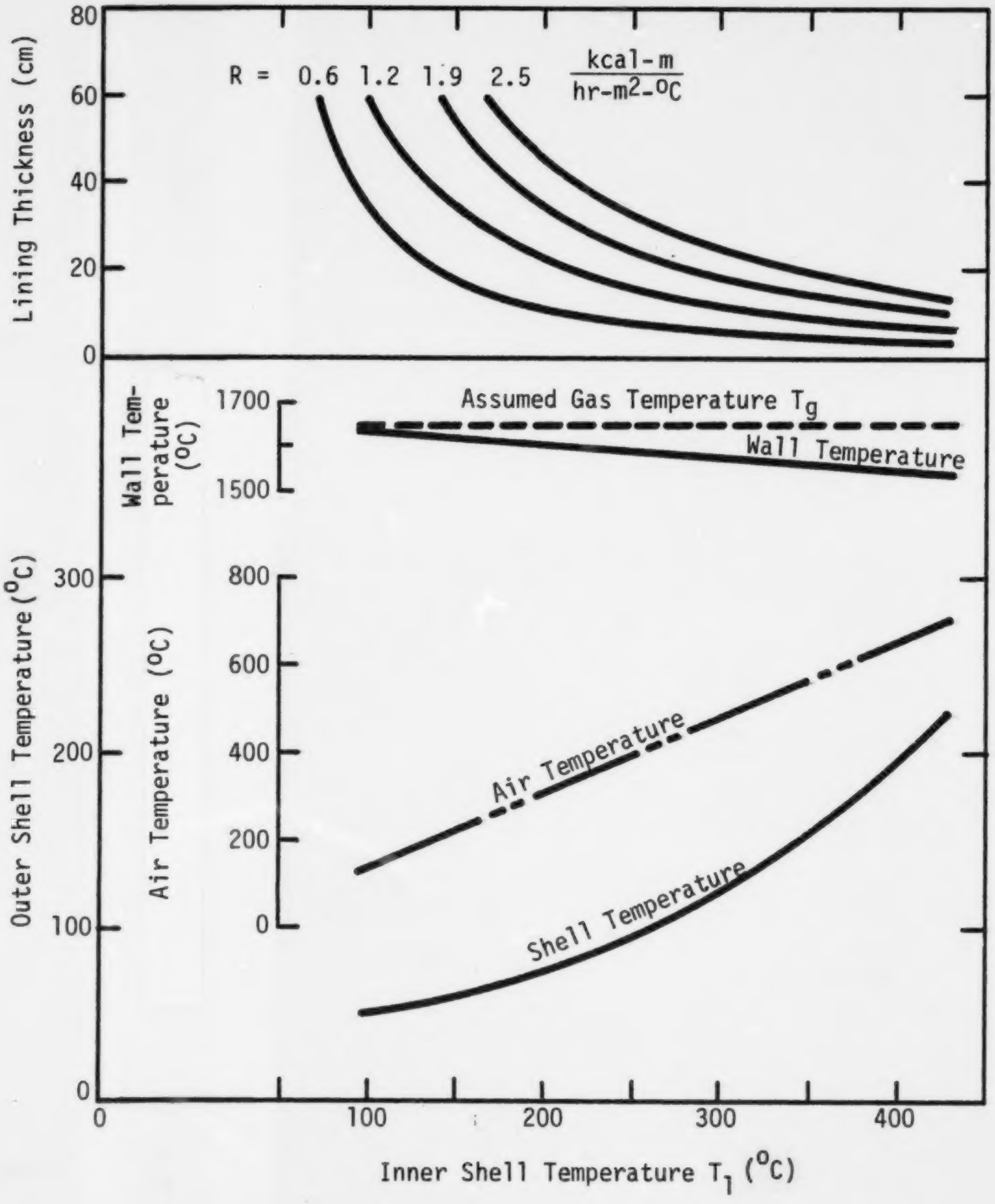

Figure 5-21. Thermal design characteristics of regenerative lining with external insulation.

transfer coefficient stays approximately constant as the air temperature increases. Substantial air preheat temperatures are achieved since both inner and outer shell surfaces are available for convective heat transfer. The calculated outer shell temperature is approximately half the inner shell temperature, and it is evident that the radiative transfer from the inner shell is significant. Calculations show the radiative transfer accounts for approximately one-third of the total heat transferred from the inner shell at temperatures around 425°C.

The approximate inner wall temperature is also shown in the figure, assuming constant gas temperature and a constant net radiative heat transfer coefficient. At high shell temperatures the inner wall temperature may be as much as 110°C below the gas temperature. This kind of temperature reduction at the hot face could increase refractory life.

The upper half of the figure shows the relationship between lining thickness and conductivity required to produce the temperatures in the lower half of the figure. A 15 cm lining of material with thermal conductivity of approximately 1.9 kcal-m/hr-$m^2$-°C yields an inner wall temperature of 1560°C, inner shell temperature of 335°C, outer shell temperature of 180°C, and an air preheat temperature of 550°C after 5 meters (assuring 43°C air at the inlet). This was chosen as the nominal design point for maximum shell and air preheat temperature.

Temperatures calculated for two different loads are shown in Table 5-17 for two lining thicknesses. The data are shown without external insulation. Inner shell temperature using a 15-cm-thick lining will rise from 328°C to 443°C if allowed to reach steady state when load is reduced from 18.3 MW to 4.6 MW at constant stoichiometry. Similarly, air preheat temperature increases from 138°C to 247°C. Increasing the lining thickness from 15 to 23 cm decreases shell temperature to 257°C at full load and to 375°C at 25 percent load. The benefit of adding 60 percent more mass (hence cost) to the refractory lining is therefore seen to be comparatively small. Table 5-18 shows similar calculations for the same configuration but using a higher thermal conductivity material. This produces slightly higher shell temperatures than the previous case but the general trends remain similar.

## TABLE 5-17. PREDICTED REGENERATIVE LINER PERFORMANCE--LOW CONDUCTIVITY REFRACTORY

Refractory Type: A. P. Green, Greenal-90

Assumed Thermal Conductivity (at 1649$^{o}$C) = $1.6\times10^{-3} \frac{\text{cal}}{\text{sec-cm-}^{o}\text{C}}$
Chamber Length = 4.0 meters
Air Gap Between Inner and Outer Shell = 3.2 cm

Inside Diameter of Refractory = 2.1 meters
Inner and Outer Shell Thickness = 7.9 mm
Stoichiometric Ratio in Primary Zone = 60 Percent

| Percent Load | 100% | | | | 25% | | | |
|---|---|---|---|---|---|---|---|---|
| Burner Heat Input (mw) | 18.3 | | | | 4.6 | | | |
| Primary Zone Air Flow (kg/s) | 3.5 | | | | 0.88 | | | |
| Primary Zone Comb. Products (kg/s) | 4.0 | | | | 0.99 | | | |
| Refractory Thickness (cm) | 15.2 | 15.2 | 22.9 | 22.9 | 15.2 | 15.2 | 22.9 | 22.9 |
| Emissivity From Shell to Shell to Surround | .9 | .6 | .9 | .6 | .9 | .6 | .9 | .6 |
| Assumed Peak Gas Temp ($^{o}$C) | 1651 | 1654 | 1642 | 1641 | 1656 | 1638 | 1641 | 1631 |
| Exit Gas Temp ($^{o}$C) | 1566 | 1571 | 1579 | 1579 | 1371 | 1371 | 1427 | 1427 |
| Average Gas Temp ($^{o}$C) | 1608 | 1613 | 1611 | 1610 | 1513 | 1504 | 1534 | 1529 |
| Refractory Hot-Face Temp ($^{o}$C) | 1566 | 1571 | 1579 | 1580 | 1472 | 1465 | 1504 | 1500 |
| Inner Shell Temp ($^{o}$C) | 328 | 357 | 256 | 276 | 443 | 503 | 375 | 427 |
| Outer Shell Temp ($^{c}$C) | 132 | 117 | 96 | 84 | 251 | 248 | 203 | 199 |
| Air Temp--Inlet ($^{o}$C) | 16 | 16 | 16 | 16 | 16 | 16 | 16 | 16 |
| Outlet ($^{c}$C) | 138 | 141 | 108 | 110 | 247 | 267 | 208 | 224 |
| Average ($^{c}$C) | 77 | 78 | 62 | 63 | 131 | 141 | 112 | 120 |
| Heat Trans. From Comb. Prod. to Refractory (mw) | 0.50 | 0.49 | 0.37 | 0.36 | 0.42 | 0.39 | 0.31 | 0.30 |
| Total Heat Loss to Surroundings (kW) | 56 | 38 | 36 | 24 | 165 | 126 | 121 | 93 |

## TABLE 5-18. PREDICTED REGENERATIVE LINER PERFORMANCE--HIGH-CONDUCTIVITY REFRACTORY

Refractory Type: H-W-Korundal-XD

Assumed Thermal Conductivity (at 1649$^{o}$C)=$2.3\times10^{-3}\frac{\text{cal}}{\text{sec-cm-}^{o}\text{C}}$
Chamber Length = 4.0 meters
Air Gap Between Inner and Outer Shell = 3.2 cm

Inside Diameter of Refractory = 2.1 meters
Inner and Outer Shell Thickness = 7.9 mm
Stoichiometric Ratio in Primary Zone = 60 Percent

| Percent Load | 100% | | | | 25% | | | |
|---|---|---|---|---|---|---|---|---|
| Burner Heat Input (mw) | 18.3 | | | | 4.6 | | | |
| Primary Zone Air Flow (kg/s) | 3.5 | | | | 0.88 | | | |
| Primary Zone Comb. Products (kg/s) | 4.0 | | | | 0.99 | | | |
| Refractory Thickness (cm) | 15.2 | 15.2 | 22.9 | 22.9 | 15.2 | 15.2 | 22.9 | 22.9 |
| Emissivity From Shell to Shell to Surround | .9 | .6 | .9 | .6 | .9 | .6 | .9 | .6 |
| Assumed Peak Gas Temp ($^{o}$C) | 1653 | 1644 | 1652 | 1644 | 1652 | 1652 | 1654 | 1647 |
| Exit Gas Temp ($^{o}$C) | 1552 | 1546 | 1577 | 1571 | 1316 | 1338 | 1399 | 1404 |
| Average Gas Temp ($^{o}$C) | 1602 | 1595 | 1614 | 1608 | 1487 | 1495 | 1526 | 1526 |
| Refractory Hot-Face Temp ($^{o}$C) | 1551 | 1544 | 1577 | 1571 | 1436 | 1447 | 1490 | 1492 |
| Inner Shell Temp ($^{o}$C) | 370 | 403 | 294 | 318 | 475 | 545 | 410 | 470 |
| Outer Shell Temp ($^{c}$C) | 157 | 137 | 115 | 101 | 268 | 268 | 226 | 226 |
| Air Temp--Inlet ($^{o}$C) | 16 | 16 | 16 | 16 | 16 | 16 | 16 | 16 |
| Outlet ($^{c}$C) | 157 | 160 | 124 | 126 | 265 | 289 | 229 | 249 |
| Average ($^{c}$C) | 86 | 88 | 70 | 71 | 140 | 152 | 122 | 132 |
| Heat Trans. From Comb. Prod. to Refractory (mw) | 0.59 | 0.57 | 0.44 | 0.43 | 0.48 | 0.46 | 0.37 | 0.35 |
| Total Heat Loss to Surroundings (kW) | 75 | 49 | 48 | 32 | 187 | 145 | 146 | 114 |

Total heat loss to the surroundings is very low even for the case with no external insulation. At full load, external heat loss to the surroundings amounts to less than 0.5 percent of the fuel input. Losses at 25 percent load are substantially higher (approximately one percent); however, extended operation at low load is very unusual in practice. The calculations show, however, that exterior shell temperatures could reach levels hazardous to personnel. A heat shield or exterior insulation could be added to prevent injury to personnel.

The most severe operating condition for the burner is reached after extended low load operation or when airflow through the shell is lost completely. Calculations show that approximately 1.5 to 2.0 hours after a sudden loss of air and flame, the shell temperature rises to a maximum temperature below the mean temperature of the brick assuming heat loss only by radiation through the first-stage exit. This would result in a potential shell temperature of 900°C for the externally insulated case. This temperature would never be reached in practice since additional heat losses due to external convection/radiation and natural draft are present. There may also be time to take corrective action and restart the blower before peak temperature is reached.

It is not possible to choose an analytical case which exactly matches the conditions of the actual burner. The calculations which have been made were chosen to evaluate conditions more severe than are likely in actual practice, and thus provide a conservative estimate of lining performance. Actual performance will have to be determined empirically.

### 5.4.2 Mechanical Design

The mechanical design for the regenerative concept is based on an existing Peabody direct-fired air heater design. The essential features of the final design are illustrated in Figure 5-22. Certain changes to the basic Peabody design were necessary in order to meet the requirements of the thermal design. Temperatures in the lining and shell are expected to be higher than in the existing air heater design, hence the major changes are to the materials of construction. A 90 percent alumina refractory lining 15 cm thick was selected after review of the design and consultation with the refractory manufacturers. The shell materials were also upgraded to a 304 stainless steel in order to withstand

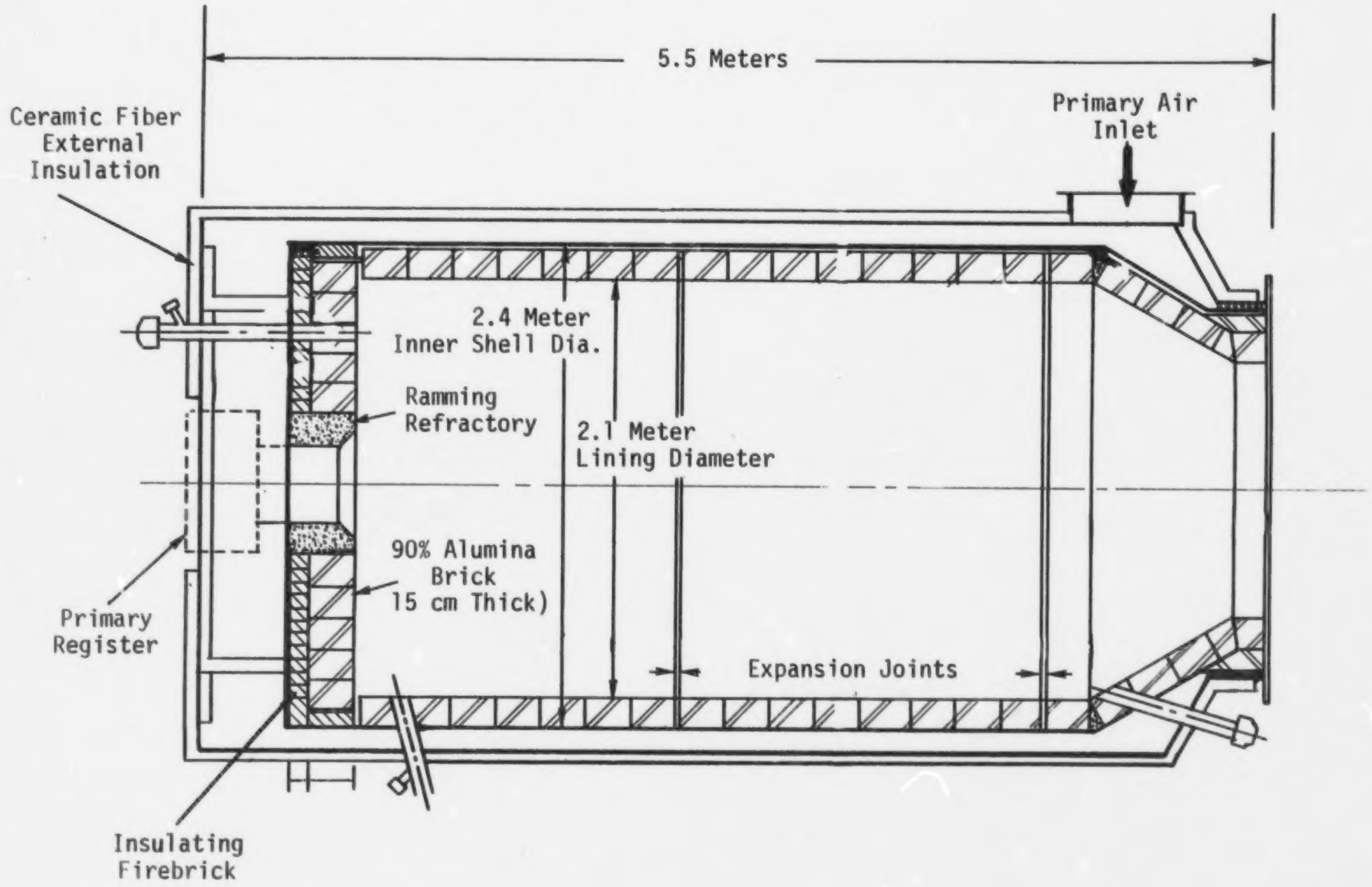
5.5 Meters
Ceramic Fiber External Insulation
Primary Air Inlet
2.4 Meter Inner Shell Dia.
Ramming Refractory
2.1 Meter Lining Diameter
90% Alumina Brick 15 cm Thick)
Primary Register
Expansion Joints
Insulating Firebrick

Figure 5-22. Regenerative first-stage design.

the more severe cases predicted from thermal analysis. Other minor design changes included revised expansion allowances and additional shell support.

Refractory brick was chosen for the lining in order to eliminate tensile loads on the brick itself. This type of lining was recommended by both Peabody and A. P. Green Refractories as being the most reliable construction for a thin lining. Peabody air heaters use a 11.5-cm-thick lining of a 50 to 75 percent alumina brick and these give satisfactory lining lifetimes in the field. The analysis presented for the insulated first-stage (Concept A) demonstrated that very high compressive stresses are developed in the lining due to thermal expansion and external dimension constraints. Several conventional and unconventional designs were explored to allow circumferential expansion without imposing dimension restraints. These concepts were centered on either allowing the steel shell to expand under constant load, or modification of the brick shapes. Figure 5-23 shows two concepts which were eventually rejected. The concept of using springs to allow expansion of the steel shell would limit the compressive force exerted on the ring of bricks, but would be very costly to fabricate and would be difficult to seal. The hot face of the brick will expand more than the cool face because of the difference in temperature. This would result in concentration of the compressive force on the inner face of the lining, which could lead to spalling failure, even for the expandable shell design. Specially shaped brick could be cut, as shown in the figure, to allow the inner face to expand unrestricted at low temperature. In order to account for the expected total expansion of the inner circumference (13 cm), approximately 1.3 mm would need to be shaved off the sides of each brick in the ring. This is beyond the tolerance of field installation equipment and normal manufacturing processes, and thus would be practically impossible. Cost to do this would also be very high.

Refractory manufacturers recommended against both of these designs in favor of simpler conventional methods. It was felt that the cost of either of these concepts would be very high and benefits would be marginal at best. According to manufacturers, brick linings relax and assume a permanently deformed shape at elevated temperature, establishing all "built-in" expansion allowance. The final design utilizes a crushable lining between the refractory brick and the top portion of the steel shell 2.5 cm thick which will

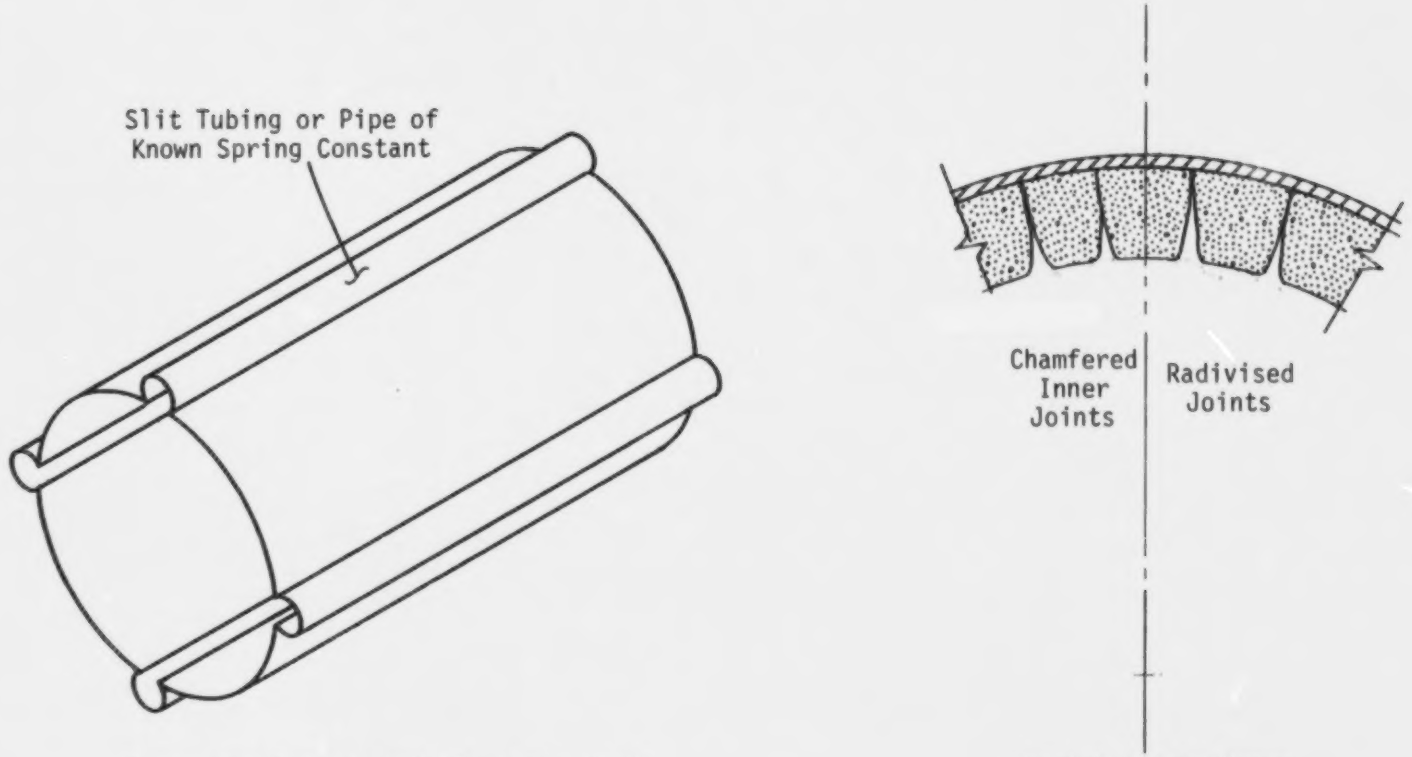
Slit Tubing or Pipe of
Known Spring Constant
Chamfered
Inner
Joints
Radivised
Joints

Spring-Loaded, Expandable Inner Shell

Special Brick Shapes

Figure 5-23. Unconventional construction concepts to reduce thermal stress.

allow for approximately two-thirds of the expected total thermal expansion (Figure 5-24). The remaining circumferential expansion is absorbed in the brick through creep at elevated temperature.

A flat front wall is also used in this design. The outer shell extends beyond the inner shell at the front to form a windbox for the primary air register. The front wall is backed up by a layer of insulation brick since there is no high-velocity air to keep the wall cool. The exit transition is conical and has been designed in accordance with current Peabody design practice. The shells are designed so that the outer shell expands from exit-end to burner-end, while the inner shell expands in the opposite direction. The shells are fixed relative to each other at the burner end. Detailed drawings of this concept are found in Appendix C.

## 5.5 Second-Stage Air Injection

The second-stage flame shape can have a strong effect on the life of refractory, tubes, and tube hangers in the radiant section of the steam generator. Direct flame impingement can occur on the side walls of the furnace if the flame is too "bushy" and cause erosion and sintering of the refractory behind the steaming tubes. The pilot-scale experiments produced lowest $NO_x$ with high-L/D flames, and excessive flame length in the steam generator can similarly destroy the refractory on the back wall of the radiant section and in the transition section. Failure of the refractory will eventually lead to failure of the outside shell.

The 1 MW pilot-scale experiments indicated that second-stage flame shape could be significantly altered by increasing the rate of secondary air mixing with the first-stage products, but that $NO_x$ emissions were not sensitive. Larger scale results (3 MW) indicated that both $NO_x$ and flame shape were affected by mixing in the second-stage, and that there is likely to be a tradeoff between decreasing flame length and increasing $NO_x$ for large-scale flames. The 3 MW tests were inconclusive with respect to the optimum velocities, swirl level, and entrainment in the second stage; therefore, it was necessary to design a mechanism allowing some control over these parameters in the full-scale prototype commercial burner. Once the optimum conditions are established at full-scale, later designs can be made fixed and hence less complicated.

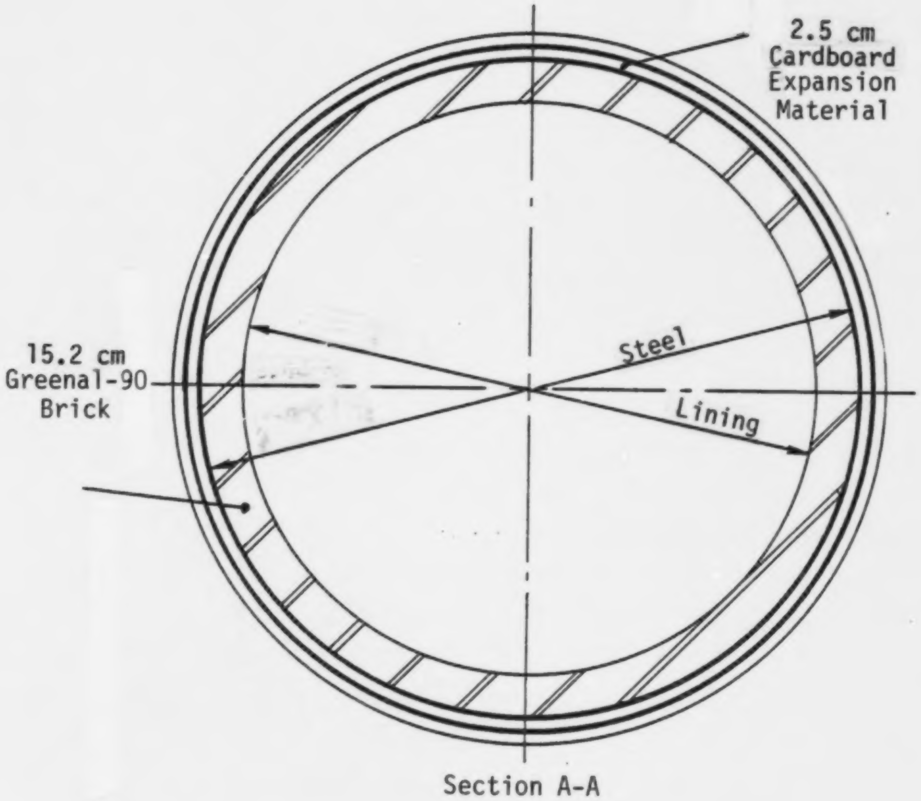
2.5 cm
Cardboard
Expansion
Material
15.2 cm
Greenal-90
Brick
Steel
Lining
Section A-A

Figure 5-24. Radial expansion allowance for regenerative first-stage concept.

The 3 MW pilot-scale tests demonstrated that optimum $NO_x$ emissions could be achieved with both annular secondary air injection and injection through ports. The degree of control over flame shape with the annular design is very limited, hence a port arrangement was favored for the full-scale design. In addition, the annular gap would need to be approximately 1.4 cm wide to achieve 30 meters per second velocity and this would be very difficult to maintain within tolerance on a 160-cm-diameter annulus subjected to harsh temperature environment. Ports allow for relatively convenient variation of secondary air injection velocity and trajectory and are much easier to construct. An arrangement of sixteen axially-oriented and sixteen radially-oriented ports was adopted for the final design.

The final design parameter considered which affects flame shape is the diameter of the first-stage exit opening. The small-scale prototypes had been designed to produce a first-stage combustion product exit velocity of 15 to 23 meters per second at 75 percent theoretical air. Secondary air velocity was designed to have a nominal ratio of secondary air to primary combustion product velocity in the range of 1:1 to 2:1, to produce relatively slow mixing between the two streams. Later tests in the 3 MW prototype indicated that increasing the primary combustion products velocity to nominally 40 meters per second increased $NO_x$, and a very short, "stiff" flame was generated. A design velocity of 15 to 20 meters per second was chosen for first-stage combustion products at the first-stage exit. This results in an exit diameter of 130 cm. This diameter can be reduced by adding more refractory to the throat.

Figure 5-25 illustrates the hardware configuration chosen for the full-scale second-stage air section. Two sets of ports allow both axial air injection and radial air injection. A sliding damper will permit the flowrate through each set of ports to be varied without shutdown. Sixteen ports are oriented parallel to the axis of the burner and sixteen ports are oriented normal to the axis. The section will be lined internally with 15 cm of 90-percent alumina brick and 90-percent alumina plastic ("ramming") refractory. The brick portion of the lining will cover 62 cm of the 112 cm total axial length and the ramming refractory will cover the remaining 50 cm around the radial ports. Construction joints within the rammed portion of the lining will prevent excessive crack formation. The face of the section exposed to

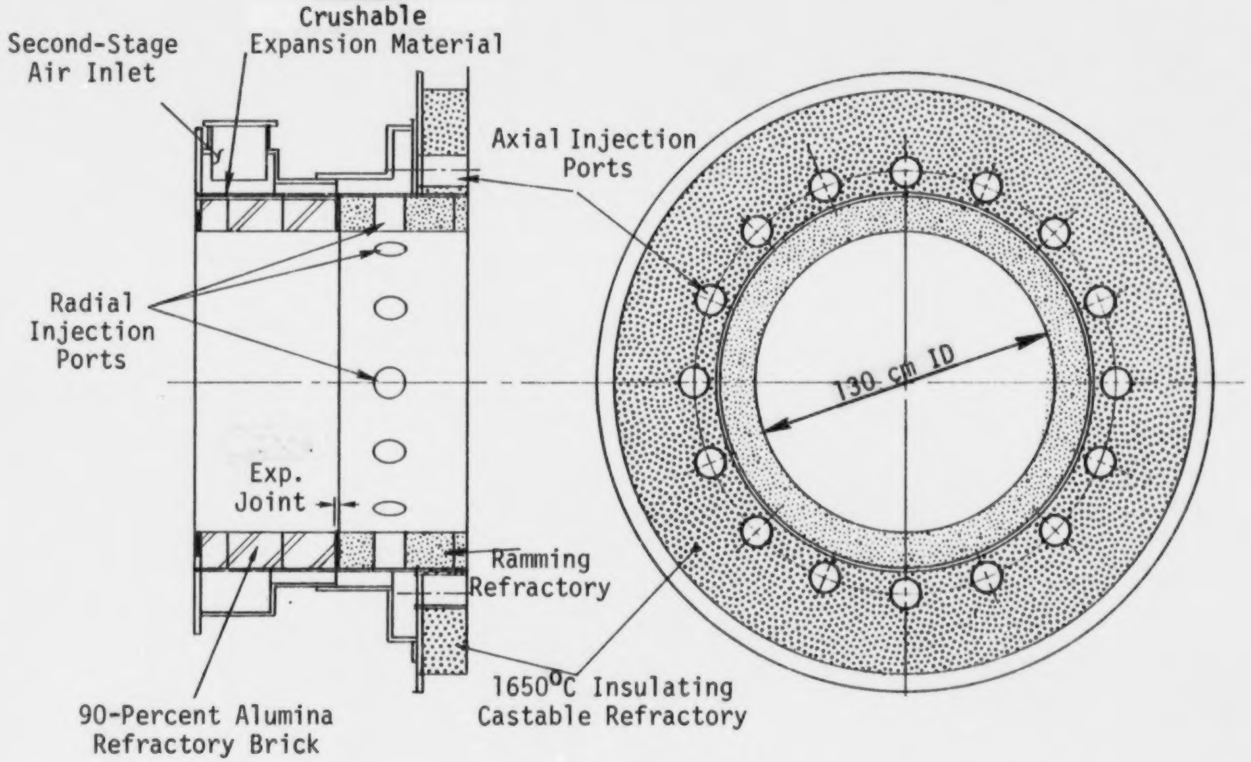
Second-Stage
Air Inlet
Crushable
Expansion Material
Axial Injection
Ports
Radial
Injection
Ports
130 cm ID
Exp.
Joint
Ramming
Refractory
1650°C Insulating
Castable Refractory
90-Percent Alumina
Refractory Brick

Figure 5-25. Variable second-stage air addition section.

the steam generator radiant section will be insulated with 20 cm of 1650°C insulating castable refractory.

The diameter of the ports was initially chosen to provide a relatively slow injection velocity of 20 meters per second. Sleeves can be inserted and rammed in place which will permit the injection velocity to be increased if necessary. The number of open ports can similarly be reduced.

Figure 5-26 presents the results of jet penetration calculations for three radial port diameters.

Final selection of optimum size and number for both radial and axial ports will be made empirically during burner optimization. Calculations of jet trajectory were made to estimate the mixing characteristics of different port configurations. The calculations show that final port size and radial/axial distribution will depend strongly on flowrates; i.e., the optimum $SR_1$ for $NO_x$ emissions. These calculations were used to select an initial port size for the preliminary burner evaluation.

Figures 5-26 and 5-27 show approximate peak jet velocity profiles as a function of velocity (i.e., flowrate) for three port diameters at two first-stage stoichiometries ($SR_1$ = 0.65 and 0.80). The total stoichiometric ratio after radial air injection is denoted $SR_2$ and is shown for each case in the table adjacent to each figure for 8 and 16 ports. Velocities of 20, 30, and 41 meters/second are shown.

As radial secondary flowrate (hence velocity) and nozzle diameter increase, penetration across the first-stage exit increases. 5 cm jets do not reach the centerline until relatively far downstream from the point of injection, particularly in the case of high first-stage stoichiometry (Figure 5-27). 10-cm-diameter ports penetrate well at high velocity and opposing jets intersect at the centerline close to the plane of injection. Comparison of the 7.6-cm-diameter port profiles for different $SR_1$ but constant $SR_2$ = 0.9 indicates that although the jets penetrate well at low $SR_1$ (5-26b), at high $SR_1$ (5-27b) penetration is very weak because of reduced flowrate.

Figure 5-28 shows penetration profiles as a function of number and diameter of radial ports, at $SR_2$ = 0.70 and 0.88 and fixed $SR_1$ = 0.65. Port

Stoichiometric Ratio in First-Stage = 65 Percent
Adiabatic Flame Temperature of Products Approaching Port = 1610°C
Velocity of Combustion Products Approaching Port = 19 m/s

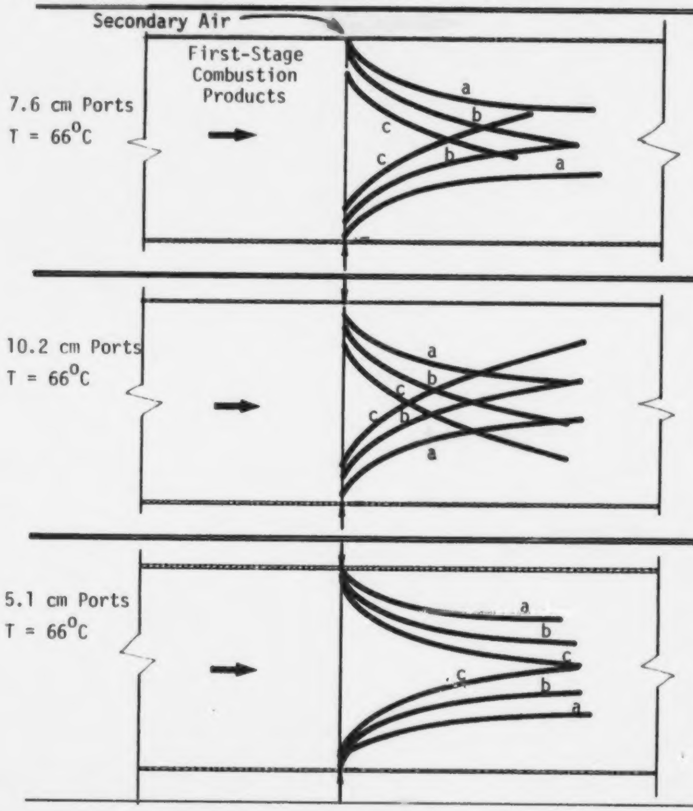
Secondary Air
First-Stage Combustion Products
7.6 cm Ports
T = 66°C
a
b
c
10.2 cm Ports
T = 66°C
a
b
c
5.1 cm Ports
T = 66°C
a
b
c

| Ports | | Stoichiometric Ratio After Radial Air Injection ($SR_2$) 8 Ports | Stoichiometric Ratio After Radial Air Injection ($SR_2$) 16 Ports | Secondary Air Velocity (m/s) |
|---|---|---|---|---|
| 7.6 cm Ports, T = 66°C | a | .78 | .91 | 20 |
| | b | .85 | 1.04 | 30 |
| | c | .91 | 1.17 | 41 |
| 10.2 cm Ports, T = 66°C | a | .88 | 1.12 | 20 |
| | b | 1.00 | 1.35 | 30 |
| | c | 1.12 | 1.58 | 41 |
| 5.1 cm Ports, T = 66°C | a | .71 | .77 | 20 |
| | b | .74 | .82 | 30 |
| | c | .77 | .88 | 41 |

Figure 5-26. Secondary air penetration for $SR_1$ = 0.65.

Adiabatic Flame Temperature of Products Approaching Port = 1879°C

Velocity of Combustion Products Approaching Port = 25 m/s

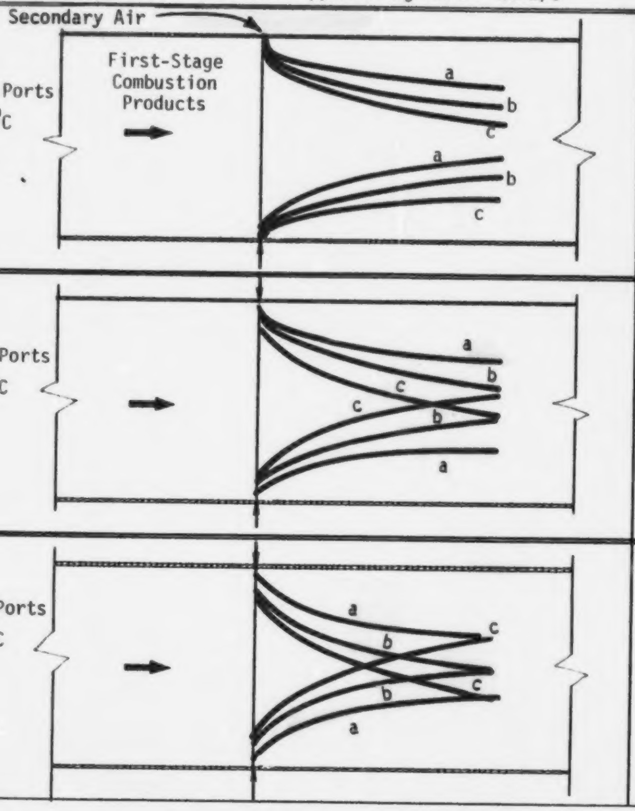
Secondary Air
First-Stage Combustion Products
a
b
c

| | | Stoichiometric Ratio After Radial Air Injection ($SR_2$) | | Secondary Air Velocity (m/s) |
|---|---|---|---|---|
| | | 8 Ports | 16 Ports | |
| 5.1 cm Ports<br>T = 66°C | a | .86 | .92 | 20 |
| | b | .89 | .97 | 30 |
| | c | .92 | 1.03 | 41 |
| 7.6 cm Ports<br>T = 66°C | a | .93 | 1.06 | 20 |
| | b | 1.00 | 1.19 | 30 |
| | c | 1.06 | 1.32 | 41 |
| 10.1 cm Ports<br>T = 66°C | a | 1.03 | 1.27 | 20 |
| | b | 1.15 | 1.50 | 30 |
| | c | 1.27 | 1.73 | 41 |

Figure 5-27. Secondary air penetration for $SR_1 = 0.80$.

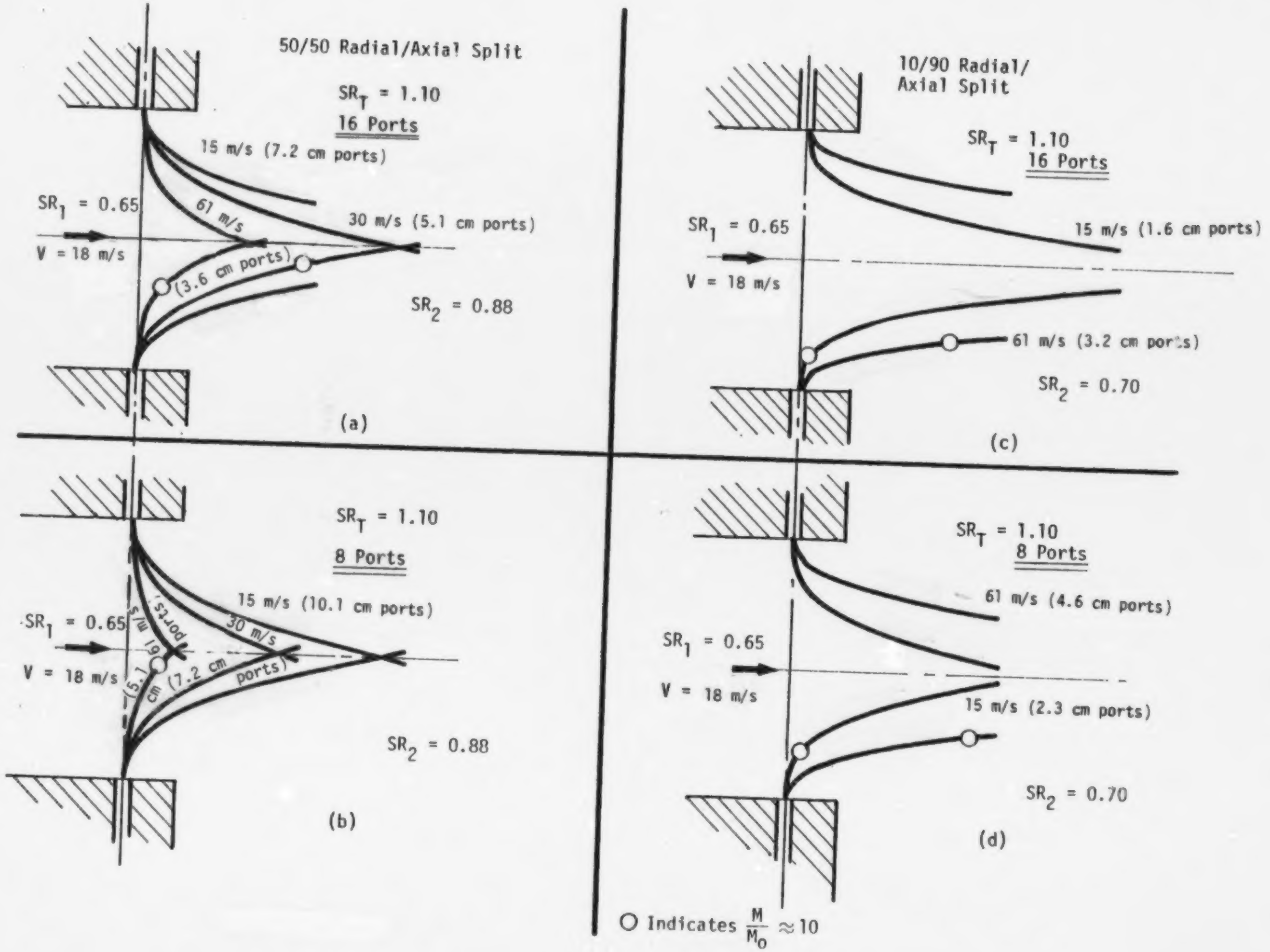
50/50 Radial/Axial Split
$SR_T$ = 1.10
16 Ports
15 m/s (7.2 cm ports)
$SR_1$ = 0.65
61 m/s
30 m/s (5.1 cm ports)
V = 18 m/s
(3.6 cm ports)
$SR_2$ = 0.88
(a)
10/90 Radial/
Axial Split
$SR_T$ = 1.10
16 Ports
$SR_1$ = 0.65
15 m/s (1.6 cm ports)
V = 18 m/s
61 m/s (3.2 cm ports)
$SR_2$ = 0.70
(c)
$SR_T$ = 1.10
8 Ports
15 m/s (10.1 cm ports)
$SR_1$ = 0.65
30 m/s
61 m/s
ports)
V = 18 m/s
(5.1 cm
(7.2 cm
ports)
$SR_2$ = 0.88
(b)
$SR_T$ = 1.10
8 Ports
61 m/s (4.6 cm ports)
$SR_1$ = 0.65
V = 18 m/s
15 m/s (2.3 cm ports)
$SR_2$ = 0.70
(d)
○ Indicates $\frac{M}{M_o} \approx 10$

Figure 5-28. Secondary air penetration for 8 and 16 ports.

diameters were chosen to yield jet velocities of 20, 30, and 41 meters/second. Decreasing the number of ports from 16 to 8 effectively increases the penetration such that the intersection point for opposing jets from the injection plane decreases by a factor of two (at $SR_2 = 0.88$). Small jets entrain mass more quickly, however. The approximate point where the jet has entrained 10 times its initial mass is indicated by a circle in the figure. This point moves closer to the injection point as port diameter decreases. This indicates that a large number of small jets could produce an overall lean mixture surrounding a centrally rich core, whereas larger and fewer jets would produce locally very lean regions which penetrate to the centerline. It can also be seen that at low $SR_2$ it is very difficult to penetrate to the centerline because of the very small port diameter (hence high velocity and pressure drop) required to do so.

Figure 5-29 compares jet trajectories for the 3 MW pilot-scale tests described in Chapter 3 and the full-scale burner. Radial secondary air injection velocity was 31 meters/second through eight ports in the pilot-scale tests, with $SR_1 = 0.65$ and $SR_2 = 1.01$. Overall excess oxygen was 3 percent ($SR_T = 1.16$), and $NO_x$ emissions were 130 ppm with residual oil. The remainder of secondary air was injected axially through the annulus. The flame produced under this condition was very short and wide, with eight "fingers" extending radially outward between adjacent radial air ports. Penetration of radial air was very rapid with relatively little entrainment between injection point and centerline (less than 5 times the initial mass). The test obstructions indicated that the eight jets intersected at the centerline close to the injection plane, creating a high-pressure, fuel-lean region. This forced the first-stage combustion products to expand radially into overall lean regions in the furnace, broken up by the lean radial air streams. The $NO_x$ emissions indicate that peak flame temperatures were probably higher for this condition than with axial air injection but still relatively cool (due to dilution and large flame surface.

Although some intuitive feeling can be obtained from the foregoing discussion with respect to penetration and mixing, several factors prevent a definitive selection from being made. The pilot-scale tests showed that (1) similar $NO_x$ could be achieved with axial ports and annular injection of

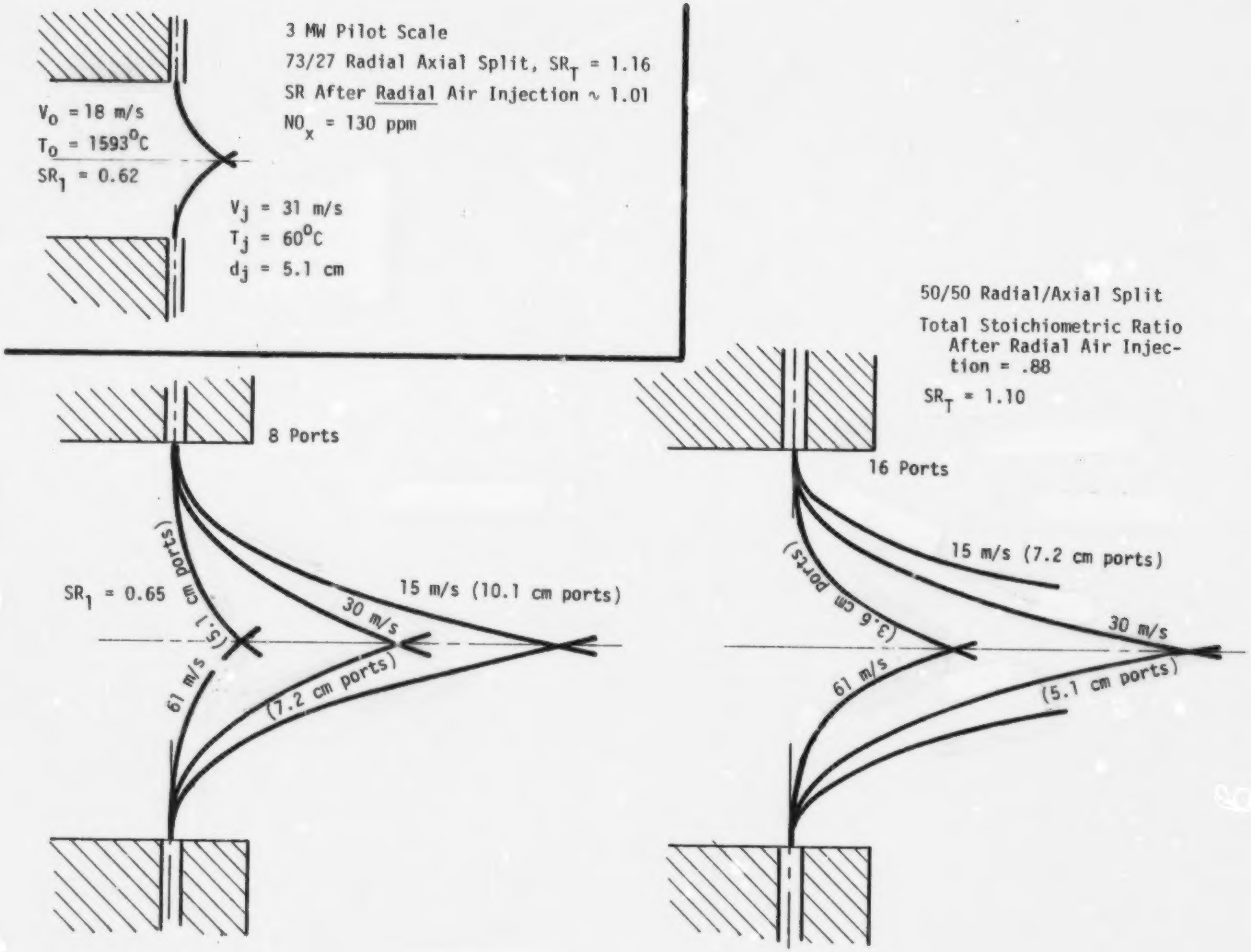
3 MW Pilot Scale
73/27 Radial Axial Split, $SR_T$ = 1.16
SR After Radial Air Injection ∿ 1.01
$NO_x$ = 130 ppm
$V_o$ = 18 m/s
$T_o$ = 1593°C
$SR_1$ = 0.62
$V_j$ = 31 m/s
$T_j$ = 60°C
$d_j$ = 5.1 cm
8 Ports
$SR_1$ = 0.65
(5.1 cm ports)
61 m/s
30 m/s
(7.2 cm ports)
15 m/s (10.1 cm ports)
50/50 Radial/Axial Split
Total Stoichiometric Ratio After Radial Air Injection = .88
$SR_T$ = 1.10
16 Ports
(3.6 cm ports)
61 m/s
15 m/s (7.2 cm ports)
30 m/s
(5.1 cm ports)

Figure 5-29. Comparison of secondary air penetration calculations for 3 MW pilot-scale burner and full-scale prototype.

secondary air, and (2) radial injection through ports could be used to control flame shape. There was not sufficient information to specify optimum $SR_2$ or injection velocity. A combination of experimental observation and experience with large flames, and interpretation of calculated jet trajectories and entrainment rates allowed selection of the initial configuration to be used for the preliminary evaluation of the burner.

## 5.6 Burner Controls

Steamer controls normally allow complete startup of the generator from a local control console mounted at the burner end of the skid. The console normally contains control elements for electric devices (motors, heaters, lights, etc.), feedwater flow, and sequencing logic in addition to burner flame controls. A combination of mechanical relays and timers provides sequencing logic for startup and shutdown. A pneumatic system is normally used for primary fuel and air flow control, and for steam pressure control. In the oil fields, pneumatic systems are preferred over electric systems for primary control because they are simpler to troubleshoot and are more reliable in a harsh environment where dust, water, wide temperature variations, and potential for power outages exist. The pneumatic control loop adjusts fuel and air flow based on feedwater flow rate.

Burner controls are relatively simple for conventional burners. A single actuator is used to drive a single air damper and fuel control valve through mechanical linkages. Air-actuated and/or electric solenoid valves are used for fuel and atomizing steam shutoff. Flame safety equipment usually includes a flame detector, limit and operating switches, and controls for a gas pilot with spark ignitor. Limit switches are used to monitor burner and steamer conditions such as fuel shutoff valve position, fuel and atomizing steam pressure, combustion air flow, main steam pressure, and various temperatures including oil, steam tube, and burner refractory. Burner control configuration varies according to the specific application; however, many contain common elements. Figure 5-30 shows features of a typical control system for a package firetube boiler.

Certain features of the prototype commercial low-$NO_x$ burner required control elements in addition to the existing steamer controls; operational

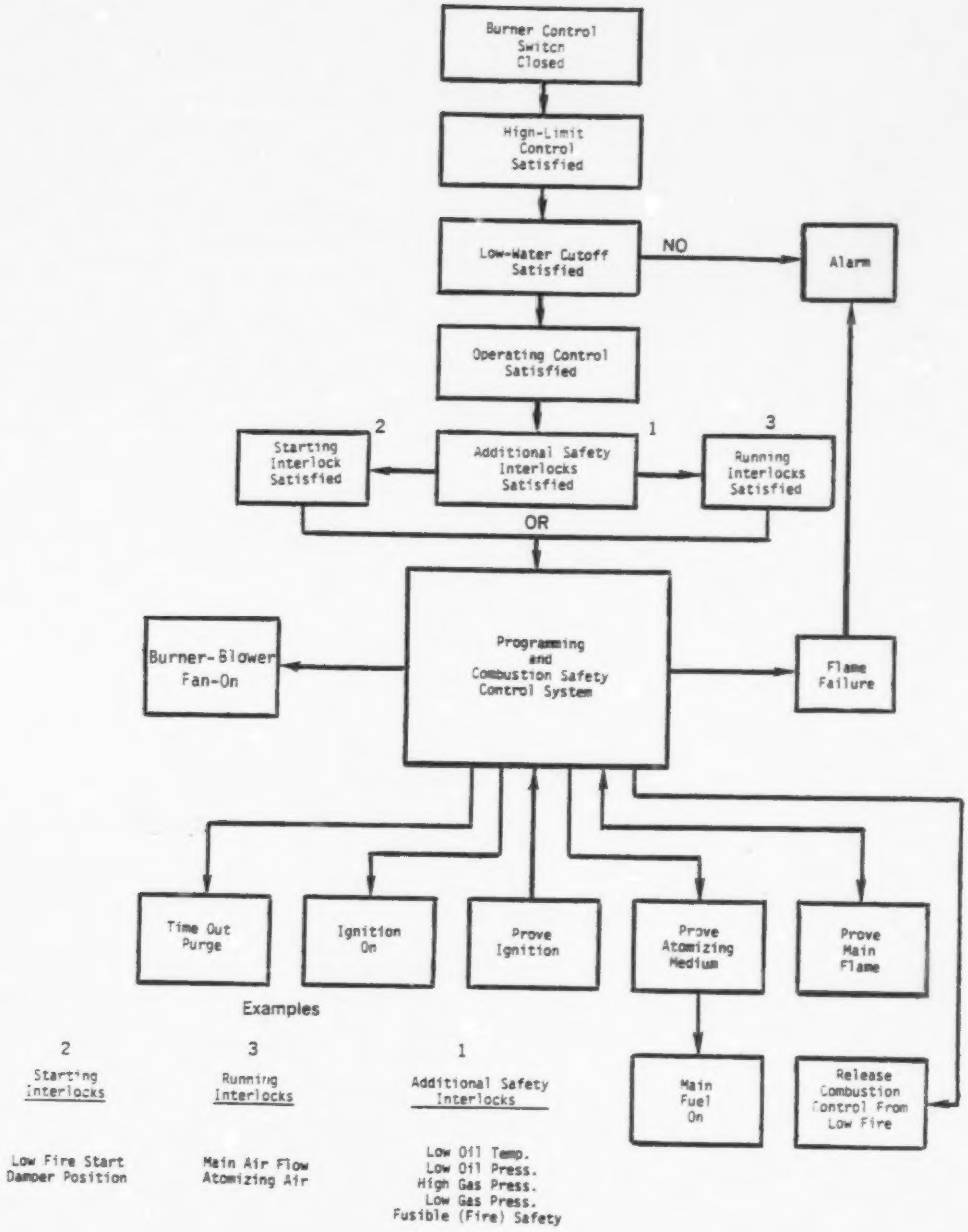
Burner Control Switch Closed
High-Limit Control Satisfied
Low-Water Cutoff Satisfied
NO
Alarm
Operating Control Satisfied
2
Starting Interlock Satisfied
Additional Safety Interlocks Satisfied
1
3
Running Interlocks Satisfied
OR
Burner-Blower Fan-On
Programming and Combustion Safety Control System
Flame Failure
Time Out Purge
Ignition On
Prove Ignition
Prove Atomizing Medium
Prove Main Flame
Main Fuel On
Release Combustion Control From Low Fire
Examples
2
Starting Interlocks
Low Fire Start Damper Position
3
Running Interlocks
Main Air Flow Atomizing Air
1
Additional Safety Interlocks
Low Oil Temp.
Low Oil Press.
High Gas Press.
Low Gas Press.
Fusible (Fire) Safety

Figure 5-30. Typical safety control system for packaged firetube boilers.

requirements are also slightly different. Table 5-19 lists some of the additional requirements of the control system. Three separately-controlled actuators for fuel, first-stage air, and second-stage air are required. First-stage stoichiometry must be very precisely controlled in order to maintain minimum $NO_x$ emissions; secondary air must be controlled for minimum excess oxygen. Normally steam generators started from cold are brought up to full-load in one-half hour. The prototype burner will require a longer heat-up and cool-down time with controlled refractory heating rate to avoid spalling of the refractory due to thermal shock. The hot refractory could cause explosive ignition if a combustible mixture of fuel and air accumulated in the steamer, therefore adequate purge periods must be guaranteed.

The final control approach which was adapted for the prototype burner is shown in Figure 5-31. The system utilizes a pneumatic primary control loop which adjusts air and oil flows based on the existing signal for feedwater flowrate. First-stage air flow is maintained at optimum using an electronic signal to bias the pneumatic signal. The pneumatic signal generated by the electronic is limited; thus, if the electronic signal fails, the pneumatic system maintains the operating condition within about 10 percent of optimum. The electronic signal is generated by a microprocessor controller which monitors instrumentation for fuel flow and primary airflow. The microprocessor controller generates a bias signal for the secondary air damper actuator based on a flue gas oxygen sensor. The controller also operates several relays for startup and shutdown sequences. Solenoid valves used in the pneumatic signal loop for startup/shutdown sequencing are not shown in Figure 5-31.

The existing flame safety and operating controls will be modified slightly to accommodate additional safety limits and controls. An additional block of relays, switches, and timers housed in a separate box will be incorporated into the current steamer controls during the field retrofit. The modification in the field will require rewiring a small number of devices to include this additional block of equipment. These changes will ensure minimum combustion air purges between ignition attempts and allow extended operation of the burner on a high-capacity pilot for initial heating of the refractory. The additional controls will also provide safety sequences in the event of a power failure, loss of combustion air, or shell overheat upset.

TABLE 5-19. CONTROL REQUIREMENTS BEYOND EXISTING STEAMER CONTROLS

| Operating Phase | Impact on Burner | Impact on Controls |
|---|---|---|
| Startup | — More time required to purge first stage<br>— Heat-up rate must be controlled<br>— Ignition off hot refractory could cause explosion<br>— Excessive purge time could cause spalling of refractory | — Tamper-proof timed purge<br>— Means for starting and heating burner without danger to steamer |
| Normal Operation | — First stage airflow must be closely controlled for optimum $SR_1$, temperature<br>— Fuel flow must follow feedwater flow<br>— Second-stage air must be controlled for minimum excess oxygen | — 3 separate burner control loops for air and fuel flows<br>— Automatic control of $SR_1$ and flue gas oxygen |
| Shutdown | — Cool-down rate must be controlled<br>— Blower must run long enough to keep shells cool | — Automatic monitoring of shell temperature<br>— Means for cooling burner slowly without damage to steamer |
| Upset/Emergency Conditions | — Avoid damage to burner or steamer components which might occur during power outage, emergency shutdown, limit trip, etc. | — Automatic "failsafe" controls for shell temperature, oil-gun, etc. |

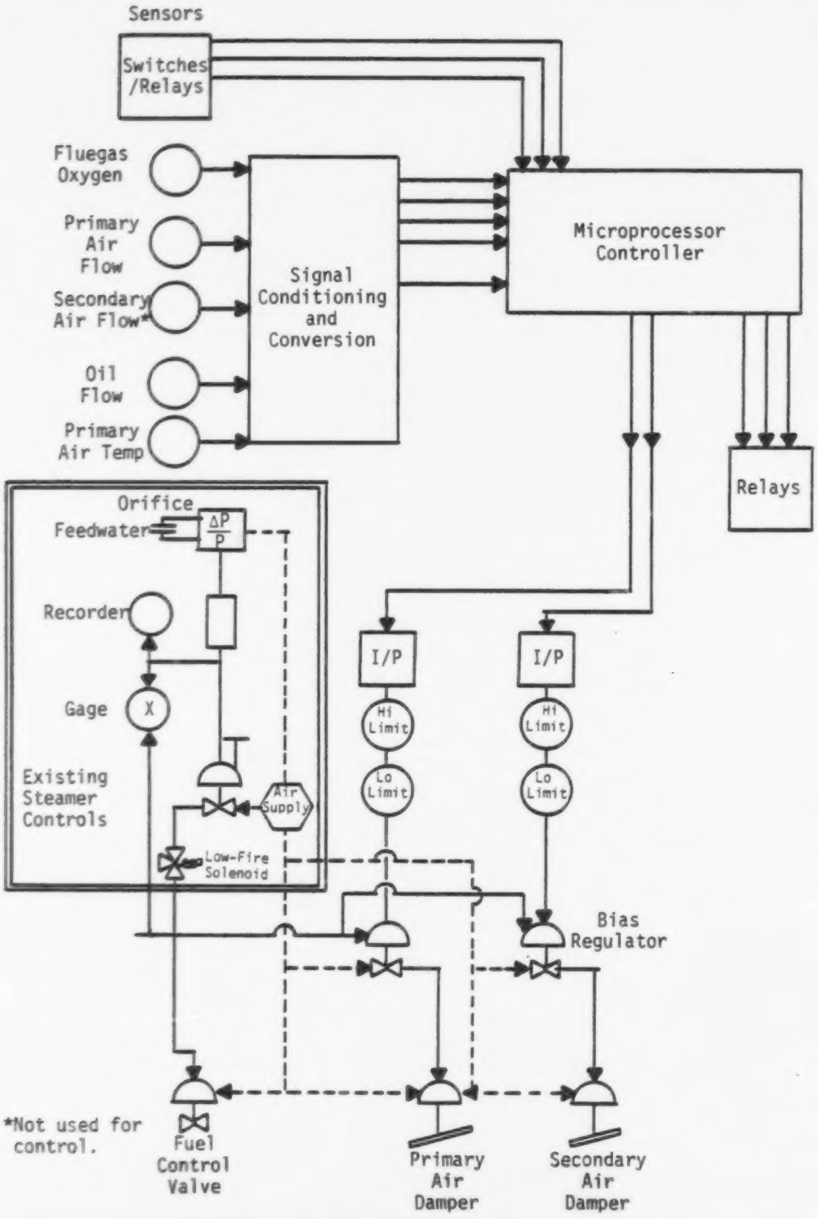
Sensors
Switches /Relays
Fluegas Oxygen
Primary Air Flow
Secondary Air Flow*
Oil Flow
Primary Air Temp
Signal Conditioning and Conversion
Microprocessor Controller
Relays
Orifice
Feedwater
ΔP P
Recorder
Gage
X
Existing Steamer Controls
Air Supply
Low-Fire Solenoid
I/P
I/P
Hi Limit
Lo Limit
Hi Limit
Lo Limit
Bias Regulator
*Not used for control.
Fuel Control Valve
Primary Air Damper
Secondary Air Damper

Figure 5-31. Burner control schematic.

The use of a hybrid electronic/pneumatic control system allows the reliability of a pneumatic control system and the flexibility of a microprocessor-based system to be incorporated. The primary emphasis on the design was to provide a system which would require minimum modification to the existing controls, and have the added flexibility needed to conduct the optimization experiments in the field. Although the basic control features of the electronic portion of the system can be duplicated with a pneumatic system, once a pneumatic system is installed to a given purpose it is difficult or expensive to modify. The microprocessor controller will also allow control of first-stage stoichiometry using an on-line $NO_x$ analyzer to be added at a later date.

## 5.7 Final Selection

At the completion of the design study it was necessary to choose between the two first-stage concepts for construction. The selection was based on a comparison of:

- Risk of mechanical failure
- Achievement of conceptual design criteria
- Thermal performance

Both concepts incorporate a certain risk of refractory lining failure primarily due to thermal stress. The required first-stage environment pushes existing refractories technology to the limit. There is very little promising experience within the refractories industry applicable to the precise operating conditions expected to be encountered. Table 5-20 compares pros and cons of the two designs. The insulated design of a conventional, state-of-the-art concept and there is more industrial experience with thick, multilayer linings for high-temperature applications; however, the environment pushes state-of-the-art to its limit, and therefore still incorporates some risk. The lining has a very large thermal inertia due to the low thermal conductivity and large mass and, even though in steady-state the temperature gradient through the inner lining is small (hence low-thermal stress), is prone to failure due to high stresses developed during heatup and cooldown. Tensile thermal stresses in the brick lining will be lower because the bricks are not strongly cemented together, and 50 percent higher thermal diffusivity means that the lining will

TABLE 5-20. COMPARISON OF INSULATED AND REGENERATIVE FIRST-STAGE CONCEPTS

| Insulated Concept | Regenerative Concept |
|---|---|
| Advantages | Advantages |
| — Refractory Installation Less Labor Untensive<br>— Single Shell (Mild Steel)<br>— Lower Temperature Gradient Through Inner Lining<br>— State-of-the-Art | — Low Mass<br>— Potentially Lower Thermal Stress<br>— More Space Efficient<br>— Substantial Air Preheat Possible |
| Drawbacks | Drawbacks |
| — High Refractory Cost<br>— Large Thermal Inertia<br>— Less Space Efficient<br>— Susceptible to Thermal Stress<br>— Higher Heat Loss to Surroundings<br>— Drying and Curing are Critical<br>— Minimum First Stage Volume | — High External Temperature and Potential for Refractory Failure Necessitates Alloy Shell<br>— High Steel, Fabrication Cost<br>— Large Temperature Gradient Through Brick |

have lower thermal stresses during heating and cooling. However, high compressive stresses leading to pinch spalling can develop on the hot face if the initial heatup of the lining is not carried out slowly. The insulated concept is also susceptible to failure during the initial curing due to shrinkage and initially low strength.

Although the labor involved in actually pouring a castable lining is much less than for laying up a brick lining, the cost savings is offset by higher materials cost and other costs associated with installing refractory anchors and curing each layer of refractory separately. This results in a higher installed cost of refractory for the insulated design. Even taking into account the alloy steel shell required for the prototype regenerative design, the net cost balance is in favor of the regenerative concept by about 20 percent. In addition, the regenerative design is more space efficient. Because of the thick lining required, the insulated concept must be 65 percent longer for the same overall outside diameter and residence time.

The regenerative design was selected for construction after evaluating the risk of mechanical failure in both concepts. The primary goal of the program is to demonstrate a commercially viable burner capable of generating very low $NO_x$ emissions. The cost advantages of the two designs were necessarily an important factor. Longer residence times are possible with the regenerative concept within the external constraints imposed by the steam generator, and a substantial degree of first-stage air preheat can be developed; therefore, first-stage conditions are closer to the ideal conceptual design criteria.

## 6.0 BURNER CONSTRUCTION AND TESTING

Procurement, fabrication, and assembly of the full-scale prototype burner is fully underway as of the date of this report. The commercial burner manufacturers involved in the burner design have assisted in the selection of materials and equipment suitable for commercial application in the oilfields.

Testing of the full-scale burner will be conducted in three phases:

- Preliminary evaluation in a test tunnel
- Optimization in the field steam generator
- 30-day performance evaluation in the field

### 6.1 Preliminary Evaluation

The objective of the preliminary evaluation is to minimize the risk of damage to the host steam generator by identifying mechanical and operational problems prior to field retrofit. The tests will be conducted at the EER test site in the Medium Tunnel (MT) facility (Figure 6-1). All fuel systems will be connected and the unit operated as though it were in the field. The burner system will undergo shakedown testing before a short continuous performance test is carried out.

The shakedown testing will occupy six weeks and will consist of:

- Checks to ensure the mechanical integrity of all components.
- A complete evaluation of all safety systems.
- Checks of the ignition system. The ignition system will be tested to ensure that the automatic ignition equipment operates satisfactorily.
- Visual inspection of the flame to ensure that flame impingement does not take place.
- The emission performance will be evaluated.
- Measurements of air flow distribution will be made to ensure that the system is operating with the optimum first-stage stoichiometry.

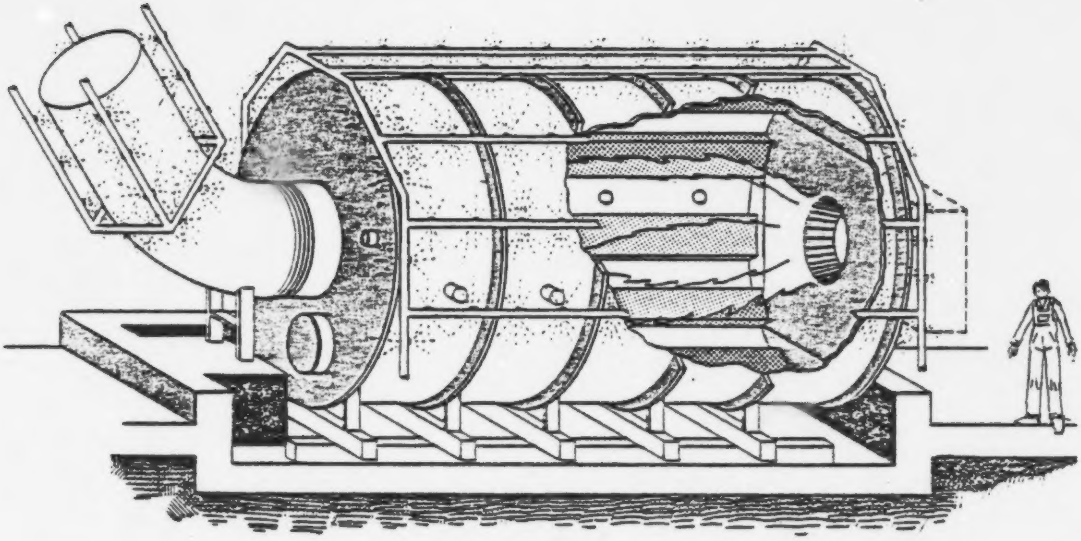

Medium Tunnel

| Parameter | EER Medium Tunnel |
|---|---|
| Capacity (MW) | 23 |
| Shape | Horizontal Cylinder |
| Firing Configuration | Cylinder End |
| Exhaust | Opposite End |
| Insulation | ≃60% of Surface Covered |
| Heat Removal | External Spray Cooling |
| Diameter (m) | 4.3 |
| Length (m) | 6.1 |
| Volume ($m^3$) | 87 |
| Total Surface Area ($m^2$) | 110 |
| Cooled Surface Area ($m^2$) | 44 |
| Heat Release/Cooled Surface Area ($MW/m^2$) | 0.53 |
| Heat Release/Volume ($MW/m^3$) | 0.082 |

* At Capacity

Figure 6-1. Medium tunnel test facility.

- Evaluation of cold start-up and shut-down performance.
- Initial set up and programming of the burner control system.

The emphasis during preliminary evaluation will be an ignition/start-up performance of the burner and control system, and on tradeoff between $NO_x$/smoke emissions and second-stage flame shape. Modifications to the burner will be made if necessary in order to bring burner performance to acceptable standards for the field installation. Input from the burner manufacturers will be solicited during this phase of burner evaluation.

The techniques to be applied for the standard furnace measurements are detailed in Table 6-1. All of the equipment required for making these measurements exists as part of the MT facility.

Exhaust concentrations are monitored continuously using a chemiluninescent analyzer for NO and $NO_x$, an NDIR analyzer for CO and $CO_2$, a paramagnetic analyzer for $O_2$, and an FID analyzer for total hydrocarbons (THC). The flue gas is withdrawn from the exhaust stack through a water-cooled, stainless steel probe using a stainless steel/Teflon sampling pump. Sample conditioning prior to the instrumentation consists of an ice bath water condenser and glass wool and Teflon fiber filters. All sample lines are Teflon with fittings type 316 stainless steel.

Detailed internal measurements will only be made to the extent necessary to bring the burner performance to expected levels.

The sampling equipment shown in Figure 6-2 will be used to measure reduced nitrogen species during these tests. EER personnel have gained considerable experience in making these measurements on a routine basis and, therefore, are aware of the potential inaccuracies. Reduced nitrogen species (HCN and $NH_3$) are sampled using the water-quench probe shown in Figure 3-33. Gas-phase HCN and $NH_3$ species are collected in a gas washing unit which consists of impingers in series with a bubbler containing a fritted glass cylinder. The sample solutions are subsequently analyzed using specific ion electrodes.

At the conclusion of this phase of testing a second interim report will be prepared to fully document the preliminary burner performance. The

## TABLE 6-1. MEASUREMENT TECHNIQUES FOR EVALUATION AND OPTIMIZATION TESTING

| Parameter | Technique |
|---|---|
| Flow Measurements | |
| - Fuel | Micro-motion mass flowmeter |
| - Combustion air | Venturis/pressure transducers |
| - Atomization air | Rotameter |
| - Atomization steam | Flow orifice/pressure transducer |
| - Primary zone flow distribution | Water-cooled pilot probe |
| Exhaust Emissions | |
| - $NO/NO_x$ | Chemiluminescent analyzer |
| - CO | NDIR |
| - $CO_2$ | NDIR |
| - $O_2$ | Paramagnetic |
| - HC | FID |
| - $SO_2$ | NDUV/Pulsed Flourescence |
| - $N_2O$ | Cryogenic concentration/GC |
| - HCN | $H_2O$ absorption/specific ion electrodes |
| - $NH_3$ | |
| - Particulate load | EPA Method 5 |
| - Particulate size distribution | In-stack Cascade Impactor |
| - Heavy hydrocarbons | Isokinetic, controlled T sampling with CAP-GC analysis |
| Temperature | |
| - Primary zone gases | suction pyrometer |
| - Furnace exit gas | |
| - Burner refractory + shell | Pt/Pt-Rh thermocouples |
| - Critical components (swirler, nozzle, etc.) | Chromel/alumel thermocouples |
| - Air | |
| - Fuel | |

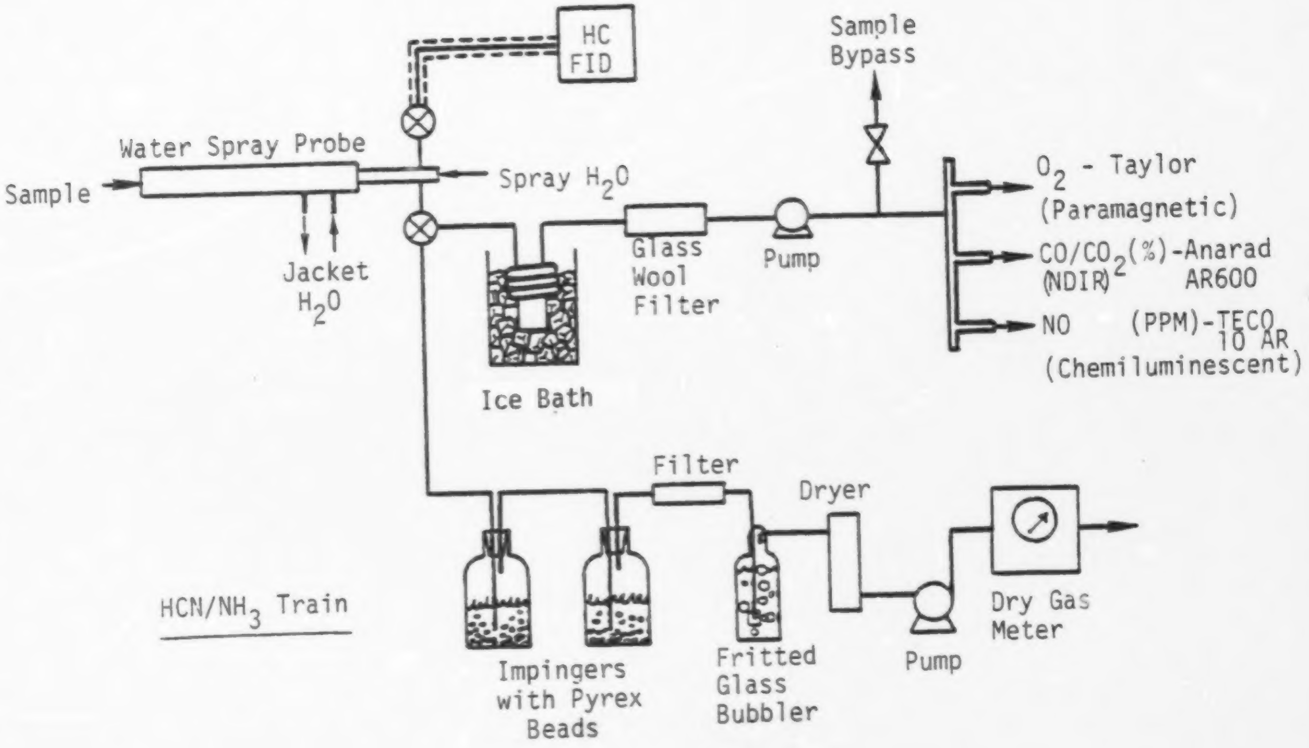
HC
FID
Sample
Bypass
Water Spray Probe
Sample
Spray $H_2O$
Jacket
$H_2O$
Ice Bath
Glass
Wool
Filter
Pump
$O_2$ - Taylor
(Paramagnetic)
$CO/CO_2$(%)-Anarad
(NDIR) AR600
NO (PPM)-TECO
10 AR
(Chemiluminescent)
Filter
Dryer
HCN/$NH_3$ Train
Impingers
with Pyrex
Beads
Fritted
Glass
Bubbler
Pump
Dry Gas
Meter

Figure 6-2. Sampling equipment for reduced nitrogen species.

test results will be reviewed by the Ad Hoc Committee in order to receive final input prior to the field installation.

## 6.2 Field Optimization Tests

The burner will be shipped to the host site and installed on the steam generator upon completion of the preliminary tests and modifications. These tests will be more extensive and specific to the steam generator requirements.

Once the low-$NO_x$ burner system has been installed and fully checked out (w.r.t. mass balances, sampling systems, etc.), the experimental evaluation will be initiated. Three sets of experimental activities are currently planned:

- A parametric evaluation of emissions and thermal performance.
- Identification and implementation of required system modifications.
- Detailed characterization measurements at the optimum operating conditions.

This testing will focus heavily on the thermal performance and operating characteristics of the system because the emissions behavior is already relatively well understood. Table 6-2 lists the measurements which will be made during these tests.

The first sequence of parametric tests will consider optimization of flame shape and pollutant emissions. These tests will most likely involve variation of second-stage air distribution (radial/axial), first-stage stoichiometry, primary air swirl, and atomizer spray angle, and excess $O_2$.
The second parametric test sequence will include an emissions and combustion performance sensitivity analysis with respect to variations in:

- Atomizing steam pressure and quality
- Ambient air temperature
- Nozzle placement
- Fuel temperature

## TABLE 6-2. INITIAL OPERATIONAL EVALUATION MEASUREMENTS

BURNER/STEAMER INPUTS

| Parameter | Test Procedure | Data Verification Procedure |
|---|---|---|
| Furnace Design<br>Burner Design<br>Burner Adjustments<br>Registers<br>Dampers<br>Others | Direct Measurement | Comparison to Final Prototype Design |
| Fuel<br>Composition | Proximate and Ultimate Analysis | Analysis by Two Independent Laboratories |
| Flow Rate (Boiler Load) | Flow Meter | Carbon Balance With Boiler Exhaust Measure-Measurements |
| Combustion Air<br>Flow Rate | Exhaust Gas Measurements by EPA Method 2 | Mass Balance of Burner Inputs and Outputs |
| Temperature | Thermocouple | Calibration of Thermocouple |
| Distribution (Stoichiometry of each stage) | Internal Flow Meters | Comparison of Burner Settings With Prototype Results |
| Boiler Water | Flow Meter | Energy Balance With Steam/Exhaust Gas Measurements |
| BURNER/STEAMER OUTPUTS | | |
| Flame Characteristics<br>Length<br>Width<br>Standoff<br>Stability | Direct Observation | Color Videotape<br>Color Photographs |
| Windbox Pressure<br>Furnace Pressure | Manometer | Calibration of Manometer |
| Burner Temperatures<br>Furnace Wall Temperatures | Thermocouple | Calibration and Use of Multiple Thermocouples |

- Fuel viscosity
- Firing rate
- Burner shell temperature (rain)
- Partial nozzle blockage

The final parametric sequence will address the performance and final programming of the automatic control system. It will define its ability to function continuously over long periods of unattended operation and to provide appropriate control for variations such as those listed above. In addition, the control tests will consider:

- Resolution and precision of the controller required to maintain the low-$NO_x$ set point in steady-state condition.
- Adjustment of sensitivity coefficients and gain settings of all variables.
- Response of the system step changes in load or other transients. Of particular interest is control action required to maintain burner stoichiometry during rapid load changes; i.e., during start-up and shut-down.
- Control action in response to individual component deterioration or malfunction, such as response to partially clogged fuel injection.
- Complete characterization and verification of all safety control actions.

Following these tests any modifications to the burner or control system will be implemented. A detailed characterization of the burner/steamer performance will be conducted after modification are complete and performance has been optimized. These tests will include the following measurements:

- Complete exhaust emissions (NO, $NO_2$, CO, $CO_2$, smoke, UHC).
- Particulate mass loading by EPA Method 5.
- Particulate size distribution by in-stack, cascade impactor.
- Steam generator thermal performance.

In addition, separate experiments will be conducted to verify the absolute integrity of the system operation. These tests will focus on the automatic control and safety systems and will include consideration of:

- Steamer start-up. Since the flame is strongly radiantly stabilized under normal operating conditions, the cold-start condition may require a significantly different air distribution than normal.
- Emission and combustion performance as a function of load under completely automatic operation.
- Transient behavior during rapid load swings.

These tests will also establish the reliability the automatic shutdown system in the event of:

- Flame out
- Nozzle blockage
- Air blower failure
- Power failure
- Steam tube rupture
- Water supply interception

Finally, the detailed characterization tests will include consideration of any problem areas which were identified and corrected previously.

### 6.3 30-Day Performance Evaluation

After the steamer operational and analytical systems have been verified for proper performance, EER will conduct a 30-day test of the unit. The objective of the 30-day test is to monitor boiler performance and emissions of criteria pollutants over 30 days so that any degradation of performance or increase in emissions can be documented.

During this test period, the boiler will be operated as a typical production oil field steam generator by host site personnel. Thus, the burner system will be evaluated over a typical range of operating conditions.

Measurements of burner/steamer input parameters during the 30-day test will be the same as the measurements made during the optimization tests.

These measurements will include continuous monitoring of fuel flow rate (boiler load) and daily collection of fuel samples for subsequent analysis. Measurements of system output parameters to be performed during the 30-day test are listed in Table 6-3. These measurements will be more completely defined in the Measurements Protocol to be prepared prior to the start of testing. The output measurements during the 30-day test are not as comprehensive as the initial field measurements because the objective of the 30-day test is to monitor the change in key performance and emission levels with time.

The output measurements will include continuous monitoring of gaseous emissions and furnace wall temperatures. Particulate and particle size tests will be conducted daily. The remaining parameters will be monitored periodically during each test day. In addition to the measurements, a log will be maintained of any system malfunctions or other operational problems. Malfunctions will be corrected before testing is continued. During at least one test, the heavy organic material associated with the particulate matter will be measured by isokinetic, controlled temperature sampling and capillary GC analysis. Thermal efficiency will be measured by two procedures. The primary procedure involves determining heat losses relative to the heat input. Losses include the latent and sensible heat of the exhaust gas, and other small losses including radiation. Thermal efficiency measurements will be verified by determining the heat absorbed by the steam relative to the heat input.

At the conclusion of the 30-day test, the relative accuracy portion of the EPA Performance Specification tests will be repeated to insure that the gaseous monitoring instrumentation has provided data comparable to EPA reference methods.

At the conclusion of the burner optimization and performance tests, a detailed assessment of overall system performance will be conducted. This work will focus on the following key questions.

Emissions

- Were the $NO_x$ smoke and CO goals achieved?
- Are the results consistent with the data obtained in the 21 kW and 1 MW tests?

TABLE 6-3. SYSTEM OUTPUT MEASUREMENTS DURING 30-DAY TEST

| Parameter | Test Procedure | Data Verification Procedure |
|---|---|---|
| Flame Characteristics | | |
| Length | Direct Observation | Color Videotape<br>Color Photographs |
| Width | | |
| Standoff | | |
| Stability | | |
| Windbox Pressure | Manometer | Calibration of Manometer |
| Furnace Pressure | | |
| Burner Temperatures | Thermocouple | Calibration and use of multiple thermocouples |
| Furnace Wall Temperatures | | |
| Gaseous Emissions | | |
| NO, $NO_2$ | Continuous monitoring instrumentation using EPA Protocol No.1 calibration gases | EPA Performance specifications 2 and 3 |
| $O_2$ | | |
| CO | | |
| $CO_2$ | | |
| Particulate Emissions | | |
| Total Particulate | EPA Method 5 | Calibration of test equipment and multiple runs |
| Condensible Hydrocarbons | EPA Method 5 "back-half" | |
| Particle Size | In-stack Cascade Impactor | |
| Thermal Efficiency | Heat Input -heat losses/ heat input | Steam Output/Heat Input |

## 7.0 REFERENCES

Cato, G. A., L. J. Muzio, and R. E. Hall. "Influence of Combustion Modifications on Pollutant Emissions from Industrial Boilers." Proceedings of the Stationary Source Combustion Symposium, EPA 600/2-76-1526, Springfield, VA (1976).

Pershing, D. W., J. E. Cichanowicz, G. C. England, M. P. Heap, and G. B. Martin. "The Influence of Fuel Composition and Flame Temperature on the Formation of Thermal and Fuel $NO_x$ in Residual Oil Flames." Seventeenth Symposium (International) on Combustion, The Combustion Institute, Pittsburgh, PA (1979).

England, G. C., M. P. Heap, D. W. Pershing, and R. K. Nihart. "Mechanisms of $NO_x$ Formation and Control: Alternative and Petroleum-Derived Liquid Fuels." Eighteenth Symposium (International) on Combustion, The Combustion Institute (1981).

Heap, M. P., et al. "Control of Pollutant Emissions from Oil-Fired Package Boilers." Proceedings of the Stationary Source Combustion Symposium, EPA 600/2-76-1526, NTIS, Springfield, VA (1976).

Beer, J. M., M. T. Jacques, W. Farmayan, and B. R. Taylor. "Fuel Nitrogen Conversion in Staged Combustion of a High Petroleum Fuel." Eighteenth Symposium (International) on Combustion, The Combustion Institute, Pittsburgh, PA (1981).

Pershing, D. W., G. B. Martin, and E. E. Berkau. "Influence of Design Variables on the Production of Thermal and Fuel NO from Residual Oil and Combustion," AIChE Symposium Series No. 148, 71 (1975).

Fenimore, C. P. Studies of Fuel Nitrogen Species in Rich Flames Gases. In: Proceedings. Seventeenth (International) Symposium on Combustion, The Combustion Institute, Pittsburgh, Pennsylvania (1979). pp. 661-671.

Folsom, B. A., C. W. Courtney, and M. P. Heap. "The Effects of LBG Composition and Combustor Characteristics on Fuel $NO_x$ Formation." Paper presented at the ASME Gas Turbine Conference and Exhibit and Solar Energy Conference, San Diego, California (1979).

England, G. C., M. P. Heap, Y. Kwan, R. Payne, and D. Pershing. "Development of a Low-$NO_x$ Burner for Enhanced Oil Recovery." Paper presented at the 1982 Joint Symposium on Stationary Combustion $NO_x$ Control, Dallas, TX (1982).

England, G. C., D. W. Pershing, and M. P. Heap. "Establishment of Design Criteria for Optimum Low-$NO_x$ Burners for Application to Heavy Fuel-Fired Package Boilers." Final Report, Vol. II, EPA Contract 68-02-3125 (In preparation) (1983).

Payne, R., T. Akiyama, and J. Witkamp. "Pollutant Emission Characteristics of Oil Fired Industrial Process Burners," Paper presented at the International Symposium on Industrial Process Combustion Technology, Newport Beach, CA, (October 1980).

Seeker, W. R., and G. S. Samuelsen, "Spray Characterization." Paper presented at 5th EPA Fundamental Combustion Research Workshop, Newport Beach, CA (1980).

Beer, J. M., and N. A. Chigier. Combustion Aerodynamics. Applied Science Publishers, LTD (1972).

Payne, R., G. Flament, S. Michelfilder, and G. England. "Characterization of Fuel Atomizers Using a Laser Defraction Dropsize Analyzer." VDI-Berichte, Nr. 346 (1979).

Mullinger, P. J., and N. A. Chigier. "The Design and Performance of Internal Mixing Multijet Twin-Fluid Atomizers." J. Inst. of Fuel, 47, 251-261 (1974).

McEwan, M. W. "Hot and Cold Studies on an Oil-Fired Burner with Swirler Fitted in a Refinery Oil Heater." Paper presented at the Second Member Conference, IFRF, Ijmuiden, Holland, May (1971).

Swithenbank, J., et al. "A Laser Diagnostic Technique for the measurement of Droplet and Particulate Size Distribution." Prog. in Astronautics and Aeronautics, Vol. 53 (1977).

Wigg, L. D. "Drop-Sizes Predictions for Twin Fluid Atomizers." J. Inst. Fuel, 27, 500-505 (1964).

Wu, H. C., and N. Fricker. "An Investigation of the Behavior of Swirling Jet Flames in a Narrow Cylindrical Furnace." Paper presented at the Second Member Conference IFRF, Ijmuiden, Holland (May 1971).

Seeker, W. R., W. D. Clark, and G. S. Samuelsen. The Influence of Scale and Fuel Properties on Fuel-Oil Atomizer Performance." Paper presented at the 1982 Joint Symposium on Stationary Combustion NO_ Control, Dallas, TX (1982).

Nelson, L. P., and B. A. Folsom. "$NO_x$ Emissions from Steam Generators Used in Thermal Enhanced Oil Recovery." Presented at California Regional Meeting of the Society of Petroleum Engineers, Bakersfield, California (1981).

Warren, K. W., and G. W. Sams. "The Control of $NO_x$ from Oilfield Steam Generators by Combustion Modification." Paper presented at Pacific Coast Oil Show, Los Angeles (November 1982).

Fryling, G. R. "Combustion Engineering." Combustion Engineering, Inc., 1966.

Perry, J. H., and C. H. Chilton. "Chemical Engineer's Handbook." 5th ed., McGraw-Hill, N.Y. (1973).

Larson, D. R., J. A. Coppola, D. P. H. Hasselman, and R. C. Bradt, "Fracture Toughness and Spalling Behavior of High-$Al_2O_3$ Refractories." Journal of the American Ceramic Society, Vol. 57, No. 10 (October 1974).

Baumister, T., "Mark's Standard Handbook for Mechanical Engineers." 8th ed., McGraw-Hill, N.Y. (1978).

Hottel, H. C., and A. I. Sarofim, "Radiative Transfer." McGraw-Hill, N.Y. (1967).

"The Handbook of Refractory Practice." Harbison-Walker Refractories, Pittsburgh, PA (1979).

"The Handbook of Castable Refractories," Catalog #36. Harbison-Walter Refractories, Pittsburgh, PA (1981).

# APPENDIX A

# LOW $NO_x$ BURNER REFRACTORY LINING DESIGN STUDIES

# REFRACTORY LINING DESIGN
# FOR A
# LOW $NO_X$ BURNER
# FOR
# ENERGY AND ENVIRONMENTAL RESEARCH CORPORATION
# BY
# DAVY McKEE CORPORATION

Subcontract No. 8450-1
Prime Contract No. EPA 68-02-3692
Davy McKee Reference: NC-5962

## TABLE OF CONTENTS

| | | Page |
|---|---|---|
| I. | OBJECTIVE | 1 |
| II. | CONCLUSIONS | 2 |
| III. | RECOMMENDATIONS | 3 |
| IV. | METHOD OF APPROACH | 5 |
| V. | MATERIAL SELECTION | 8 |
| | A. Operation | 8 |
| | B. Method of Construction | 8 |
| | C. Physical Properties | 11 |
| VI. | PRELIMINARY CALCULATIONS | 13 |
| | A. Thin Linings | 13 |
| | B. Thick Linings | 15 |
| | C. Reference Design | 19 |
| | D. Thermal Shock | 21 |
| VII. | DETAILED ANALYSIS | 25 |
| | A. Method of Analysis | 25 |
| | B. Models Analyzed | 29 |
| | C. Results | 30 |
| VIII. | SUMMARY | 43 |
| | REFERENCES | 44 |
| | DESIGN DRAWINGS | |

## I. OBJECTIVE

Energy and Environmental Research Corporation (E.E.R.) is developing a low NOx burner on behalf of the U.S. Environmental Protection Agency to mate with standard steam generators which provide steam for enhanced oil well production. E.E.R. has retained Davy McKee Corporation (DMC) to assist them in the detailed design of the burner shell, lining and air preheat features. The broad design goals for the lining and shell were to provide:

- o Minimum heat loss to the surroundings.
- o Maintaining gas temperatures within the first stage greater than 2600°F and as close to adiabatic as possible.
- o Desired minimum refractory lifetime of 5-7 years without catastrophic failure or major repairs.
- o Optimum cost vs. performance.

To accomplish these goals the engineering services provided by DMC were conducted in three phases:

- o A kick-off meeting during which general consultation was provided and specific design goals of the refractory liner and shell were prescribed.

- o A design study in which a range of conceptual designs for the liner and shell were evaluated.

- o A detailed design phase in which the conceptual design selected in Phase II was developed.

The purpose of this report is to summarize the work performed, to present the conclusions reached, and to make certain recommendations concerning the design of the burner system.

## II. CONCLUSIONS

A. The recommended refractory lining is based on a thorough theoretical analysis of the temperature and stress distributions as well as a careful review of available refractory and insulating materials for optimum design.

B. A number of important considerations should be noted:

1. The maximum thermal stresses will be seen at the juncture of the conical and cylindrical sections.

2. Because the lining is relatively thick, the temperature of the outer portions will rise more slowly than that of the hot face.

3. A very slow heat-up rate should be followed.

C. Some cracks must be expected even with a slower heat-up rate. However, it is not expected that these cracks will affect the intended performance of the lining.

D. The temperature rise of the steel shell is expected to be about 58°F. The burner shell will therefore expand about 3/4 inch. This expansion is accomplished by fixing it at one end only and allowing the expansion to take place in one direction. The saddle support is slotted to accomodate this expansion.

## III. RECOMMENDATIONS

A. Construction and dryout proccedures shown in DMC drawings 5962A-X-01 and 5962A-X-02 should be followed.

B. Startup should be very gradual in accordance with the schedule shown on the following page. Note the fact that the gas temperature is held periodically to prevent large temperature differences between the gas and the liner.

C. Means should be provided to automatically block off the entrance to the burner and the exit of the steam generator and flue to prohibit cooling by natural convection in case of a power failure.

D. Cool down should be accomplished by reversing the startup procedure.

| Time Hours | Gas Temp. oF | Time Hours | Gas Temp. oF | Time Hours | Gas Temp. oF |
|---|---|---|---|---|---|
| 0 | 200 | 29 | 1150 | 58 | 2100 |
| 1 | 250 | 30 | 1200 | 59 | 2100 |
| 2 | 300 | 31 | 1200 | 60 | 2100 |
| 3 | 300 | 32 | 1250 | 61 | 2150 |
| 4 | 350 | 33 | 1300 | 62 | 2200 |
| 5 | 400 | 34 | 1300 | 63 | 2200 |
| 6 | 400 | 35 | 1350 | 64 | 2250 |
| 7 | 450 | 36 | 1400 | 65 | 2300 |
| 8 | 500 | 37 | 1400 | 66 | 2300 |
| 9 | 500 | 38 | 1400 | 67 | 2350 |
| 10 | 550 | 39 | 1450 | 68 | 2400 |
| 11 | 600 | 40 | 1500 | 69 | 2400 |
| 12 | 600 | 41 | 1500 | 70 | 2450 |
| 13 | 650 | 42 | 1550 | 71 | 2500 |
| 14 | 700 | 43 | 1600 | 72 | 2500 |
| 15 | 700 | 44 | 1600 | 73 | 2550 |
| 16 | 700 | 45 | 1650 | 74 | 2600 |
| 17 | 750 | 46 | 1700 | 75 | 2600 |
| 18 | 800 | 47 | 1700 | 76 | 2650 |
| 19 | 800 | 48 | 1750 | 77 | 2700 |
| 20 | 850 | 49 | 1800 | 78 | 2700 |
| 21 | 900 | 50 | 1800 | 79 | 2750 |
| 22 | 900 | 51 | 1850 | 80 | 2800 |
| 23 | 950 | 52 | 1900 | 81 | 2800 |
| 24 | 1000 | 53 | 1900 | 82 | 2850 |
| 25 | 1000 | 54 | 1950 | 83 | 2900 |
| 26 | 1050 | 55 | 2000 | 84 | 2900 |
| 27 | 1100 | 56 | 2000 | 85 | 2950 |
| 28 | 1100 | 57 | 2050 | 86 | Final Gas Temp. |

## IV. METHOD OF APPROACH

The low NOx burner liner is exposed to hot gas with a temprature of the order of 3000°F. The integrity of the liner is critical to the performance of the burner. Failure of the liner can expose the steel shell to the hot gas. At these temperatures the steel shell will fail, resulting in leakage of outside air which will negate the design concept of supplying only about 60% of the stoichiometric air requirements inside the burner and possibly raise the NOx emissions above the desired level.

Refractory failures may be attributed to several causes:

- Chemical attack
- Erosion
- Improper dry-out procedures
- Thermal shock due to excessively fast heat-up rates
- Thermal stresses
- Improper design or installation

If the refractory liner materials have been properly selected and proper design and dry-out procedures followed, then the probable cause of failures is generally excessive thermal stresses either during heat-up or cool down (thermal shock) or during steady state operations.

Thermal stresses are of two general classes:

- Stresses caused by external constraints.
- Stresses caused by internal constraints. If a body which is unrestrained physically is heated in a non-uniform manner, that portion which is at a higher temperature may be restrained from expansion by colder material. A similar effect may be found in a composite body in which the elements have different temperature coefficients of expansion.

Closed form solutions for thermal stress have been derived for some simple cases. For the vast majority of practical problems, closed form solutions do not exist. For these cases recourse is usually made to numerical solution on a digital computer. However, insight as to possible design approaches may be gained by examining the closed form solution for a thick-walled cylinder of a single material with uniform inner and outer temperatures and a constant temperature coefficient of expansion. The maximum stresses occur at the inner and outer surfaces in the tangential direction and are given by (1):

Outer Surface: $S = \dfrac{\Delta T\ \alpha E}{2(1-\upsilon)\ \ln \frac{c}{b}} \left(1 - \dfrac{2b^2}{c^2-b^2} \ln \dfrac{c}{b}\right)$ tension (1)

Inner Surface: $S = \dfrac{\Delta T\ \ \alpha E}{2(1-\upsilon)\ \ln \frac{c}{b}} \left(1\ \dfrac{2c^2}{c^2-b^2} \ln \dfrac{c}{b}\right)$ compression (2)

Where $\Delta T$ = Difference in temperature between inner and outer surface, $^{o}F$

$\alpha$ = Temperature coefficient of expansion, $\frac{1}{^{o}F}$

E = Young's modulus, psi

$\upsilon$ = Poisson's ration, dimensionless

b = inner radius

c = outer radius

These expressions could also be written as:

$$S = \frac{E\alpha\Delta T}{2\ (1-\upsilon)}\ (F)$$

Where F is a function of geometry.

Thus, apart from geometry, thermal stress is determined by material constraints and by temperature differences.

To prevent failure we must minimize the thermal stress or pick a material with high failure stress. If we wish to minimize the stress we have the following choices, given a fixed geometry:

1. Choose a material with low E or low $\alpha$. However if E is low, the failure stress is also likely to be low.

2. Limit the temperature difference $\Delta T$

   Now consider: $\Delta T = \frac{\partial T}{\partial r} (\Delta r)$

   Thus, to minimize $\Delta T$ we must either minimize the temperature gradient $\frac{\partial T}{\partial r}$, minimize the thickness $\Delta r$, or minimize both.

In minimizing the thickness, care and judgement must be exercised. There are practical limits which should not be exceeded; too thin a lining could endanger the material behind it should cracks appear. Further, tolerances in installing a cast or gunned lining can be large, resulting in localized areas which are too thin. In addition, the thickness of a layer of the lining must be sufficient to lower the temperature which the next layer sees to an acceptable value. For these reasons the emphasis is first to minimize the radial temperature gradient through the lining.

The procedure is thus to select materials, to conceptualize lining configurations and calculate steady state temperature distributions using a simple cylindrical model, to determine methods of construction, and to determine appropriate start-up rates.

## V. MATERIAL SELECTION

Material selection is made after considering the following factors:

### A. Operation

It is anticipated that the burner will be operated for 25-30 days at a time. Thus, if heat-up and cool-down rates can be minimized, the liner thermal stresses may not be much greater than those at steady state. If there is a power failure, however, shutdown will occur. If there is no provision to block off the burner inlet and exits, atmospheric air will be drawn in by natural convection. It is expected that severe thermal stresses could occur as a result. Further, the environment changes from a reducing atmosphere to an oxidizing atmosphere. The refractory selected must therefore be compatible with either of these atmospheres.

Another factor strongly influencing material selection is the temperature of the gas. Data from E.E.R. indicates that the temperature is expected to be about 2960°F when 60% of the stoichiometric air requirement is supplied. Hence, the allowable service temperature of the hot face material selected must be at least 3000°F. This requirement precludes the use as a hot face material of entire classes of refractories such as insulating castables, fireclay castables, and all fireclay brick except superduty.

### B. Method of Construction

Three basic methods of liner construction were considred: monolithic, brick and segmented monolithic.

1. Monolithic

This application is ideal for monolithic construction. A smooth transition between the different diameters of the main burner chamber and the inlet to the steam generator can easily be made. Joints can easily be provided where desired by the judicious placement of a burnable material such as cardboard. This type of construction lends itself to anchoring to the steel shell without excessive heat losses. Finally, installation costs are less than with brick construction.

2. Brick

The key element in brick construction furnaces is the roof. For this application either an arch construction or a suspended roof could be used. Note that even if the cross section were completely circular the roof could be considered an arch. The problem with arch construction is that it is statically indeterminate. Thus, the location of the line of action of the thrust forces within the arch is uncertain and varies with the temperature and the flatness or closeness of fit of the brick surfaces. Mortar is used to provide a better fit at installation. However, with the movement of the arch due to temperature rise, the mortar frequently crumbles. With this temperature rise, then, the bricks tend to gap at the outside near the crown and touch only at the inner edge. This leads to pinch spalling and instability. Arch construction therefore requires the very highest quality of workmanship. Even then, the high expected temperatures expected for this application raise the question of stability. Hence this method of construction was eliminated from consideration.

Suspended roofs, whether flat or curved, have the advantage that stability does not depend on the arch effect. For these temperatures, a refractory hanger type of construction must be employed. These hangers are rather large, and a large number of them must be used to suspend the tiles. The heat losses are therefore comparatively large for this construction and the tiles and hangers are very expensive. For these reasons, a suspended roof was removed from consideration.

3. Segmented Monolithic

Suppose the shell were made in segments with cast or gunned material, suspended by ceramic anchors, used for the lining as shown in the sketch below.

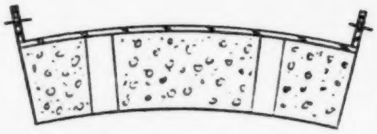

Such a construction would have the advantage of ease of transportation. The burner would be assembled by bolting the flanges of the segments together and placing burnable inserts between the adjoining liner segments. In theory, these inserts would burn out at just the right temperature, allowing the refractory to expand and close the gaps. In practice, this is extremely difficult to achieve. The gaps do not close completely, the steel shell is exposed to hot gases, and the refractory is supported only by the anchors. For these reasons this type of construction was not chosen.

C. Physical Properties

It has already been shown that thermal stresses can be minimized by choosing a material with low E or low $\alpha$. The stresses can also be minimized by minimizing the temperature gradient $\frac{\partial T}{\partial r}$. Thus, a hot face material having a relatively high thermal conductivity would minimize the temperature gradient.

Ideally, we would also prefer to have a material with a high failure stress at operating temperatures. It is customary to arrive at a measure of this quantity by testing bricks in bending at various temperatures. The stress at which they fail is computed from standard beam formulas and is called the Modulus of Rupture (MOR). According to Trinks, the tensile strength is approximately two-thirds the MOR[2].

Examination of MOR data of possible hot face linings shows that the strength of all materials decreases rapidly after a temperature of about 2500°F is reached. For example, chemically bonded chrome castable shows a MOR of only 40 psi at 2500°F[3]. The strongest materials appear to be of the high alumina group.

There is one other important parameter of interest and that is the ability of a refractory to resist crack propagation. Whereas the MOR is a measure of the ease of crack initiation, Hasselman found that the driving force for crack propagation is provided by the elastic energy stored at fracture[4]. Hasselman also developed a unified theory of thermal shock fracture initiation and crack propagation and defined a thermal stress damage resistance parameter $R''''$ which was proportional to the work of fracture[5]. Crack progation is minmized when $R''''$

is maximized. Unfortunately, simultaneous maximization of both the resistance to initiation of fracture and damage resistance is impossible. A compromise is therefore necessary. For example, Larson, et. al. measured R'''' for a number of high alumina refractories.[6] Table 1 lists the results for those materials with the highest resistance to crack initiation and propagation.

TABLE 1

Resistance to Crack Initiation and Propagation

| Refractory No. | % Alumina | MOR, psi | R'''', cm |
|---|---|---|---|
| 1 | 99 | 3600 | 1.71 |
| 4 | 90 | 2830 | 2.14 |
| 8 | 85 | 1980 | 3.08 |
| 10 | 85 | 4400 | 0.56 |
| 20 | 70 | 1590 | 1.73 |
| 25 | 70 | 412 | 12.63 |

Note that refractory No. 25 had the highest resistance to crack propagation, but its low MOR would make it a poor choice in applications where high thermal stresses were expected. Similarly, refractory No. 10 had the highest MOR, but the lowest R''''. Selection must therefore be based on considerations of both quantities.

## VI. PRELIMINARY CALCULATIONS

Using simple cylindrical models, hand calculations of steady-state temperature distributions were made for a number of different candidate linings. As a result of these calculations a reference design was selected and a more detailed analysis was made.

### A. Thin Linings

One approach to design is to employ a relatively thin lining backed by a steel shell. To lower the temperature of the steel backing shell sufficiently another shell is located concentric with and exterior to the backing shell to form an annulus. Air is blown into the annulus, cooling the shell and raising the temperature of the air prior to admitting it to the burner. Figure 1 shows the result of steady-state heat transfer calculations for liner thickness of 4½, 6, 9 and 12 inches based on the following assumptions:

- Hot face temperature 2940°F.
- Air temperature 70°F
- Convective heat transfer coefficient 13.5 $\mathrm{Btu/hr.ft^2\ ^oF}$
- High density alumina liner with low expansion coefficient, high thermal conductivity, high MOR and R''''. Properties evaluated at mean temperature of lining.
- Neglibible radiation from internal shell to external shell.

The temperature of the internal shell is seen to vary from about 760°F to 350°F for the various liners, and their temperature gradients are seen to be comparatively steep. Calculating the thermal stresses in accordance with equations (1) and (2) we find that, for the 4½ inch thick liner:

# STEADY STATE TEMPERATURE DISTRIBUTION SINGLE COMPONENT LINING WITH REGENERATIVE AIR COOLING

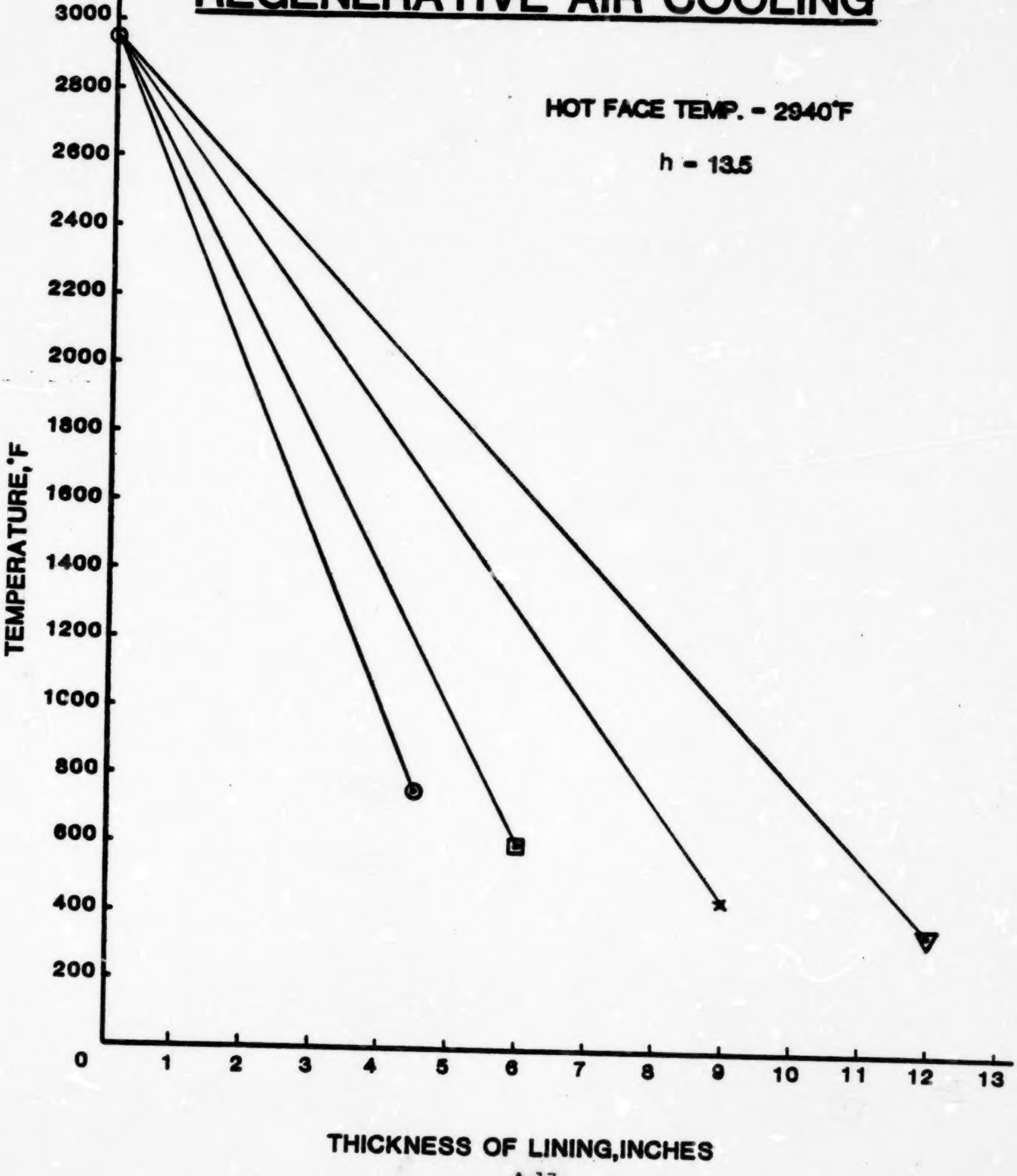

FIGURE-1

S = 44,493 psi tension at the outer surface
S = 46,867 psi compression at the inner surface

For the 12 inch thick liner these values are:

S = 50,291 psi tension
S = 58,344 psi compression

Two things are immediately obvious: first, the stresses are extremely high; secondly, although the temperature gradient is smaller for the thicker liner, the geometrical factors combine to make the stress higher.

The next step is to examine the effect of changing the heat transfer coefficient. The liner material is the same and the thickness is constant at 4½ inches. The heat transfer coefficient is varied from 6 to 30. Figure 2 shows the results. The temperature of the steel shell should be kept below about 800$^{o}$F in order to maintain adequate strength. Thus, the heat transfer coefficient must be about 13.5 or greater with a 4½ inch thickness of this liner material. Although one can lower the temperature of the shell by designing the annulus to give a higher heat transfer coefficient, the penalty that must be paid is one of accepting higher thermal stresses in the refractory.

## B. Thick Linings

To show the effect of using both regenerative air cooling and a thick lining, the heat transfer coefficient was varied from 3 to 24 and the steady-state temperature distribution was calculated. The conditions assumed were:

- Hot face temperature 2940$^{o}$F
- Air temperature 70$^{o}$F
- Same high density alumina liner properties used as in section V-A.

# EFFECT OF VARYING HEAT TRANSFER COEFFICIENT WITH A THIN LINING

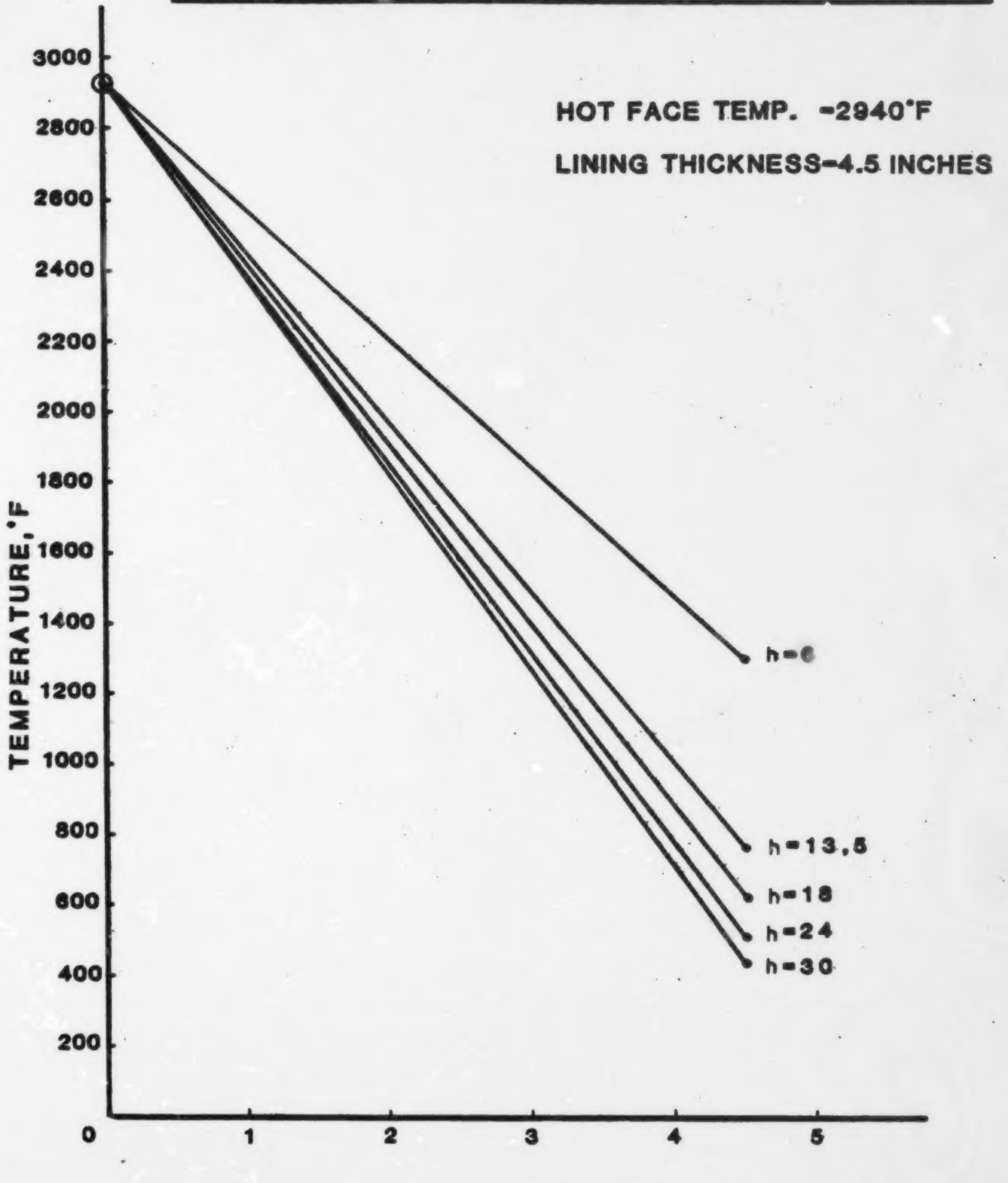

FIGURE-2

Figure 3 shows the results. As expected, when the heat transfer coefficients are equal, the thermal gradients are smaller with the 21 inch thick liner. The temperature of the steel shell can be brought down to about 160°F with a heat transfer coefficient of 24 using the thick lining. For the thin lining and the same heat transfer coefficient, the shell temperature is about 494°F. For the thick liner case when the heat transfer coefficient is 3 (the minimum thermal gradient) the thermal stresses are calculated to be:

$S = 41{,}848$ psi tension at the outer surface

$S = 53{,}248$ psi compression at the inner surface

Again, the thermal stresses are much too high. The next step is to try a thick composite lining composed of three layers. Each succeeding layer has a thermal conductivity lower than the layer preceeding it. Using a liner composed of 9 inches LW33 followed by 6 inches LW26 and 6 inches of block insulation backed by a 3/8 inch steel shell, the heat transfer coefficient was varied from 3 to 15 and the steady-state steel shell temperature was calculated. Table 2 shows the results.

TABLE 2

Effect of Varying Heat Transfer Coefficient On Shell Temperature with a Thick Composite Liner

| h, $\frac{\text{Btu}}{\text{hr ft}^2\ ^\circ\text{F}}$ | T, °F |
|---|---|
| 3 | 118.6 |
| 6 | 94.5 |
| 9 | 86.4 |
| 12 | 82.2 |
| 15 | 79.7 |

# EFFECT OF VARYING HEAT TRANSFER COEFFICIENT WITH A THICK LINING

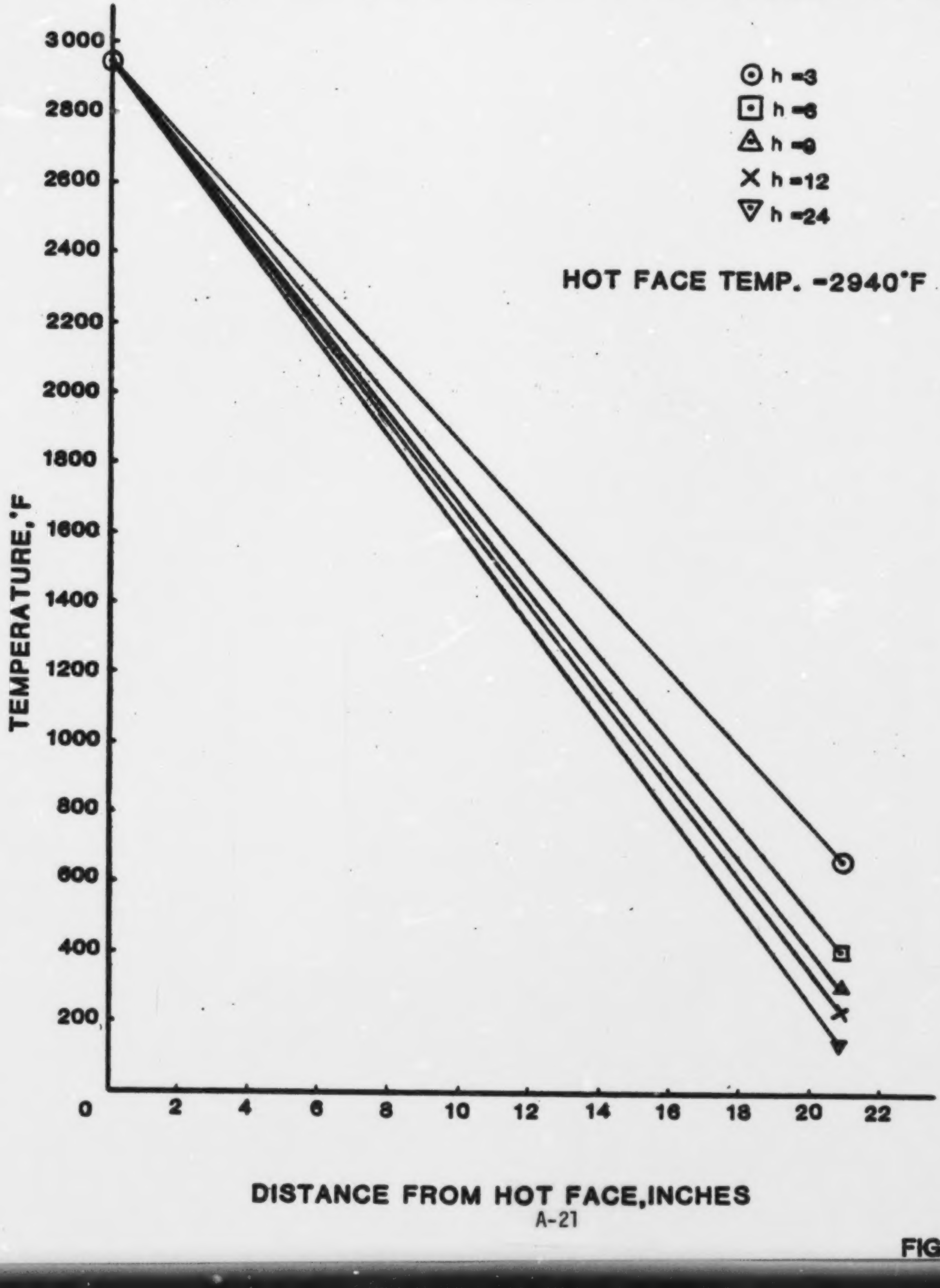

FIGURE-3

It is noted that the resulting steel shell temperature is rather insensitive to varying heat transfer coefficient. For example, raising h by a factor of 5 only reduces the shell temperature by 38.9°F. The reason for this is the much higher thermal resistance of the composite liner; the thermal resistance of the annulus air is therefore only a small faction of the total thermal resistance. Hence the temperature drop between the annulus air and the shell is relatively small. DMC therefore concluded that is was not worth the expense to provide an annulus for regenerative air cooling. This recommendation was approved by EER and the reference design was therefore based on a thick composite liner with natural convection cooling exterior to the shell. Further, it was decided to use bubble alumina as the hot face material in order to minimize crack propagation.

## C. Reference Design

Figure 4 shows the results of steady-state temperature distribution calculations for a number of candidate linings.

- For the 6" LW33 (bubble alumina) + 6" LW26 (insulating castable) combination, a very steep temperature gradient through the hot face material is obtained. This would cause excessive thermal stresses.

- The gradient can be improved by using 9" LW33 backed by 9" block insulation. However, this results in too high a block insulation temperature.

# STEADY STATE TEMPERATURE DISTRIBUTION FOR VARIOUS LININGS

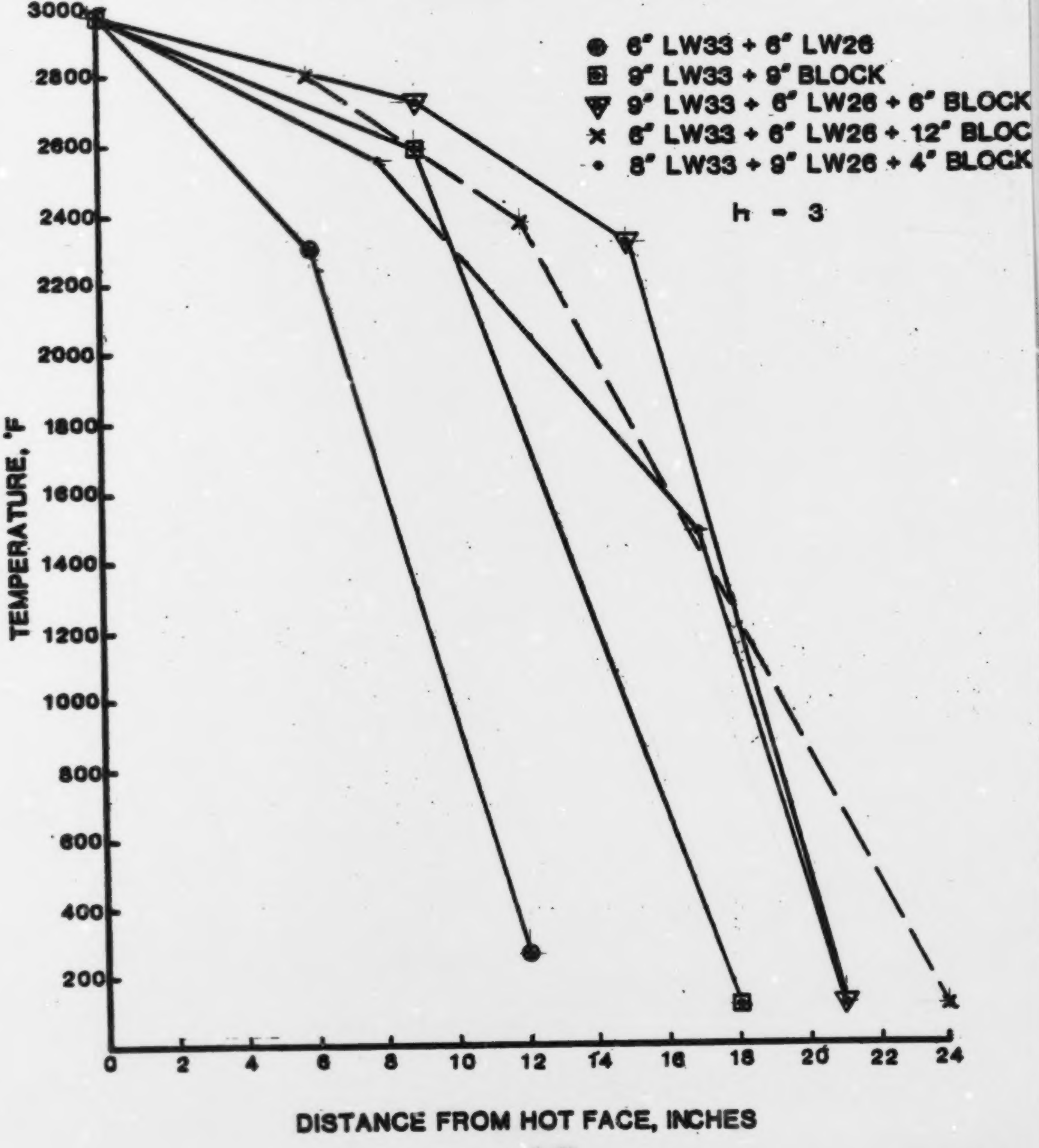

FIGURE-4

- A further improvement in temperature gradient through the hot face lining is obtained by using 9" LW33 + 6" LW26 + 6" block insulation. However, the resulting temperatures for the block and LW26 are higher than the service temperature ratings for these materials.

- A 24 inch thick lining composed of 6" LW33 + 6" LW26 + 12" block insulation shows a low thermal gradient through the LW33, but temperatures too high for the LW26 and block insulation. Further, the 24 inch thick liner results in a greater burner length.

- The recommended design is a compromise. A lining thickness of 21 inches is used, composed of 8" LW33 + 9" LW26 + 4" block insulation. The maximum temperature of the LW26 is 2565$^{o}$F, and the maximum temperature of the block insulation is 1489$^{o}$F.

## D. Thermal Shock

Thermal shock is a condition wherein high thermal stresses are caused by rapid cooling or heating. To avoid such conditions industrial furnaces are always brought up to temperature slowly and cooled down slowly. EER asked that DMC calculate heat-up thermal stresses assuming that the burner was operated at the "low fire", or one-quarter full load, rate. Calculations of the flame shape for the low fire rate assuming stoichiometric conditions indicated that the flame length would be longer than the burner length and the diameter only slightly less than the burner diameter. Therefore, the interior of the burner was assumed to be filled with a uniformly radiating gas at a temperature of 2960°F. Figure 5 shows the results of heat-up transient temperature calculations based on a simple cylindrical model with an inside diameter of 8 feet. Hand calculations were made for a one foot thick refractory liner of 94% alumina backed by a 1/4 inch steel shell. The computer calculations used a liner consisting of 6 inches of the 94% alumina followed by 6 inches of a 70% alumina castable and a 1/4 inch steel shell. The convective heat transfer coefficient exterior to the steel shell was assumed to be 3 Btu/hr $ft^2$ °F in each case. The thermal gradients are seen to be quite steep at the hot face. For example, one hour after start-up, a gradient of about 1167°F/inch is reached. By comparison, a steady-state thermal gradient of only about 52°F/inch is reached for the reference design (figure 4). This results in significantly higher thermal stress values and emphasizes the importance of a slow heat-up rate.

To obtain an estimate of safe heat-up rates consider the following formulae for the tangential stress at the outer and inner surfaces of a hollow cylinder.[7]

$$\text{Outer:}\quad S = \frac{E\alpha m}{8A\,(1-\upsilon)}\left[3\,b^2 - c^2 - \left(\frac{4\,b^4}{c^2 - b^2}\right)\left(\ln\,\frac{c}{b}\right)\right]\ \text{tension}$$

$$\text{Inner:}\quad S = \frac{E\alpha m}{8A\,(1-\upsilon)}\left[b^2 + c^2 - \left(\frac{4\,b^2\,c^2}{c^2 - b^2}\right)\left(\ln\,\frac{c}{b}\right)\right]\text{compression}$$

Where: A is the thermal diffusivity = $\frac{k}{c\rho}$

m is the steady rate of rise of the temperature of the inside surface

# HEAT-UP TRANSIENT CURVES

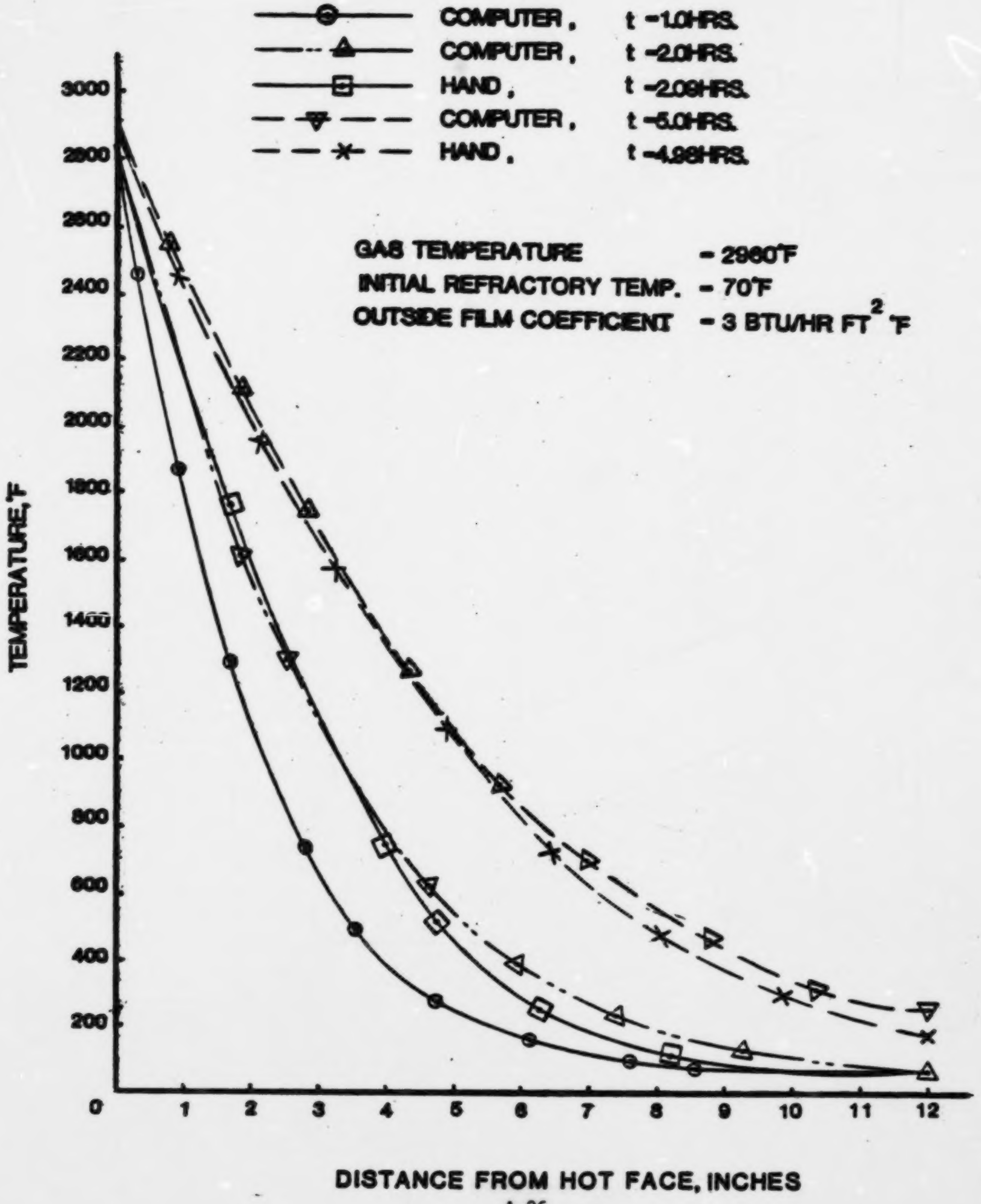

FIGURE-5

We wish to find the heat-up rate, m, which will result in tangential stresses no larger than those at steady-state. The procedure is to substitute the steady-state stresses into the equations and calculate m. The results for the reference design are:

Outer: $m = 27.6\ ^{o}/hr$
Inner: $m = 56.6\ ^{o}/hr$

# VII. DETAILED ANALYSIS

## A. Method of Analysis

### 1. Digital Computer Program

As previously indicated, closed form solutions for thermal stress exist for only a few simple cases. For this reason, and because of the complicated physical model and the temperature-dependent properties of the materials involved. an existing general-purpose digital computer program, ANSYS, was used to analyze the linings.

ANSYS is a powerful finite element program developed and maintained by Swanson Analysis Systems, Inc. for performing analyses in such fields as heat transfer, stress analysis, dynamics, plasticity and fluid mechanics. Plane, axisymmetric and three-dimensional modeling may be used, and either batch or interactive modes may be used. Three options may be used to run the program: data check, model check, and solution execution. The program uses the wave-front solution procedure for the system of simultaneous linear equations developed from the assembled finite elements. In this procedure, the nodal point numbers of all elements are scanned to determine which element is the last to use each nodal point. As the total system of equations is assembled from the element matrices, the equations for a nodal point which occur for the last time are algebraically solved in terms of the remaining unknowns and eliminated from the assembled matrix in core. The equations for a nodal point which occur for the first time are added to the assembled matrix as the solution progresses. Thus, the program is a very efficient one since the size of the matrix can expand or contract as necessary, thereby minimizing core requirements and matrix inversion time. A complete description of the program may be found in the ANSYS users manual and theoretical manual which are available from Swanson Analysis Systems, Inc.

## 2. Boundary Conditions

Inside the burner, the entire volume is considered to consist of a uniformly radiating gas. Radiation heat transfer from the gaseous medium to a solid is completely different than radiation between solids. In the latter, the heat flux is a continuum over the entire spectrum. A gas, however, radiates only in discrete narrow band frequencies. Further, at the temperatures reached in industrial furnaces only radiation from the heteropolar gases such as carbon monoxide, carbon dioxide, water vapor, the hydrocarbons, sulfur dioxide, ammonia, hydrogen chloride and the alcohols are important. Hottel has given the most practical method of analyzing gas radiation.[8,9] He prepared graphs of emissivity as a function of temperature for the various gases. The curves are plotted with the parameter PL, where P is the pressure in atmospheres and L is the beam length in feet. The beam lenth may be approximated by:

$$L = \frac{3.4 \times \text{Volume of enclosure}}{\text{Area of enclosure}}$$

The procedure, then, is as follows:

1. Find the beam length
2. For each constituent gas find PL and the emissivity.
3. Find the correction to the emissivities due to spectral overlap.
4. Add the corrected individual emissivities to find the total gas emissivity.

The net heat transfer between the gas and a black surface may be found from:

$$q/A = (4 + a + b - c)\ \varepsilon\ T^3_{avg}\ (T_g - T_s)$$

Where: a, b, c are functions of gas temperature and are found from curves

$T_g$ is the gas temperature

$T_s$ is the surface temperature

$\varepsilon$ is the emissivity

$T_{avg}$ is the average of $T_g$ and $T_s$

For a gray surface this equation must be multiplied by a factor which lies between 1 and the emissivity of the surface. For the surface emissivity $\varepsilon_s \geq 0.7$ we multiply by the factor $\frac{\varepsilon_s + 1}{2}$ as suggested by Kreith[10]. For $\varepsilon_s \leq 0.7$ the equation is multipled by $\varepsilon_s$. When this is done, the quantity in brackets may be considered a heat transfer coefficient for radiation, $h_r$.

In addition to radiation the effect of convective heat transfer must be considered. To calculate the convective heat transfer coefficient the Dittus-Boelter correlation is used[11]:

$$\frac{h_c D_e}{K} = 0.023\ (R_e)^{0.8}\ (P_r)^{0.4}$$

Where: $h_c$ is the convective heat transfer coefficient
$D_e$ is the equivalent diameter
$K$ is the thermal conductivity of the gas
$R_e$ is the Reynold's number
$P_r$ is the Prandtl number

The total heat transfer coefficient is given by:

$$h_T = h_r + h_c$$

Table 3 lists the total heat transfer coefficient data input to the computer.

Outside the burner shell, the mode of heat transfer is convection. Heat transfer coefficients were assumed for the designs studied in detail.

## TABLE 3

Gas Emissivity as a Function of Mean Temperature

| $T_{avg}$, °R | $\varepsilon_g$ |
|---|---|
| 680 | 0.353 |
| 880 | 0.319 |
| 1080 | 0.345 |
| 1280 | 0.312 |
| 1480 | 0.294 |
| 1680 | 0.268 |
| 1880 | 0.254 |
| 2080 | 0.232 |
| 2280 | 0.209 |
| 2480 | 0.193 |
| 2680 | 0.169 |
| 2880 | 0.159 |
| 3080 | 0.144 |
| 3280 | 0.123 |

### B. Models Analyzed

Two models each consisting of a cylindrical section joined to a conical section, were evaluated. The first model consisted of a 12 inch layer of bubble alumina backed by a steel shell. Ceramic anchors of high density alumina were used, and varying air temperatures and heat transfer coefficients were used outside the steel shell. The gas temperature was constant at 2960°F. Transient and steady-state temperature and stress distributions were calculated through the model.

The second model, the reference design, consisted of a three component lining 21 inches thick with high density alumina anchors. The hot face consisted of 8 inches LW33. This was followed by 9 inches of LW26 and 4 inches of block insulation and a steel shell. As directed by EER, the start-up condition was modeled by raising the gas temperature 200°F each hour until a temperature fo 2960°F was reached. A constant air temperature and heat transfer coefficient outside the steel shell was used. Transient and steady-state temperature and stress distributions were calculated.

## C. Results

### 1. Single Component Model with Anchors

Figure 6 depicts the node and element numbering system used in the 12 inch single refractory component liner model. Figure 7 shows the results of the computer-determined temperature distributions for several lines of nodes at steady-state and for nodes 1-13 one hour after start-up. Note that the steady-state thermal gradient for nodes 1-13 is about 185°F/inch. This is more than three times the thermal gradient for the reference design at steady-state (figure 3), again showing the susceptability of thin liners to excessive thermal stresses even with low heat transfer coefficients exterior to the burner. The steady-state temperature distribution at the juncture of the core and shell (nodes 99-111) is seen to be comprised of three distinct portions: a steeply-sloped straight line near the surface, a more gradually sloped curve in the central portion of the liner and an

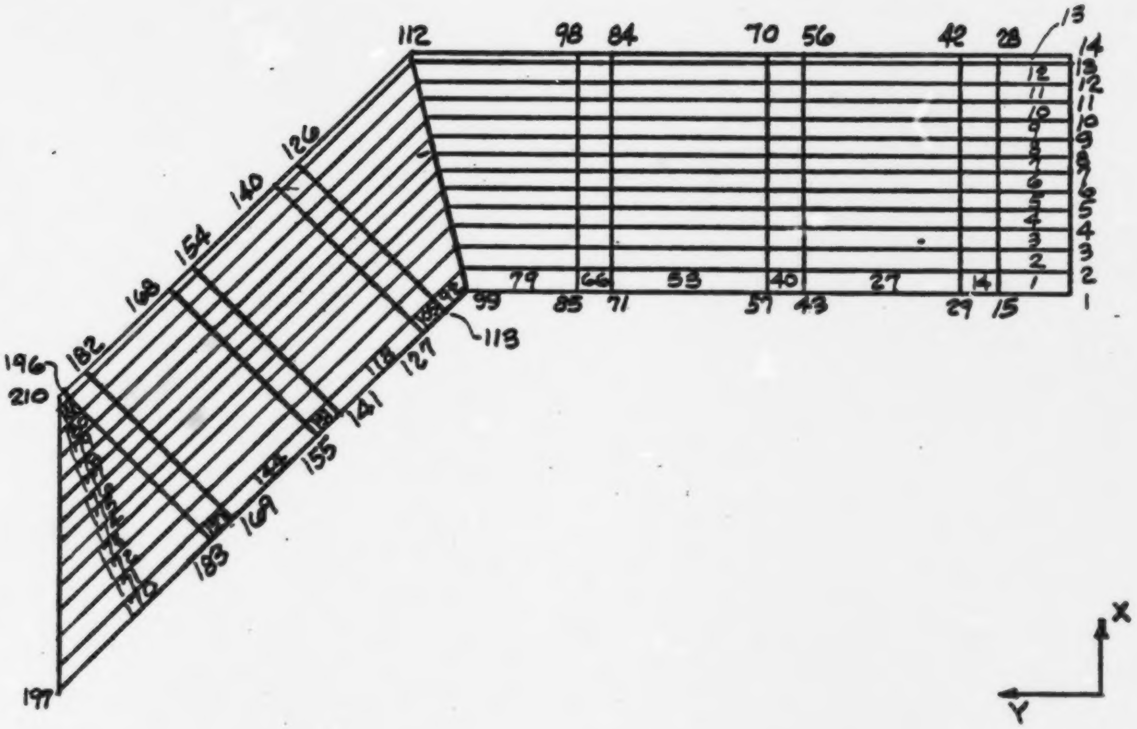
112
98
84
70
56
42
28
13
14
13
12
11
10
9
8
7
6
5
4
3
2
1
12
11
10
9
8
7
6
5
4
3
2
1
79
66
53
40
27
14
99
85
71
57
43
29
15
113
126
140
154
168
182
196
210
127
141
155
169
183
197
X
Y

SINGLE COMPONENT MODEL WITH ANCHORS

FIGURE 6

# TEMPERATURE DISTRIBUTIONS THROUGH SINGLE COMPONENT BUBBLE ALUMINA LINING

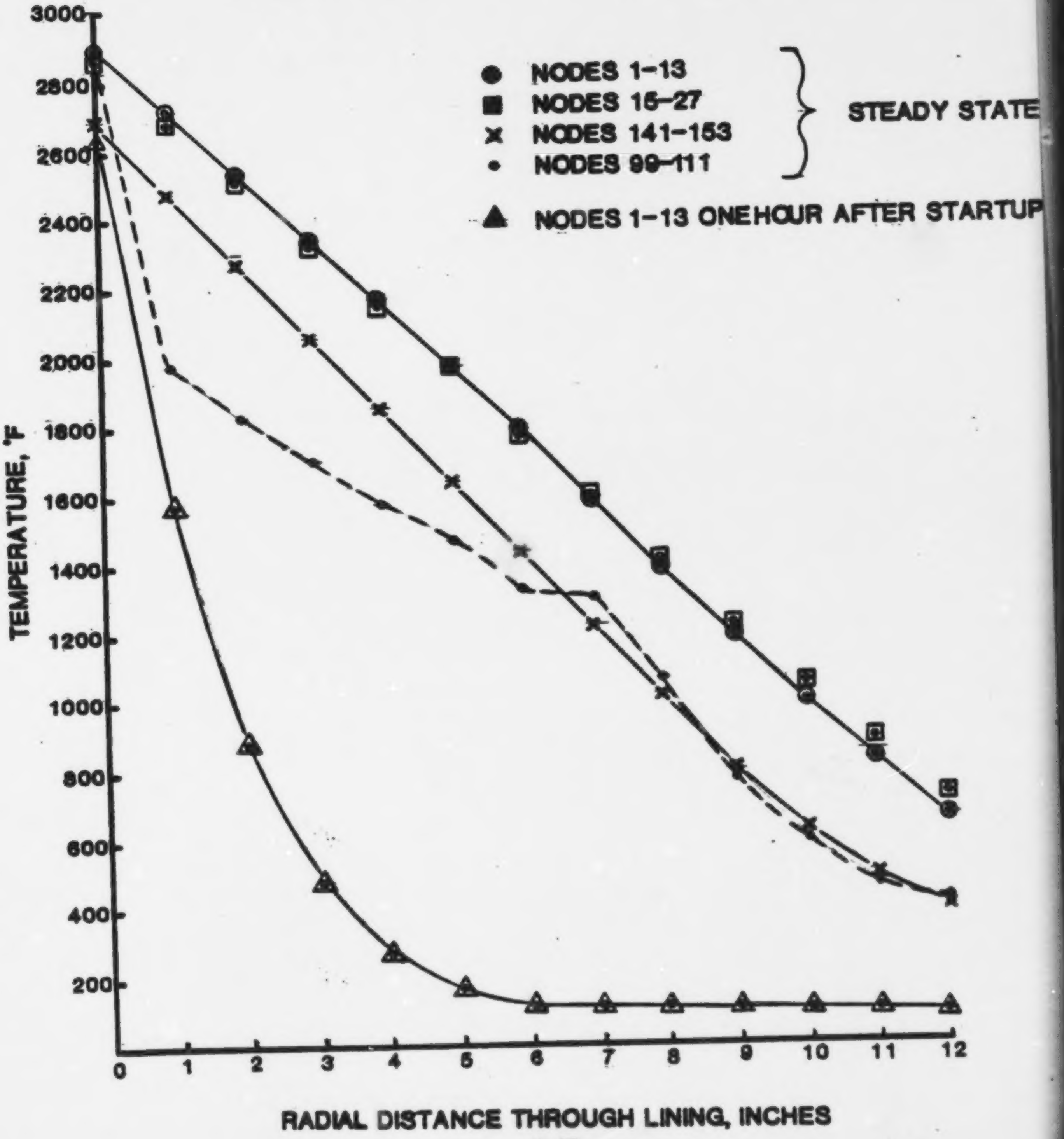

FIGURE-7

exponentially-decaying curve in the outer region. The slope of the inner portion is about the same as that shown for the transient curve for the near hot face nodes one hour after start-up. Exceedingly high thermal stresses would therefore result in this cone-cylinder juncture area even at steady-state. Figure 8 shows tangential thermal stress versus time for element no. 1 of the single component model.

### 2. Three Component Model with Anchors

Figure 9 depicts this model. Upon analyzing the results of the single component model it was possible to eliminate a portion of the cylindrical section since conditions did not vary greatly. This led to savings in the computer run. At the same time, the elements in the vicinity of the cone-cylinder junction were divided into a finer mesh by two lines of nodes: 70 through 92 and 116 through 138. This provided greater accuracy in this region of concern.

Figure 10 shows the time varying temperature distribution of the bubble alumina at the hot face (node 1) and 8 inches behind the hot face (node 9). Also plotted for reference is the gas temperature which was modeled as a step change of 200°F as previously described. Several facts are immediately evident:

- The hot face temperature gradient gradually increases until it is somewhat greater than 200°F/hr. At 13.6 hours from start-up, the temperature curve starts to gradually approach the steady-state temperature of 2938°F.

# TANGENTIAL THERMAL STRESS DURING STARTUP

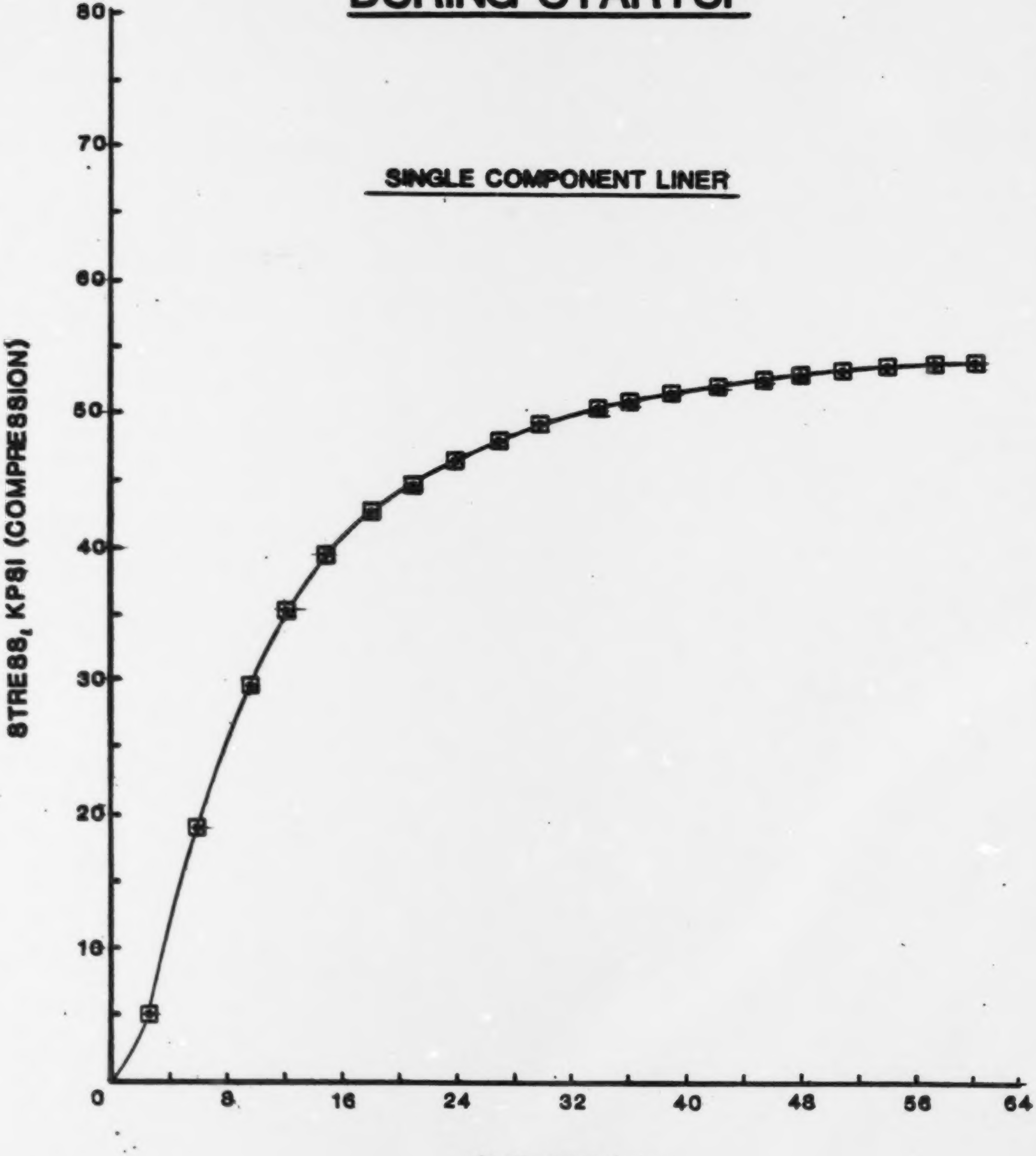

FIGURE-8

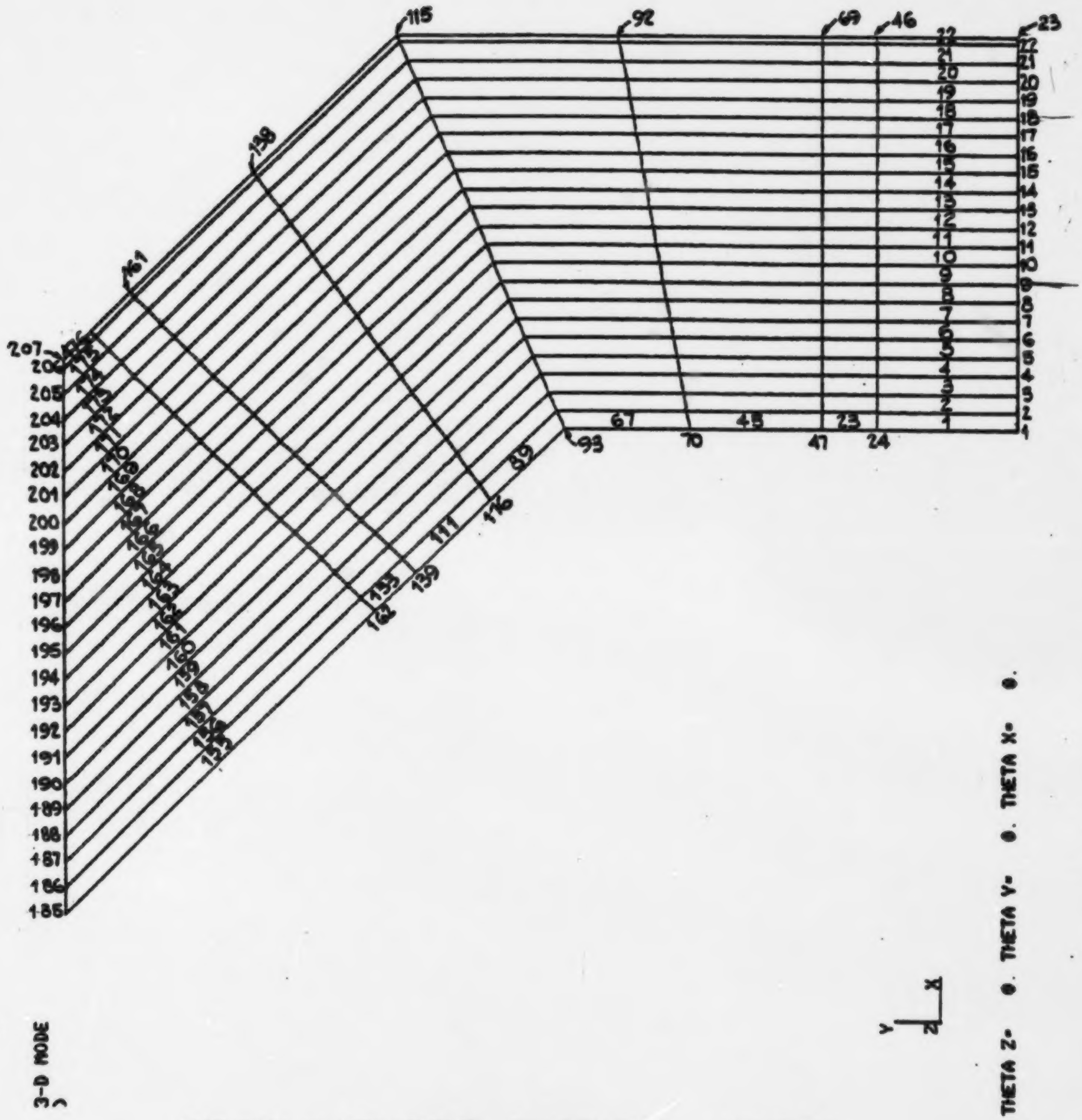
115
92
69
46
23
22
21
20
19
18
17
16
15
14
13
12
11
10
9
8
7
6
5
4
3
2
1
67
70
45
47
23
24
93
138
161
207
206
205
204
203
202
201
200
199
198
197
196
195
194
193
192
191
190
189
188
187
186
185
89
176
111
133
139
162
160
159
Y
X
Z
3-D MODE
THETA Z= 0. THETA Y= 0. THETA X= 0.

RECOMMENDED DESIGN MODEL

FIGURE - 9

# HOT FACE TEMPERATURE DURING STARTUP

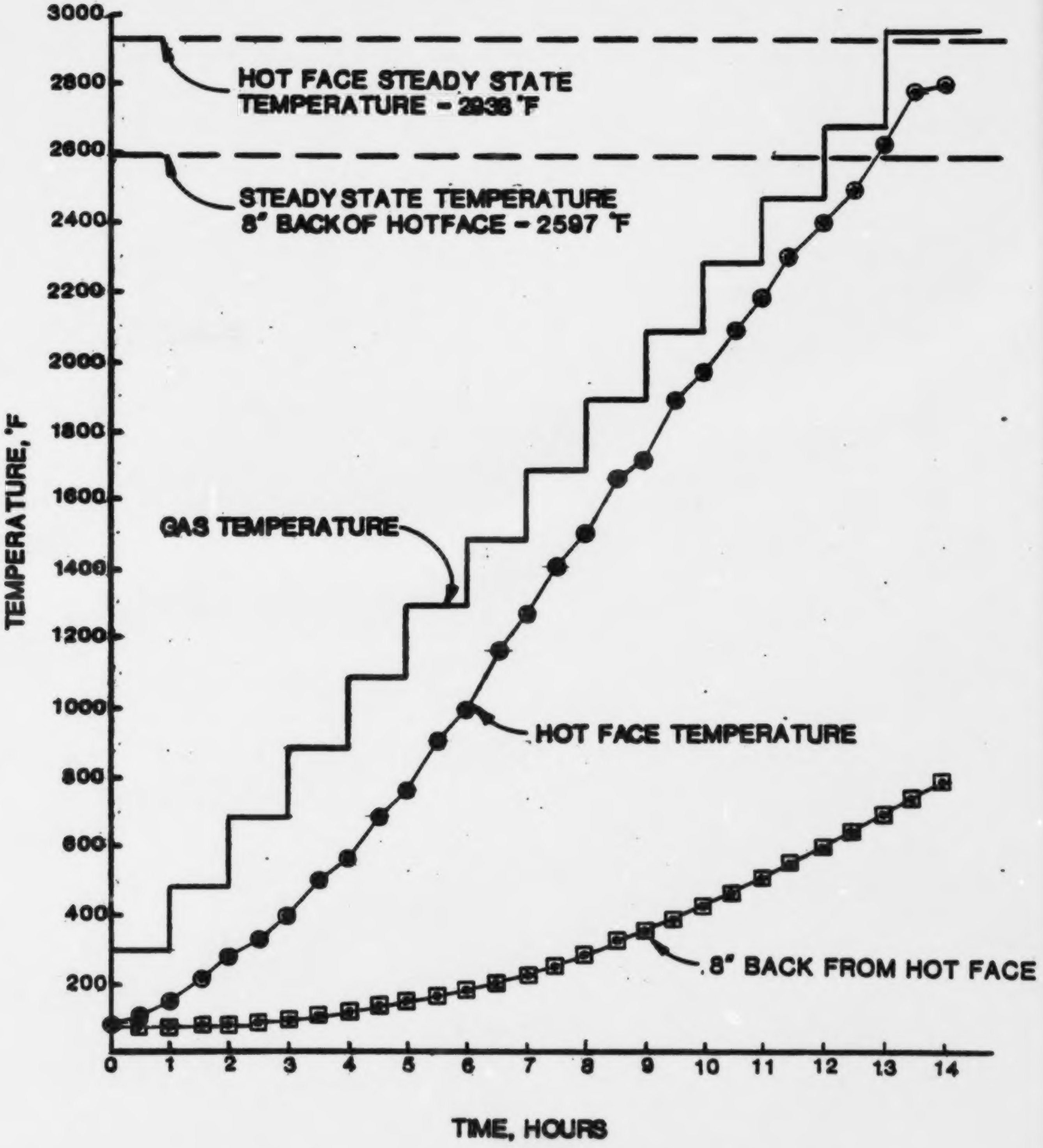

FIGURE-10

- The temperature of node 9, which is the end of the bubble alumina layer, increases in a much slower fashion. If the slope is extrapolated to the final steady-state temperature of 2597°F, it is evident that this start-up regime will require a very long time to reach steady-state.

- Since the difference between the temperatures of nodes 1 and 9 is increasing (at least until t = 13.6 hours), the thermal stresses must be increasing with time.

Table 4 shows the tangential stresses as a function of time as well as the steady-state thermal stress for elements 1, 67 and 89.

Comparing Table 4 with Figure 8, it is evident that the slower heat-up rate, coupled with the thicker lining, lowers the thermal stresses considerably. However, even this heat-up regime is far too fast. It is noted that the steady-state stress for element 1 is a factor of three lower than the stress at 14 hours. Note also that the highest stresses are in the elements at the juncture of the cone and cylinder, as might be expected.

Figure 11 shows the steady-state temperature distributions through a section of the cylinder containing the bubble alumina, insulating castable and block as well as through a section containing the anchor and the block. The maximum temperature is slightly higher than the maximum service temperature of the block, 1900°F. However, shrinkage of the insulating castable after curing is expected to open up a gap between the castable and the block, thus lowering the temperature to a safe level.

## TABLE 4

## TANGENTIAL THERMAL STRESS VARIATION, PSI

| Time, hrs. | Element 1 | Element 67 | Element 89 |
|---|---|---|---|
| 0.9 | -495.0 | -667.2 | -646.1 |
| 1.0 | -581.8 | -815.4 | -788.5 |
| 1.3 | -970.2 | -1368.8 | -1324.2 |
| 1.9 | -1333.3 | -1955.1 | -1910.7 |
| 2.2 | -1960.4 | -2839.3 | -2776.6 |
| 3.0 | -3014.6 | -4449.7 | -4358.3 |
| 4.0 | -5419.3 | -7965.4 | -7776.9 |
| 5.0 | -9022.7 | -13011 | -12634 |
| 6.0 | -13801 | -19413 | -18831 |
| 7.0 | -19153 | -26500 | -25864 |
| 8.0 | -24345 | -33596 | -33124 |
| 9.0 | -29037 | -40380 | -40221 |
| 10.0 | -33313 | -46897 | -47092 |
| 11.0 | -37204 | -53109 | -53655 |
| 12.0 | -41008 | -59292 | -60128 |
| 13.0 | -45874 | -66704 | -67580 |
| 14.0 | -50143 | -73719 | -74965 |
| Steady State | -16811 | -36471 | -38817 |

# STEADY STATE TEMPERATURE DISTRIBUTION

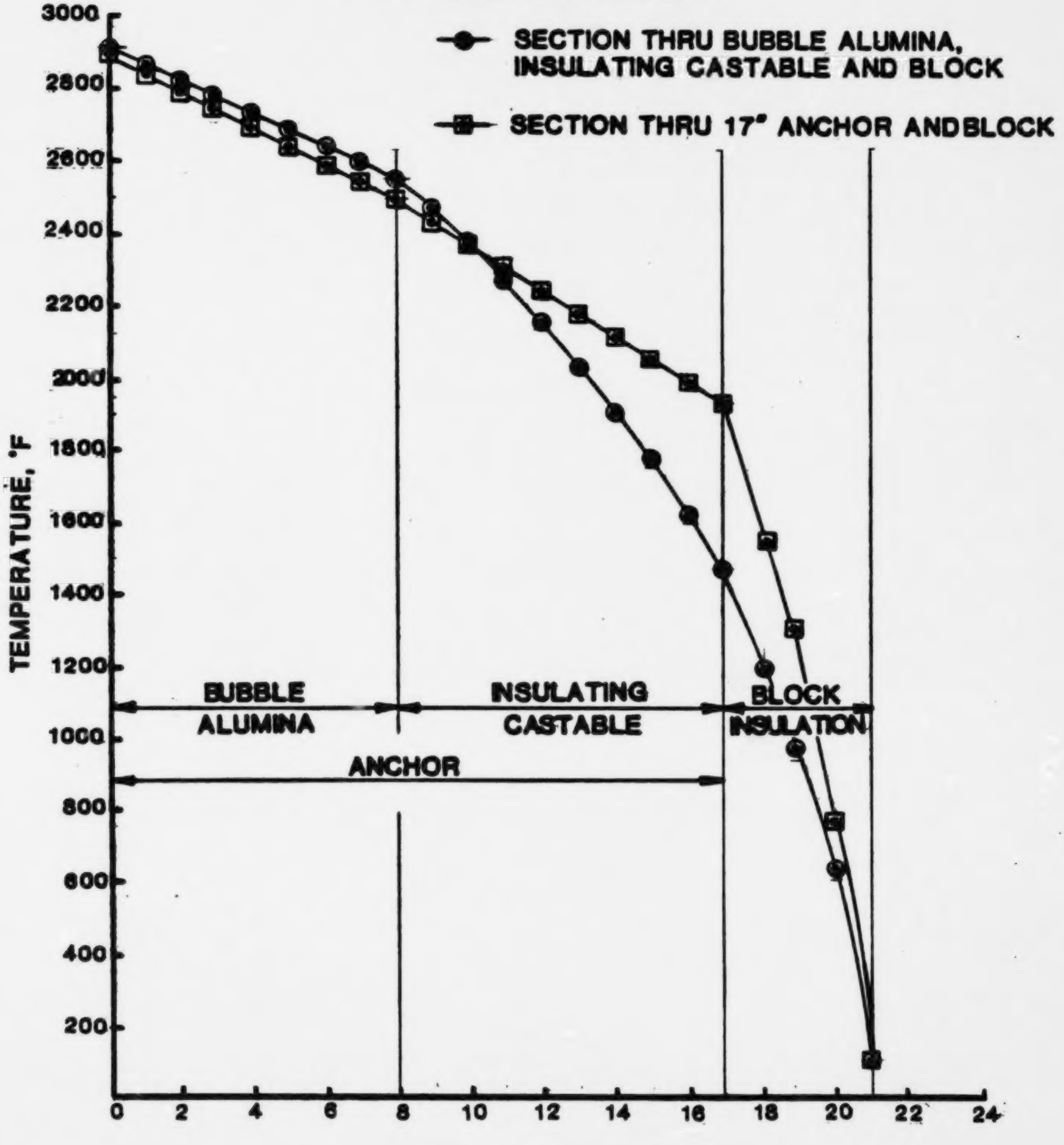

FIGURE-11

Figure 12 shows the axial temperature distribution 4 inches and 8 inches from the hot face. The sharp temperature drop and reversal shown for both cases occurs at the juncture of the cone and shell. Because of this temperature reversal anchors are not placed in this location.

Figure 13 shows steady-state tangential and axial stress distributions through the cylindrical portion of the lining. The stresses shown for the block may not be accurate since these materials may not be purely Hookian, but they are expected to be low.

The indicated stresses in these analyses would never be reached because cracks would develop which would relieve the stresses. Further, there is yet another factor which can be used to good advantage: when a castable refractory is cured, it undergoes chemical changes which cause a permanent shrinkage, depending upon the final temperature to which the material is heated. Our recommended curing procedure calls for curing the two castable layers separately. This will result in a small radial gap between the bubbble alumina and the insulating castable. This gap will serve as a "built-in" expansion joint during service; expansion of the inner layer cannot result in applied pressure to the inner face of the outer layer, thus tending to lower the thermal stresses.

# AXIAL TEMPERATURE DISTRIBUTION
## -STEADY STATE
## -THREE COMPONENT LINER

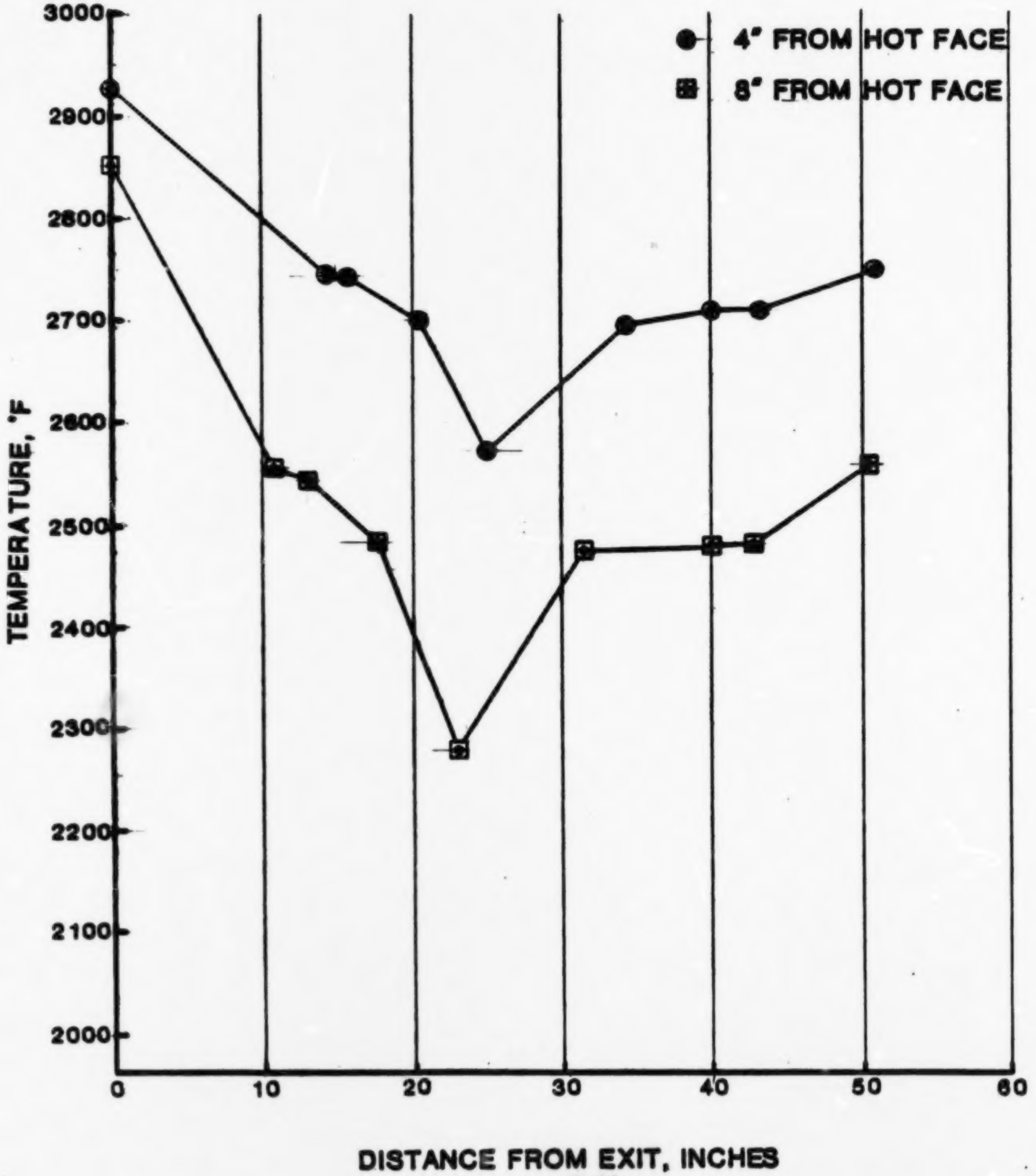

FIGURE 1

# STEADY STATE STRESS DISTRIBUTION

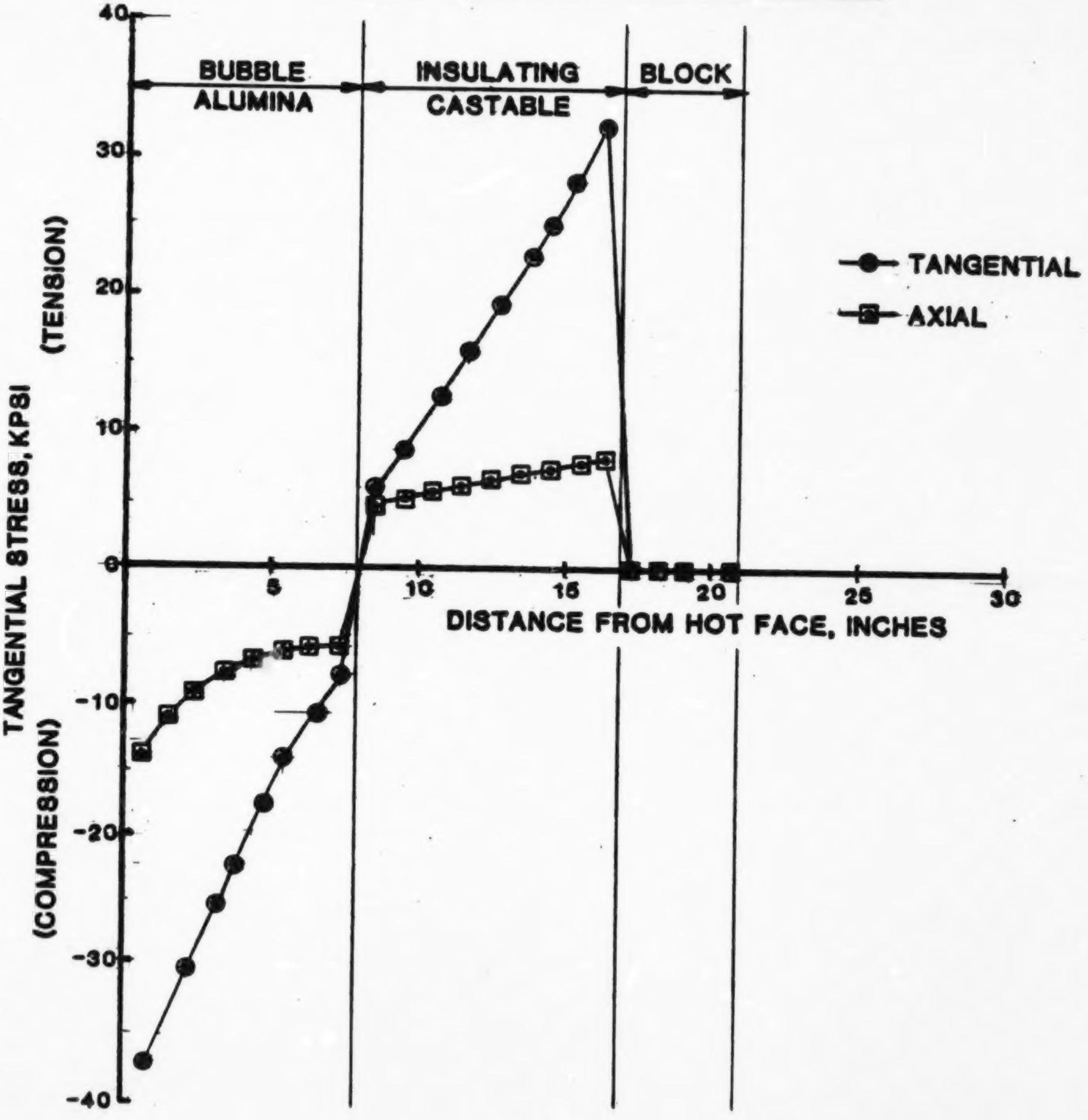

FIGURE-13

## VIII. SUMMARY

This report combines the results of the Phase II Design Study, the Final Report and the Construction Blueprints into one document. In addition, a complete set of the computer printouts for the thermal and stress calculations has previously been forwarded to E.E.R.

This completes submittal of the contract deliverables. Davy McKee Corporation appreciates the opportunity to work on this interesting and challenging design study.

Richard E. Harkness

Richard E. Harkness, Ph.D., P.E.
Senior Staff Engineer

REH/dk

# REFERENCES

1. Goodier, J.N., Trans. A.S.M.E., J. Appl. Mech., 4, 1, March 1937.
2. Trinks, W. and Mawhinney, W.A., Industrial Furnaces, Vol. I, John Wiley and Sons, 1961.
3. Criss, G.H. and Kisko, K.A., "Hot Modulus of Rupture of Refractory Castables", Harbison-Walker Refractories Company.
4. Hasselman, D.P.H., J. Am. Cer. Soc., 46, 11, 1963.
5. Hasselman, D.P.H., J. Am. Cer. Soc., 52, 11, 1969.
6. Larson, D.R., Coppola, J.A. and Hasselman, D.P.H., J. Am. Cer. Soc., 57, 10, 1974.
7. Kent, C.H., Trans. A.S.M.E., 54, 18, 185, 1932
8. McAdams, W.H., Heat Transmission, Chapter 4, McGraw-Hill Book Company, 1954.
9. Hottel, H.C. and Sarofim, A.F., Radiative Transfer, McGraw-Hill Book Company, 1967.
10. Kreith, F., Principles of Heat Transfer, International Textbook Company, 1964.
11. Dittus, F.W., and Boelter, L.M.K., Univ. Calif. Pubs. Eng., 2, 443, 1930.

(Published by permission of Davy McKee)

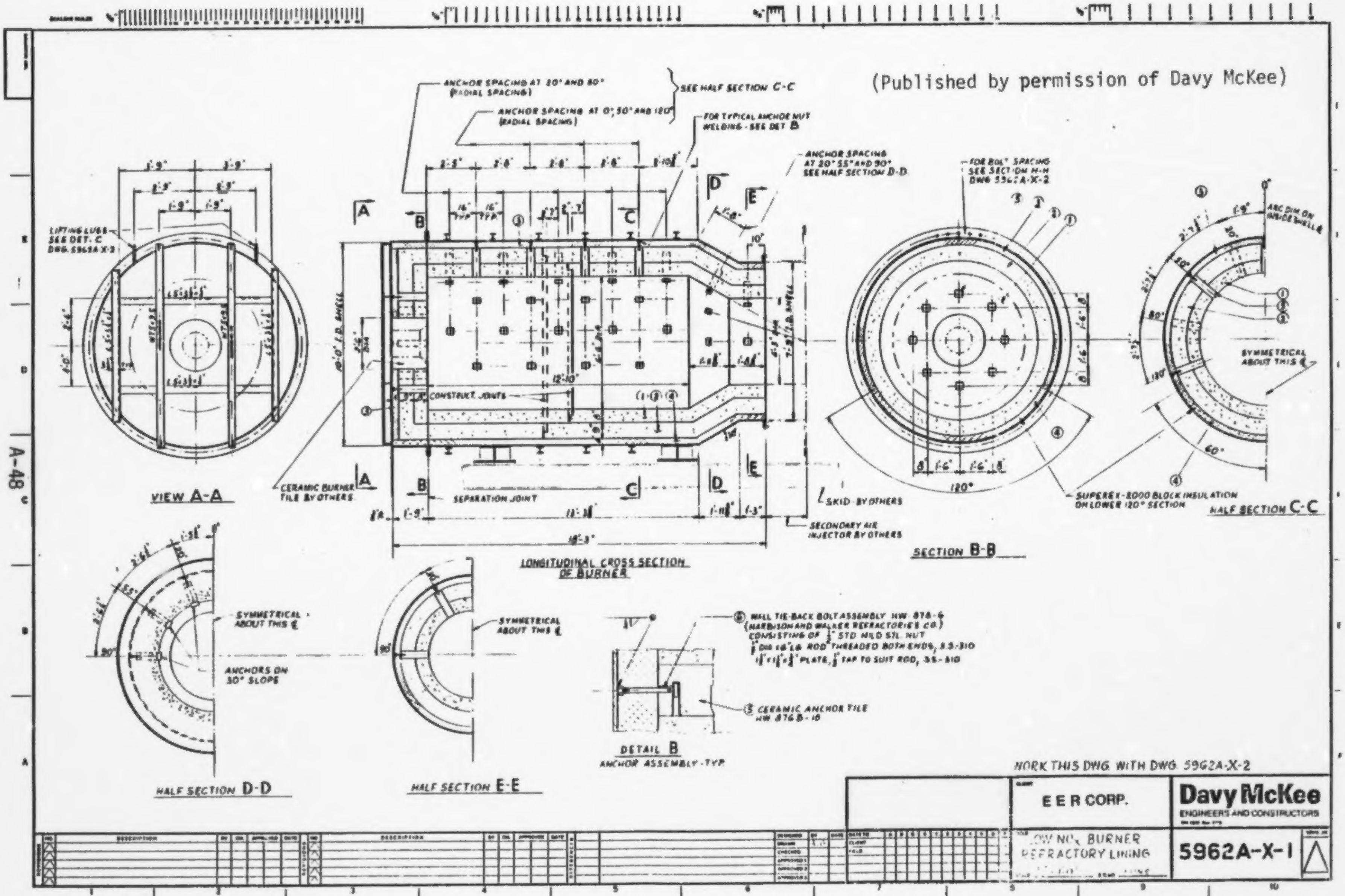
ANCHOR SPACING AT 20° AND 80° (RADIAL SPACING)
ANCHOR SPACING AT 0°, 50° AND 120° (RADIAL SPACING)
SEE HALF SECTION C-C
FOR TYPICAL ANCHOR NUT WELDING - SEE DET B
ANCHOR SPACING AT 20° 55° AND 90° SEE HALF SECTION D-D
LIFTING LUGS SEE DET. C DWG. 5962A-X-2
10'-0" I.D. SHELL
CONSTRUCT. JOINTS
CERAMIC BURNER TILE BY OTHERS
SEPARATION JOINT
SKID - BY OTHERS
SECONDARY AIR INJECTOR BY OTHERS
12'-10"
13'-3"
18'-3"
VIEW A-A
LONGITUDINAL CROSS SECTION OF BURNER
FOR BOLT SPACING SEE SECTION H-H DWG 5962A-X-2
SECTION B-B
120°
SUPEREX-2000 BLOCK INSULATION ON LOWER 120° SECTION
ARC DIM ON INSIDE SHELL
SYMMETRICAL ABOUT THIS ℄
60°
HALF SECTION C-C
SYMMETRICAL ABOUT THIS ℄
ANCHORS ON 30° SLOPE
HALF SECTION D-D
SYMMETRICAL ABOUT THIS ℄
HALF SECTION E-E
④ WALL TIE-BACK BOLT ASSEMBLY HW 878-6 (HARBISON AND WALKER REFRACTORIES CO.) CONSISTING OF 1/2" STD MILD STL NUT 1/2" DIA 16" LG ROD THREADED BOTH ENDS, SS-310 1 1/2" x 1 1/2" x 1/4" PLATE, 1/2" TAP TO SUIT ROD, SS-310
⑤ CERAMIC ANCHOR TILE HW 876 B-10
DETAIL B
ANCHOR ASSEMBLY - TYP.
WORK THIS DWG. WITH DWG. 5962A-X-2
E E R CORP.
Davy McKee
ENGINEERS AND CONSTRUCTORS
LOW NOx BURNER
REFRACTORY LINING
5962A-X-1

(Published by permission of Davy McKee)

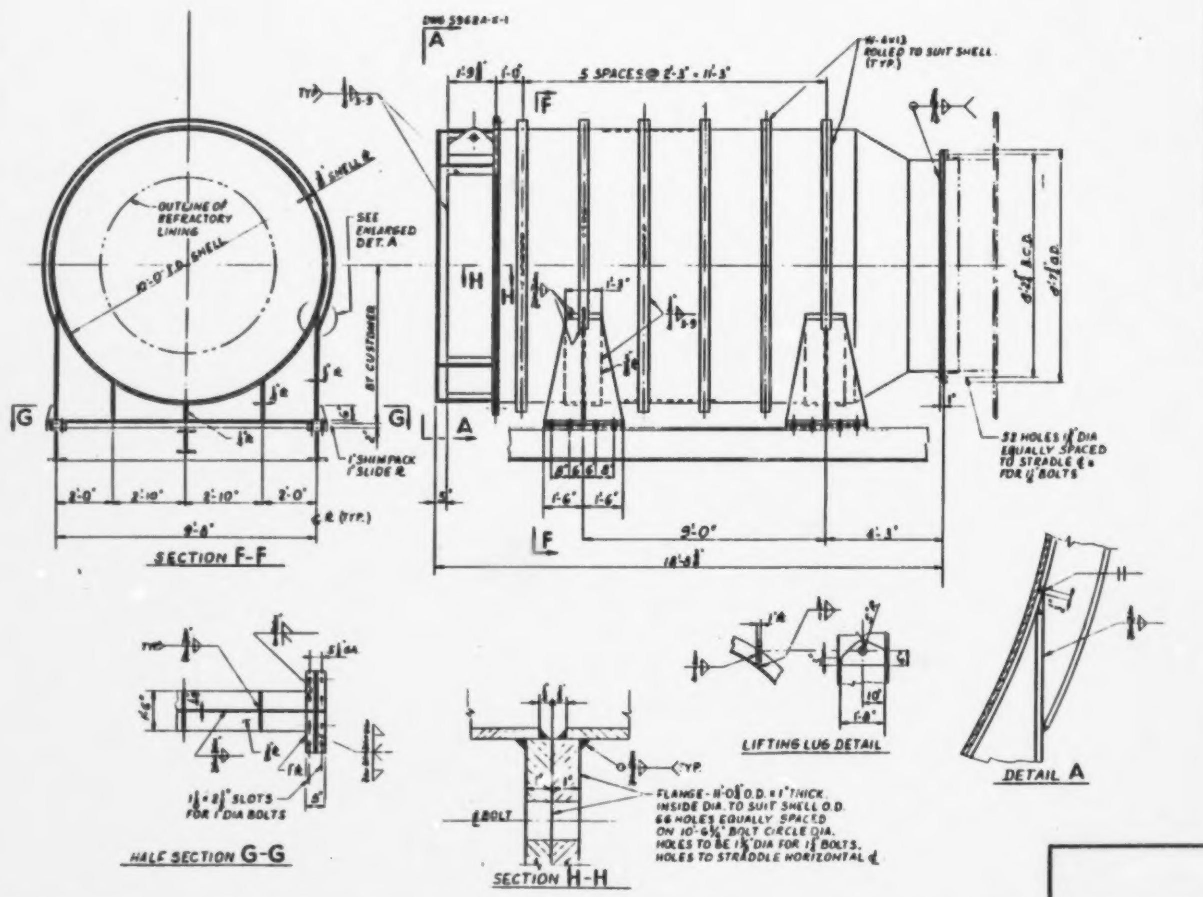
DWG 5962A-X-1
A
5 SPACES @ 2'-3" = 11-3"
W-6x13 ROLLED TO SUIT SHELL (TYP.)
OUTLINE OF REFRACTORY LINING
10'-0" I.D. SHELL
SEE ENLARGED DET. A
BY CUSTOMER
1" SHIM PACK 1" SLIDER
C.R. (TYP.)
2'-0"
2'-10"
2'-10"
2'-0"
9'-8"
SECTION F-F
F
H
G
1'-6"
1'-6"
9'-0"
4'-1"
18'-9"
32 HOLES 1 1/8" DIA EQUALLY SPACED TO STRADLE ℄ FOR 1" BOLTS
HALF SECTION G-G
1 1/8" × 2 1/2" SLOTS FOR 1" DIA BOLTS
FLANGE - 11'-0 1/2" O.D. × 1" THICK. INSIDE DIA. TO SUIT SHELL O.D. 66 HOLES EQUALLY SPACED ON 10'-6 3/4" BOLT CIRCLE DIA. HOLES TO BE 1 1/8" DIA FOR 1" BOLTS. HOLES TO STRADDLE HORIZONTAL ℄
℄ BOLT
SECTION H-H
LIFTING LUG DETAIL
DETAIL A
TYP.

## REFRACTORY AND INSULATING MATERIAL REQ'D FOR ONE BURNER LINING

| ITEM NO. | MATERIAL | SUPPLIER | QUANTITY REQ'D. | OVERAGE | TOTAL QUANTITY | REMARKS |
|---|---|---|---|---|---|---|
| ① | H-W LIGHT WEIGHT CASTABLE - 33 (BUBLE ALUMINA) | HARBISON - WALKER | 254 CU.FT. | 5 % | 270 CU.FT. | |
| ② | H-W LIGHT WEIGHT CASTABLE - 26 | HARBISON - WALKER | 383 CU.FT. | 5 % | 403 CU.FT. | |
| ③ | INSBLOK - 19 BLOCK INSULATION 4" × 6" × 36" | A.P. GREEN | 300 PCS. | 15% | 345 PCS | |
| ④ | J-M SUPEREX - 2000 BLOCK INSULATION 4" × 6" × 36" | MANVILLE CORP | 130 PCS. | 15% | 150 PCS | |
| ⑤ | CERAMIC ANCHOR TILE HW 876-B-18 KORUNDAL XD QUAL. | HARBISON - WALKER | 58 PCS | | 62 PCS | |
| ⑥ | METAL ANCHOR LINKS HW-878-6 (6" LG.) S.STL. TYPE 310 | HARBISON - WALKER | 58 PCS | | 60 PCS | |
| ⑦ | SAIRSET MORTAR | A.P. GREEN | | | 200 LBS. | FOR HOLDING BLOCK INSUL. IN PLACE DURING INSTALLATION. |

THE USE OF TRADE NAMES IS INTENDED ONLY TO DESCRIBE THE KIND AND QUALITY OF THE MATERIAL REQUIRED

### INSTALLATION INSTRUCTIONS FOR THE REFRACTORY LINING

THE INSTALLATION SHALL BE DONE WITH THE BURNER IN VERTICAL POSITION, RESTING ON THE BURNER INLET WALL.

THE SUPEREX BLOCK INSULATION, CERAMIC ANCHOR TILES, AND WOODEN FORMS, IF ANY, SHALL BE WATER PROOFED BEFORE POURING THE CASTABLE.

EACH CASTABLE LINING SHALL BE DRIED SEPARATELY.

A "NON-STICK" COATING SHALL BE APPLIED BETWEEN EACH LAYER OF LINING.
PROPER FORMS SHALL BE USED TO ASSURE LINING THICKNESS AND POSITION OF CERAMIC ANCHOR TILES.

SUPPLIERS DRY-OUT PROCEDURE AND INITAL HEAT-UP SCHEDULE TO BE FOLLOWED
WRAP ANCHORS WITH .030" TO .045" THICK TAPE BEFORE POURING CASTABLE LININGS.

### GENERAL NOTES:

ALL PLATE STEEL TO CONFORM TO LATEST ASTM SPEC. A285-GRADE B OR C. ALL STRUCTURAL SHAPES TO ASTM. SPEC. A36.
BOLTS TO BE A 307 GRADE 'A
ALL WELDING TO BE ELECTRIC, FULL PENETRATION IF NOT SHOWN OTHERWISE AND TO CONFORM TO THE LATEST A.W.S. STANDARDS
SHOP PAINT: NO PAINT ON INSIDE SURFACE OF BURNER

OUTSIDE SURFACE SHALL BE CLEANED IN ACCORDANCE WITH STEEL STRUCTURE PAINT COUNCIL SSPC SP6 AND SHALL BE GIVEN ONE PRIME COAT OF "THURMALOX # 8". ONE FINISH COAT OF "THURMALOX # 7", BLACK COLOR

WORK THIS DWG. WITH DWG. 5962A-X-1

E E R CORP.

**Davy McKee**
ENGINEERS AND CONSTRUCTORS

LOW NO$_x$ BURNER
STEEL SHELL AND DETAILS
SCALE 1/2" = 1'-0"

5962A-X-2

# APPENDIX B

# THE DEVELOPMENT OF DESIGN CRITERIA FOR LOW-$NO_x$ OIL BURNERS SUITABLE FOR APPLICATION TO TEOR STEAMERS

# The Development of Design Criteria for Low $NO_x$ Oil Burners Suitable for Application to TEOR Steamers

Glenn C. England, Michael P. Heap,
Roy Payne, and David W. Pershing
Energy and Environmental Research Corporation
Irvine, California

W. Steven Lanier
U.S. Environmental Protection Agency
Research Triangle Park, North Carolina

Mr. England is Group Leader of Liquid Fuels Systems Development, Dr. Heap is Executive Vice President, Dr. Payne is Systems Development Manager, and Dr. Pershing is Senior Scientist with Energy and Environmental Research Corporation, 18 Mason, Irvine, California, 92714. Mr. Lanier is with the Combustion Research Branch of the U.S. Environmental Protection Agency, Research Triangle Park, North Carolina, 27711.

Prepared for

75th Annual Meeting
Air Pollution Control Association
New Orleans, Louisiana
June 20-25, 1982

March 15, 1982

# ABSTRACT

THE DEVELOPMENT OF DESIGN CRITERIA FOR LOW $NO_x$ OIL BURNERS SUITABLE FOR APPLICATION TO TEOR STEAMERS. G. England, M. Heap, R. Payne, and D. Pershing, Energy and Environmental Research Corp., 18 Mason, Irvine, CA 92714 and W. Steven Lanier, U.S. Environmental Protection Agency, Research Triangle Park, NC 27711.

The body of information presented in this paper is directed to individuals concerned with the design, performance and application of low $NO_x$ burners for liquid and gaseous fuels, particularly those with high fuel nitrogen content such as crude oils and synthetic fuels. Emissions of $NO_x$ can be minimized by application of a staged combustion process in which the first stage is thermally isolated and provides long residence time under high temperature, optimally fuel-rich conditions. The design criteria for this process were developed in a previous study which was carried out in a 70,000 Btu/hr refractory tunnel furnace, and from these criteria two pilot-scale prototype burners have been developed and tested at 2 x $10^6$ Btu/hr and 12 x $10^6$ Btu/hr. The paper describes the results of the development tests and compares results of all three scales of experiment. Firing a heavy fuel oil containing 0.6 percent bound nitrogen, test results indicate that $NO_x$ emissions of below 85 ppm (at 3% $O_2$) are possible while carbon monoxide and smoke are within acceptable limits. Translation of the design requirements to practical burner designs, and additional requirements for initial fuel/air contacting and second-stage air addition are presented and discussed. Data obtained over a scale range of 30:1 shows that residence time and temperature in the first stage are the single most important scaling parameters for this low $NO_x$ burner design and aerodynamic effects are second order. A current EPA program to translate the bench-scale and pilot-scale experience into a 50 x $10^6$ Btu/hr burner design which can be retrofitted to existing thermally-enhanced oil recovery (TEOR) steam generators is discussed. TEOR steamers are required to operate on difficult fuels with minimal environmental impact.

## Introduction

Nitrogen oxide emissions from stationary combustors can be reduced by combustion modification techniques which involve staging the heat release process. However, optimization of these techniques to control $NO_x$ emissions from liquid fuel-fired combustors has proved difficult because of the limited knowledge of the controlling phenomena and the problems associated with the scaling of combustion systems. This paper describes the development and verification of design criteria for low $NO_x$ liquid fuel-fired combustors based upon fundamental information generated in bench-scale reactors. This criteria is currently being applied to design and construction of a prototype $50 \times 10^6$ Btu/hr low $NO_x$ burner for field demonstration on a thermally-enhanced oil recovery (TEOR) steam generator early next year.

Many studies have been carried out to determine the mechanism of NO formation in flames both from molecular nitrogen (thermal NO) and from nitrogen contained in the fuel (fuel NO). Field test data(1) and laboratory studies(2,3) have established the importance of fuel NO to the total emission of nitrogen oxides from residual fuel oil flames. Thermal NO formation is strongly dependent upon temperature and its formation can be reduced by decreasing flame temperatures by techniques such as the addition of cooled combustion products to the combustion air (flue gas recirculation). However, since the majority of NO formed in residual fuel oil flames is fuel NO and its formation is not strongly dependent upon temperature, flue gas recirculation is not an effective $NO_x$ control technique(4). Fuel NO formation is very sensitive to reactant stoichiometry. Fuel-rich conditions promote the formation of molecular nitrogen from fixed nitrogen species ($NO + NH_3 + HCN = TFN$) which are formed as the liquid fuel decomposes. Consequently, staged combustion, which involves the formation of a fuel-rich zone either by delaying fuel air mixing or by dividing the combustion air supply into two and injecting one portion downstream from the burner is the most effective $NO_x$ control technique for residual fuels(5).

In a previous study(3) the parameters controlling the effectiveness of staged combustion for a wide range of liquid fuels containing bound nitrogen were defined in a series of bench-scale studies which were carried out in a refractory tunnel furnace. Exhaust NO levels from a staged combustion system are dependent upon:

1. First-Stage Processing. TFN is minimized if the residence time of the fuel-rich reactants is maximized at high temperatures and at an optimum stoichiometry which is temperature dependent.

2. Mixedness. Since stoichiometry must be controlled it is important that the reactants are well mixed.

3. Second-Stage Processing. Exhaust NO levels are the sum of thermal NO formation and conversion (or retention) of TFN species to NO during heat release in the second stage and the second stage must be designed to minimize these effects.

4. Fuel Properties. The rate of evolution of nitrogen species from the liquid fuel droplets has an impact because it dictates the time

available for $N_2$ formation in the first zone. This can be overcome by minimizing droplet size.

The goal of the investigation reported in this paper was to use this information to construct a combustor which would have $NO_x$ emissions less than 100 ppm (corrected to 0% $O_2$) and have acceptable emission levels for CO and smoke when firing fuels containing greater than 0.5 percent nitrogen.

The bench-scale tests indicated that TFN concentration is minimized most effectively by increasing the temperature of the fuel-rich zone. The combination of high first-stage temperature, optimum stoichiometry and long first-stage residence time resulted in exhaust $NO_x$ levels below 100 ppm irrespective of the nitrogen content of the liquid fuel. To translate this information into a full-scale burner (circa 50 x $10^6$ Btu/hr) requires information on how the controlling parameters scale. This paper describes results from experimental studies performed to achieve this understanding. The approach used was to obtain experimental results with 2 x $10^6$ Btu/hr and 10 x $10^6$ Btu/hr prototype combustors, and thereby, confirm the appropriate scaling criteria for the design and fabrication of the full-scale combustor.

## Experimental Equipment

Two prototype low $NO_x$ burners, shown in Figure 1, were constructed with nominal design firing rates of 2 x $10^6$ Btu/hr (small pilot scale or SP) and 10 x $10^6$ Btu/hr (intermediate pilot scale or IP). Each of the two test burners contains three major elements:

1. an air/fuel injection system,
2. a fuel-rich holdup zone, and
3. a secondary air injection section.

The primary zone is constructed from high temperature refractories and insulation to minimize heat loss through the walls and permit near-adiabatic conditions in the primary zone. Fuel and primary air are injected at the entry of a divergent which forms the initial section of the fuel-rich holdup zone. The residence time in the fuel-rich zone calculated at a first-stage stoichiometric ratio of 0.7 is approximately 0.50 sec. for the SP burner and 0.43 sec. for the IP burner. The primary products are directed through a convergent section which serves to minimize radiative heat loss, ensure complete mixing of the primary products, and minimize backmixing of secondary air into the primary zone. Secondary air is injected parallel to the burner axis annularly around the primary exit.

Two different commercial atomizers were used, an ultrasonic, air-assist atomizer and an internal mixing steam-assist atomizer. The ultrasonic atomizer produced droplets with a narrow size distribution about a mean diameter of 20 μm and the internal mixing atomizer produced droplets with a much broader size distribution about a mean diameter of 40 μm(3).

The combustor tests were conducted in two different combustors:

- Firetube Simulator (FS). The combustion chamber is 10.5 feet long with an internal diameter of 23.5 inches. The chamber is composed of calorimetric sections cooled by heat transfer fluid and has a nominal wall temperature of 450 F. Only the SP burner was tested in this facility.

- Small Watertube Simulator (SWS). The furnace is 17 feet in length and 6 feet inside diameter and is externally spray-cooled with a partial refractory lining. The total heat extraction is controlled by varying the percentage of internal surface which is covered by refractory. Both the SP and IP burners were tested in this facility.

The fuel and air flow to both furnaces were monitored continuously. The equipment used to measure exhaust gas concentrations and TFN levels in the first stage have been described in detail elsewhere(3).

## First Stage Parameters

### Stoichiometry

Figure 2 shows the influence of the first-stage stoichiometric ratio ($SR_1$) on exhaust emissions from the bench-scale studies carried out in the tunnel furnace and the prototype tests with different residual oils containing approximately 0.6 percent nitrogen. The curves are generally lower but similar in shape to those obtained in other staged combustion studies. As $SR_1$ decreased, $NO_x$ emissions decreased rapidly until a minimum was reached and then increased. Smoke and CO emissions from the SP burner were low for $SR_1 > 0.7$, but under more fuel-rich conditions emissions increased sharply. CO was less than 100 ppm and smoke number was generally less than 5 at the point where the minimum $NO_x$ level occurred. CO and smoke emissions from the IP burner were also low for $SR_1$ greater than the point where minimum $NO_x$ occured; however, the sharp increase in emissions below this point was not observed. Differences in second-stage thermal environment between the $2 \times 10^6$ Btu/hr firetube simulator and the $10 \times 10^6$ Btu/hr small watertube simulator may contribute to the observed difference in burnout of CO and smoke. Comparison of the three sets of results indicates that concept scale-up shifted the optimum $SR_1$ from 0.8 to 0.7 in going from 70,000 Btu/hr to $2 \times 10^6$ Btu/hr, and to 0.56 in going to $8 \times 10^6$ Btu/hr. This shift can be attributed to reduced heat losses and therefore higher temperatures associated with the increase in scale.

In the SP burner tests, TFN (NO, HCN, $NH_3$) species concentrations were made at the exit of the fuel-rich zone to define the influence of scale on the fuel-rich processing. These data (Figure 3) show that the increased reactor temperature in the small pilot-scale prototype resulted in a reduction of minimum TFN level and a shift of the location of the minimum from 0.8 to 0.7. Equilibrium calculations (free energy minimization) confirmed that the optimum $SR_1$ should move more fuel-rich with increased temperature; however, the TFN concentrations shown in Figure 3 are greatly (circa $10^2$) in excess of equilibrium values. Hence, even with the first-stage exit temperature of 2950°F ($SR_1 = 0.7$) and a first-stage residence time of 500 msec., kinetic limitations are significant. Decreasing $SR_1$ reduced first-stage NO, but below approximately $SR_1 = 0.8$, significant amounts of $NH_3$ were formed. Thus, as in the bench-scale studies, there exists a minimum in the exhaust $NO_x$ because of a competition between decreased first-stage NO and increased oxidizable nitrogen species. Other than shifting the optimum $SR_1$, concept scale-up did little to alter this competition or the TFN species distribution.

## Time and Temperature

The residence time in the fuel-rich zone to achieve the desired TFN concentration is an important practical design parameter. Figure 4 summarizes minimum exhaust $NO_x$ and TFN data for the tunnel furnace and the prototype burners firing in both the firetube simulator and the small watertube simulator as a function of the first-stage residence time. At both bench and small pilot scales, increasing the first-stage residence time significantly decreased exhaust $NO_x$ because of an associated decrease in TFN. (Increasing first-stage residence time allows HCN, $NH_3$ and NO to decay further toward equilibrium values.) Both the exhaust $NO_x$ and the TFN from the SP burner were lower than from the tunnel furnace because of the increased rich-zone temperature associated with the increase in scale.

Variations in first-stage residence time were achieved in the SP burner/firetube simulator tests by altering the firing rate (2 and 3 x $10^6$ Btu/hr) and in the SP burner/watertube simulator tests by changing the reactor length (8.8 feet to 6.3 feet) at 2 x $10^6$ Btu/hr. A strong correlation between the two sets of experiments suggests that the controlling processes are dominated by kinetic effects (time and temperature) and not by aerodynamics and that the principle influence of firing rate is on residence time. Clearly, increasing firing rate also increases first-stage temperature, but this effect is small because even at 2 x $10^6$ Btu/hr, the prototype heat losses were low. First-stage exit temperatures measured at $SR_1$ of 0.7 were 2950°F compared to adiabatic flame temperature of 3180°F.

Since the time/temperature history of the fuel-rich zone was found to be the primary scaling parameter, one-dimensional kinetic calculations were conducted to quantify this influence. The model assumed a 2 msec. well-stirred reaction ignition zone followed by a variable-length plug-flow reactor and the fuel was $CH_4$ containing one weight percent N as HCN. Preliminary runs showed that the initial fuel nitrogen speciation input to the first stage had little effect on the ultimate TFN level. The model showed that TFN decay is rapid at high temperature, but that the decay slows dramatically where the temperature drops below 2600°F. Thus, increasing first-stage residence time is only beneficial if the heat extraction rate is low enough to keep the local gas temperature above 2600°F. Further, even if the fuel-rich temperature is maintained at a high level, the rate of NO decay decreases precipitously when the $NH_3$ concentration falls to zero indicating that TFN speciation is important in first-stage processing. These calculations support the concept that reactions in the form:

$$NO + NH_i \rightarrow N_2 \qquad (1)$$

are controlling the fuel-rich TFN reduction and that it is essential to have both high temperature (>2600°F), and a proper TFN species distribution to achieve very low exhaust $NO_x$. The calculations also indicate the need for a long residence time in the primary zone but that this requirement decreases with increasing first-stage temperatures for a fixed TFN level.

### Fuel/Air Contacting

The influence of fuel/air contacting parameters early in the fuel-rich zone (e.g., nozzle design, atomization pressure, atomizing fluid, and air swirl) on prototype performance was investigated. Steam and air atomization both produced satisfactory results when the atomization pressure was high enough to provide adequate atomization. With long first-stage residence times (>600 msec.), fuel injector parameters had little effect on minimum $NO_x$; however, both poor mixing and poor atomization (mean droplet diameter >100 microns) resulted in unacceptably high smoke.

As first-stage residence time was decreased, the importance of the fuel injection system design became more apparent. Figure 5 compares data obtained with a premixed burner to that obtained with the standard axial fuel nozzle arrangement. Both were fired in the SP burner mounted on the watertube simulator. The premixer was based on a high-swirl gas-turbine design(6) which utilized ultrasonic atomization. In the short first-stage residence time configuration (350 msec. at $SR_1 = 0.7$), the premixer slightly reduced the exhaust NO emissions, and broadened the $SR_1$ for minimum emissions. A similar conclusion was reached by comparing data for a propane/$NH_3$ fuel (which represents a limit of instant fuel vaporization) to the California residual with the standard fuel nozzle. Thus, unless the first-stage residence time is extremely short (<200 msec), the characteristic time for fuel vaporization and mixing is small relative to the rich-zone residence time and hence atomizer design has a much greater effect on smoke formation than on minimum NO. This conclusion, however, is probably scale dependent.

## Second Stage Parameters

### Temperature

All the TFN which exists in the first stage does not result in NO in the combustion products of the second stage. Thus, it is important to design the second-stage air injection system to minimize NO formation from TFN species. In addition, thermal NO formation must be minimized which requires that second-stage flame temperatures must be maintained below some critical threshold. Heat extraction between the fuel-rich zone and the secondary air injection system allows some control over temperature in the second-stage. Figure 6 presents SP burner/SWS results obtained when water cooling tubes were placed around the periphery of the second-stage throat. This cooling removed approximate 120,000 Btu/hr (6 percent of the heat input) and decreased the minimum exhaust $NO_x$ by approximately 20 ppm. Exactly analogous results were achieved when 40 percent flue gas recycle was introduced with the second-stage air ($\Delta NO = 18$ ppm). In both tests there was a minor impact on smoke emissions; thus, it appears that at the optimum operating conditions, second-stage thermal NO formation accounts for approximately 20 percent of the exhaust emissions with the burner. Use of interstage cooling may become more important in subsequent scale-up if air preheat is added and/or rich-zone heat loss is reduced further.

### TFN Conversion

Variation in the temperature of the reactants exiting the first stage can affect exhaust NO levels because of a change in TFN distribution and/or reduced conversion rates in the second stage. Generally TFN conversion is high when NO is the dominant TFN species and when significant amounts of hydrocarbon are not carried into the second-stage flame. As TFN concentration increases below $SR_1 = 0.8$, TFN conversion decreases due to increasing amounts of HCN and $NH_3$. The general conversion decrease is the result of a competition between $N_2$ formation reactions which are second-order in XN and first-order NO formation reactions. Folsom, et al(7) have shown that in a simple diffusion flame the conversion of HCN and $NH_3$ to NO and the retention of NO are affected by the hydrocarbon content of the fuel. $NH_3$ conversion is low when hydrocarbons are absent, and hydrocarbons are necessary for the reduction of NO or HCN to $N_2$. Thus, staged combustion requires the minimization of TFN as well as the production of an optimum TFN/fuel mixture for burnout.

## Mixing

The method of secondary air injection could impact exhaust NO levels and two different methods were investigated to determine the sensitivity of emissions to changes in secondary fuel/air mixing in the prototype burner system. The standard annular (parallel) air injector provided a relatively slow mixing rate; rapid mixing was obtained by injecting the second-stage air radially through a water-cooled boom inserted along the firetube axis from the rear. $NO_x$ emissions remained essentially constant when the ratio of air between the axial and radial injectors was varied; however, smoke emissions were substantially decreased as secondary air was transferred from the parallel injector to the radial injector. Similar results were obtained when swirl vanes were added to the second-stage air injection system. The insensitivity of $NO_x$ emissions to changes in mixing suggests that local stoichiometry does not have a strong influence on either thermal NO formation or TFN conversion to NO in the second stage. Figure 7 shows the effect of overall excess oxygen on $NO_x$ emissions from the IP burner firing at $8 \times 10^6$ Btu/hr ($SR_1 = 0.56$) and at $12 \times 10^6$ Btu/hr ($SR_1 = 0.62$). $NO_x$ increased by approximately 12 ppm at $8 \times 10^6$ Btu/hr and by 15 ppm at $12 \times 10^6$ Btu/hr in varying excess oxygen from 0.5 to 5.0 percent, which again points to the importance of the first stage parameters in determining final emissions. Bacharach smoke number ranged from 1 to 4 and CO emissions less than 50 ppm (except at $12 \times 10^6$ Btu/hr and 0.3 percent excess $O_2$) for the data shown in Figure 7.

## Scaling and Applicability of the Low $NO_x$ Concept

The results of these tests have provided an understanding of the controlling mechanisms of $NO_x$ formation and control in staged liquid fuel combustion. One application of these concepts is by constructing a staged burner which consists of three major components with the following characteristics:

- Fuel Injection System
  - High quality atomization to produce a mean drop size less than 50 microns.
  - Premixed fuel/air.
  - Minimal heat extraction to maximize fuel vaporization rate.

- First-Stage Fuel-Rich Zone
    - Stoichiometric ratio approximately 0.7 to minimize TFN concentration.
    - Residence time in excess of 400 msec. to allow sufficient TFN decay.
    - Control of heat loss to produce a first-stage exit temperature in excess of 2600°F.
- Second-Stage Air Injection
    - Partial quenching to minimize thermal NO formation in the second stage.
    - Refractory choke to prevent backmixing and reduce heat loss.
    - Intermediate to rapid second-stage mixing for minimizing smoke formation.

A program under EPA sponsorship is currently underway to demonstrate a burner based on these criteria in a 50 x $10^6$ Btu/hr oilfield steam generator (commonly referred to as "steamers") in the Kern County area of California. These units typically operate on lease crudes varying in nitrogen content from 0.6 to 0.8 percent, and under constant load for extended periods of time. Local regulations for the emission of $NO_x$, $SO_x$, and particulates are very stringent in Kern County and maximum total $NO_x$ emission levels of 0.14 lb/MMBtu (125 ppm at 0% $O_2$) are currently under consideration. Such low levels have traditionally been difficult to achieve with high nitrogen fuels through combustion modification while maintaining practical flame conditions within the steamer.

The influence of fuel-nitrogen content on the performance of the small-scale low $NO_x$ prototype burner was established by conducting tests with a distillate oil, residual oils, a coal-liquid, and propane/$NH_3$. Data obtained in these tests are shown in Figure 8 which indicates that with the SP burner minimum NO emissions are only weakly dependent upon total fuel nitrogen content. Figure 8 also summarizes similar data obtained in the small-scale tunnel furnace. Concept scale-up reduced the dependence on fuel-nitrogen; this is probably because of the increased fuel-rich temperature. Thus this low $NO_x$ concept should be capable of producing $NO_x$ emissions less than 100 ppm at 0 percent $O_2$ (85 ppm at 3 percent $O_2$) even when firing the high nitrogen crude oils typical of Kern County oilfields.

Figure 9 illustrates how this concept may be incorporated into an existing steamer. The major features of this design are:

- isolated first-stage combustion chamber with appropriate time/temperature characteristics;
- regenerative primary air preheat;

- single conventional fuel nozzle;
- variable first-stage air swirl and swirl distribution;
- variable second stage air swirl.

The current program will provide a preliminary evaluation of this burner in an experimental test furnace prior to final development in a field-operating steamer. The program will conclude with a 30-day field demonstration scheduled for February 1983.

## Acknowledgements

This work was supported by the U.S. Environmental Protection Agency Combustion Research Branch under Contracts 68-02-3125 and 68-02-3692.

## References

1. Cato, G.A., L.J. Muzio, and R.E. Hall. "Influence of Combustion Modifications on Pollutant Emisisons from Industrial Boilers," Proceedings of the Stationary Source Combustion Symposium, EPA 600/2-76-1526 NTIS, Springfield, VA (1976).

2. Pershing, D.W., J.E. Cichanowicz, G.C. England, M.P. Heap, and G.B. Martin, "The Influence of Fuel Composition and Flame Temperature on the Formation of Thermal and Fuel $NO_x$ in Residual Oil Flames", Seventeenth Symposium (International) on Combustion, The Combustion Institute, Pittsburgh, PA (1979).

3. England, G.C., M.P. Heap, D.W. Pershing, and R.K. Nihart, "Mechanisms of $NO_x$ Formation and Control: Alternative and Petroleum-Derived Liquid Fuels", Eighteenth Symposium (International) on Combustion, The Combustion Institute, (1981).

4. Heap, M.P., et al., "Control of Pollutant Emissions from Oil-Fired Package Boilers", Proceedings of the Stationary Source Combustion Symposium, EPA 600/2-76-1526, NTIS, Springfield, VA (1976).

5. Beer, J.M., M.T. Jaques, W. Farmayan, and B.R. Taylor, "Fuel Nitrogen Conversion in Staged Combustion of a High Nitrogen Petroleum Fuel", Eighteenth Symposium (International) on Combustion, The Combustion Institute, Pittsburgh, PA (1981).

6. Pierce, R.M., S.A. Mosier, C.E. Smith, and B.S Hinten, "Advanced Combustion Systems for Stationary Gas Turbine Engines: Volume II. Bench-Scale Evaluation", Final Report, EPA 600/7-80-0176, NTIS, Springfield, VA (1980).

7. Folsom, B.A., C.W. Courtney, and M.P. Heap, "The Effects of LBG Composition and Combustor Characteristics on Fuel $NO_x$ Formation," Transactions of the ASME, Vol. 102, No. 2, April 1980.

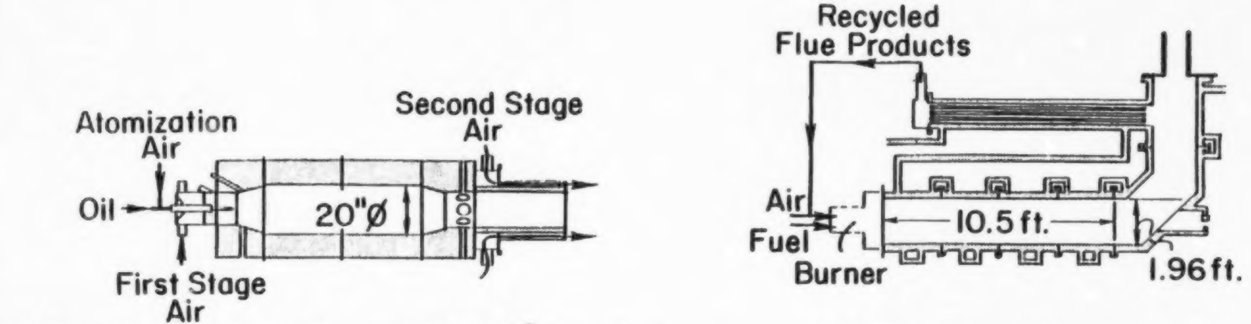
Atomization
Air
Oil
First Stage
Air
20"Ø
Second Stage
Air
Recycled
Flue Products
Air
Fuel
Burner
10.5 ft.
1.96 ft.

(a) Small Prototype Burner ($2 \times 10^6$ Btu/hr)

(b) Firetube Simulator

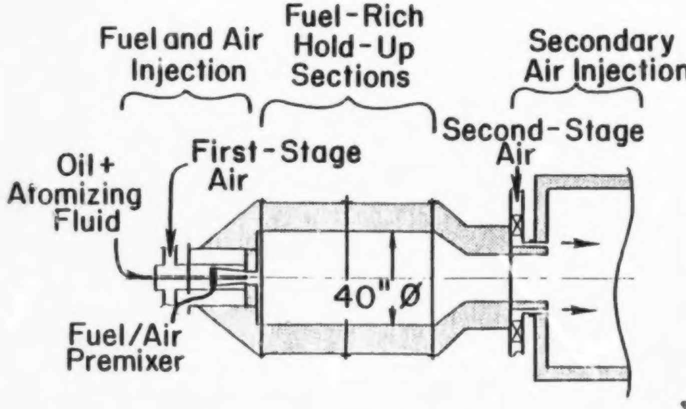
Fuel and Air
Injection
Fuel-Rich
Hold-Up
Sections
Secondary
Air Injection
Oil +
Atomizing
Fluid
First-Stage
Air
Second-Stage
Air
40"Ø
Fuel/Air
Premixer

(c) Intermediate Prototype Burner ($10 \times 10^6$ Btu/hr)

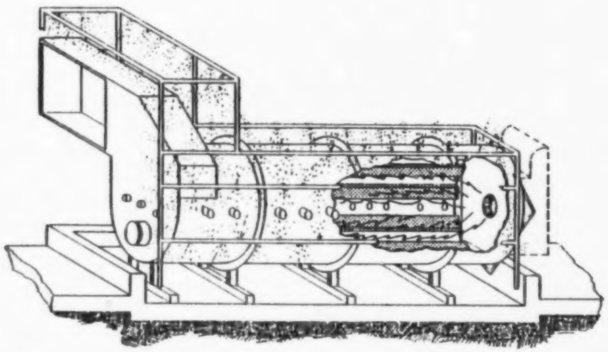

(d) Small Watertube Simulator

Figure 1. Prototype burners and experimental test furnaces.

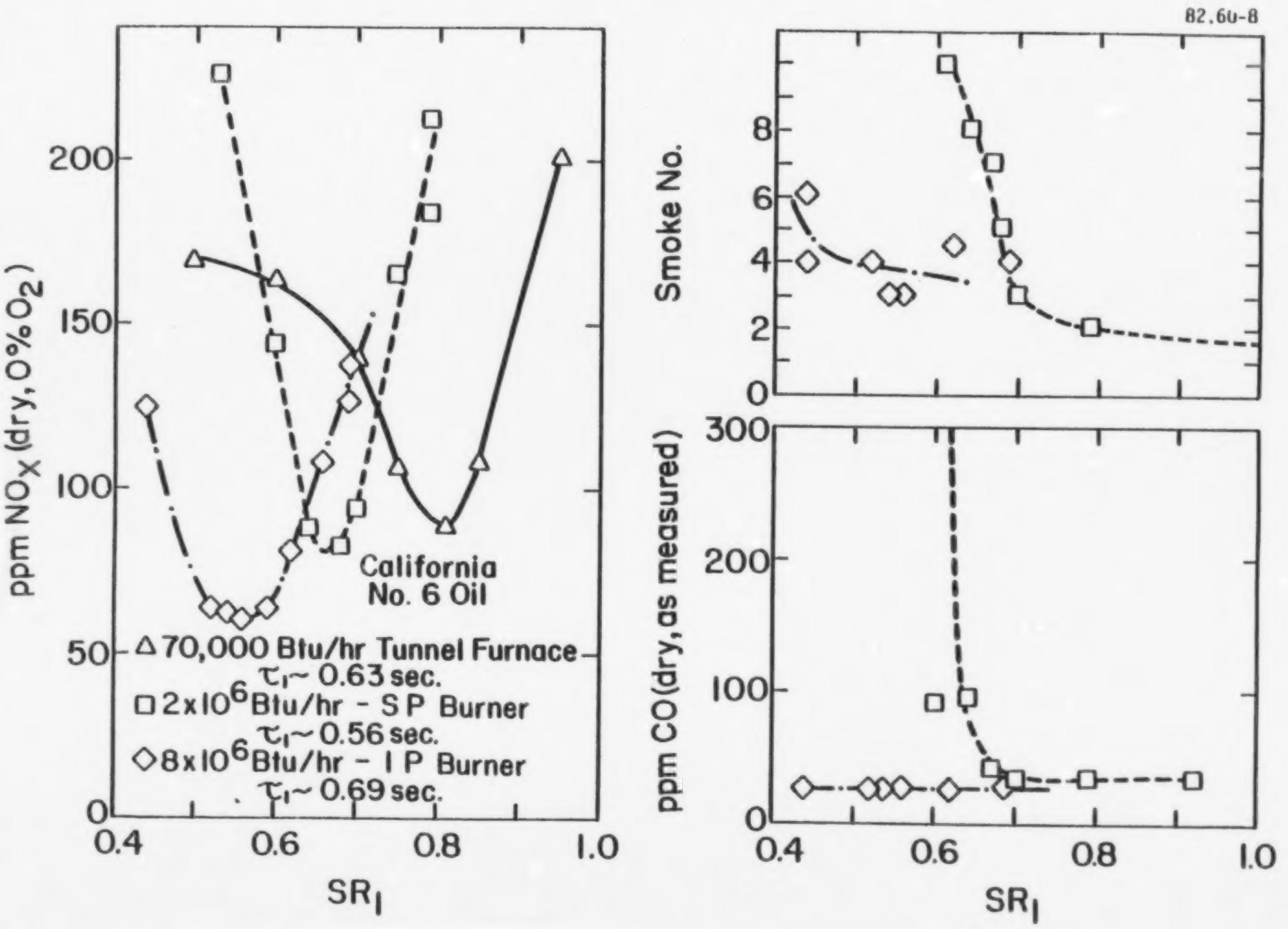

Figure 2. Influence of first-stage stoichiometry on NO$_x$, CO, and smoke emissions (bench scale and pilot scale).

82-60.6

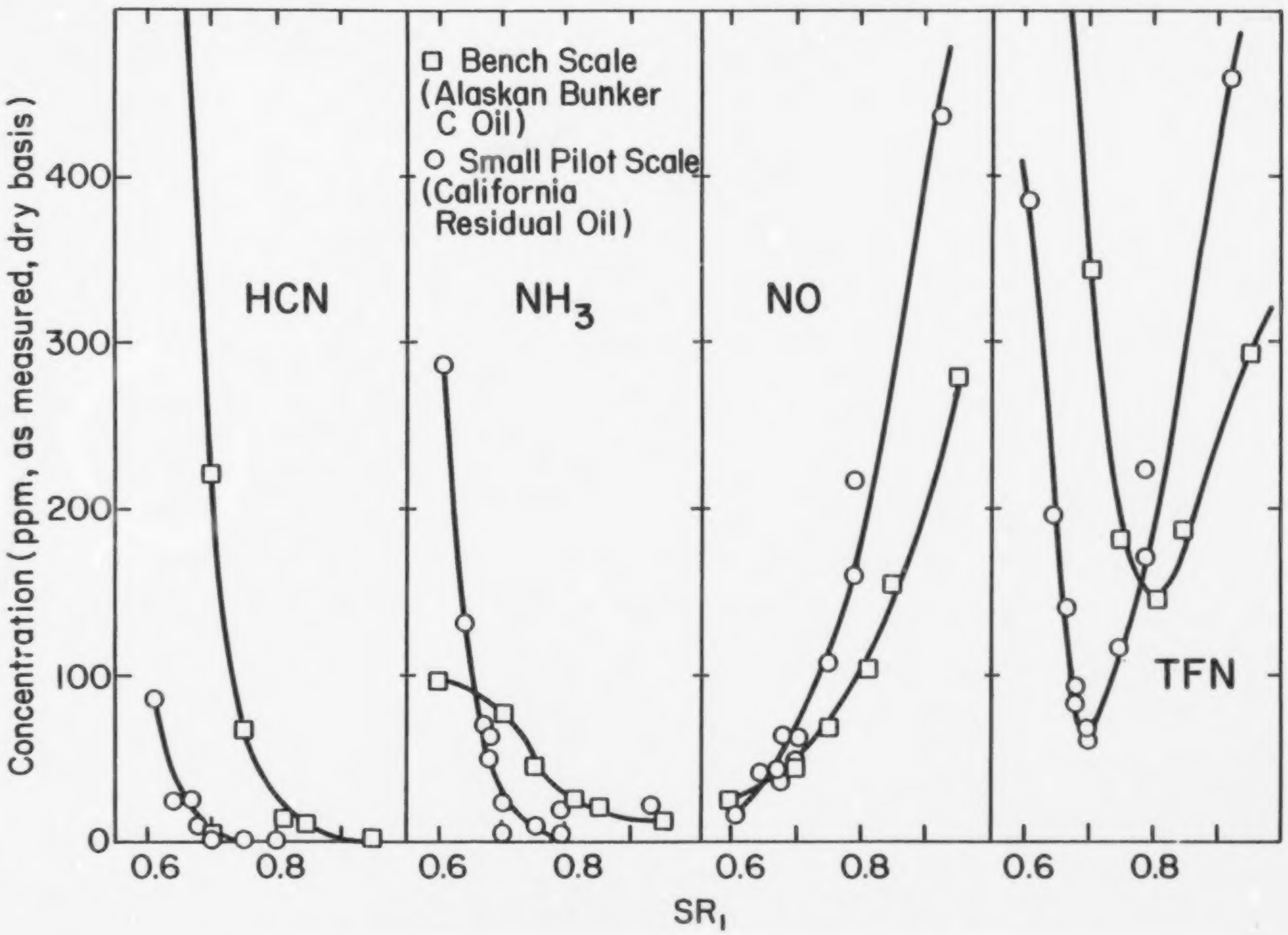

Figure 3. Influence of scale on first-stage exit total fixed nitrogen (TFN) species (primary zone mean residence time approximately 600 msec).

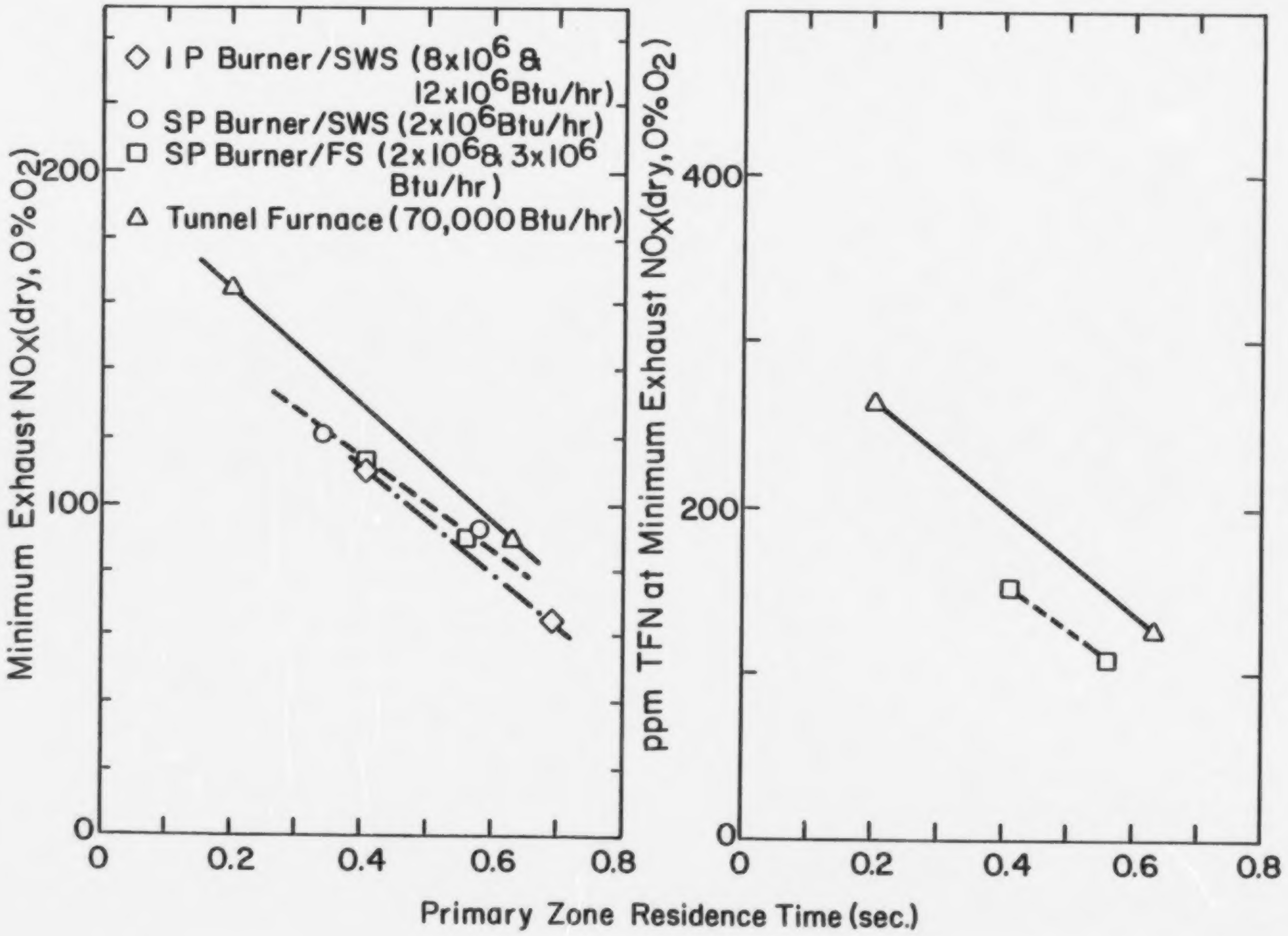

Figure 4. Second-stage $NO_x$ production and first-stage TFN decay for bench scale and pilot scale.

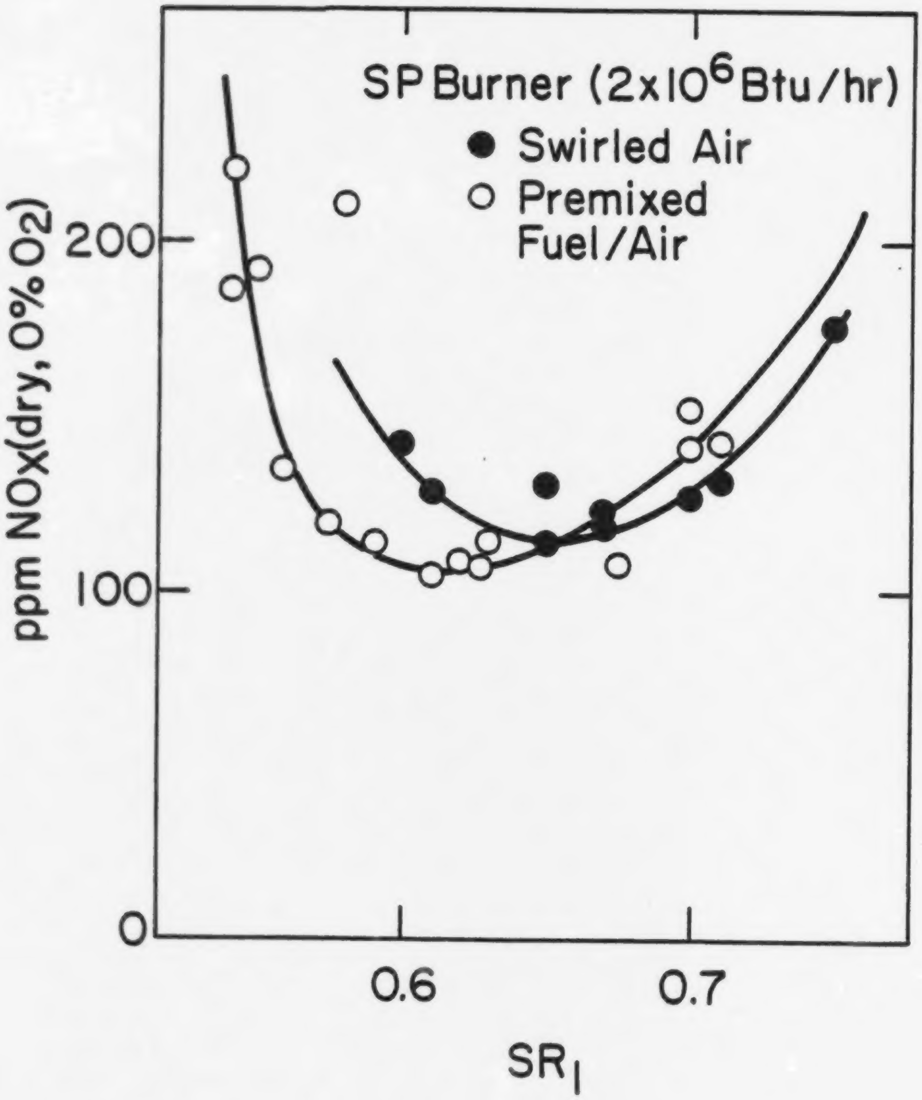

Figure 5. Pilot-scale second-stage $NO_x$ emissions for premixed and non-premixed first-stage reactants ($2 \times 10^6$ Btu/hr; California residual oil; 350 msec. first-stage residence time at $SR_1 = 0.7$).

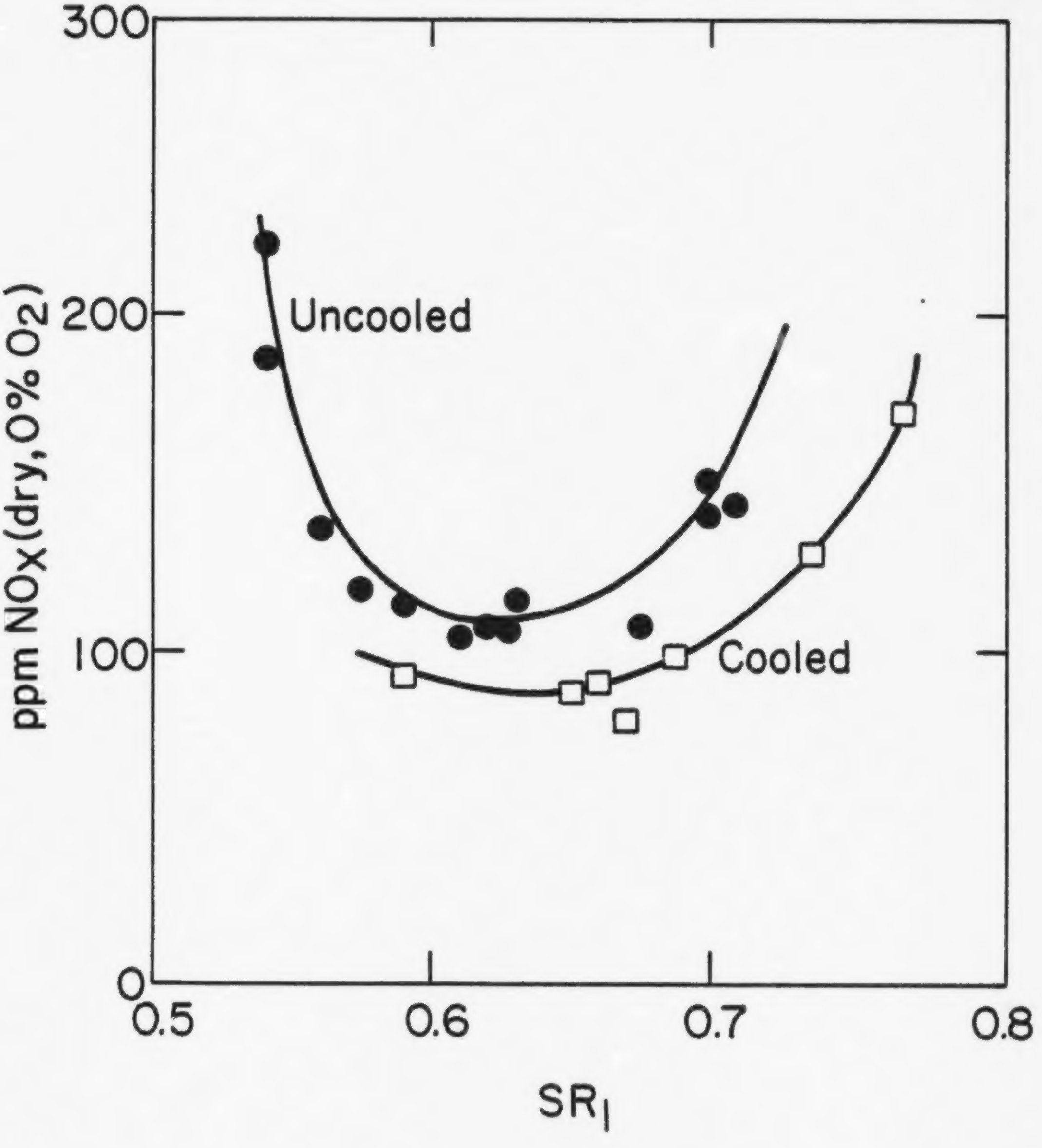

Figure 6. Pilot-scale second-stage $NO_x$ emissions with and without interstage heat extraction ($2 \times 10^6$ Btu/hr; 120,000 Btu/hr interstage heat removal in cooled case).

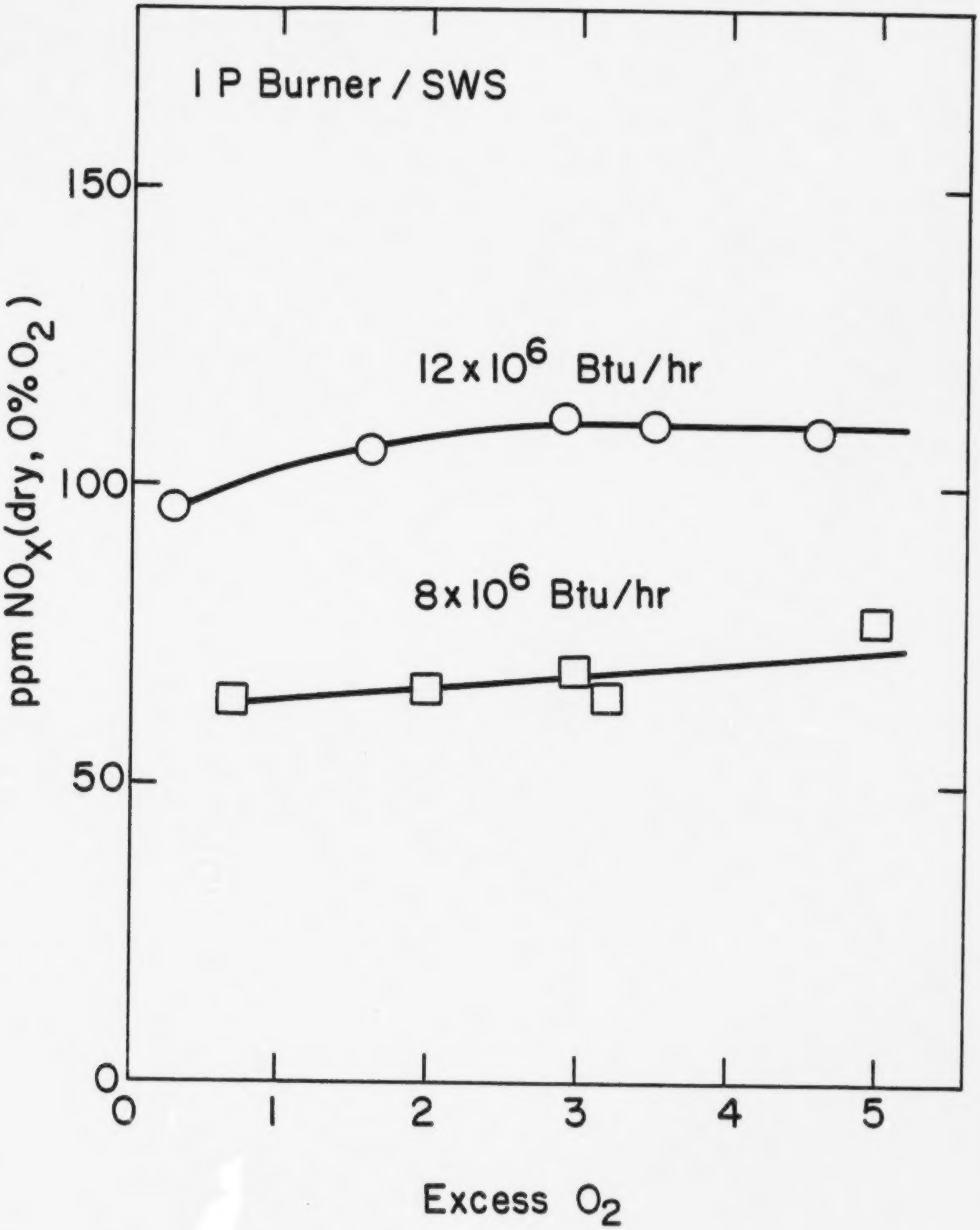

Figure 7. Influence of excess air on second-stage $NO_x$--IP burner.

82-60.8

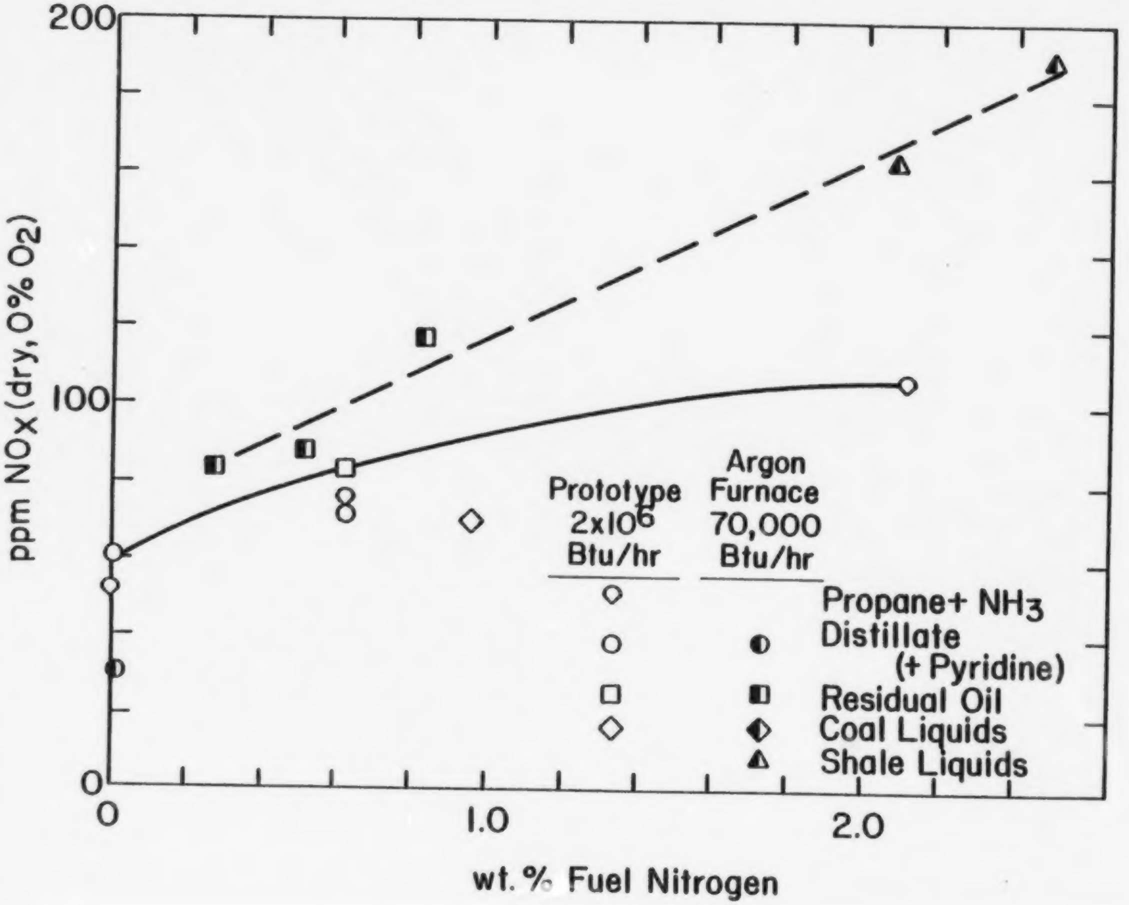

Figure 8. Influence of fuel nitrogen on second-stage $NO_x$--Bench-scale and pilot-scale data.

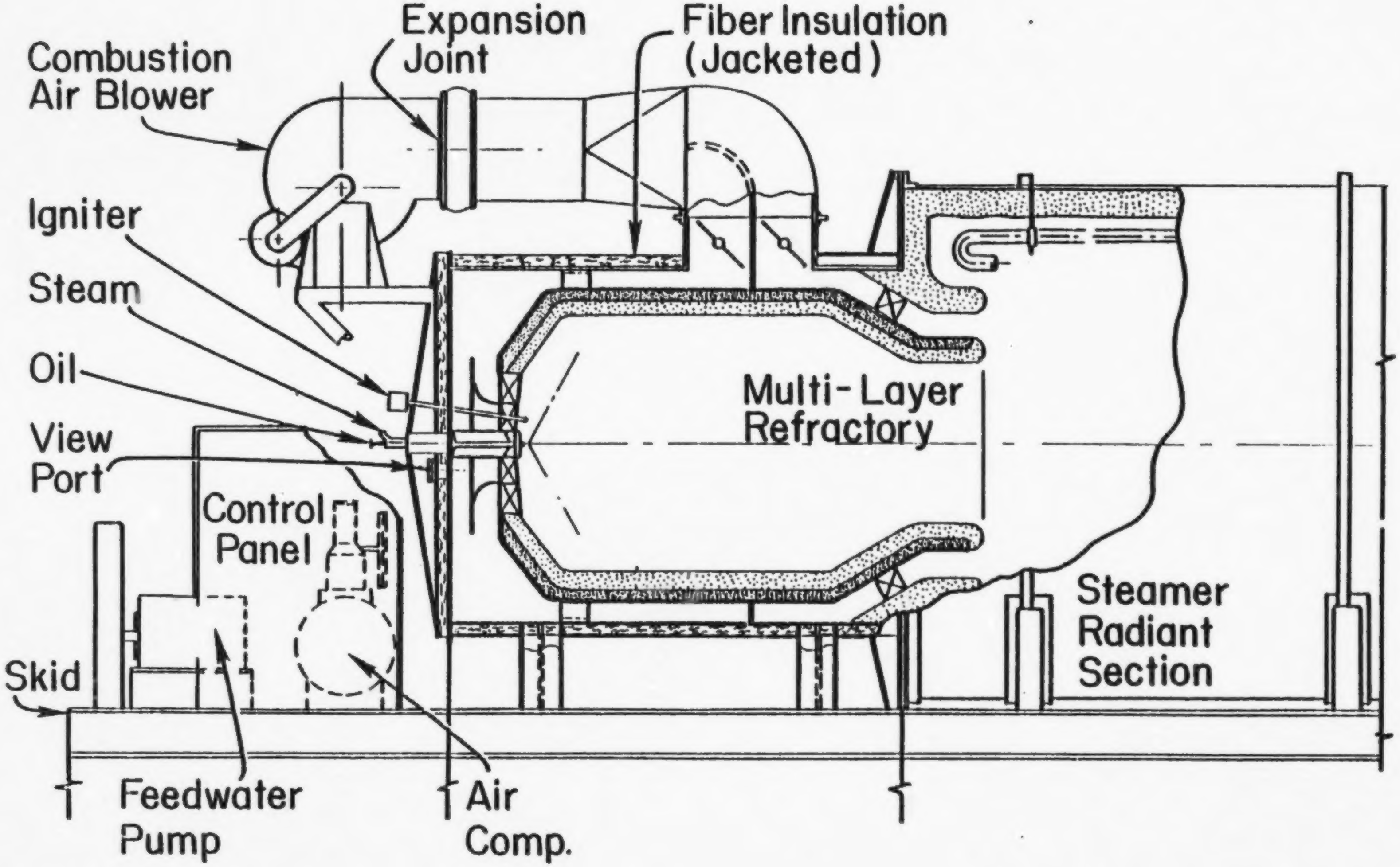
Combustion Air Blower
Expansion Joint
Fiber Insulation (Jacketed)
Igniter
Steam
Oil
View Port
Control Panel
Multi-Layer Refractory
Steamer Radiant Section
Skid
Feedwater Pump
Air Comp.

Figure 9. Conceptual burner design for TEOR steam generator.

# APPENDIX C

## COMMERCIAL PRACTICE BURNER
## DESIGN DRAWINGS

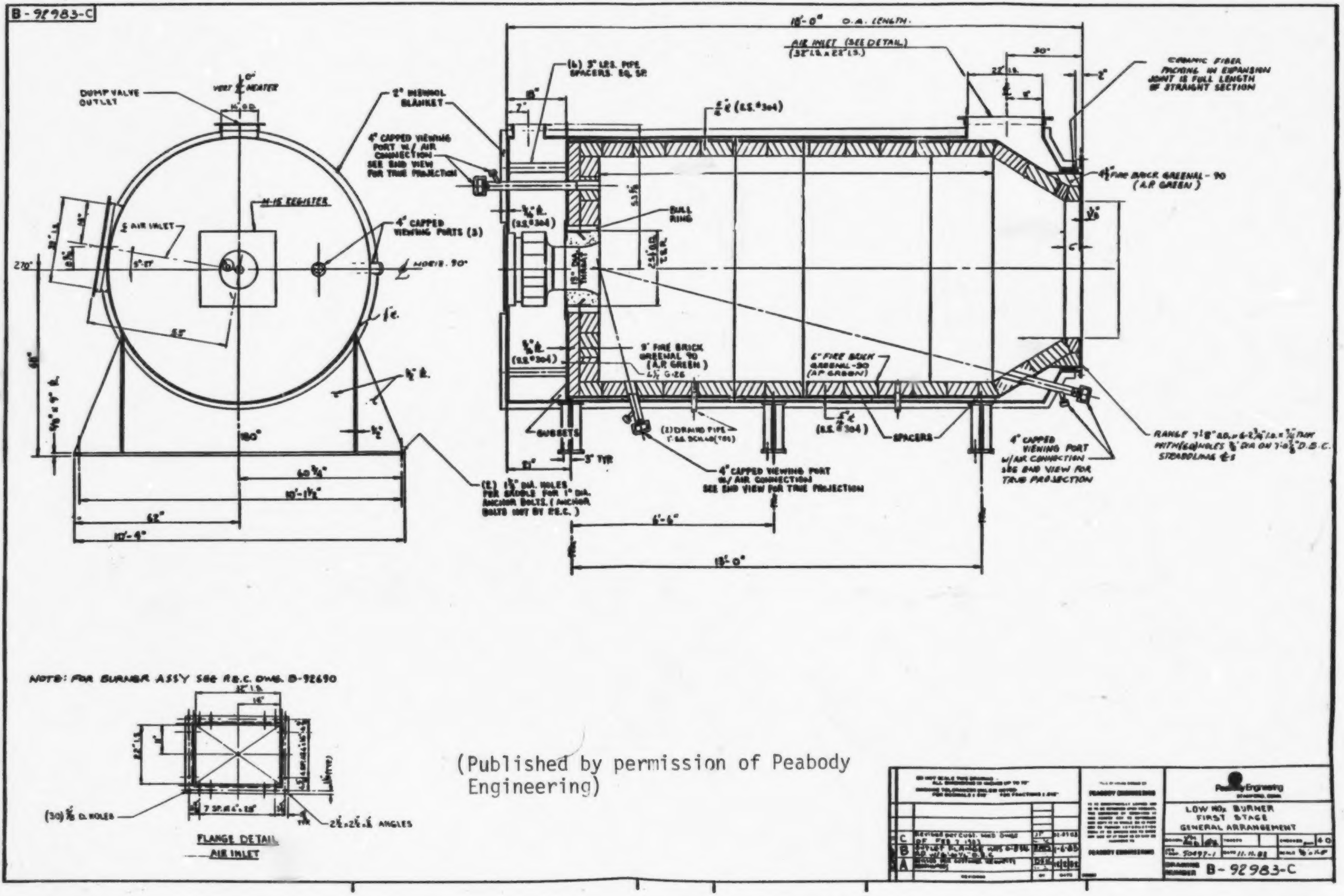
B-92983-C
DUMP VALVE OUTLET
VENT & HEATER
2" INSWOOL BLANKET
M-15 REGISTER
AIR INLET
4" CAPPED VIEWING PORT W/ AIR CONNECTION SEE END VIEW FOR TRUE PROJECTION
4" CAPPED VIEWING PORTS (3)
HORIZ. 90°
270°
180°
60¾"
10'-1½"
62"
10'-4"
(2) 1⅛" DIA. HOLES PER SADDLE FOR 1" DIA. ANCHOR BOLTS. (ANCHOR BOLTS NOT BY P.E.C.)
18'-0" O.A. LENGTH
AIR INLET (SEE DETAIL) (32" I.D. x 22" I.D.)
30"
(6) 3" LEG. PIPE SPACERS. EQ. SP.
CERAMIC FIBER PACKING IN EXPANSION JOINT IS FULL LENGTH OF STRAIGHT SECTION
4½" FIRE BRICK GREENAL-90 (A.P. GREEN)
BULL RING
9" FIRE BRICK GREENAL 90 (A.P. GREEN)
4½" G-26
6" FIRE BRICK GREENAL-90 (A.P. GREEN)
GUSSETS
3" TYP.
(2) DRAIN PIPE 1" SS. SCH. 40 (T.O.E.)
4" CAPPED VIEWING PORT W/ AIR CONNECTION SEE END VIEW FOR TRUE PROJECTION
SPACERS
4" CAPPED VIEWING PORT W/AIR CONNECTION SEE END VIEW FOR TRUE PROJECTION
6'-6"
13'-0"
NOTE: FOR BURNER ASS'Y SEE P.E.C. DWG. B-92690
(30) ⅞ D. HOLES
2½ x 2½ x ¼ ANGLES
FLANGE DETAIL
AIR INLET
Peabody Engineering
LOW NOx BURNER
FIRST STAGE
GENERAL ARRANGEMENT
50497-1
11.11.81
DRAWING NUMBER B-92983-C

(Published by permission of Peabody Engineering)

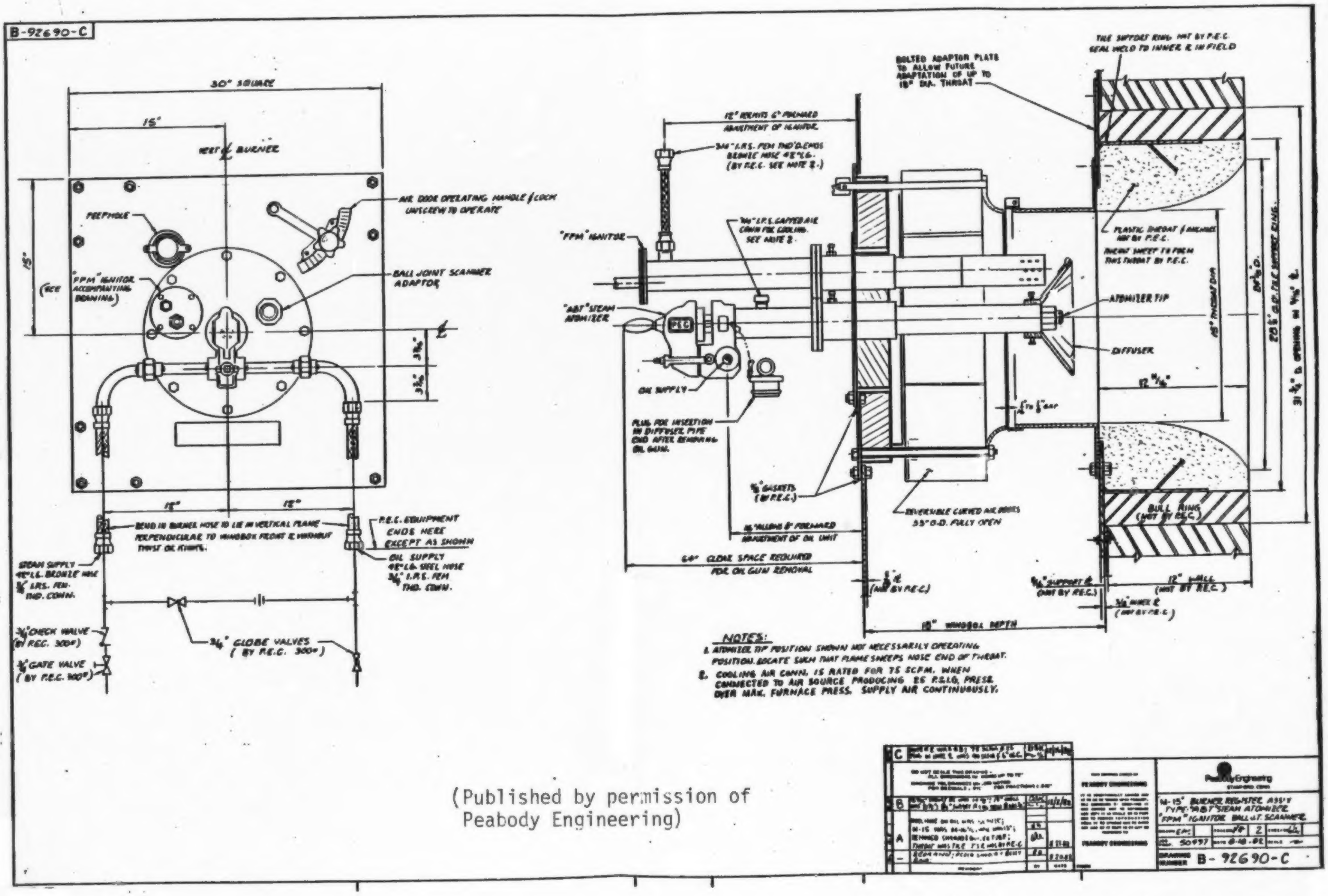
B-92690-C
30" SQUARE
15"
VERT ℄ BURNER
15"
(SEE
"FPM" IGNITOR
ACCOMPANYING
DRAWING)
PEEPHOLE
AIR DOOR OPERATING HANDLE & LOCK
UNSCREW TO OPERATE
BALL JOINT SCANNER
ADAPTOR
℄
3⅝"
3⅝"
12"
12"
BEND IN BURNER HOSE TO LIE IN VERTICAL PLANE
PERPENDICULAR TO WINDBOX FRONT & WITHOUT
TWIST OR KINKS.
P.E.C. EQUIPMENT
ENDS HERE
EXCEPT AS SHOWN
STEAM SUPPLY
48" LG. BRONZE HOSE
¾" I.P.S. FEM.
THD. CONN.
OIL SUPPLY
48" LG. STEEL HOSE
¾" I.P.S. FEM
THD. CONN.
¾" CHECK VALVE
(BY P.E.C. 300#)
¾" GATE VALVE
(BY P.E.C. 300#)
¾" GLOBE VALVES
( BY P.E.C. 300# )
BOLTED ADAPTOR PLATE
TO ALLOW FUTURE
ADAPTATION OF UP TO
18" DIA. THROAT
THE SUPPORT RING NOT BY P.E.C.
SEAL WELD TO INNER & IN FIELD
12" PERMITS 6" FORWARD
ADJUSTMENT OF IGNITOR.
3/4" I.P.S. FEM THD'D. ENDS
BRONZE HOSE 48" LG.
(BY P.E.C. SEE NOTE 2.)
"FPM" IGNITOR
3/4" I.P.S. CAPPED AIR
CONN FOR COOLING.
SEE NOTE 2.
"ABT" STEAM
ATOMIZER
PEC
OIL SUPPLY
PLUG FOR INSERTION
IN DIFFUSER PIPE
END AFTER REMOVING
OIL GUN.
PLASTIC THROAT & ANCHORS
NOT BY P.E.C.
THROAT SHEET TO FORM
THIS THROAT BY P.E.C.
ATOMIZER TIP
DIFFUSER
15" THROAT DIA
24½" O.D.
20½" O.D. TILE SUPPORT RING.
31¾" D. OPENING IN ¼" ℄
12 ¹¹⁄₁₆"
⅛" to ¼" GAP
⅝" GASKETS
(BY P.E.C.)
REVERSIBLE CURVED AIR DOORS
35" O.D. FULLY OPEN
BULL RING
(NOT BY P.E.C.)
16" ALLOWS 8" FORWARD
ADJUSTMENT OF OIL UNIT
64" CLEAR SPACE REQUIRED
FOR OIL GUN REMOVAL
⅜" ℄
(NOT BY P.E.C.)
5/16" SUPPORT ℄
(NOT BY P.E.C.)
12" WALL
(NOT BY P.E.C.)
3/8" INNER ℄
(NOT BY P.E.C.)
18" WINDBOX DEPTH
C
B
A
–
DO NOT SCALE THIS DRAWING
PEABODY ENGINEERING
Peabody Engineering
STAMFORD, CONN.
M-15" BURNER REGISTER ASS'Y
TYPE "ABT" STEAM ATOMIZER
"FPM" IGNITOR BALL JT. SCANNER
50997
6-10-82
2
DRAWING NUMBER
B - 92690-C

NOTES:

1. ATOMIZER TIP POSITION SHOWN NOT NECESSARILY OPERATING POSITION. LOCATE SUCH THAT FLAME SWEEPS NOSE END OF THROAT.
2. COOLING AIR CONN. IS RATED FOR 75 SCFM. WHEN CONNECTED TO AIR SOURCE PRODUCING 25 P.S.I.G. PRESS. OVER MAX. FURNACE PRESS. SUPPLY AIR CONTINUOUSLY.

(Published by permission of
Peabody Engineering)

# APPENDIX D

## TEOR AD-HOC COMMITTEE REPRESENTATIVES

## TEOR AD-HOC COMMITTEE REPRESENTATIVES

| COMMITTEE MEMBER | COMPANY | TELEPHONE |
|---|---|---|
| Frank Cassick | JOHN ZINK COMPANY<br>4401 South Peoria<br>P.O. Box 7388<br>Tulsa, OK 74105 | (918) 747-1371 |
| Peter Nutcher | PROCESS COMBUSTION CORPORATION<br>1675 Washington Road<br>Pittsburgh, PA 15228 | (412) 561-6200 |
| Sherman Eaton | COEN COMPANY, INC.<br>1510 Rollins Road<br>Burlingame, CA 94010 | (415) 697-0440 |
| Ted Davies | NORTH AMERICAN MANUFACTURING COMPANY<br>4455 East 71st Street<br>Cleveland, OH 44105 | (216) 271-6000 |
| Jack Hagan | PEABODY ENGINEERING COMPANY<br>39 Maple Tree Avenue<br>Stamford, CT 06906 | (203) 327-7000 |
| Sam Davis | CHEVRON U.S.A., INC.<br>2003 Diamond Blvd.<br>Concord, CA 94520 | |
| Berwin King | STRUTHERS THERMO FLOOD CORP.<br>P.O. Box 753<br>Winfield, KS 67156 | (316) 221-4050 |
| Ken Warren | C. E. NATCO<br>Box 1710<br>Tulsa, OK 74101 | (918) 663-9100 |
| Don Harvey | ENVIRONMENTAL PROTECTION AGENCY<br>Region 9<br>215 Fremont Street (A-2-2)<br>San Francisco, CA 94105 | (415) 974-8223 |
| Tom Paxson | Kern COUNTY AIR POLLUTION<br>CONTROL DISTRICT<br>1601 "H" Street<br>Bakersfield, CA 93301 | (805) 861-3682 |

## TEOR AD-HOC COMMITTEE REPRESENTATIVES--Continued

| COMMITTEE MEMBER | COMPANY | TELEPHONE |
|---|---|---|
| Bill Nurick | ENERGY SYSTEMS ASSOCIATES<br>2522 Chambers Rd., Suite 213<br>Tustin, CA 92680 | (714) 730-5990 |
| W. Steven Lanier | COMBUSTION RESEARCH BRANCH-MD-65<br>ENVIRONMENTAL PROTECTION AGENCY<br>Research Triangle Park, NC 27711 | (919) 541-2432 |
| Alan Goodley | ENERGY STRATEGY DEVELOPMENT BRANCH<br>STATE OF CALIFORNIA AIR RESOURCES BOARD<br>1102 "Q" Street<br>Sacramento, CA 95812 | (916) 322-6020 |
| Mike Pearlsweig | CONTROL TECHNOLOGY SYSTEMS DIVISION<br>FOSSIL ENERGY (FE-23)<br>U.S. DEPARTMENT OF ENERGY<br>Washington, DC 20545 | (301) 353-2843 |
| Roy Payne | ENERGY AND ENVIRONMENTAL RESEARCH CORP.<br>18 Mason<br>Irvine, CA 92714 | (714) 552-1803 |